



HAL
open science

Kernel-nulling for the direct detection of exoplanets

Peter Marley Chingaïpe

► **To cite this version:**

Peter Marley Chingaïpe. Kernel-nulling for the direct detection of exoplanets. Sciences of the Universe [physics]. Université Côte d'Azur, 2024. English. NNT : 2024COAZ5019 . tel-04673824v2

HAL Id: tel-04673824

<https://hal.science/tel-04673824v2>

Submitted on 14 Oct 2024

HAL is a multi-disciplinary open access archive for the deposit and dissemination of scientific research documents, whether they are published or not. The documents may come from teaching and research institutions in France or abroad, or from public or private research centers.

L'archive ouverte pluridisciplinaire **HAL**, est destinée au dépôt et à la diffusion de documents scientifiques de niveau recherche, publiés ou non, émanant des établissements d'enseignement et de recherche français ou étrangers, des laboratoires publics ou privés.

THÈSE DE DOCTORAT

Kernel-nulling pour la détection directe des exoplanètes

Peter Marley Chingaipe

Laboratoire J.-L. Lagrange (UMR 7293), Observatoire de la Côte d'Azur

Présentée en vue de l'obtention
du grade de docteur en Sciences de la
Planète et de l'Univers
d'Université Côte d'Azur
Dirigée par : Frantz Martinache
Soutenue le : 27 Mai 2024

Devant le jury composé de :
Marcel Carbillet, Professeur, Observatoire
de la Côte d'Azur
Nicolas Forget, Directeur de recherche, In-
stitut de Physique de Nice
Nemanja Jovanovic, Professor, California
Institute of Technology
Lucas Labadie, Professor, Universität zu
Köln
Sylvestre Lacour, Chargé de recherche, Ob-
servatoire de Paris

Kernel-nulling pour la détection directe des exoplanètes

Kernel-nulling for the direct detection of exoplanets

Jury :

Président du jury

Marcel Carbillet, Professeur, Observatoire de la Côte d'Azur

Rapporteurs

Nemanja Jovanovic, Professor, California Institute of Technology

Sylvestre Lacour, Chargé de recherche, Observatoire de Paris

Examineurs

Nicolas Forget, Directeur de recherche, Institut de Physique de Nice

Lucas Labadie, Professor, Universität zu Köln

Directeur de thèse

Frantz Martinache, Maître de conférences, Observatoire de la Côte d'Azur

Résumé et mots clés

Résumé : La découverte et la caractérisation de planètes autour d'autres étoiles (ou exoplanètes) sont l'un des sujets les plus passionnants de l'astronomie moderne. Les méthodes de détection indirecte, qui représentent jusqu'à présent la grande majorité des exoplanètes confirmées, ont révélé l'ubiquité et la diversité de ces mondes extrasolaires. Une alternative: la détection directe par imagerie de la lumière infrarouge émise ou réfléchie par les planètes elles-mêmes, offre le meilleur moyen d'aller au delà d'une caractérisation de base et permet d'envisager la recherche de signes d'activité biologique et de déterminer leur habitabilité.

Peu de planètes ont été directement imagées. Cette entreprise particulièrement difficile nécessite en effet la combinaison simultanée d'un pouvoir de résolution angulaire élevé à une capacité d'imagerie à haute dynamique. Il faut en effet détecter des objets séparés par quelques unités astronomiques et situés à des dizaines de parsecs et surmonter le problème du grand contraste de luminosité entre une planète et son étoile hôte brillante. Ce rapport de luminosité ou contraste planète/étoile varie entre $\sim 10^{-4}$ pour un analogue de Jupiter observé dans l'infrarouge moyen et $\sim 10^{-10}$ pour les exoplanètes semblables à la Terre imagées dans le visible. Pour le moment, l'imagerie directe s'est limitée à détecter l'émission thermique des planètes géantes. Les jeunes étoiles (< 100 Myr) sont en effet des cibles idéales car: leurs planètes sont généralement plus chaudes, et donc intrinsèquement plus brillantes, ce qui se traduit par des contrastes moindres.

Pour relever ce défi d'imagerie directe, l'approche la plus commune utilise un coronographe au foyer d'un grand télescope unique bénéficiant de correction du front d'onde via une optique adaptative extrême. De tels systèmes sont caractérisés par un angle de travail interne (IWA) de quelques éléments de résolution exprimés en unités de λ/D , où λ est la longueur d'onde d'observation et D le diamètre du télescope. Les planètes directement imagées ont donc été détectées à de larges séparations orbitales ($\sim 10 - 250$ AU). Pour obtenir une résolution angulaire élevée, on peut recourir à l'interférométrie longue base et mettre en oeuvre une recombinaison annulante, fonctionnant de la même manière qu'un coronographe en supprimant la lumière d'une étoile non-résolue, avec un IWA

bien amélioré qui peut être plus petit que λ/B , où B est la ligne de base interférométrique.

Bien que cette approche soit une perspective alléchante, elle se heurte à de nombreux défis pratiques. La performance du nuller est en particulier très sensible aux différences résiduelles de chemin optique entre les faisceaux entrants du télescope, même après une optique adaptative ou une correction du suivi de franges. Une architecture d'annulation et une technique de réduction des données récemment proposées, appelées kernel-nulling, tentent d'atténuer ce problème en permettant une solution d'imagerie fiable à contraste élevé, indépendante des perturbations de phase induites par les pistons atmosphériques de second ordre.

Cette thèse évalue le potentiel astrophysique d'un kernel-nuller à 4 entrées et 7 sorties s'il était mis en oeuvre au VLTI (Very Large Telescope Interferometer). Elle explore ensuite les façons de fabriquer un tel nuller à base d'optique intégrée. Une implémentation plus simple, d'un nuller à 4 entrées et 4 sorties, peut être fabriqué à partir d'une seule cavité à interférences multi-modes (MMI) en optique intégrée. Cette thèse décrit un travail de caractérisation expérimental d'un tel kernel-nuller simplifié, aboutissant à la formation d'au moins un observable auto-étalonné appelé kernel-nul. Un spectrographe permet d'examiner le comportement chromatique de cette technologie et permet d'imaginer des stratégies qui le rendront utilisable sur une plus large bande spectrale.

Mots clés : interférométrie, optique, exoplanètes

Abstract and keywords

Abstract : The discovery and characterisation of planets around other stars (or exoplanets) is one of the most exciting topics in modern astronomy. Indirect detection methods, which account for the vast majority of confirmed exoplanets thus far, have revealed the ubiquity and diversity of these worlds beyond our Solar System. However, rather than inferring their existence and properties, the direct detection (a.k.a., direct imaging) of the infrared light emitted or reflected by the planets themselves could offer the best means of searching for indications of biological activity, and the possibility of determining their habitability.

Few planets have been directly imaged as it is an especially difficult endeavour that requires the simultaneous combination of a high angular resolving power, needed to detect objects separated by a few astronomical units and located tens of parsecs away, with high dynamic imaging capability to overcome the large contrast between the faint planet and its bright host star. The planet/star contrast ratio ranges between $\sim 10^{-4}$ for a Jupiter analogue observed in the mid-infrared to $\sim 10^{-10}$ for Earth-like exoplanets imaged in the reflected light from their primary. Consequently, direct imaging has predominantly been the detection of the thermal emission of giant planets. Indeed, young stars (< 100 Myr) make for ideal targets as they are generally warmer, and therefore intrinsically brighter exoplanets result in even lower contrasts.

To address this direct imaging challenge, the conventional approach has been the use of a single aperture coronagraph with wavefront correction via extreme adaptive optics on a large telescope. Such systems are limited to observing beyond an inner working angle (IWA) of a few resolution elements expressed in units of λ/D , where λ is the wavelength of observation and D the diameter of the telescope. This is why most of the directly imaged planets have been detected at wide orbital separations (10 - 250 AU). To gain a high angular resolution, one can resort to long-baseline nulling interferometry, which works in a similar way as a coronagraph in suppressing the on-axis light of a star, with a much improved IWA that is smaller than λ/B , where B is the interferometric baseline.

Although the use of interferometric nulling for the detection and characterisation of the thermal emission from young giant exoplanets is a tantalising prospect, it encounters many practical challenges when deployed on telescopes.

The largest limitation being the extreme sensitivity of a nuller to residual optical path differences between the incoming telescope beams even after adaptive optics or fringe-tracker correction. A recently proposed nulling architecture and data reduction technique, called kernel-nulling, attempts to alleviate this by enabling a reliable high-contrast imaging solution that is independent of second-order atmospheric-piston-induced phase perturbations.

This thesis evaluates the astrophysical potential of a 4-input/7-output kernel-nuller as the prime high-contrast imaging mode of the Very Large Telescope Interferometer (VLTI). Apart from a complete design, kernel-nulling solutions can also be found with a reduced number of outputs that nevertheless result in the formation of at least one self-calibrating observable. Consequently, the thesis investigates the spectral behaviour of one such solution - a 4-input/4-output kernel-nuller embedded on a 16-mm x 16-mm photonic chip.

Keywords : interferometry, optics, exoplanets

For Mama, Father, Santilla and Delia

Foreword

The main objective of this PhD was to study a new approach to nulling interferometry, relying on a concept called kernel-nulling. My work on kernel-nulling has focused on numerical simulations and the experimental characterisation of a photonic kernel-nuller.

One of the most exciting topics in modern astronomy is the discovery and characterisation of planets around other stars (or exoplanets). Indirect detection methods, which infer their existence and properties, have revealed the ubiquity and diversity of these worlds beyond our Solar System. However, the direct detection (a.k.a., direct imaging) of the infrared light emitted or reflected by the planets themselves could offer the best means of searching for indications of biological activity, and the possibility of finding out if they are habitable. In Chapter 1 of this manuscript I review the indirect methods that account for the vast majority of confirmed exoplanets thus far, and consider why direct imaging is an especially difficult endeavour that requires requires high-contrast imaging at high angular resolution.

Direct imaging has predominantly been the detection of the thermal emission of young giant planets as the contrast between them and a bright host star is favourable in the mid-infrared ($\sim 10^{-4}$). Most of these ideal targets have been detected at wide orbital separations ($\sim 10 - 250$ AU) by way of a single aperture coronagraph with wavefront correction via extreme adaptive optics on a large telescope. Chapter 2 looks at how a gain in angular resolution can be achieved with nulling interferometry, which works in a similar way as a coronagraph in suppressing the on-axis light of a star. This chapter presents the theory behind nulling interferometry, building from a simple two-aperture interferometer and onto a four-aperture architecture (the so-called double Bracewell) that was employed for the ESA/Darwin and NASA/TPF-I space missions.

Nulling interferometry encounters many practical challenges when deployed on ground-based telescopes. The largest limitation being the extreme sensitivity of a nuller to residual optical path differences between the incoming telescope beams even after adaptive optics or fringe-tracker correction. Chapter 3 introduces kernel-nulling, a nulling architecture and data reduction technique

that enables a reliable high-contrast imaging solution independent of second-order atmospheric-piston-induced phase perturbations. The kernel-nuller replicates several properties of the double-Bracewell architecture, but its theory is quite general and leads to a wider family of self-calibrating solutions, which I show in this chapter.

Initially, this work was supposed to be entirely on the laboratory characterisation of a kernel-nuller photonic chip. The arrival of the Covid-19 pandemic meant that my objective shifted towards developing a numerical simulation that could enable us to evaluate the astrophysical potential of a kernel-nuller as the prime high-contrast imaging mode of the Very Large Telescope Interferometer (VLTI). This simulation modelled baseline projection effects induced by Earth rotation in order to determine the response of a kernel-nuller, and was used to design an observing program for the detection and characterisation of the thermal emission from young giant exoplanets. The published results of this study are the focus of Chapter 4.

Chapter 5 gives a general overview of waveguiding photonic components that are applied in astronomy to overcome the deficiencies of conventional bulk optics instrumentation. This includes integrated optics beam combiners that perform several functions (i.e., routing, beam splitting, and recombination) in a microchip. The overwhelming majority of these devices employ pairwise beam combination, which does not facilitate a kernel-nuller architecture requiring the simultaneous nulling of multiple baselines. However, a multimode interference (MMI) coupler can be used. In this chapter, I present the 16 x 16 mm kernel-nuller photonic chip that includes numerous kernel-nuller architectures implemented with MMIs.

After the pandemic, lab activities resumed and the first task I had was to design and integrate a spectrograph on the kernel test bench located at the Lagrange Laboratory. This project entailed the use of inexpensive commercial off-the-shelf optical elements including the simulation of their assembly in CAD software. Chapter 6 describes the kernel test bench and its spectrograph.

The spectrograph enabled me to perform the spectral characterisation of a four-input kernel-nuller, whose results were initially published in the proceedings of the 2022 SPIE Montréal conference, and are the subject of chapter 7. This manuscript concludes by expanding on these results that I aim to submit for journal publication.

Contents

| | | |
|----------|--|-----------|
| 1 | Introduction | 11 |
| 1 | Indirect Detection Methods | 11 |
| 1.1 | Radial velocity | 12 |
| 1.2 | Transit photometry | 14 |
| 1.3 | Current exoplanets statistics | 17 |
| 2 | Direct imaging | 19 |
| 2.1 | High-contrast direct imaging in operation | 21 |
| 3 | Summary | 27 |
| 2 | Optical Interferometry | 29 |
| 1 | Nulling Interferometry | 31 |
| 1.1 | Bracewell nuller response | 33 |
| 1.2 | Transmission map | 35 |
| 1.3 | The null-depth | 36 |
| 1.4 | Geometric stellar leakage | 37 |
| 2 | Two-telescope on-sky nulling | 37 |
| 2.1 | Numerical self calibration | 39 |
| 2.2 | Exozodiacal dust | 43 |
| 3 | Nulling with more than two telescopes | 45 |
| 3.1 | Phase modulation and array configurations | 45 |
| 3.2 | Systematic noise | 49 |
| 3.3 | Space and ground-based nulling with a double Bracewell | 51 |
| 4 | Summary | 56 |
| 3 | Kernel-nulling interferometry | 59 |
| 1 | A brief introduction to kernel-nulling | 60 |
| 2 | Simplified kernel-nuller architecture | 67 |
| 3 | 3x3 kernel-nuller | 69 |
| 4 | 4x4 kernel-nuller | 73 |
| 5 | 5x5 kernel-nuller | 78 |
| 6 | Summary | 82 |

| | | |
|----------|--|------------|
| 4 | High-contrast detection of exoplanets with a kernel-nuller at the VLT | 85 |
| 5 | Photonics | 99 |
| 1 | A brief introduction to astrophotonics | 99 |
| 1.1 | Integral field units | 101 |
| 1.2 | Interferometric beam combiners | 105 |
| 2 | Integrated optics beam combiners | 107 |
| 3 | Multimode interference coupler | 114 |
| 4 | Photonic chip components | 116 |
| 5 | Summary | 122 |
| 6 | Kernel test bench | 125 |
| 1 | Experimental setup | 125 |
| 2 | Injection optimisation and phase set-point | 129 |
| 3 | Spectrograph | 132 |
| 3.1 | Optical elements | 132 |
| 3.2 | Spot diagrams | 137 |
| 3.3 | Integration and wavelength calibration | 138 |
| 4 | Summary | 149 |
| 7 | Spectral characterisation of a 4x4 kernel-nuller | 151 |
| 1 | SPIE publication | 151 |
| 2 | Characterisation results continued | 163 |
| 2.1 | Nuller response matrix | 163 |
| 2.2 | Characterisation of a 4x4 MMI | 165 |
| 2.3 | Spectral behaviour of a 4x4 MMI | 171 |
| 3 | Summary | 176 |
| 8 | Conclusions | 177 |
| | Appendix A: Kernel-nulling at CHARA | 181 |

Chapter 1

Introduction

Our Sun is one amongst an estimated 250 billion stars in the Milky Way galaxy. Yet it hosts eight planets, so planets may be more numerous than stars and it is probable that some of these so-called exoplanets may be habitable or possibly even life-bearing. Such a prospect has the potential to revolutionise humanity's perception of its own place in the cosmos.

1 Indirect Detection Methods

Exoplanets are dim and distant, so much so that taking an image of one remains exceedingly difficult, even with powerful telescopes. Which is why nearly all of the 5,000+ exoplanets discovered within our galaxy have been detected through indirect methods. These indirect detection methods infer the presence of the planet by measuring stellar perturbations such as its reflex motion in response to an orbiting planet (i.e. radial velocity or astrometric measurement) or in its temporal intensity variations caused by planetary transit or microlensing events. The study of exoplanets is a fairly new branch of astrophysics, with the first confirmation of detection made in 1992 by Aleksander Wolszczan and Dale Frail. They discovered a multi-planet system orbiting a rapidly rotating neutron star (also known as a pulsar). As a pulsar rotates it emits an intense electromagnetic radiation on timescales of milliseconds that is detected on Earth as a pulse. A change in period of the received pulses can be attributed to the movement of the pulsar in an orbit with one or more planets. This indirect method —called pulsar timing— enabled Wolszczan & Frail to detect two super-Earths orbiting the millisecond pulsar PSR1257+12 ([Wolszczan & Frail 1992](#)).

Earth is still the only place in the cosmos we know to be home to life. But super-Earths are easier to detect than Earth-sized planets as they are more massive though smaller than ice giants like Uranus and Neptune. It seems reasonable, at least initially, to search for life on these exoplanets that are similar to our own. One would then assume that M-type stars would be prime targets due to the

great abundance of these stars in the galaxy, their long lifetimes and that the habitable zone resides much closer (around 0.1 AU) in cool M-type stars than for solar-type primaries (F8 to K2). However, concerns have been raised over their suitability as hosts to life-bearing planets. [Hawley & Pettersen \(1991\)](#) observed a heightened stellar activity on the M-type star AD Leonis, and according to [Kasting et al. \(1993\)](#), a planet orbiting such a star is often tidally locked.

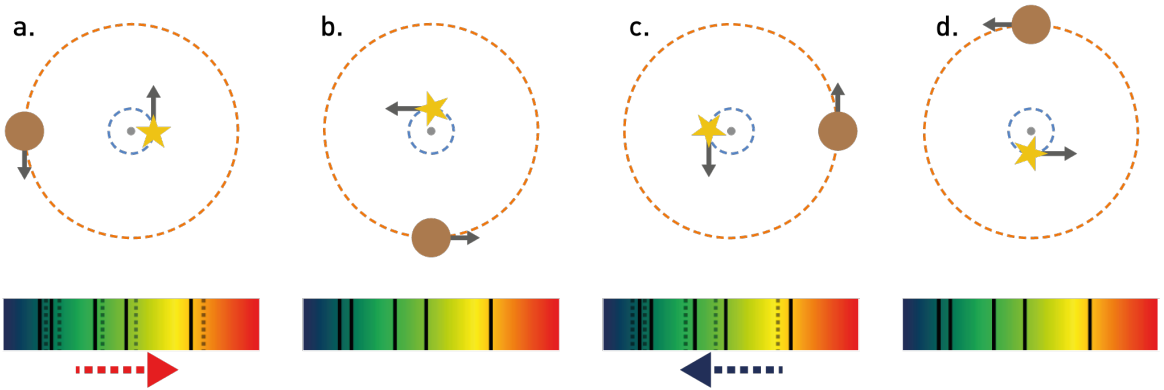


Figure 1: Exoplanet detection with the radial velocity method. The planet and star both orbit around a common centre of mass which is represented by a grey dot. The presence of a planet will induce a periodic change of the stellar velocity vector, whose radial component can be measured by monitoring the stellar spectrum. As the star moves away from Earth (panel a), light waves leaving the star are "stretched" and move towards the red end of the spectrum, i.e., spectral lines are red-shifted. As the star moves towards Earth (panel c), light waves leaving the star are "compressed" and move towards the blue end of the spectrum, i.e., spectral lines are blue-shifted. The solid black lines in the spectra represent the rest-frame of the star; the dotted lines indicate the red-shift (panel a) and blue-shift (panel c) of absorption lines due to the orbital motion of the planet. Measuring the periodic change in the stellar radial velocity allows us to constrain the planet's mass and orbital period.

1.1 Radial velocity

A few years after the two pulsar planets were found, Michel Mayor and Didier Queloz discovered the first exoplanet orbiting a main sequence (G2-type) star which led to the award of the Nobel Prize in Physics in 2019. This planet, designated as 51 Pegasi b ([Mayor & Queloz 1995](#)), was discovered using the radial velocity method (see Fig. 1). The method consists of observing a star for signs of movement which are caused by the gravitational tug of a planet. The slight movements (i.e. radial velocity change) of the star will affect its light spectrum. If the orbital plane of the distant planetary system appears edge-on ($i = 90^\circ$) when

observed from Earth, the entire movement of the star will be towards or away from an observer, and can be detected with an extremely sensitive spectrograph. Through what is known as the Doppler shift, an observer can deduce whether the star is moving towards them if its spectrum appears shifted toward shorter wavelengths (called blue-shift). If the star is moving away, then its spectrum will be shifted toward longer wavelengths (red-shift). From this shift, the stellar radial velocity fluctuations can be determined, whose period is equal to the planet's orbital period. Measuring the planet's orbital period allows us to infer its minimum mass. The minimum mass (usually labelled $M_p \sin i$) is related to the amplitude Δv of the radial velocity signal by the following expression (assuming a circular orbit):

$$\Delta v = \left(\frac{2\pi G}{P} \right)^{1/3} \frac{M_p \sin i}{(M_\star + M_p)^{2/3}}, \quad (1.1)$$

where G is the gravitational constant, P the orbital period of the planet, M_p the planetary mass, i the inclination of the orbit ($i = 0^\circ$ for a face-on system) and M_\star the stellar mass. In most cases a planetary system's orbital plane is neither edge-on nor face-on when observed from Earth. More often than not, the orbital plane is tilted at some unknown angle to the line of sight.

Equation (1.1) implies that without an accurate determination of the orbital inclination, only an estimate of the planet's minimum mass can be determined. This is because a heavy planet/small star on a close-to face-on orbit can cause the same radial velocity signal as a low-mass planet orbiting almost edge-on. Although Δv theoretically increases with decreasing M_\star (from Eq. (1.1)), this does not necessarily mean that low mass M-type stars are the best targets to search for radial velocity planets. Other factors such as their stellar activity, which is a source of noise, and low luminosity can be practical limitations to the sensitivity of the radial velocity method. Despite these challenges, [Anglada-Escudé et al. \(2016\)](#) discovered a super-Earth with a minimum mass of $1.3M_\oplus$ and an orbital period of ~ 11.2 days around the nearest-known star to the Sun, the M-type star Proxima Centauri.

Considering that Δv also increases for close-in planets, this means that the radial velocity signal is more sensitive to massive planets orbiting close to their host star. Discoveries such as 51 Pegasi b consequently introduced an entirely new class of exoplanet called a hot-Jupiter. These gas giants, similar to our neighbour Jupiter, typically have masses spanning $0.3 - 11.8 M_{\text{Jup}}$ and orbital periods less than 10 days. To confirm a detection, at least one orbital period should be

observed, which is short for hot-Jupiter's but will require years of reliable observations for planets orbiting further away from their host star. Fischer et al. (2008) confirmed several long period planets on the nearby solar analog 55 Cancri (K0-type) with 18 years of Doppler shift measurements.

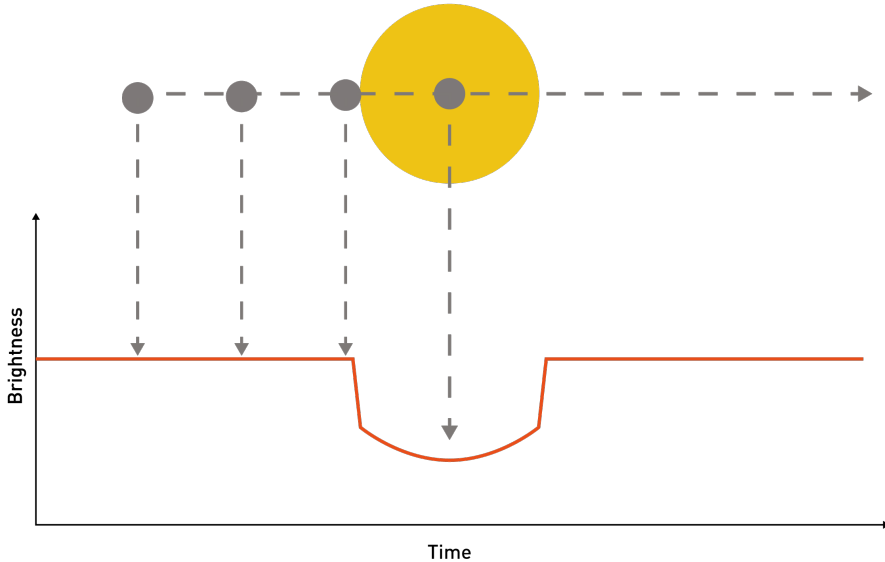


Figure 2: Exoplanet detection with the transit photometry method. The passage of a planet across the line of sight between an observer and a star is called a transit. Although we cannot see the planet, we can observe the starlight dim, which corresponds to a dip in the light curve. Repeat transits result in a periodic dimming event that can be measured via continuous monitoring of the stellar luminosity. Measuring the periodic change in stellar luminosity allows us to constrain the planet's diameter and orbital period.

1.2 Transit photometry

Although the radial velocity method did dominate the earliest exoplanet discoveries, transit photometry (see Fig. 2) has been the most prolific indirect method thus far. The first exoplanet to be detected with this method was the planetary-mass companion HD 209458b (Charbonneau et al. 2000) in 1999. For this detection, a 10-cm diameter telescope set-up in a laboratory car park observed the passage of the planet across the stellar disk. As the planet passes in front of the star, it blocks out a portion of the starlight, similar to a solar eclipse observed on Earth but of a much smaller magnitude. Assuming a full planet is like the grey

disk —shown in Fig. 2— transiting a homogeneous photosphere, the decrease in stellar intensity is described as the depth of transit $\frac{\Delta F}{F}$, and is given as:

$$\frac{\Delta F}{F} = \left(\frac{R_p}{R_\star} \right)^2, \quad (1.2)$$

where R_p and R_\star are the respective radii of the planet and star. HD 209458b orbits a Sun-like (G0-type) star and has a transit depth of around 1.7%. For a star the size of the Sun, the transit of a Jupiter-size planet will cause a transit depth of about 1%, while this decrease will be about 0.001% for a planet the size of the Earth. Due to their smaller stellar radii, M-type stars are favourable targets for planet searches as the transit depth is relatively larger (and therefore easier to detect) compared to solar-type primaries. This advantage revealed the presence of seven rocky Earth-sized planets in the habitable zone of the M-type star TRAPPIST-1 (Gillon et al. 2017).

In order to observe a transit, the planet must be in a nearly edge-on orbit around its host star, but this is only true for a small minority. Assuming that the size of the planet is much smaller than the star's, the probability that its orbit coincides with an observer's vantage point is given as:

$$p = \frac{R_\star}{a}, \quad (1.3)$$

where a is the orbital semi-major axis. For a star the size of the Sun, the probability of a planetary transit at an Earth-Sun distance is about 0.5%, while the probability for a Jupiter-Sun distance is about 0.1%. Indeed, there is a higher probability of detection for short-period planets orbiting a large star, however, the method is most effective when surveying a very large sample of stars simultaneously. With this purpose in mind, NASA's first exoplanet-hunting mission —Kepler (Borucki et al. 2010)— monitored about 200,000 stars for such transiting events and has detected more than half of all planets known today. Based on Kepler's findings, super-Earths and mini-Neptunes are the two most common type of planets observed in our galaxy.

The precise photometry provided by the Kepler spacecraft enabled Gautier et al. (2012) to discover two Earth-sized planets orbiting the solar analog (G8-type) Kepler-20. Here, the respective transit depths of Kepler-20e and Kepler-20f were approximately 0.008% and 0.01%. Due to the high rate of false detections, an observation of a single transit is not sufficient to be fully accepted as a planet. To confirm a detection, the planetary transit has to occur periodically, which allows us to determine its orbital period. If the stellar mass is known, the orbital

separation can be derived from the period according to Kepler's 3rd law. For the planets orbiting Kepler-20, the two small signals recur with periods of 6.1 days (Kepler-20e) and 19.6 days (Kepler-20f).

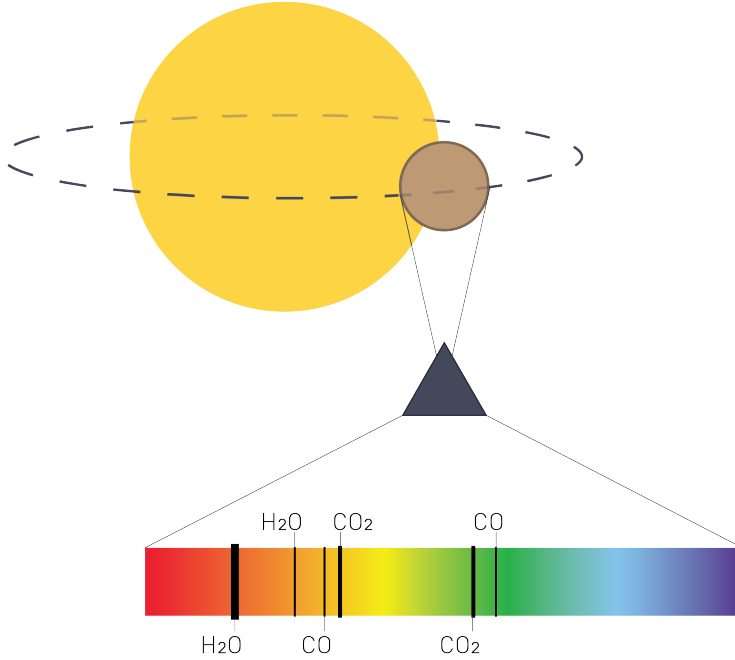


Figure 3: Exoplanet characterisation with the transit spectroscopy technique. As a planet transits a star, a small fraction of the stellar light passes through its atmosphere. Molecules present in the planetary atmosphere such as H_2O , CO and CO_2 will absorb some of this light at specific wavelengths while light of other wavelengths can pass through unhindered. With a prism spectrograph, we can take the spectrum of this starlight which is filtered through the planet. By comparing this spectrum to the spectrum of the unfiltered starlight detected outside a transit, we can determine the chemical composition of the planetary atmosphere. The black lines that appear in the spectrum are called absorption lines, which correspond exactly to the absorption spectrum of an element. Adapted from <http://esa.int/>.

The gas giant HD 209458b had already been confirmed with radial velocity measurements by the time the transit observations were carried out. The planetary mass and radius derived from these respective methods can be combined to provide constraints on the interior properties of the planet - i.e., determining if it is a rocky one similar to Earth, an icy planet like Uranus, or a gas giant like Jupiter. Beyond the planet mass and radius, the planet's atmosphere can be studied in search of biosignatures by combining transit photometry with spectroscopy. This technique, called transit spectroscopy (see Fig. 3), has been utilised

with the JWST Near-Infrared Imager and Slitless Spectrograph (NIRISS) to reveal the atmospheric characteristics of WASP-96b (Samra et al. 2022). The transmission spectrum of this gas giant which orbits a G8 primary is made by comparing starlight filtered through the planet's atmosphere during a transit, to the unfiltered starlight detected outside a transit. Each element present in the planet's atmosphere is associated with a specific set of wavelengths that it blocks due to its chemical properties. This will result in the appearance of black lines in the spectrum called absorption lines. If the absorption lines of the stellar spectrum correspond exactly to the absorption spectrum of an element, then it indicates its presence. The spectrum of WASP-96b confirmed the presence of water, as well as providing indications of haze, and evidence for clouds that were previously reported by Nikolov et al. (2018) to be absent.

In addition to the primary transits discussed thus far, we are also interested in secondary transits, which occur when a planet passes behind the star. A planet's spectrum can be determined by measuring the stellar luminosity and then subtracting it from measurements of the luminosity before the secondary transit. One can deduce the planet's temperature from its spectrum, and infer the composition of its atmosphere.

1.3 Current exoplanets statistics

Using data from <http://exoplanet.eu/>, an online database which provides a list of confirmed exoplanets along with their characteristics, I have generated a plot of the planets discovered in terms of the planet mass vs. planet-star separation as shown in Fig. 4. Approximately 90% of the exoplanets discovered thus far have been detected with radial velocity and transit photometry. Hot-Jupiter's reside in the upper left corner of the figure and cooler gas giants in the upper right. The majority of detected planets are in the $0.01 - 3 M_{\text{Jup}}$ range with semi-major axes from 0.01 AU to 10 AU. Brown dwarfs, considered to be objects between planets and stars are found in the $13 - 80 M_{\text{Jup}}$ range.

Though many of the planets shown in Fig. 4 don't seem to have Jupiter's orbital period (4331 days), a large number of them either have a mass greater than Jupiter's or an orbital period smaller than that of Mercury (88 days). Before the discovery of exoplanets, the general consensus was that the smaller sized planets would orbit closer to the star and perhaps the massive ones remained further out. The exoplanets discovered so far are not like our solar system in terms of planetary positioning which suggests that planet formation occurs in a wide variety of initial conditions, and together with theories of planetary migration gives rise to such a wide distribution.

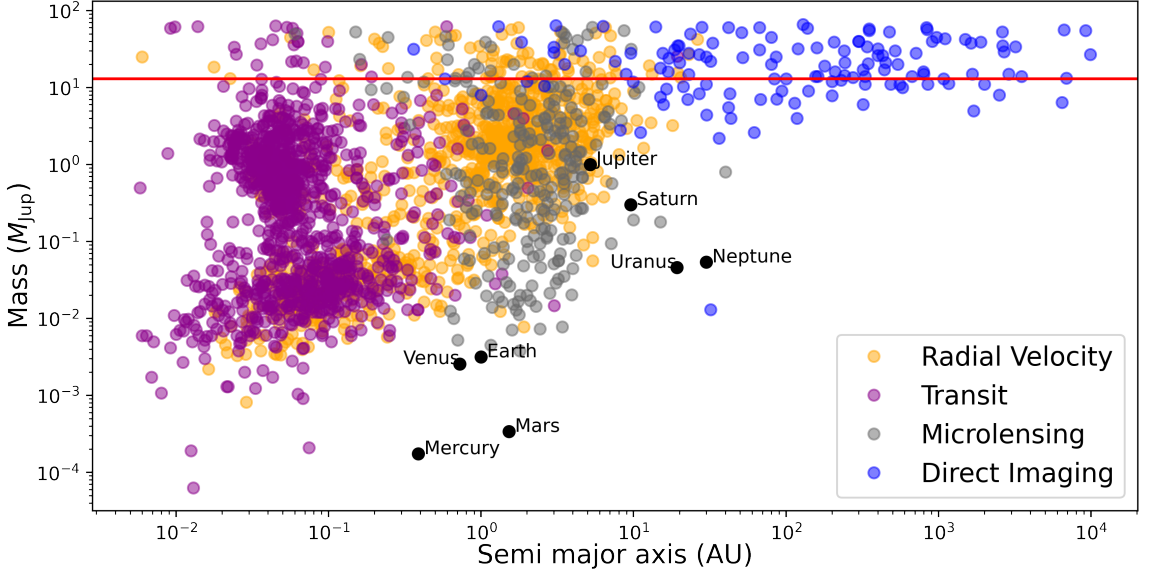


Figure 4: Planet mass as a function of semi-major axis for confirmed exoplanets, and comparison with solar system planets. Exoplanets are categorised according to the detection method, as indicated by the coloured labels in the bottom right. The solid red line marks the conventional upper mass limit for the definition of a planet. Data extracted from <http://exoplanet.eu/> in October 2023.

The technological and methodological biases of the detection methods explains some of the blank regions in Fig. 4. For instance, in the mass range of $10^{-3} - 10^{-4} M_{\text{Jup}}$, we can detect planets up to about 0.1 AU. However, as the semi-major axis of which radial velocity and transit observations are dependent increases, the planets become much harder to detect. The amplitude of the radial velocity signal (see Eq. (1.1)) decreases with increasing orbital period and similarly the transit probability (see Eq. (1.3)) of a planet decreases with increasing semi-major axis. This is why many planets have been detected in the upper left corner, but none in the lower right corner of Fig. 4.

A much smaller subset of detections have been made with other methods such as gravitational microlensing, which infers the presence of a planet by the deflection it inflicts on the light of a background star. This method is sensitive to a wide range of planet-star separations and will play an important role in mapping out the planet distribution with the Nancy Grace Roman Space Telescope (Penny et al. 2019). Only $\sim 4\%$ (233 out of 5506 as of October 2023) have been discovered by taking a direct image of the companion. This small number is due to the challenging nature of imaging a faint planet right next to its host star that

is many orders of magnitude brighter, which is why most of these planets are at wider separations. Although transit photometry also provides the planet’s thermal emission, high-contrast imaging at high angular resolution can be applied to planetary systems of any orientation, and with planets encompassing diverse orbital periods.

2 Direct imaging

Most of the directly imaged planets shown in Fig. 4 lie above the conventional upper mass limit (marked by the solid red line) for the definition of a planet, but they are all classified as gas giants, which are thought to form in two possible ways. In the core accretion (Pollack et al. 1996) scenario, dust particles in the protoplanetary disk that surrounds young stars coagulate and form solid cores. Gas giants develop when these cores are heavy enough such that they can accrete the gas in the protoplanetary disk. This scenario which is believed to be the formation mechanism of Jupiter and Saturn has been described to work effectively in the inner regions of the disk (few AU). On account of the low initial entropy of the planet after formation, it is also referred to as the “cold-start” model. In the opposing disk instability (Boss 1997) paradigm, the planet forms from an over-density in the protoplanetary disk such that the gas collapses directly to form a giant planet. Here the planet retains most of its initial entropy, which is higher than in the core accretion formation process, thus we refer to it as the “hot-start” model. Planet formation through gravitational instabilities is deemed to operate in the outer disk regions (tens to hundreds of AU) and in the earliest stages of disk evolution. Due to the differing predictions made by both models about the location of planet formation and the planet’s initial entropy, observable differences can be used to distinguish whether a giant planet formed by core accretion or disk instability. These differences are considerable when the planet is young and diminish as it ages. To understand planet formation, we should detect planets shortly after birth.

The direct imaging discovery of PDS 70b (Keppler et al. 2018) enabled the observation of the dynamical interaction between the young planet and the protoplanetary disk in which it was formed. As a disk will outshine a planet, it is extremely challenging to detect the forming planet’s faint emission. The emission from a planetary companion can generally be separated into two sources: stellar emission reflected by the planet surface and/or atmosphere, and thermal emission from the planet itself. For either of these two emission sources, the wavelength-dependent ratio of the observed planetary flux and the stellar flux

(or planet/star contrast) is a key parameter used to determine the detectability of an exoplanet. For reflected light it can be approximated by:

$$c_R(\lambda) = A \left(\frac{R_P}{a} \right)^2, \quad (1.4)$$

where A is the monochromatic geometric albedo, R_P the planetary radius and a the orbital semi-major axis. For a mature (5 Gyr) Earth analog with a geometric albedo of 0.3, Eq. (1.4) provides a contrast of 5×10^{-10} . Meanwhile, the detection of a Jupiter analog ($A = 0.5$) is not more favourable as the larger orbital separation reduces the amount of reflected stellar emission, providing a contrast of 4×10^{-9} .

The planet/star flux ratio for self-luminous planets assumed to have a black-body spectrum is given as:

$$c_T(\lambda) = \left(\frac{R_P}{R_\star} \right)^2 \frac{T_P}{T_\star}, \quad (1.5)$$

where R_\star is the stellar radius, T_P and T_\star are the respective temperatures of the planet and star. Here, an Earth and Jupiter analog yield contrasts of 4×10^{-6} and 2×10^{-4} , respectively (where $T_\star = 5800 \text{ K}$, $T_P = 250 \text{ K}$ for Earth and $T_P = 130 \text{ K}$ for Jupiter). The 4-5 orders of magnitude contrast reduction is the reason why direct imaging has predominantly been the detection of the thermal emission of a planet.

Young stars ($< 100 \text{ Myr}$) are more favourable targets for direct imaging as they are generally warmer, and therefore intrinsically brighter exoplanets result in even lower contrasts. At a projected separation of $\sim 22 \text{ AU}$, PDS 70b orbits a young K7 primary, which is classed as a T-Tauri star (Joy 1945). This is a star of spectral type F, G, K or M and a mass of up to $2 M_\odot$. Its intermediate mass (2-8 M_\odot) counterpart, of spectral type A or B is known as a Herbig star (Herbig 1960). Warm (1000-2000 K) self-luminous planets orbiting such stars can be found in nearby young moving groups that typically lie within a few hundred parsecs from the sun. These include: AB Doradus (Bell et al. 2015), Coma Berenices (Silaj & Landstreet 2014), ϵ Chamaeleontis (Murphy et al. 2013), Lower Centaurus Crux (Pecaut & Mamajek 2016), Taurus (Kenyon & Hartmann 1995), etc. The PDS 70 system is a member of the Upper Centaurus-Lupus (Pecaut & Mamajek 2016) subgroup of the Scorpius-Centaurus association, at a distance of $\sim 113 \text{ pc}$. Young star-forming regions located further away are similar in many respects and are distinguished by signs of very recent or ongoing star-formation such as nebulosity.

At infrared wavelengths, the planets are more luminous and a star has less flux, which provides an advantageous contrast ratio. However, some objects found in the infrared may not be exoplanets. Brown dwarfs are also low-mass, faint, and detected most easily in this wavelength domain. Given that the Earth’s atmospheric transparency is limited, the H , K and L infrared wavebands are commonly used atmospheric windows in direct imaging. Some wavebands are better suited for observing certain objects than others, as demonstrated by the discovery of HD 95086b (Rameau et al. 2013) in the L' -band ($3.8\mu\text{m}$). This $\sim 5 M_{\text{Jup}}$ companion, whose mass was estimated from hot-start evolutionary models, orbits a young A8 Herbig star and had previously been undetected in the H ($1.65\mu\text{m}$; Meshkat et al. 2013) and K_s ($2.3\mu\text{m}$) bands. The different wavebands bring a new constraint on the target of interest, which was the case with the first ever image of an exoplanet – 2M1207b (Chauvin et al. 2004). Three exposures – in the H , K_s and L' wavebands – were combined to create one image that revealed a planetary mass companion orbiting a brown dwarf located in the young TW Hydrae Association (Bell et al. 2015).

The mid-infrared domain ($6\text{--}20\mu\text{m}$) contains a number of spectral features that could be detectable with low resolution spectroscopy. Based on a space telescope concept for mid-infrared spectroscopy of Earth-like planets, Angel et al. (1986) showed that the mid-infrared is remarkably informative and can reveal valuable absorption features such as: $6\text{--}8\mu\text{m}$ (H_2O) can allow us to infer whether a planet is habitable, $7.7\mu\text{m}$ (CH_4) would require a higher spectral resolution but can suggest biological activity, $9.6\mu\text{m}$ (O_3) is a tracer of O_2 , and $15\mu\text{m}$ (CO_2) can indicate a similarity with the atmospheres of Venus, Earth and Mars which all contain CO_2 . Studying the chemistry of exoplanet atmospheres may potentially lead to constraints on their composition and formation process.

2.1 High-contrast direct imaging in operation

To achieve the ambitious goal of directly imaging an exoplanet requires at the very least spatially resolving the planet from its host. The fundamental limit of angular resolution is imposed by diffraction, whose characteristic scale is given by the ratio:

$$\theta = 200 \frac{\lambda}{D}, \quad (1.6)$$

where θ (in mas) is the angular resolution, λ (in μm) is the wavelength of observation and D (in metres) is the diameter of the aperture. 10-m class telescopes are the largest category of currently operating optical telescopes. Applying Eq. (1.6)

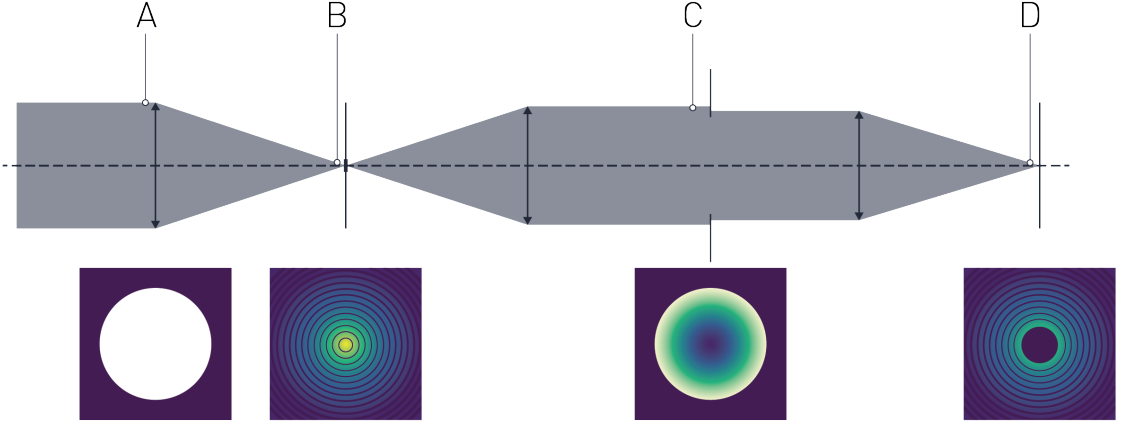


Figure 5: Optical design of a Lyot coronagraph. The light enters through the pupil (A), and is imaged onto the focal plane (B). Here, we see the resulting diffraction pattern as a bright spot in the centre, with a series of concentric rings of decreasing intensity around it, called the Airy pattern. The diameter of this pattern is related to the wavelength and the size of the aperture. At the focal plane, an opaque mask is placed, which forces most of the light from the central part of the Airy pattern (i.e. where a bright source is located) to diffract around its edges. As the light from an off-axis source enters the optical system at an angle, it avoids the mask and isn't diffracted to the edges. The mask is usually at least three Airy rings wide. When the pupil is re-imaged, the majority of the remaining light from the on-axis source is distributed at the edges of the pupil image. Next, a Lyot-Stop (C) blocks out the on-axis light diffracted on the pupil edges while allowing most of the light from an off-axis source to pass through the system. Finally the coronagraphic image is formed on the detector (D). Adapted from [Guyon et al. \(1999\)](#).

for an observation in the L-band ($\lambda = 3.6 \mu\text{m}$) gives a 72 mas angular resolution. Large aperture sizes are therefore required to probe tiny angular scales of a few tens of milliarcseconds.

The vast distances (> 100 pc) to young star-forming regions means that these planets are located at very small angular separations from their host star where typically the contrast of the imaging system will degrade. One can compute the maximum angular separation $\Delta\theta$ (in mas) of the planet and star by:

$$\Delta\theta = 1000 \frac{a}{d}, \quad (1.7)$$

where a (in AU) is the orbital semi-major axis and d (in parsecs) is the distance to the system. The majority of sub-stellar companions detected to date have separations < 10 AU (see Fig. 4). This translates to angular separations < 100 mas at a distance of 100 pc. For a 10-m telescope, planet's with separations ≤ 7 AU will be undetectable. While this estimation is in theory correct, there are other effects that need to be considered when performing observations from the ground.

Overcoming a large contrast ratio is not particular to the detection of exoplanets. Up until the 1930's, observing the solar corona, which is 10^{-6} of the photospheric intensity, was only possible during a total solar eclipse. A breakthrough for the observation of this faint outer component of the Sun outside of solar eclipses was made by Bernard Lyot, using what is now known as the Lyot coronagraph (Lyot 1939). The idea behind coronagraphy is to suppress the diffraction effects of the star in order to allow off-axis light surrounding it to be detectable with a sufficient signal-to-noise ratio. The Lyot coronagraph works in the following way: light enters through the telescope aperture, or pupil (Fig. 5 A), and is imaged onto the focal plane (Fig. 5 B). Here, an opaque mask forces most of the light from the centre of the field of view (i.e. where a bright source is located) to diffract around its edges. As the light from an off-axis source enters the optical system at an angle, it avoids the mask and isn't diffracted to the edges. In the re-imaged pupil any remaining light from the on-axis source is concentrated in a ring around the edges of the pupil. Next, an aperture stop, called a Lyot-Stop (Fig. 5 C) after its inventor, blocks out the on-axis light diffracted on the pupil edges while allowing most of the light from an off-axis source to pass through the system. Finally the coronagraphic image is formed on the detector (Fig. 5 D).

In as much as a Lyot coronagraph reduces the amount of light diffracted away from a star, the device becomes inefficient very close to it. A metric generally used to define the closest spatial separation from the on-axis source that can be observed is known as the inner working angle (IWA). Modern concepts of coronagraphs, which enable a small IWA, use masks that apply a modification of the phase rather than of the amplitude, such as the phase mask proposed by Roddier & Roddier (1997). The phase mask introduces a phase shift on the on-axis source that sends its light outside the pupil. Other variants of the phase mask include the four-quadrant phase mask (Rouan et al. 2000). Here, the mask is divided into four quadrants centred on the optical axis: two quadrants on one diagonal with a phase of 0 and the other two with a phase of π . Although this mask improves on-axis rejection, the four phase transitions between adjacent quadrants create so-called dead-zones that can attenuate a potential companion's signal. Mawet et al. (2005) introduced the annular groove phase mask which suppresses these dead-zones. The various coronagraphs have been shown to work reasonably well in controlled environments. Galicher et al. (2020) utilised the Trés Haute Dynamique 2 (THD2; Baudoz et al. 2018) testbed to investigate different phase masks for broadband coronagraphy. Trauger & Traub (2007) demonstrated a contrast of 0.1×10^{-10} on the High Contrast Imaging Testbed (HCIT; Trauger et al. 2004) at NASA JPL.

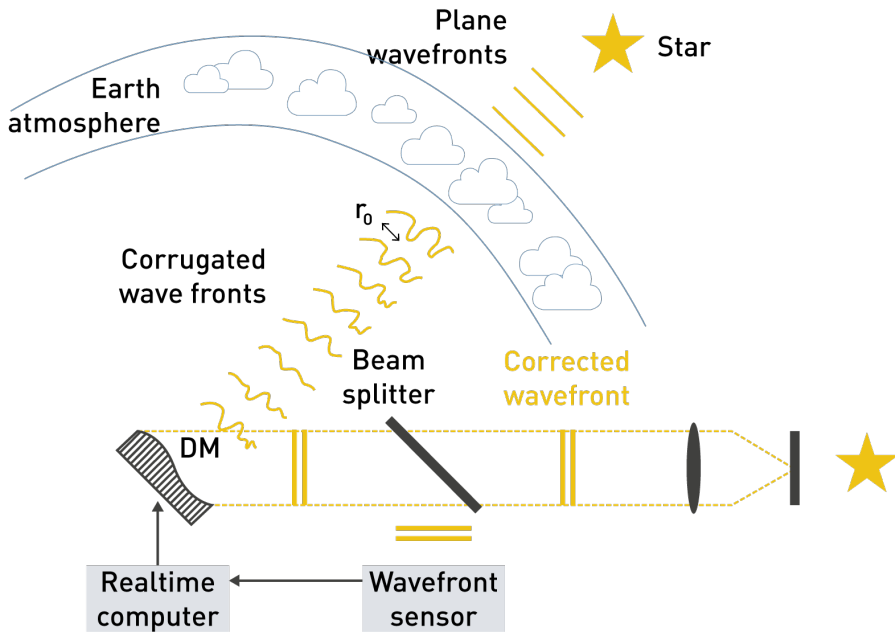


Figure 6: Schematic setup of a closed-loop Adaptive Optics system. A plane wavefront of light from a distant astronomical source travels through the Earth's atmosphere composed of turbulent air with varying refractive index, which corrugates it (i.e., distorts its shape). A deformable mirror reflects the corrugated wavefront onto a beam splitter, which redirects a fraction of the light onto a detector and the rest to a sensor (i.e., a Shack-Hartmann wavefront sensor). The sensor estimates the shape of the wavefront and transmits this information to a real-time computer that determines the optimal shape —of the correcting wavefront— for the deformable mirror, which applies the correction.

Above the Earth’s atmosphere, the wavefront of light from a distant astronomical source is perfectly flat. But by the time it reaches the telescope, it is distorted by the turbulent air that impresses on it corrugations (or distortions) with typical dimensions of a few centimetres in the optical and up to several meters in the mid-infrared. This departure of the incoming wavefront from its ideal form will limit the usefulness of large telescopes, and therefore the angular resolution, which now becomes:

$$\theta = 200 \frac{\lambda}{r_0}, \quad (1.8)$$

where r_0 is the Fried parameter (Fried 1966) that is defined as the length over which a wavefront remains undistorted, i.e., approximately flat. The larger the Fried parameter, the better the atmospheric conditions. On the 8.2-m Subaru Telescope located at the Maunakea Observatory, IYE (2021) reports $r_0 \sim 0.1$ -m for $0.55\mu\text{m}$, and $r_0 \sim 0.4$ -m at $2.2\mu\text{m}$.

Wavefront corrugations will also produce diffraction features whose contribution can dominate that of faint objects such as exoplanets. To correct for these distortions, an adaptive optics (AO) system (Babcock 1953) is used (see Fig. 6). The principle of a closed-loop AO system is the following: the corrugated wavefront from the astronomical source is incident upon a deformable mirror (DM) that is made either segmented or with continuous control surfaces. A beamsplitter then sends a fraction of the light to a detector and the rest to a wavefront sensor. Commonly used sensors include the pyramid wavefront sensor (Ragazzoni 1996), Zernike wavefront sensor (Zernike 1934, N’Diaye et al. 2013) or the standard Shack-Hartmann wavefront sensor (Hartmann 1900a,b, Shack et al. 1971), which consists of an array of lenses (called lenslets) whose size is determined by the Fried parameter.

A wavefront sensor estimates the shape of the wavefront from a reference (or guide) star. The guide star will, in general, be a bright star that is close to the object being studied. Unfortunately, such stars are not available everywhere so an artificial guide star is created by focusing a powerful laser beam into the Earth’s upper atmosphere at a small angle from the target object. The back-scattered light (the laser guide star) is used by the wavefront sensor to measure the residual wavefront errors. This information is then transmitted to a real-time computer that determines the optimal shape to give to the DM for minimising the residuals. Finally, the DM applies the correction typically with a few hundred actuators at rates of 0.2-1 kHz. State-of-the-art extreme AO like VLT/SPHERE (Beuzit et al. 2019), the Gemini Planet Imager (GPI; Macintosh et al. 2014) or the Subaru

Coronagraphic Extreme Adaptive Optics system (SCExAO; [Jovanovic et al. 2015](#)) have wavefront control loop speeds ≥ 1 kHz and DMs with ≥ 1000 actuators, which enables these systems to obtain higher-quality AO corrections required by the high-performance coronagraph. Indeed, AO planet imagers have facilitated exoplanet discoveries such as 51 Eri b ([Macintosh et al. 2015](#)), detected with GPI at $\sim 10\lambda/D$ (449 mas), and HIP 65426b ([Chauvin et al. 2017](#)) with VLT/SPHERE at $\sim 20\lambda/D$ (830 mas). However, the correction applied in the optical path of an AO system is never perfect and the final imaging performance will be limited by uncorrected residual wavefront errors.

Post-processing techniques, which exploit the specific difference between the stellar light and planet light, are used to complement extreme AO-fed observations. For instance, with Angular Differential Imaging (ADI; [Marois et al. 2006](#)), where a companion seemingly moves around the star as the Earth rotates during an observation. This technique can decouple the planetary signal from diffraction features such as speckles. Spectral Differential Imaging (SDI; [Racine et al. 1999](#)) uses spectral differences between the planet and star, and Polarisation Differential Imaging (PDI; [Kuhn et al. 2001](#)) exploits the difference in their polarisation states. Other techniques include point spread function subtraction ([Lafrenière et al. 2007](#)) and kernel phase ([Martinache 2010](#)), which can resolve angular separations at or below λ/D by treating a telescope aperture as an interferometric array but cannot be used in conjunction with a coronagraph.

Assuming similar correction quality that is currently achieved on the 8-10 meter telescope generation, an extreme AO-fed coronagraph at the focus of a larger telescope (i.e., the 39.3-m Extremely Large Telescope currently under construction) will make it easier to detect currently inaccessible or barely resolvable planets, and increase the SNR of previously-imaged planet observations. Another way to benefit from high angular resolution with today's ground-based observatories is to use an interferometer. When using the long baselines (up to 130-m) of the four Very Large Telescope Interferometer (VLTI) 8.2-m Unit Telescopes (UTs), previously-imaged planets are well resolved. With the first direct detection of an exoplanet by the GRAVITY instrument on the VLTI (HR 8799e; [GRAVITY Collaboration et al. 2019](#)), optical interferometry has demonstrated high-contrast imaging at high angular resolution. GRAVITY's integrated optics beam combiner—in dual-field mode—enables astrometry and *K*-band spectroscopy of exoplanets. Although an observation with GRAVITY necessitates a prior knowledge of the planet location (on which the second arm of the interferometer is pointed), it nevertheless led to very interesting results with HR 8799e.

3 Summary

The vast majority of confirmed exoplanets thus far have been detected through indirect means such as the primary transit and radial velocity methods. These methods infer the presence of the planet by measuring stellar perturbations and are mainly sensitive at close (< 10 AU) separations. Although these methods have revealed the ubiquity and diversity of exoplanets, few terrestrial planets have been discovered in terrestrial orbits. On the other hand, direct imaging not only provides the astrometric parameters of a planet, but also enables the characterisation of its atmosphere. The method has had a lower yield as it is an especially difficult endeavour that requires the simultaneous combination of a high angular resolving power, needed to detect objects separated by a few astronomical units and located tens of parsecs away, with high dynamic imaging capability to overcome the large contrast between the faint planet and its bright host star. The planet/star contrast ratio ranges between $\sim 10^{-4}$ for a Jupiter analogue observed in the mid-infrared to $\sim 10^{-10}$ for Earth-like exoplanets imaged in the reflected light from their primary. Consequently, direct imaging has predominantly been the detection of the thermal emission of giant planets. Indeed, young stars (< 100 Myr) make for ideal targets as they are generally warmer, and therefore intrinsically brighter exoplanets result in even lower contrasts.

To address this direct imaging challenge, the conventional approach has been the use of a single aperture coronagraph with wavefront correction via extreme adaptive optics on a large telescope. Such systems are limited to observing beyond an inner working angle (IWA) of a few resolution elements expressed in units of λ/D , where λ is the wavelength of observation and D the diameter of the telescope. This is why most of the directly imaged planets have been detected at wide orbital separations ($\sim 10 - 250$ AU). To gain a high angular resolution, one can resort to long-baseline nulling interferometry, which works in a similar way as a coronagraph in suppressing the on-axis light of a star, with a much improved IWA that is smaller than λ/B , where B is the interferometric baseline.

This thesis work focuses on the direct detection of young giant exoplanets, which is enabled by a nulling interferometer that allows for high-contrast on-axis observations.

Chapter 2

Optical Interferometry

Based on the theory of light coherence introduced by Thomas Young, the light collected by an array of two or more independent telescopes can be coherently combined as if it were coming from different regions of a single large aperture. The greater the distance between two sub-apertures, the higher the angular resolution. Baselines formed by pairs of telescopes yield amplitude and phase measurements of the so-called complex visibility, which directly relates to a target's spatial brightness distribution. A baseline samples the complex visibility at a spatial frequency B/λ (where B is the interferometric baseline and λ is the wavelength of observation) labelled with coordinates u and v . The accumulation of sufficient complex visibility measurements eventually leads to enough constraints that an image or a parametric representation of the target can be reconstructed by virtue of the Van Cittert–Zernike theorem ([van Cittert 1934](#), [Zernike 1938](#)).

In general, a two-aperture interferometer only provides a measurement of the complex visibility amplitude. Even if its phase is unobtainable, much work of astrophysical interest is possible. Toward the end of the 19th century, Hippolyte Fizeau proposed to monitor the visibility (or contrast) evolution of starlight interference fringes relative to the distance separating two apertures, as a method of measuring the angular diameter of stars. In 1874, Édouard Stéphan reported the implementation of Fizeau's idea by placing a two-hole aperture mask above the primary mirror of the 80-cm telescope at Observatoire de Marseille. Being constrained to a maximum 65-cm baseline, Stéphan was unable to observe any visibility loss on the observed stars. By increasing the baseline up to ~ 6.1 -m (with a boom holding a double periscope setup at the upper end of the 2.5-m Hooke telescope), [Michelson \(1920\)](#) & [Michelson & Pease \(1921\)](#) made the first successful measurement of a stellar diameter. With the Michelson stellar interferometer at the Mount Wilson observatory, they found the angular diameter of an M-type star –Betelgeuse– to be 47 mas, consistent with prior predictions.

The requisite long baselines and the stringent requirement to maintain stable optical path differences during observations led the technique to lay dormant for

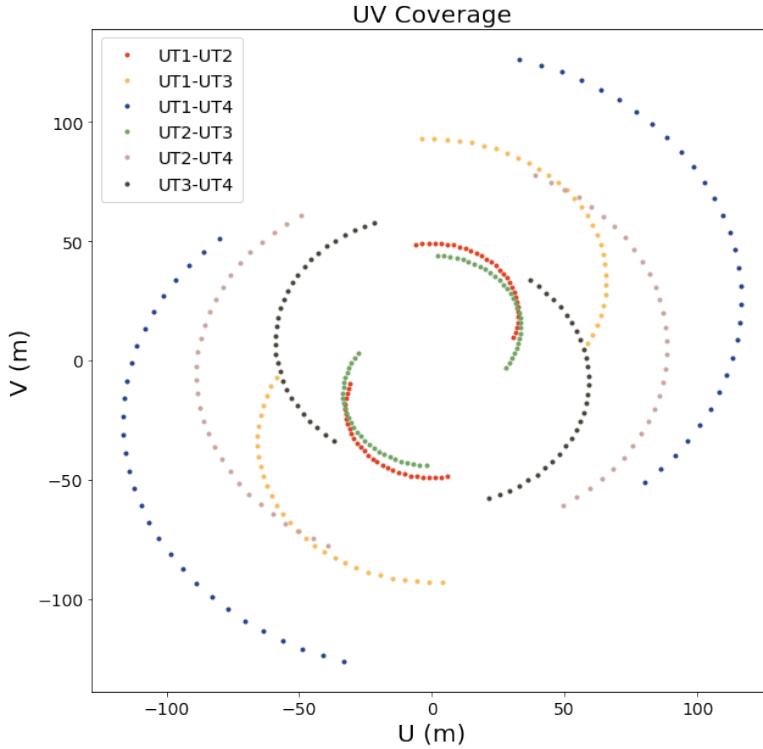


Figure 7: Evolution of the (u, v) plane coverage of the four VLTI UTs observing the target HIP 107773 over a ± 4 hr range of hour angle. We see the 2D projection of the six baselines of the four UTs on a plane perpendicular to the direction of the target. As the Earth rotates, the baselines formed by pairs of telescopes sample the complex visibility function at spatial frequencies labelled with coordinates u and v , sweeping out tracks that are rather circular on account of the favourable celestial location.

half a century. As the resolution of a telescope is diffraction limited, and whose practical limits are imposed by the atmosphere that introduces speckles (a pattern of airy disk-sized spots), telescope performance was also inadequate. The introduction of speckle interferometry (Labeyrie 1970) laid the foundation for the first successful application of optical interferometry to separate telescopes by Labeyrie (1975). This was achieved with l’interféromètre à deux télescopes (I2T), a two-telescope interferometer separated by a 12-m baseline.

Since then, mature infrastructure for long-baseline interferometry include the Very Large Telescope Interferometer (VLTI) and the Centre for High Angular Resolution Astronomy (CHARA). The VLTI has four fixed 8.2-m Unit Telescopes (UTs) and four relocatable 1.8-m Auxiliary Telescopes (ATs) with baselines up to 130-m, which corresponds to $\theta \approx 5.5$ mas in the L-band. CHARA operates

six 1-m telescopes with a maximum baseline of 330-m, giving $\theta \approx 2.2$ mas at mid-infrared wavelengths. These observing facilities take advantage of aperture synthesis techniques first developed for radio astronomy in the late 1940s to improve the (u, v) plane coverage (adapted to projected array coverage in [Chingaipe et al. 2023](#)) by making use of the Earth’s rotation. As the Earth rotates, the projected baseline vector —as seen from the source— and the corresponding spatial frequencies vary with time, sweeping out tracks in the (u, v) plane. Such tracks are conveniently summarised by a (u, v) coverage plot (see Fig. 7) whose overall density and distribution are good diagnoses of the richness of the observation. The enhancement in angular resolution —which is given as λ/B — provided by long-baseline interferometry will therefore make it possible to detect sources or constrain the extent of features around objects at separations at and beyond the formal diffraction limit.

1 Nulling Interferometry

The conventional approach to direct imaging has been the use of a single aperture coronagraph with wavefront correction via extreme adaptive optics on a large telescope. However, such systems are limited to observing beyond an IWA (or half power angle) of $\lambda/4D$, where λ is the wavelength of observation and D the diameter of the telescope. This is why most of the directly imaged planets have been detected at wide orbital separations ($\sim 10 - 250$ AU). An alternative observing technique is nulling interferometry ([Bracewell 1978](#), [Bracewell & MacPhie 1979](#)), which works in a similar way as a coronagraph in suppressing the on-axis light of a star but with a much improved IWA that is $\lambda/4B$.

In nulling interferometry, the requirement to redirect away the on-axis stellar light implies that the complex visibility of the source brightness distribution is in general not directly accessible. A nuller records the observed flux of a faint off-axis source acquired by a finite number of nulled outputs after the light from an on-axis source has been optically redirected toward one or more bright outputs. Even in ideal observing conditions, the link between the nulled outputs and the astronomical source is no longer described by a direct, linear relation such as the Van Cittert-Zernike theorem.

Figure 8 provides a visual representation of the Bracewell nulling interferometer, whose basic principle is the following: the light from a star is incident on two apertures separated by a distance B (the baseline) and coupled into a re-combiner made up of a beamsplitter (depicted as M). A beamsplitter having equal transmitted and reflected intensities combines the signals from each input (represented

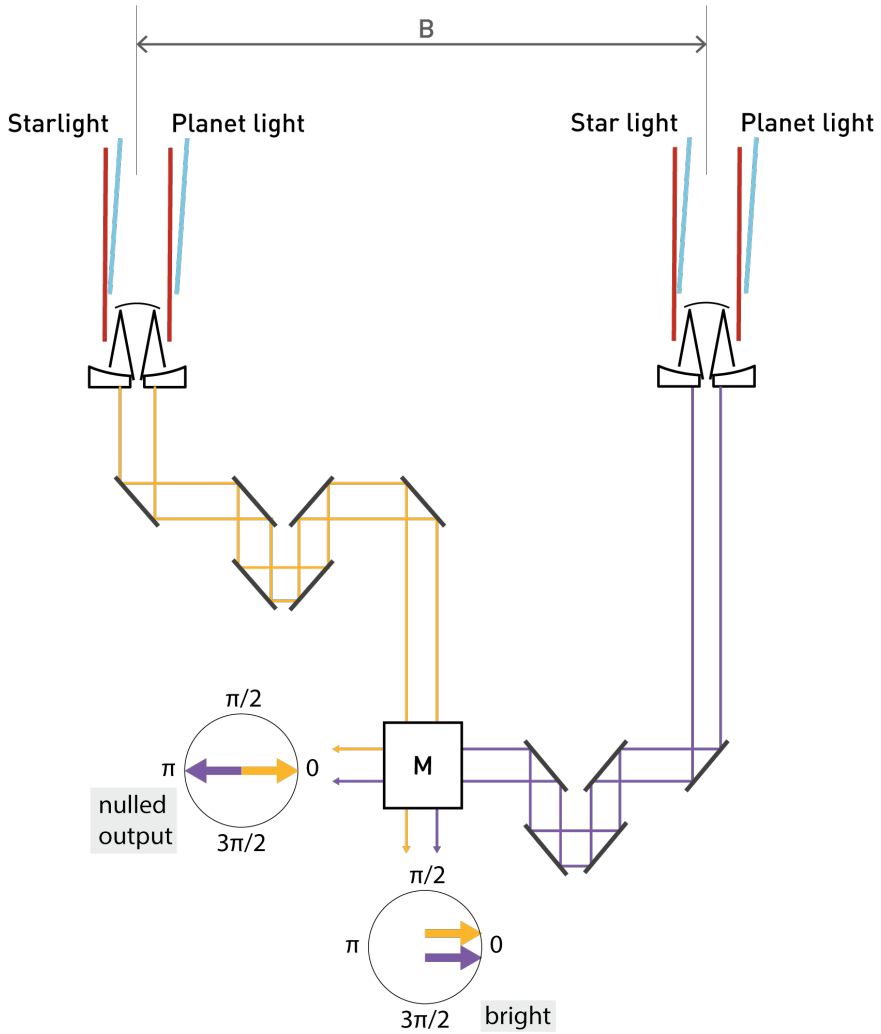


Figure 8: Schematic representation of a Bracewell nulling interferometer. Light from two telescopes is coupled into a re-combiner M , which produces two outputs. Two in-phase ($\varphi = 0$) signals interfere constructively to produce a bright output (where most of the on-axis starlight is directed). For the nulled output, a phase shift ($\varphi = \pi$) is applied to the signal from one input. This means that when the light is combined, one input is out of phase from the other and so destructive interference occurs, leaving no starlight. Given a suitable baseline B , a close planet's emission will reinforce (constructive interference) in the nulled output. A useful way to visually depict M is with complex matrix plots (Laugier et al. 2020). The phase of each input is represented by a coloured arrow whose length encodes the amplitude. At each output, the resulting electric field is the sum of all arrows. In the bright output, the arrows sum up constructively. For the nulled output, the on-axis light is suppressed when the electric fields sum up to zero, requiring specific combinations of the amplitude and phase. Here, one arrow has a zero phase shift and the other of equal amplitude has a π phase shift, which sum up to form a classical Bracewell null.

by coloured arrows) to produce two outputs. Two in-phase signals interfere constructively to produce a bright output (where the on-axis starlight is directed). The complex matrix plot (CMP; Laugier et al. 2020) of this output shows both arrows aligned with the real axis of the complex plane where the phase for both inputs is zero. For the second output, a π phase shift is applied to the signal from one input (purple arrow in the CMP of the nulled output). This means that when the light is combined, one input is out of phase from the other and so destructive interference occurs, leaving no starlight. Given a suitable baseline, the off-axis light of a potential companion will reinforce (constructive interference) in this so-called nulled output.

1.1 Bracewell nuller response

A 2-element vector \mathbf{U} (commensurate with the number of apertures) of input n electric fields with wavelength λ can be described as:

$$U_n(\alpha, \delta) \propto e^{(-2\pi i/\lambda) \cdot (x_n \alpha + y_n \delta)}, \quad (2.1)$$

where (x_n, y_n) are the coordinates of the different apertures that collect the electric field emitted by an off-axis test source of right ascension and declination offset (α, δ) . One of the apertures is chosen as the phase reference so that the phase of the different electric field sampled by the other aperture is measured relative to this reference.

The action of the beam-splitter on the input electric fields can be summarised by a two input/two output (2×2) complex matrix \mathbf{M} , which is given as:

$$\mathbf{M} = \frac{1}{\sqrt{2}} \times \begin{bmatrix} 1 & 1 \\ 1 & -1 \end{bmatrix}. \quad (2.2)$$

Rows of \mathbf{M} represent the nuller outputs and the columns serve as the inputs. An ideal equal intensity split of the signal in the outputs is expressed by the $\frac{1}{\sqrt{2}}$ factor. In row 1, all inputs interfere constructively to produce a bright output. Row 2 combines the pair of inputs in phase opposition, resulting in a classical Bracewell null. As the input phase is measured relative to one sub-aperture, here the convention is to use input 1 as the phase reference, explaining why the first column of \mathbf{M} only contains 1, or equivalently, why all yellow arrows in Fig. 8 remain aligned with the real axis of the complex plane.

\mathbf{M} acts on \mathbf{U} and leads to the production of an output electric field vector \mathbf{V} :

$$\mathbf{V} = \mathbf{M} \cdot \mathbf{U}. \quad (2.3)$$

For each nuller output k , a detector located after the nuller records at time t , the intensity $I_k(t)$:

$$I_k(t) = |V_k|^2 = \left| \sum^n \mathbf{M}_{k,n} \cdot U_n(\alpha, \delta, t) \right|^2. \quad (2.4)$$

Considering that the response is the squared modulus of the sum of all input vectors, a nuller is insensitive to any global phase shift applied to an output (or row of \mathbf{M}), which would correspond to an overall rotation of the arrows in a CMP (visible at the bottom of Fig. 8).

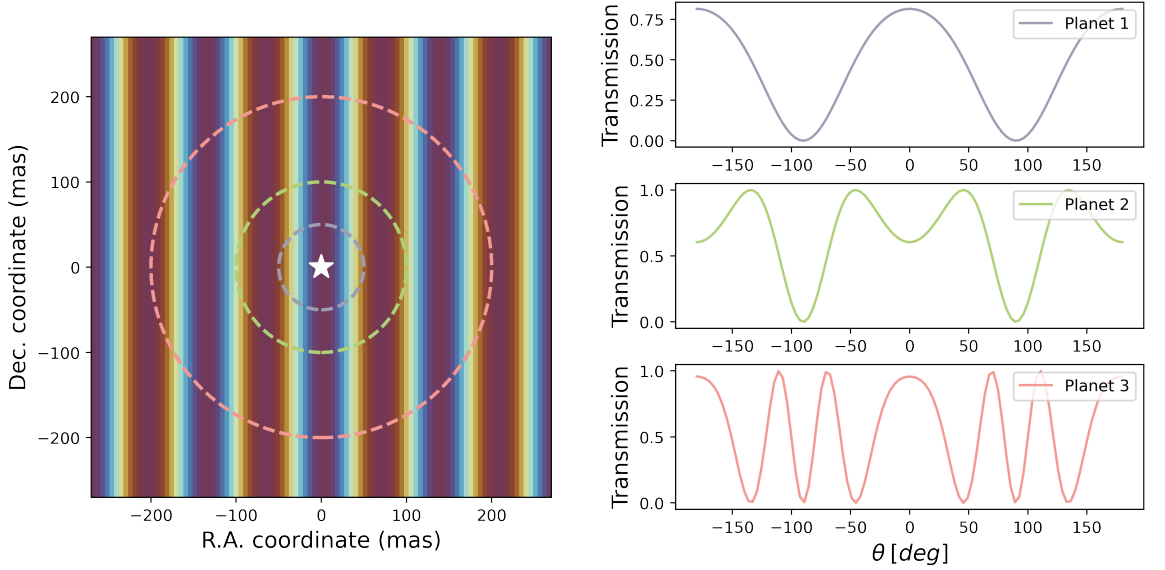


Figure 9: **Left:** Bracewell nuller transmission map computed for a wavelength of $2.3\mu\text{m}$ over a ± 275 mas field of view, with a 3.4-m baseline for a single snapshot pointing. The transmission map shows the parts of the field that are transmitted (bright stripes) and those that are blocked (dark stripes, including the central null). When the interferometer goes through a 360° rotation while pointing to the star, a planet describes a circle with radius: 50 mas (planet 1), 100 mas (planet 2), and 200 mas (planet 3) in the transmission plane, as indicated with the coloured dashed lines. A white star in the map marks the location of the central star where the transmission is equal to zero, by design. **Right:** As the nulling interferometer rotates around the line-of-sight, the transmission pattern centred on the star rotates with it. As the transmission pattern rotates, the bright and dark stripes sweep across the position of the planets (1, 2, and 3), modulating their transmitted flux. For larger off-axis offsets, more stripes cross the planet’s position, and so the higher the modulation frequency. The modulation frequency of the signal thus determines the companion’s angular offset from the central star. The horizontal axis (Dec = 0) in the transmission map is the reference axis for θ .

1.2 Transmission map

A direct way of interpreting the effect of a nuller recombining two or more apertures is to compute transmission maps, which describe the response of the different outputs to the presence of a test point source over the field of view of the interferometer. These transmission maps predict what fraction of the total flux of an off-axis source will find its way through to the nulled outputs. I will refer to the two-dimensional response of the nuller outputs as nuller output transmission maps $\tau_k(\alpha, \delta, t)$:

$$\tau_k(\alpha, \delta, t) = I_k(\alpha, \delta, t). \quad (2.5)$$

One example of such maps is shown in the Left Panel of Fig. 9 for a two-aperture Bracewell interferometer. I have computed this map for a single snapshot pointing in the K_s -band ($\lambda = 2.3 \mu\text{m}$), with the 3.4-m rotating baseline of the Palomar Fibre Nuller (PFN; Serabyn et al. 2010), which employs the classical Bracewell architecture. The interferometric baseline of the PFN is implemented across a pair of 1.5-m sub-apertures located within the 5.1-m Hale Telescope at the Palomar Observatory. This provides an IWA of 32 mas ($0.36\lambda/D$) and an outer working angle (OWA) of 275 mas at the observation wavelength. Baseline rotation with the PFN, rather than Earth rotation, modulates the signals from off-axis sources in a manner similar to that of a space-based nulling interferometer, as originally envisaged by Bracewell.

The monochromatic transmission map —shown in the Left Panel of Fig. 9— is characterised by a series of bright and dark stripes that correspond to the high and low transmission regions respectively, and are regularly spaced by a distance that depends on λ/B . When the wavelength is shorter or the baseline longer, the stripes become narrower. The optimal configuration for a nuller is when the bright target is positioned at the centre of the map and the off-axis feature is situated in an area that is mostly driven toward the nulled output. As the location of the off-axis feature may be unknown, its detection in a snapshot is not guaranteed. Even in case some signal is detected, we cannot directly tell where the flux is coming from, since the signal is the result of a summation over the field of view (see Eq. (2.4)). This is why Bracewell proposed to rotate the interferometer: the on-axis star remains nulled, while the bright and dark stripes sweep across the position of the off-axis companion, resulting in intensity modulations with a predictable frequency at the nulled output. Appropriate demodulation of this output gives the flux of the planet and its position relative to the star.

In the Right Panel of Fig. 9 we can see that the signal modulation of an off-axis source varies as a function of angular separation from the central star. For larger

off-axis offsets, more stripes cross a planet's position during a complete array rotation, and so the higher the modulation frequency. The modulation frequency of the signal thus determines the companion's angular offset from the central star. However, one can observe that the signals are symmetric about a 180° rotation of the interferometer, imposed both by the re-combiner and the arrangement of the apertures. Subsequently, each point source in a recovered image appears twice (modulo π), reflected through the central star, and it can be difficult to separate its signal from other sources of emission.

1.3 The null-depth

Nulling interferometry differs from normal long-baseline interferometry in that the requirement to redirect away the on-axis stellar light means that the phase of the complex visibility \mathcal{V} is not measured. Rather, a nuller measures the astrophysical null-depth N_A :

$$N_A = \frac{I_d}{I_b}, \quad (2.6)$$

where I_d and I_b are the intensities measured in the dark and bright outputs, respectively. N_A represents the contrast improvement between a star and a planet. To detect a terrestrial planet, an N_A of $\sim 10^{-6}$ would be required at mid-infrared wavelengths, where the contrast ratio between a star and the thermal emission from its planet is more favourable. For a two-input nuller, N_A is related to the visibility amplitude via:

$$N_A = \frac{1 - |\mathcal{V}|}{1 + |\mathcal{V}|}. \quad (2.7)$$

Despite the 180° ambiguity observed in a Bracewell transmission map, [Serabyn et al. \(2019\)](#) constrained the position of η Peg B, which has a null-depth of $4.8 \pm 1.6 \times 10^{-4}$, at ~ 30 mas ($0.23\lambda/B$) and a position angle of 170° . This was achieved with a baseline rotation of 180° at seven observed baseline position angles. The companion's position angle was determined from the angle of the peak null-depth (note that Eq. (2.4) is a function of (α, δ)). According to [Serabyn et al. \(2019\)](#), a full rotation is required when searching for unknown companions, but it isn't if a companion's position is known, though a minimum is essential to remove any stellar leakage.

1.4 Geometric stellar leakage

Even when the star is perfectly centred on the optical axis (see Left Panel of Fig. 9), and with precise optics, the instrument's transmission would be zero on-axis only. This is due to the finite extent of the stellar disk, an effect known as geometric stellar leakage. Considering that light from the edges (the limb) of the star will trickle through to the nulled output, we can therefore determine the angular diameter of stars via their null-depth measurements. The relationship between the limb-darkened diameter of a star and the astrophysical null-depth can be described by the following expression shown in Absil, den Hartog, et al. (2006) & Absil et al. (2011) as:

$$N_A = \left(\frac{\pi B \theta}{4\lambda} \right)^2 \left(1 - \frac{7\mu}{15} \right) \left(1 - \frac{\mu}{3} \right)^{-1}, \quad (2.8)$$

where B is the baseline length, θ is the limb-darkened stellar diameter, λ is the central wavelength of observation and μ is the limb darkening coefficient.

Limb-darkening is an effect observed in stars where the brightness of the star decreases from the centre of the disk toward the edge, or limb. A reasonable approximation to the brightness distribution of a resolved star is the model of a uniform disk, which can be assumed by setting $\mu = 0$ in Eq. (2.8). The effect of limb-darkening may also be negligible if the wavelength is longer or the baseline shorter, as the central dark stripe shown in the Left Panel of Fig. 9 would widen. But a short baseline may not lead to full constructive interference of a planet in close proximity to the central star. It may also preclude planets to be resolved from each other or from a dust cloud in the external system. Nevertheless, N_A is quite sensitive to μ because it is precisely the edges of the star that mostly contribute to stellar leakage in the nulled output, which may render a faint planet undetectable.

With a 2-aperture configuration, one can infer from Eq. (2.8) that the ideal null-depth for an unresolved star is proportional to the square of the angular separation to the optical axis, i.e., the interferometer produces a second-order null, commonly referred to as a θ^2 null. The null rises as θ^α , where $\alpha = 2, 4, \dots$, according to the interferometer design.

2 Two-telescope on-sky nulling

The expression of the astrophysical null-depth given in Eq. (2.8) is valid only for a perfect Bracewell nuller. In practice, the measured on-sky interferometric

null-depth is not strictly equal to N_A as it also incorporates flux leakage due to atmospheric phase perturbations. A nuller will require precise phase matching (co-phasing) between the inputs for an applied phase shift of π to produce full destructive interference in the nulled output. Any deviation from this specified phase shift can therefore lead to a finite extinction. Although an adaptive optics system corrects high-order atmospheric wavefront distortions, it does not sense, and therefore cannot compensate for the differential phase between the apertures. One can mitigate the residual optical path differences (OPDs) by reducing the integration time to a few milliseconds, though this will limit observations of faint targets. An alternative way is to use a fringe tracker, which partly removes the atmospheric piston turbulence that a nuller is extremely sensitive to.

After the first demonstration by [Shao & Staelin \(1980\)](#), fringe tracking has become a common feature of modern optical interferometers, including the Keck Interferometer Nuller (KIN; [Colavita et al. 2013](#)), which combines light from two 10-m telescopes that are 85-m apart, and is equipped with two fringe trackers operating in the *H*, *K* and *L* bands. For a two-aperture interferometer, the basic principle of fringe tracking is the following: the two incoming beams are combined in a fringe sensing unit (FSU) that measures the OPD error between them at a given sampling frequency. To be efficient, fringe tracking requires phase measurements on very short time scales that are typically between 0.1 and 1 ms. It also needs measurements with a high signal-to-noise ratio, which is why it is usually performed in the near-infrared where the thermal background is reduced and the detector read noise is low.

The FSU transmits the measured OPD to a controller. A proportional–integral–derivative (PID) controller is a basic controller typically used for closed-loop control, which is a control loop that incorporates feedback in order to produce the minimum OPD error between the two beams. In contrast, open-loop control does not use feedback to determine if the applied correction has reduced the phase error. The controller computes the compensation to be applied to one of the beams by an optical delay line (ODL). Besides the FSU, the ODL will also introduce noise in the fringe tracking system. As the ODL may not efficiently correct for OPD fluctuations at high frequencies, a fringe tracker should be equipped with a low-noise ODL that is optimised for high repetition frequencies. [Colavita et al. \(2013\)](#) reports that the KIN implements proportional-derivative control of a custom piezoelectric actuator delay line with a 4 kHz repetition frequency.

Even after fringe-tracker correction, where residual OPDs will remain, various instrumental effects will lead to phase differences, intensity mismatches, and polarisation errors. This contribution, called instrumental leakage (or systematic

noise) adds to the geometric stellar leakage at the nulled output of the interferometer. Unlike geometric leakage, an analytical expression for systematic noise cannot be obtained as it depends on the particular shape and amplitude of the power spectral densities of the various seeing-induced and instrumental perturbations. I will refer back to systematic noise in Sect. 3.2 where its nature and mitigation are described.

2.1 Numerical self calibration

Analysing interferometric data is a complex process that requires accurate instrument calibration in order to extract a target's astrophysical information. For the mid-infrared KIN, Colavita et al. (2009) implemented a data reduction method analogous to that used for calibrating visibility measurements in conventional optical interferometry. In this classical approach (as shown in Hanot et al. 2011), the fluctuating instantaneous null-depth of a target is averaged over a large number of data points, and can be expressed as:

$$\langle N(t) \rangle = N_A + \langle N_I(t) \rangle, \quad (2.9)$$

where $\langle N(t) \rangle$ is the measured null-depth, N_A is the astrophysical null-depth and $\langle N_I(t) \rangle$ is the mean instrumental null-depth averaged over the observing sequence. A similar measurement is made on a calibrator star of known diameter, located close to the target, and with a similar magnitude at the wavelength of observation. For the calibrator star, Eq. (2.9) is rewritten as:

$$\langle N_{\text{cal}}(t + \Delta t) \rangle = N_{A,\text{cal}} + \langle N_{I,\text{cal}}(t + \Delta t) \rangle, \quad (2.10)$$

$N_{A,\text{cal}}$ is deduced from photospheric models or from separate observations. Assuming that the instrumental null is constant in both measurements, the target's astrophysical null is estimated by:

$$N_A = N_{A,\text{cal}} + \langle N(t) \rangle - \langle N_{\text{cal}}(t + \Delta t) \rangle. \quad (2.11)$$

Owing to the fast fluctuations of phase and intensity errors, a bias is introduced by averaging the null-depth for both the target and calibrator star. Besides the long integration time required on the calibrator star, precise knowledge of its properties is essential in order to obtain an accurate N_A , which will also depend on the stability of the instrumental null and the uncertainty of $N_{A,\text{cal}}$.

A method that does not need any observation of calibrator stars is known as numerical self calibration (NSC; Hanot et al. 2011). It uses statistical distributions

of the various systematic errors along with the measured null-depth to determine the astrophysical null-depth. Indeed, NSC is not limited by the magnitude of the instrumental bias —as is the case with the classical reduction method— rather by the statistical uncertainty on the probability density function (PDF) of each measurable quantity. Consequently, the method has improved the accuracy of null-depth measurements by about an order of magnitude than was previously possible.

First demonstrated with the PFN, NSC has also been adapted to the Large Binocular Telescope Interferometer (LBTI; [Defrère et al. 2015](#)), and the Guided-Light Interferometric Nulling Technology (GLINT; [Norris et al. 2020](#) & [Martinod et al. 2021](#)). On these state-of-the-art facilities, NSC has yielded null-depth accuracies of $\sim 10^{-4}$. With such precision, [Kühn et al. \(2015\)](#) detected hot dust within 4–10 AU of the Herbig star AB Aurigae, and exozodiacal dust was observed around Vega by [Mennesson et al. \(2011\)](#). This data reduction method has also enabled the GLINT instrument integrated into SCEXAO to deliver angular diameter measurements of a number of resolved and partially-resolved stars that were 2.5 times smaller than the diffraction limit of the 8-m Subaru Telescope.

The NSC model presented by [Hanot et al. \(2011\)](#) is derived from the definition of the observed null-depth described by [Serabyn \(2000\)](#). Here, I present a summary of this model, adopting the nomenclature used in [Hanot et al. \(2011\)](#):

For a Bracewell nuller, the intensity measured at the bright $I_+^*(t)$ and nulled output $I_-^*(t)$ at time t is given as:

$$I_{\pm}^*(t) = \frac{1}{2} \left[I_1^*(t) + I_2^*(t) \pm 2 \cos(\Delta\phi(t)) \cos(\alpha_{\text{rot}}) \sqrt{I_1^*(t) I_2^*(t)} \right], \quad (2.12)$$

where $I_1^*(t)$ and $I_2^*(t)$ are the intensities measured at input 1 and 2, respectively, and $\Delta\phi(t) = \phi_1(t) - \phi_2(t)$ is the relative phase delay, and α_{rot} is the relative polarisation rotation angle. Equation (2.12) can be rewritten as:

$$I_{\pm}^*(t) = \langle I^*(t) \rangle \left[1 \pm \cos(\Delta\phi(t)) \cos(\alpha_{\text{rot}}) \sqrt{1 - (\delta I(t))^2} \right], \quad (2.13)$$

where $\langle I^*(t) \rangle = (I_1^*(t) + I_2^*(t))/2$ is the average input beam intensity, $\delta I(t) = (I_1^*(t) - I_2^*(t))/2\langle I^*(t) \rangle$ is the fractional deviation from the mean intensity.

The null-depth, which is the intensity ratio of a nulled output over the bright output is then:

$$N(t) = \frac{I_-^*(t)}{I_+^*(t)} = \frac{I_-(t) - I_b(t)}{I_+(t) - I_b(t)}, \quad (2.14)$$

where $I_{\pm}(t)$ are the bright and nulled output intensities that include the background, and $I_b(t)$ is the background intensity. According to Serabyn (2000), if $\Delta\phi(t)$, α_{rot} , and $\delta I(t)$ are all small (i.e., $\ll 1$), the nulled output $I_{-}^{*}(t)$ simplifies to:

$$I_{-}^{*}(t) = \frac{\langle I_{+}^{*}(t) \rangle}{2} [(\delta I(t))^2 + (\Delta\phi(t))^2 + (\alpha_{\text{rot}}(t))^2]. \quad (2.15)$$

While the bright output $I_{+}^{*}(t)$ becomes:

$$I_{+}^{*}(t) = 2\langle I_{+}^{*}(t) \rangle. \quad (2.16)$$

The measured null-depth can then be approximated by:

$$N(t) \simeq \frac{1}{4} [(\delta I(t))^2 + (\Delta\phi(t))^2 + (\alpha_{\text{rot}}(t))^2]. \quad (2.17)$$

Section 1.3 described the relationship between the limb-darkened diameter of a star and the astrophysical null-depth due to the finite extent of the stellar disk. For a source of finite extent, $N(t)$ also depends on Eq. (2.8). The measured null-depth for small values of N_A is then expressed as:

$$N(t) \simeq N_A + \frac{1}{4} [(\delta I(t))^2 + (\Delta\phi(t))^2 + (\alpha_{\text{rot}}(t))^2]. \quad (2.18)$$

As the device may not measure $I_b(t)$ or $I_{+}(t)$ at the same time as $I_{-}(t)$, estimates of their values are denoted as $\hat{I}_b(t)$ or $\hat{I}_{+}(t)$, while $\hat{I}_{+}^{*}(t) = \hat{I}_{+}(t) - \hat{I}_b(t)$. This means that rather than measuring $N(t)$, one determines an estimate of it given by:

$$\hat{N}(t) = \frac{I_{-}(t) - \hat{I}_b(t)}{\hat{I}_{+}(t) - \hat{I}_b(t)} = N(t) \frac{I_{+}^{*}(t)}{\hat{I}_{+}^{*}(t)} + \frac{I_b(t) - \hat{I}_b(t)}{\hat{I}_{+}^{*}(t)} \quad (2.19)$$

or

$$\hat{N}(t) = I_r(t)N(t) + N_b(t), \quad (2.20)$$

where $I_r(t) = I_{+}^{*}(t)/\hat{I}_{+}^{*}(t)$ is the relative intensity deviation and $N_b(t) = (I_b(t) - \hat{I}_b(t))/\hat{I}_{+}^{*}(t)$ is the background-induced instantaneous error in the estimated null-depth.

The estimated null-depth $\hat{N}(t)$ is then expressed as:

$$\hat{N}(t) \simeq I_r(t) \left[N_A + \frac{1}{4} [(\delta I(t))^2 + (\Delta\phi(t))^2 + (\alpha_{\text{rot}}(t))^2] \right] + N_b(t). \quad (2.21)$$

The idea behind NSC is to estimate the PDF of the measured null-depth from

the observations by constructing a histogram, and then fitting a model PDF (via Eq. (2.21)) to the histogram in order to constrain the free parameters. As the two sub-aperture beams of the PFN are injected into a common single-mode fiber, polarisation effects are expected to be common between them, therefore $\alpha_{\text{rot}}(t)$ is neglected in the PFN analysis. Here, $\hat{N}(t)$ is derived from the observations, and measured PDFs of $I_r(t)$, $\delta I(t)$ and $N_b(t)$ are injected into Eq. (2.21). In order to fit a sequence of observed null-depth values, these PDFs are combined with a simulated phase error $\Delta\phi(t)$ from a Gaussian distribution of mean $\mu_{\Delta\phi}$ and standard deviation $\sigma_{\Delta\phi}$, according to Eq. (2.21). Typically, a χ^2 minimisation procedure is used for the fitting, where the free parameters are adjusted to find the best fitting values from which the astrophysical null-depth is derived.

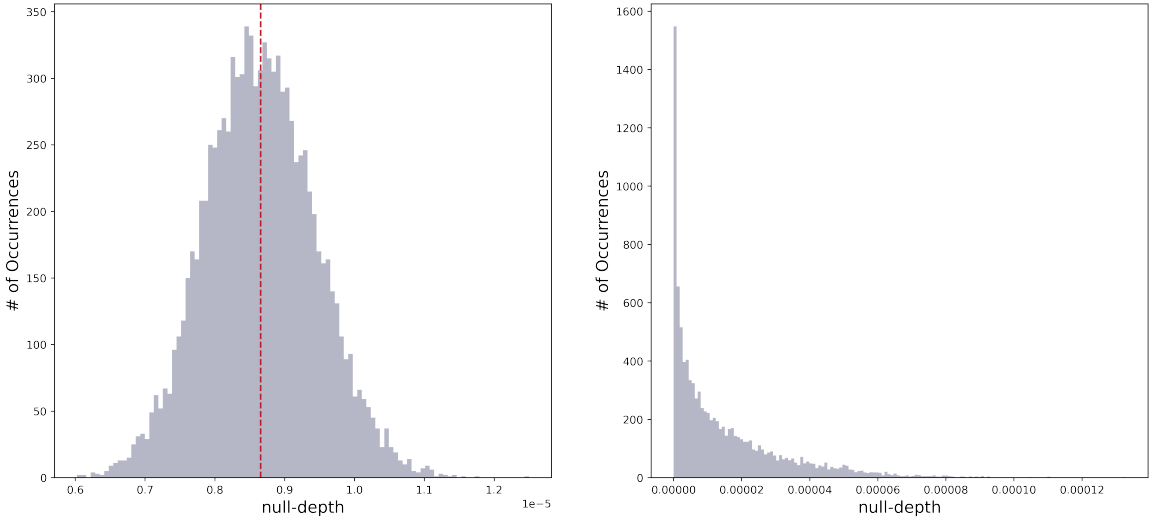


Figure 10: Statistical distribution of a Bracewell nuller output during an observation of an off-axis companion located at $\alpha = +70.0$ mas, $\delta = +70.0$ mas, and with a contrast $c = 10^{-4}$. *Left*: In the presence of 5 nm RMS fringe-tracking residuals. To estimate the astrophysical null, one can compute the median of this symmetric distribution (marked by the red vertical dashed line). *Right*: With 100 nm residual piston errors. Here, NSC would be required to deduce the astrophysical null. Each Monte Carlo simulated data-set consists of 10^4 acquisitions.

An extreme adaptive optics system is used to stabilise the phase on the 1.5-m sub-apertures of the PFN, which are 5/8 the size of the Hubble Space Telescope. With Strehl ratios of 0.6-0.95, Serabyn et al. (2019) reports atmospheric piston errors between the sub-apertures that reach ~ 100 nm. The electric field emitted by an off-axis test source will be affected by the residual piston ρ , and Eq. (2.1) now becomes:

$$U_n(\alpha, \delta) \propto e^{(-2\pi i/\lambda) \cdot (\rho + (x_n \alpha + y_n \delta))}. \quad (2.22)$$

Piston values are also quoted relative to the reference aperture. To illustrate the effect of the phase errors on the measured null-depth at the PFN, I performed a series of simulated nulling observations with the two-aperture Bracewell nuller presented in Sect. 1.2. The simulation includes an off-axis companion conveniently located at $\alpha = +70.0$ mas, $\delta = +70.0$ mas (for a contrast $c = 10^{-4}$), where—according to Fig. 9—the sensitivity of the nuller is expected to be optimal. Figure 10 presents the results of these simulations (10^4 acquisitions per simulation) for an observation scenario with 5 nm phase errors (Left Panel), and in the presence of 100 nm piston excursions (Right Panel). With a reduced amount of phase residuals, the null-depth PDF is symmetric with relatively straightforward statistics. This allows for a direct estimation of the astrophysical null by simply computing the median of the distribution. But with an increase in piston excursions, the null-depth PDF is asymmetric, trailing off more sharply on one side than the other. On-sky observations with PFN and GLINT exhibit such skewed PDFs of the measured null-depth that rely on NSC to deduce the astrophysical null-depth.

Building accurate models as required with NSC necessitates the acquisition of a large data-set to sample the statistical distribution of the error parameters, which include all of the phase and intensity fluctuations that need short integration times. Besides, the method assumes that the differential phase follows a Gaussian distribution and that the individual beam intensities are uncorrelated, which could be potential sources of bias. Indeed, NSC does pose a limitation on observational sensitivity/efficiency, and could also be fairly complex to implement with an increment in nuller inputs.

2.2 Exozodiacal dust

After the Sun, the zodiacal dust cloud is the most luminous component detected in our solar system with an infrared luminosity that amounts to $\sim 10^{-7}$ of the solar bolometric luminosity. This dust, which originates from asteroid collisions and/or cometary activity, peaks at a wavelength of approximately $19\mu\text{m}$ ($T \sim 270$ K). It extends well beyond the habitable zone with an emission at $10\mu\text{m}$ that is ~ 300 times larger than the flux of an Earth-sized planet. However, very little is known about the exozodiacal dust (exozodi) that is expected to be present in the inner regions of main-sequence planetary systems. Exozodi can be much brighter and located at different radial locations than the solar zodiacal dust. To detect

exozodi, the stellar emission must be separated from the dust emission that can amount to $\sim 1\%$ of the photospheric flux in the K-band, which is about 1000 times more than the solar zodiacal dust in the same spectral range. Such hot ($T > 300$ K) exozodi have been detected in the near-infrared with the Fiber Linked Unit for Optical Recombination (FLUOR, [Absil, di Folco, et al. 2006](#), [Absil et al. 2013](#)) at CHARA and the Precision Integrated Optics Near Infrared Experiment (PIONIER, [Ertel et al. 2014, 2016](#)) at the VLTI. A combined FLUOR and PIONIER sample of stars (~ 125 stars) presented by [Ertel et al. \(2014\)](#) shows evidence of a decreasing exozodi detection rate from early-type stars ($\sim 15.4\%$ for *A*-type stars) toward late-type stars ($\sim 7.7\%$ for *G* and *K*-type stars), which suggests a common origin for both phenomena.

Mid-infrared observations are ideal to probe warm ($T \sim 300$ K) exozodi located in the habitable zone of stars. A Bracewell nuller deployed on the Multiple Mirror Telescope (MMT) was used by [Hinz et al. \(1998\)](#) to detect such exozodi surrounding the late-type giant stars α Orionis and R Leonis. Images of these stars were nulled with a 5-m baseline provided by two of the six segments of the 6.5-m MMT primary mirror. The $10.3\mu\text{m}$ nulled images revealed dust surrounding the stars that was previously not visible. But these nulling observations did not correct for atmospheric wavefront perturbations, therefore, short exposures were used and the best nulled selected. This approach was refined by the Bracewell Infrared Nulling Cryostat (BLINC; [Hinz et al. 2000](#)), which was also installed on the MMT. BLINC made use of the telescope's adaptive optics system to achieve a greater suppression of the on-axis light, and served as a prototype for the LBTI. The Hunt for Observable Signatures of Terrestrial planetary Systems (HOSTS, [Ertel et al. 2020](#)) survey on the LBTI measured the *N*-band dust levels around 38 nearby main-sequence stars. Similar to the two sub-apertures of BLINC, the two 8.4-m primary mirrors of the LBTI are installed on a common mount, and a 14.4-m baseline gives it a large field-of-view with ~ 100 mas resolution.

Although the observation of exozodi may indicate the existence of planets, it remains a major source of photon noise for direct imaging. With the Bracewell nuller deployed on the LBTI, the signal of a faint companion would be inhibited not only by the presence of exozodi, which we can assume is centro-symmetric by analogy with our own solar system, but also by its symmetric response. According to [Léger et al. \(1996\)](#), a centrally symmetric transmission map (see [Fig. 9](#)) does not distinguish between a point source and two point sources located symmetrically with respect to the central star. Consequently, as the interferometer rotates, and if the exozodi dust cloud is seen edge-on ($i = 90^\circ$), the nuller will modulate its signal at the same frequency as a planet's. On the contrary, if the

system is observed face-on ($i = 0^\circ$), the centro-symmetric exozodi signal is not modulated, and the planetary signal fluctuates with a predictable frequency, making it easier to isolate. However, as the LBTI relies on Earth rotation to provide relative baseline-source rotation, this imparts a slow modulation of the planetary signal versus other sources of background emission. Due to the instability of the background over long time spans, the interferometer's sensitivity is reduced unless the rotation period of the array is much smaller than the typical timescale of background drifts.

3 Nulling with more than two telescopes

While a two-telescope nulling interferometer could be used to detect the thermal emission of giant exoplanets, as proposed by Bracewell, a planetary companion would be identified as twice the rotation frequency of the array. But array rotation provides a low modulation frequency of the planetary signal, which can make it susceptible to background and detector drifts. Considering that residual stellar and background signals are much stronger than a faint planetary signal, their fluctuations on long time-scales can mimic it. Either these signals are kept stable for a very long time or accurately monitored to compensate for their fluctuations, as is the case with NSC. Another solution is to implement a signal modulation scheme, which requires more telescopes that add complexity to the system. But a greater suppression of the on-axis source is also possible with more than two apertures.

3.1 Phase modulation and array configurations

Angel (1990) extended Bracewell's original concept to an interferometer with four telescopes arranged in a diamond array, known as the Angel Cross. Variations on this design include the 3-telescope Degenerate Angel Cross (DAC) and the 4-telescope Generalized Angel Cross (GAC) that both feature different aperture sizes. Large —8-m diameter— telescopes were envisioned for the Angel Cross not only for the high-contrast detection of terrestrial exoplanets, but also to overcome the solar zodiacal light in Earth orbit (1 AU). It uses two Bracewell interferometers, where the two nulled outputs are recombined with no additional phase shift, resulting in a fourth-order (θ^4) null. While it is straightforward to generalise to any number of apertures in a multi-axial mode, it is not for a co-axial combiner (beam combiners using beam-splitter type arrangements). In the case of four inputs, since $4 = 2^2$, one will need to consider a beam combiner of second-order ($m = 2$). Combining 2^m inputs requires $m \times 2^{m-1}$ beam-splitters.

The fourth-order null generated by the Angel Cross is efficient in reducing the flux leakage due to the finite size of stellar disks. Although an improved rejection is achieved, the design produces a symmetric response, which would make it difficult to separate the contribution of a planet from background sources such as solar zodiacal and exozodiacal light. It is also vulnerable to small drifts in the stray light level or in the gain of the system as the design does not implement any phase modulation. By changing the relative phase between the nulled outputs of the interferometer, the off-axis signal can be modulated, which can also provide an asymmetric response so that every planetary system can be treated the same way, whatever its inclination.

An alternative scheme based on the Angel Cross was conceived for the European Space Agency (ESA) mission – Darwin (Cockell et al. 2009), whose primary goal was the detection and characterisation of terrestrial planets in terrestrial orbits around ~ 200 F, G, K and some M-type stars within 30 pc of the Sun. This space-based nulling interferometer operating in the mid-infrared was initially designed with four to five 1-m formation flying telescopes observing from 4–5 AU, where the $10\ \mu\text{m}$ solar zodiacal emission would be reduced. With five telescopes ($5 = 2^2 + 1$), a third-order ($m = 3$) co-axial combiner would be required. Indeed, this would mean an architecture with eight inputs but three of them are not fed and do not contribute to any additional noise (see Mennesson & Mariotti 1997 for an example of a 5-telescope beam combiner). Léger et al. (1996) found that by using five telescopes distributed symmetrically around a 30–50 m diameter circle, a fourth-order null is produced with a response that modulates the exozodi signal at approximately twice the frequency of the planetary signal, thereby enabling both to be distinguished without any ambiguity. However, the symmetry in aperture location results in a transmission map featuring five lobes of high transmission (at $2\pi/5$ intervals) around the central null. This leads to five possible planet locations instead of the two obtained with a linear configuration.

Mennesson & Mariotti (1997) changed the geometry of the array to an ellipse of about 50-m \times 25-m, yielding a transmission map where the central symmetry is broken. With such a response, the signal of a potential companion has many distinctive frequencies, which allows for an uncomplicated image recovery with one planet position. On an ellipse, the five telescopes would be located at different distances from a central re-combiner. Subsequently, variable delay lines would be required to equalise the optical path lengths of the incoming beams, though this would also be needed in the other concepts to compensate for any phase mismatch. I will refer back to the circular and elliptical configurations in Chapter 3 when investigating the 5-telescope design of the proposed Large Interferometer For Exoplanets (LIFE; Quanz et al. 2022).

Almost simultaneously to Darwin, the National Aeronautics and Space Administration (NASA) proposed a similar mission called the Terrestrial Planet Finder Interferometer (TPF-I; [Beichman et al. 1999](#)). The initial concept considered for TPF-I was a 4-aperture linear array (a.k.a., Outpost for Analysis and Spectroscopy of Exo Systems – OASES). It was designed by [Angel & Woolf \(1997\)](#) & [Woolf & Angel \(1997\)](#), who proposed that an array should not only provide a high level of rejection at the centre of the field, but it must also be able to phase or modulate its response around the target star. Such a technique –known as phase chopping– is implemented in order to combat small changes in the detector gain, thermal emission, and stray light that would otherwise render a faint planet undetectable. OASES uses two Bracewell nullers with different spacings and aperture sizes. The two nulled outputs of this interferometer have a phase shift of 0 and π , respectively. Taking the nulled output difference of these two phase chop states produces the chopped response. Though this design did not eliminate the 180° imaging ambiguity –on the planet position angle– that is typically associated with a linear array, it yielded a sixth-order (θ^6) null. In the case of a linear interferometer having a central symmetry, an exoplanet can only be detected if it is sufficiently resolved, so much so that its signal exhibits a high modulation frequency as the array is rotated.

[Velusamy & Beichman \(2001\)](#) performed a simulated OASES observation of an Earth analogue with an exozodi emission inclined at 30° , and produced the so-called sin-chop by chopping between phase shifts $\pi/2$ and $3\pi/4$. A cos-chop output is generated by chopping between phase shifts 0 and π , as was the case in the original design of [Angel & Woolf \(1997\)](#) & [Woolf & Angel \(1997\)](#). By using the maximum correlation method (MCM) –akin to the Fourier transform used in radio astronomy– for image reconstruction, MCM images of the respective responses were compared with that of the array without any chopping (similar to the Angel Cross, though that was a 2-D array). Little difference was found between the cos-chop and the case without chopping. Both recovered images were heavily contaminated by exozodi emission and the planet was barely detectable. On the other hand, the sin-chop had an asymmetric response around the nulled star, which enabled the planet to be detected with a high contrast.

Chopping between phase shifts of $\pm\pi/2$ was applied by [Mennesson et al. \(2005\)](#) in a technique known as internal modulation. This chopping scheme imposes rapid changes on the interferometer response in order to modulate the planetary signal, and occurs without array rotation. The basic principle of internal modulation is to apply a time-varying alternating phase shift $\pm\phi(t)$ between the nulled outputs, recombine them and make the detection. Since we obtain two transmission maps –from each chop state– that are both asymmetric, a planet has two

different contributions. When it is located on a bright region in the first map, it is on a dark region in the second map. Thus, by alternately detecting these two outputs, we acquire a final signal where only the planetary part is modulated. Phase shifts that are accurately flipped between $\pm\pi/2$ not only eliminate the centro-symmetric exozodi signal at any time from the resulting output, but also ensure a maximum modulation efficiency of the planetary signal, regardless of where it may reside. With the application of internal modulation, [Mennesson et al. \(2005\)](#) report that the frequency of planetary signals can be much higher — in the range of 5×10^{-2} - 1 Hz. Meanwhile, when the array is rotated, the modulation frequencies vary between 3×10^{-5} - 3×10^{-4} Hz, which corresponds to one full rotation over a few hours.

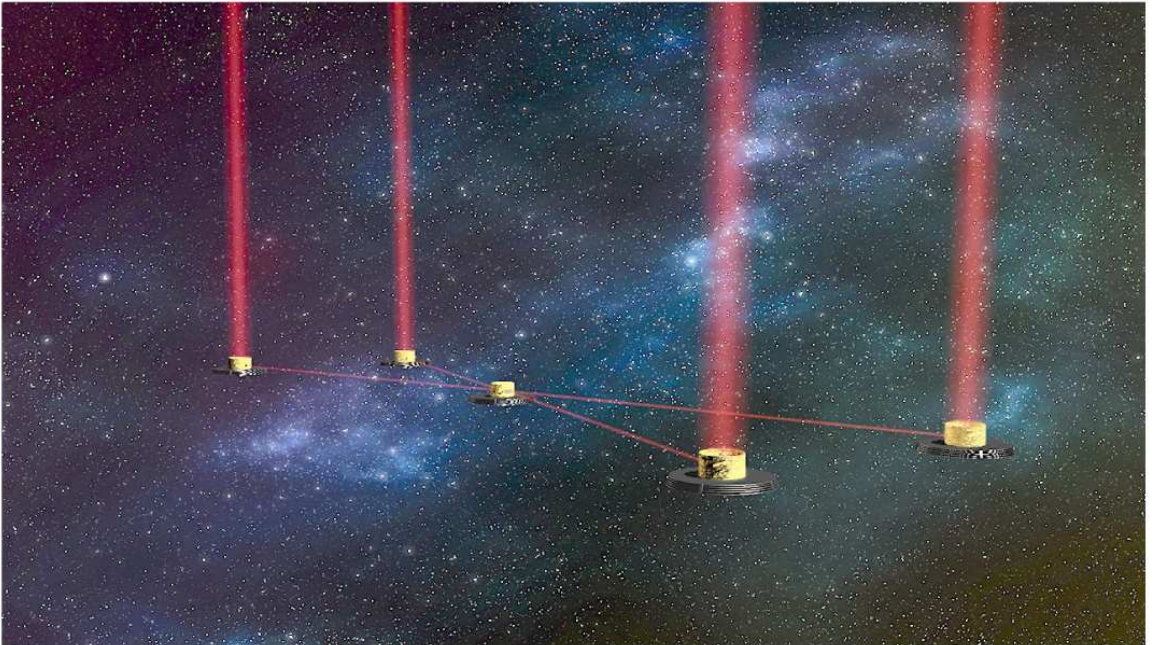


Figure 11: Artist's Impression of the LIFE space mission in an X-array configuration. This configuration, which was adopted for the ESA/Darwin and NASA/TPF-I missions, has a double Bracewell architecture, comprising four telescopes —in a rectangular formation— that feed a single beam combiner spacecraft where the nulled outputs are recombined with relative phase shifts of $\pm\pi/2$. During the Darwin/TPF-I era, the combiner spacecraft was initially located in the same plane as the telescopes, normal to the target direction (as shown in the figure). ESA later proposed the Emma X-array configuration, where the combiner is moved out ~ 1 -km towards the target, and the telescopes are reduced to a single spherical mirror. According to [Hansen et al. \(2022\)](#), the 4-telescope double Bracewell may not be the ideal nulling architecture for the LIFE mission, and that a 5-telescope kernel-nuller design could yield an improved scientific return for the same collecting area. Image from [Quanz et al. \(2022\)](#).

3.2 Systematic noise

Equation (2.4) describes how the electric fields of the light from separate apertures are combined with a specific set of amplitudes and phases. For this idealised implementation of a nuller, the integration times required for planet detection and characterisation will mainly depend on the strength of the planetary signal and the level of photon noise (i.e., solar zodiacal and exozodiacal light, flux leakage due to the finite size of stellar disks, and instrumental thermal emission). In reality, however, it will not be possible to maintain the precise set of amplitudes and phases that produce a perfect extinction on the on-axis source. Lay (2004) reports that the origin of the amplitude errors can be attributed to tip/tilt of the input beams, the reflectivity of the optics, beam shear, defocus, and differential transmission. Whereas OPD vibration, fringe tracking offset, dispersion, and birefringence produce phase errors. The power spectra of these instrumental effects mix with each other (i.e., errors from one input mix with those from others and amplitude fluctuations mix with phase fluctuations) so that perturbations at all frequencies have an effect. Amplitude and phase errors—including polarisation errors—will therefore lead to a deteriorated null response that causes a time-varying stellar flux leakage (a.k.a., systematic noise), which is an analogue of speckle noise in a coronagraph (see Guyon 2004), and results in an increased integration time on a target.

According to Lay (2004), phase chopping removes some of the systematic errors (i.e., slow drifts in stray light, thermal emission, and detector gain that can mimic the planet signal), but it has no effect on the dominant second-order amplitude–phase cross terms and the co-phasing error. This analysis, which considered a double Bracewell (with input phases in quadrature) operating at $10\mu\text{m}$, revealed that a $\sim 10^{-5}$ null-depth is sufficient to control the level of photon noise. However, a $\sim 10^{-6}$ null-depth is needed to prevent systematic noise from becoming the main source of noise. Such a null requires that the phase of the signal from each input is controlled to ~ 1 mrad (1.5 nm at $10\mu\text{m}$) and the amplitude to $\sim 0.1\%$. These conditions must be met simultaneously at all spectral channels, and for both horizontal and vertical polarisation states. Therefore, systematic noise, rather than photon noise drives the performance of a nuller.

In order to relax these stringent requirements, fine wavelength-dependent corrections to the amplitude and phase of the electric field can be applied with adaptive nulling (see Lay et al. 2003, Peters et al. 2010), consequently reducing tolerances of the various optical components. Adaptive nulling compensates for imbalances in the amplitude and phase by spectrally dispersing the light of each input onto a deformable mirror (DM). The mechanical stroke of the DM tunes

the phase and the tilt controls the amplitude. Both are adjusted independently at each wavelength and polarisation before being fed into a nuller. The range of the phase shift can be extended by setting the DM at an angle to a spectrograph, or by using the adaptive nuller simultaneously with other phase-shifting components such as a Mach-Zehnder interferometer. A laboratory demonstration of adaptive nulling by [Peters et al. \(2010\)](#) achieved a 10^{-5} null-depth across a $3.4 \mu\text{m}$ bandwidth (more than a third of the $7\text{--}17 \mu\text{m}$ wavelength range intended for TPF-I) centred on $9.9 \mu\text{m}$. Indeed, this result was obtained with an on-axis null produced in a classical pairwise fashion (where a π phase shift is applied on one of the input beams), but adaptive nulling can be applied to more complex beam combinations and input phase shifts.

[Lay \(2006\)](#) shows that the mechanisms responsible for amplitude and phase errors not only have a spectral dependence, but also a temporal nature (i.e., static or dynamic). A dynamic mechanism such as tip/tilt, which reduces the light coupled to the detector, produces a time-varying amplitude error that is proportional to λ^{-2} . Fringe tracker offset is also time-varying and results in a phase error that scales as the inverse of wavelength. Although static mechanisms (i.e., reflectivity, dispersion and birefringence) have a more complex spectral dependence than dynamic mechanisms, they can be mitigated with adaptive nulling. On the other hand, systematic noise (generated by the mixing of the dynamic mechanisms, i.e., amplitude–phase cross terms and the co-phasing error) has a slow dependence with wavelength, which allows it to be removed by the so-called ‘stretch and fit’ technique (see [Lay 2006](#)) that is based on the X-array ([Lay & Dubovitsky 2004](#)).

The X-array configuration for a space interferometer (see [Fig. 11](#)) has a double Bracewell architecture, comprising four telescopes—in a rectangular formation—that feed a single beam combiner spacecraft where the nulled outputs are recombined with relative phase shifts of $\pm\pi/2$. Stretching the array from a 2:1 aspect ratio (with 35-m nulling baselines and 70-m imaging baselines) to a 6:1 ratio (with 35-m nulling baselines and 210-m imaging baselines) will increase the angular resolution and the modulation frequency of the planetary signal that includes photon noise and systematic noise (see [Fig. 13](#)). In the approach presented by [Lay \(2006\)](#), systematic noise is shown to be a polynomial function of the optical frequency (or wavelength) multiplied by the stellar spectrum. Considering that systematic noise varies slowly with wavelength, it can be eliminated with polynomial fitting, though this also removes almost all of the signal when observing with the 2:1 X-array. However, as the 6:1 X-array generates a higher modulation frequency, a smaller fraction of the signal is removed with the fitting. A cubic polynomial is fitted at short wavelengths while a quadratic is applied for the long

wavelengths where the systematic noise is lower. Indeed, the decoupling of the nulling and imaging functions makes the X-Array ideal for the stretch and fit, but the technique could be applied to any array configuration.

ESA and NASA both studied various array configurations, each defined by the number and location of the telescopes, including their relative phase offsets that modulate the response around a deep on-axis null. The size of the array needed to observe a given target system is determined by the angular resolution and inner working angle, which is the smallest angular offset from the nulled star at which the array is sensitive to planetary light. ESA’s priority was to minimise the number of telescopes used in the initial concepts of Léger et al. (1996) & Mennesson & Mariotti (1997) whilst NASA focused on improving the imaging properties of the array as the design proposed by Angel & Woolf (1997) & Woolf & Angel (1997) featured a 180° imaging ambiguity on the planet position angle. Eventually, both sides of the Atlantic adopted the X-array, whose initial design had the combiner spacecraft located in the same plane as the telescopes, normal to the target direction (as shown in Fig. 11). ESA later proposed the Emma X-array configuration, where the combiner is moved out ~ 1 -km towards the target, and the telescopes are reduced to a single spherical mirror.

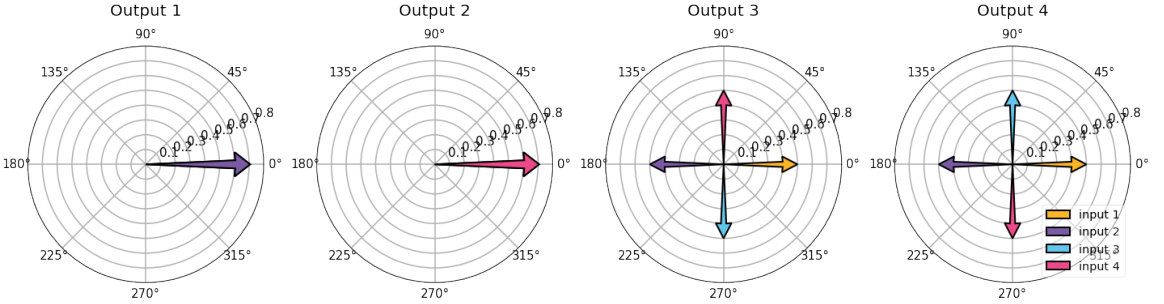


Figure 12: Complex matrix plots describing the theoretical M_{db} of a double Bracewell nuller. The phase of each input is represented by a colored arrow whose length encodes the amplitude. At each output, the resulting electric field is the sum of all arrows. Outputs 1 & 2 (bright outputs) are an in-phase constructive recombination of the inputs. Outputs 3 & 4 both result in nulls (with the sum of the four arrows leading back to zero), though they differ in the applied input phase shifts that are multiples of $\pi/2$.

3.3 Space and ground-based nulling with a double Bracewell

A two-aperture Bracewell interferometer requires only one beam-splitter, whose action is represented by the complex matrix M (see Eq. (2.2)). In a similar way, the input phase offsets and beam combinations for a double Bracewell, which needs

four beam-splitters in a co-axial scheme, can be described by a nuller response matrix that is given as:

$$\mathbf{M}_{\text{db}} = \frac{1}{2} \times \begin{bmatrix} \sqrt{2} & \sqrt{2} & 0 & 0 \\ 0 & 0 & \sqrt{2} & \sqrt{2} \\ 1 & -1 & -e^{\frac{\pi j}{2}} & e^{\frac{\pi j}{2}} \\ 1 & -1 & e^{\frac{\pi j}{2}} & -e^{\frac{\pi j}{2}} \end{bmatrix}. \quad (2.23)$$

Figure 12 provides a visual representation of the desired reorganisation of the input electric fields (represented by coloured arrows) in the complex plane that is summarised by \mathbf{M}_{db} . Since one can only record the intensity (absolute square), the nuller is insensitive to any global phase shift applied to an output (or row of \mathbf{M}_{db}), which would correspond to an overall rotation of the arrows in a complex matrix plot (CMP). Only relative phase offsets introduced by the device between the inputs matter, and the convention here is to take input 1 as the phase reference, explaining why all yellow arrows in Fig. 12 remain aligned with the real axis of the complex plane.

Pairs of inputs are combined in-phase ($\varphi = 0$) to produce two bright outputs: output 1 (1-2) & output 2 (3-4). The following two –nulled– outputs represent the two chop states, arranged such that the response for one state is the same as the response for the other, rotated through 180° . One can observe that these outputs are mirror images of each other from the CMPs shown in Fig. 12. The input phases for output 3 are: $\varphi = 0, \pi, \frac{3\pi}{2}, \frac{\pi}{2}$, respectively. Whereas for output 4: $\varphi = 0, \pi, \frac{\pi}{2}, \frac{3\pi}{2}$. Some systematic errors will be incoherent between the inputs, and thus identical for the two nulled outputs, whose flux difference will eliminate them, while preserving the asymmetric planetary signal.

To illustrate the properties of a double Bracewell interferometer, it is useful to examine the transmission maps and the subsequent modulation maps of the linear and X-array configurations. The response of the different configurations is dependent on \mathbf{M}_{db} and the n telescope coordinates (x_n, y_n) that can be computed as:

2 kernel-nulling for the direct detection of exoplanets

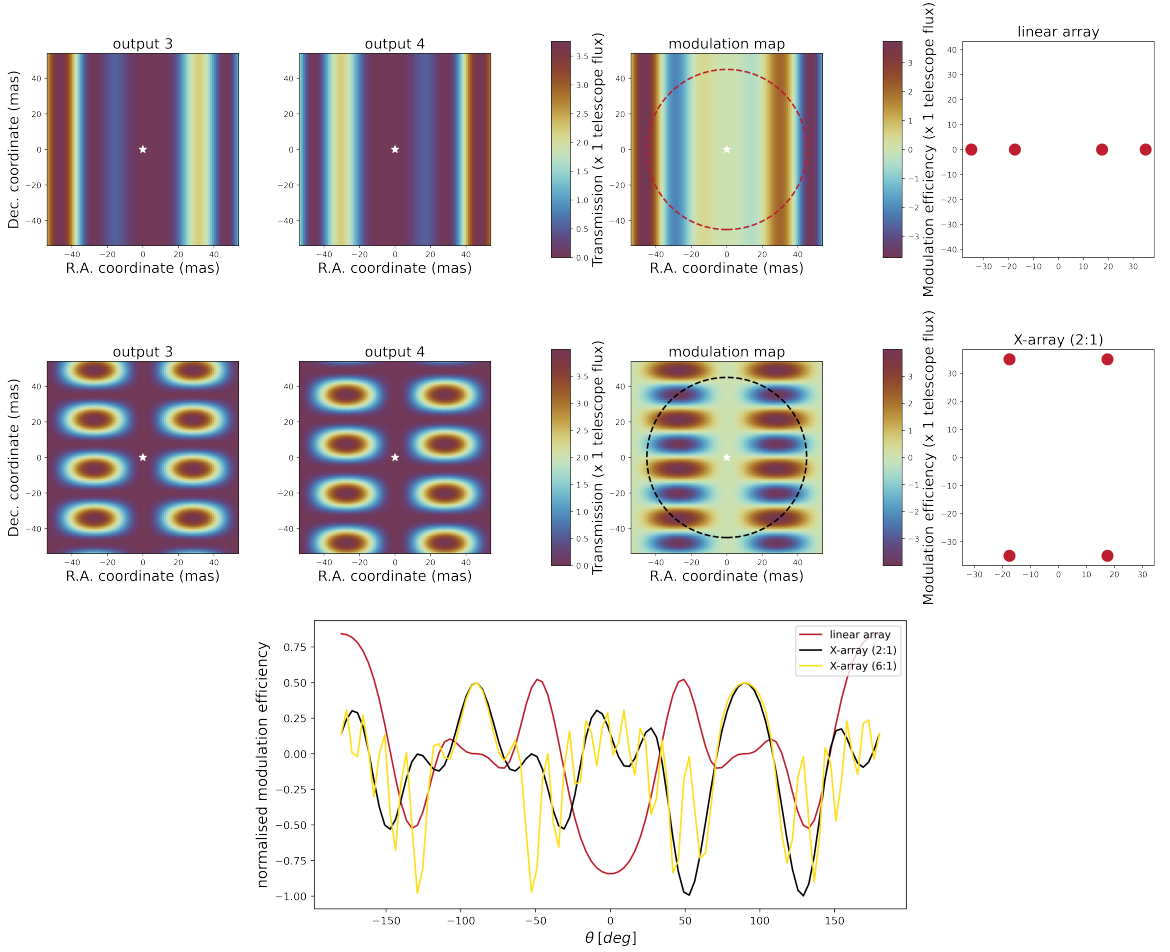


Figure 13: **Top panel:** Double Bracewell nuller transmission and modulation maps computed for a wavelength of $9.6\mu\text{m}$ over a ± 55 mas FOV, with a linear array for a single snapshot pointing. Outputs 3 & 4 represent the two chop states, arranged such that the response for one state is the same as the response for the other, rotated through 180° . These outputs share the same color scale where the transmission is expressed in units of the planet flux. Taking the difference (phase chopping) of the two outputs produces the modulation map, which contains positive and negative values by construction (shown by the color scale on the right of the map where the transmission is expressed in units of modulation efficiency). Phase chopping introduces an additional modulation to the planet signal that allows it to be isolated from some systematic errors. When the interferometer goes through a 360° rotation while pointing to the star, a hypothetical planet describes a circle with radius 45 mas in the transmission plane, as indicated with the red coloured dashed lines in the modulation map. A white star in each map marks the location of the central star where the transmission, by design, is equal to zero. The telescope coordinate positions for the linear array are shown on the far right. **Middle panel:** Here, we see the richness and diversity brought by the 2D X-array configuration with a 2:1 aspect ratio (shown in the far right). A hypothetical planet describes a circle with radius 45 mas in the transmission plane, as indicated with the black coloured dashed lines in the modulation map. **Bottom panel:** Normalised modulation efficiency —by total flux— as a function of rotation angle for a planet (at 45 mas) detected with the linear array, 2:1 X-array, and 6:1 X-array. As the nulling interferometer rotates around the line-of-sight, the modulation map centred on the star rotates with it. As the map rotates, the bright and dark regions in the map sweep across the position of the planet, modulating its signal. The horizontal axis (Dec = 0) in the modulation map is the reference axis for θ .

| Configuration | n | x_n | y_n |
|---------------|---|-------|--------|
| Linear array | 1 | -B | 0 |
| | 2 | -0.5B | 0 |
| | 3 | 0.5B | 0 |
| | 4 | B | 0 |
| X-array | 1 | 0.5B | 0.5qB |
| | 2 | -0.5B | 0.5qB |
| | 3 | -0.5B | -0.5qB |
| | 4 | 0.5B | -0.5qB |

For the X-array, the baseline B can be optimised for starlight rejection and the aspect ratio q tuned for angular resolution. The decoupling of the nulling and imaging functions makes the X-Array more flexible than other designs.

Utilising Eq. (2.5), with $B = 35$ -m (for both array configurations) and $q = 2$ (for the X-array), I compute the maps shown in Fig. 13 at $9.6\mu\text{m}$, which is the classical signature of biological activity in the mid-infrared (i.e., where O_3 is used as a tracer of O_2). The field of view (FOV) of a single snapshot in these maps has been set by the baseline ($\lambda/B \approx 55 \text{ mas}$).

The linear array transmission maps (see top panel of Fig. 13) of output 3 & 4 exhibit a left–right asymmetry. Output 3 produces the ‘left’ chop state as there is a peak in the response immediately to the left of the central star (bright stripe that corresponds to a high transmission region), whereas output 4 generates the ‘right’ chop state. Rapidly switching between these two states, recombining the outputs, and making a detection is the technique of internal modulation. Taking the difference of the two transmission maps yields the asymmetric modulation map (or ‘chopped’ response), which contains positive and negative values by construction.

Besides the benefit of a superior (u, v) coverage, using more telescopes can allow for complex transmission patterns as shown with the X-array maps in the middle panel of Fig. 13. With such maps, more regions of high and low transmission cross the planet’s position as the interferometer is rotated, subsequently increasing the modulation frequency of the planetary signal, which can alleviate planet position ambiguities in image reconstruction. In the bottom panel of Fig. 13 we see that the 6:1 X-array has a higher modulation frequency than the 2:1 X-array and the linear array. The 6:1 X-array is not only less susceptible to systematic noise than these configurations, but also has a smaller IWA.

Although an increment in apertures provides a high level of rejection at the centre of the modulated field, the null should also enable a small IWA. Indeed,

both are difficult to meet simultaneously because a higher angular resolution requires a longer baseline (which would result in a narrow central dark stripe in the transmission maps shown in the top panel of Fig. 13), while a low stellar leakage requires just the opposite. For an exoplanet characterisation program using adjustable aperture separations (as would be the case with spacecraft formation flying or the relocatable VLTI ATs), the constraints on the null could be relaxed since the transmission map can be tuned for each target. This would allow for longer observation periods that provide a spectrum where possibly biosignatures are detected.

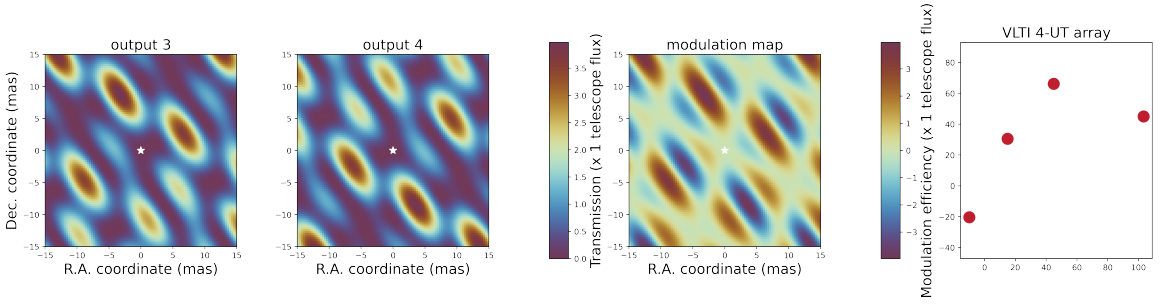


Figure 14: Double Bracewell nuller transmission and modulation maps computed for a wavelength of $3.6\mu\text{m}$ over a ± 15 mas FOV, with the VLTI 4-UT array for a pointing exactly at zenith. The transmission maps of output 3 & 4 differ from one another and this diversity in the output response provides a constraint on the properties of a potential companion in the vicinity of a much brighter star. About the centre of the field, the maps are asymmetric. For transmission maps, this asymmetry is a desirable trait as it allows for the elimination of centro-symmetric astrophysical features that would otherwise hide a planetary companion. Both maps share the same color scale where the transmission is expressed in units of the planet flux. Taking the difference of the two outputs produces the modulation map, which contains positive and negative values by construction (shown by the color scale on the right of the map where the transmission is expressed in units of modulation efficiency). A white star in each map marks the location of the central star where the transmission, by design, is equal to zero. The coordinate positions of the four 8-m diameter unit telescopes (UTs) of the VLTI are shown on the far right. To better illustrate the effects of nulling close to the central star, the FOV of a single snapshot in these maps has been set by the shortest ($B = 46.6$ meter) baseline of the array ($\lambda/B \approx 15$ mas).

Apart from space-based interferometry, the double Bracewell architecture has also been implemented on ground-based long-baseline interferometers. The KIN combined both 10-m Keck telescopes to conduct a survey —of exozodiacal dust around 47 nearby main sequence stars— that utilised 10 spectral channels ranging from $8\mu\text{m}$ to $13\mu\text{m}$. High-contrast detection of planetary companions with a double Bracewell is the objective of the Nulling Observations of dust and planets (NOTT; [Laugier et al. 2023](#)) instrument: one of the modules of the planned Asgard instrument suite to be installed at the focus of the VLTI in 2025. NOTT will aim to characterise young giant planets in the L' -band down to the snow

line of their host system by combining light from the four VLTI UTs or ATs (see Fig. 14 for double Bracewell L' -band transmission and modulation maps with the VLTI 4-UT array). The large AT quadruplet configuration offered in P110¹ features a maximum baseline length of 132.4-m, which sets an IWA of 5.4 mas (6.9 mas for the medium). For L' -band observations, the single-mode (diffraction-limited) FOV of the ATs extends to an outer working angle (OWA) of ~ 400 mas. These IWA and OWA constraints suggests that NOTT can detect giant planets on orbits ranging from 0.24 to 18 AU (0.31–18 AU for the medium) for an object located at a distance of ~ 45 pc. The Asgard suite also includes HEIMDALLR (Ireland et al. 2018): a high-precision fringe tracker and injection stabilisation module. A HEIMDALLR prototype (Cvetojevic et al. 2023) was tested on the kernel test bench (presented in Chapter 6) and demonstrated that for targets brighter than $K = 11$, closed-loop fringe tracking residuals can be brought down to ~ 4 nm RMS.

4 Summary

With nulling interferometry, the high-angular resolution information on the observed object is encoded in the null-depth, which is the intensity ratio of a nulled output (where off-axis planetary light is collected) over the bright output (where most of the on-axis starlight is directed). To detect a terrestrial planet, a null-depth of $\sim 10^{-6}$ would be required at mid-infrared wavelengths, where the constraints on phase stability are more relaxed than at shorter wavelengths. The measured null-depth is biased by fluctuations in the amplitude and phase of the input electric fields, whose origin can be attributed to various seeing-induced and instrumental perturbations. Accurate null-depth measurements can be achieved with statistical data analysis and fitting methods such as NSC. NSC has yielded on-sky null-depth accuracies of $\sim 10^{-4}$ on state-of-the-art facilities such as the near-infrared PFN, GLINT, and the mid-infrared LBTI that all use the classical Bracewell architecture. This data reduction method requires the acquisition of a large data-set to sample the statistical distribution of the error parameters, which include all of the phase and intensity fluctuations that need short integration times. Indeed, NSC does pose a limitation on observational sensitivity/efficiency, and could also be fairly complex to implement with an increment in nuller inputs.

While a two-telescope nulling interferometer could be used to detect the thermal emission of giant exoplanets, as proposed by Bracewell, it is limited by its

¹<https://www.eso.org/sci/facilities/paranal/telescopes/vlti/configuration/P111.html>

incapacity to remove extraneous signals (i.e., solar zodiacal and exozodiacal light, flux leakage due to the finite size of stellar disks, and instrumental thermal emission) that add to the planetary signal. A solution is to implement a signal modulation scheme, which requires more telescopes that add complexity to the system. But a greater suppression of the on-axis source is also possible with more than two apertures.

The four-telescope 2D X-array configuration, which was adopted for the Darwin and TPF-I missions, has a double Bracewell architecture, where the nulled outputs are recombined with relative phase shifts of $\pm\pi/2$ to produce a single self-calibrating observable that can be derived without the use of NSC. However, according to [Lay \(2004\)](#), this observable removes some of the systematic errors, but it has no effect on the dominant second-order amplitude–phase cross terms and the co-phasing error. To prevent systematic errors from becoming the main source of noise, a null-depth of $\sim 10^{-6}$ is needed. Such a null requires that the phase of the signal from each input is controlled to ~ 1 mrad (1.5 nm at 10 μm) and the amplitude to $\sim 0.1\%$. These conditions must be met simultaneously at all spectral channels, and for both horizontal and vertical polarisation states.

This thesis work focuses on an advanced nulling architecture and data reduction technique called kernel-nulling, which replicates several properties of the double-Bracewell but leads to a wider family of self-calibrating solutions.

Chapter 3

Kernel-nulling interferometry

Although the double Bracewell architecture produces a single self-calibrating observable that can be derived without the use of NSC, it produces two bright outputs. According to [Guyon et al. \(2013\)](#), an optimal beam combiner optically redirects the on-axis light to the fewest number of outputs. While it is not possible to concentrate all starlight (for a partially resolved on-axis source) in a single output, one can identify the coefficient values of a nuller response matrix that maximises the stellar flux in it. As much of the residual flux is then collected in a second output, with the process repeated over the number of outputs until a full matrix is constructed. This iterative process which ensures that the stellar flux decreases as a function of the interferometer outputs is performed by singular value decomposition (SVD).

An SVD-based approach is applicable to a 1D or 2D aperture geometry, and can also be used to construct more complex nulling architectures that mitigate the constraints of observing from the ground as the measurement errors due to varying OPD are a dominant factor. [Lacour et al. \(2014\)](#) proposed a solution that aims to deal with such effects by integrating nulling with closure phase (see [Jennison 1958](#)). This self-calibration concept produces nulled outputs in a classical pairwise fashion, where a π phase shift is applied on one of the input beams. The outputs are then combined to retrieve the complex visibility, from which self-calibrating closure phase observable quantities are derived.

Drawing on these advances in beam combiner design and self-calibration, [Martinache & Ireland \(2018\)](#) developed a nulling architecture and data reduction technique called kernel-nulling. Kernel-nulling, which follows the Bracewell concept, enables a reliable high-contrast imaging solution that is independent of second-order atmospheric-piston-induced phase perturbations. This allows for deeper nulls in the presence of residual fringe tracker errors. Indeed, a kernel-nuller replicates several properties of the double-Bracewell architecture described in [Chapter 2](#), but its theory is quite general and leads to a wider family of self-calibrating solutions that can be found for any interferometer simultaneously recombining at least three sub-apertures.

The four-input kernel-nuller proposed by [Martinache & Ireland \(2018\)](#) was designed to produce a complete set of six high-contrast (nulled) outputs, that give access to three self-calibrating observable quantities (a.k.a., kernel-nulls), matching the number of independent closure-phases provided by a four-aperture interferometer. Using this nuller as a starting point, the following section revisits some important properties of kernel-nulls: their robustness to small phase perturbations, and the asymmetric nature of the signal they provide.

1 A brief introduction to kernel-nulling

Equation (2.3) expresses the relationship between the interferometer outputs V and inputs U , which are linked by a complex matrix \mathbf{M} that describes the interferometric combinations performed between the apertures. $\|V\|^2 = \|U\|^2$ if these combinations preserve total flux, meaning that \mathbf{M} must be a complex unitary matrix. The solution of [Martinache & Ireland \(2018\)](#) builds from a four-input/four-output combiner that one could build out of beam-splitters and π phase-shifters as described by [Guyon et al. \(2013\)](#). This nuller is summarised by the matrix \mathbf{N} :

$$\mathbf{N} = \frac{1}{\sqrt{4}} \times \begin{bmatrix} 1 & 1 & 1 & 1 \\ 1 & 1 & -1 & -1 \\ 1 & -1 & 1 & -1 \\ 1 & -1 & -1 & 1 \end{bmatrix}. \quad (3.1)$$

Apart from the first row (bright output) of \mathbf{N} where the input complex amplitudes are constructively combined, each row combines differences of complex amplitudes that result in a distinct nulled output. An ideal equal intensity split of the signal in the outputs is expressed by the $1/\sqrt{4}$ factor, which also makes \mathbf{N} a complex unitary matrix. Only relative phase offsets between the inputs matter, and the convention here is to take input 1 as the phase reference, explaining why the first column of \mathbf{N} only contains 1. Phase or piston values are quoted relative to this sub-aperture.

Although a nuller will benefit from a fringe tracker that will co-phase the inputs, it will be affected by some amount of residual OPD. These atmospheric piston residuals can be assumed to be small, and a first order Taylor expansion of piston ρ dependence on the input electric field at a wavelength λ is approximated as:

$$u_k = e^{-j\varphi_k} \approx 1 - j\varphi_k, \quad (3.2)$$

where at output k , the chromatic phase $\varphi_k = 2\pi\rho/\lambda$. Accounting for the fact that the interferometric recombination process preserves total flux (i.e., $\|V\|^2 = \|\mathbf{N} \cdot U\|^2$):

$$\|V\|^2 = \frac{1}{4} \times \begin{bmatrix} (\varphi_1 - \varphi_2 - \varphi_3)^2 \\ (-\varphi_1 + \varphi_2 - \varphi_3)^2 \\ (-\varphi_1 - \varphi_2 + \varphi_3)^2 \end{bmatrix}. \quad (3.3)$$

A further expansion of Eq. (3.3) gives:

$$\|V\|^2 = \frac{1}{4} \times \begin{bmatrix} (\varphi_1^2 + \varphi_2^2 + \varphi_3^2 - 2\varphi_1\varphi_2 - 2\varphi_1\varphi_3 + 2\varphi_2\varphi_3) \\ (\varphi_1^2 + \varphi_2^2 + \varphi_3^2 - 2\varphi_1\varphi_2 - 2\varphi_1\varphi_3 + 2\varphi_2\varphi_3) \\ (\varphi_1^2 + \varphi_2^2 + \varphi_3^2 + 2\varphi_1\varphi_2 - 2\varphi_1\varphi_3 - 2\varphi_2\varphi_3) \end{bmatrix}. \quad (3.4)$$

According to [Serabyn et al. \(2012\)](#), in the absence of geometric leakage due to the finite extent of the stellar disk, the measured output intensity is a function of quadratic terms, each arising from a distinct error source. Equation (3.4) shows that the piston induced leak of \mathbf{N} is a function of six parameters: three second-order terms (φ_k^2) and three crossed-terms ($\varphi_k\varphi_l$).

We recall the double Bracewell response matrix (see Eq. (2.23)), where the rows reflect a two-stage approach. In a first stage, pairs of inputs (i.e., inputs 1-2 & 3-4) are nulled in two single Bracewell combiners. The nulled outputs are then recombined with one of the outputs receiving an additional phase shift of $\frac{\pi}{2}$ in a second stage. This produces two asymmetric outputs that can be used to apply phase chopping, which as described by [Lay \(2004\)](#) will remove some of the systematic errors but has no effect on the dominant second-order amplitude-phase cross terms and the co-phasing error. Here, \mathbf{N} represents a first stage (nulling function) and to produce self-calibrating observables, one needs to further break down each nulled output of \mathbf{N} into two asymmetric outputs that will remove a few of the errors identified in Eq. (3.4) when properly mixed. Akin to the second stage of the double Bracewell, [Martinache & Ireland \(2018\)](#) incorporated a split (or chop) matrix \mathbf{S} :

$$\mathbf{S} = \frac{1}{\sqrt{4}} \times \begin{bmatrix} 2 & 0 & 0 & 0 \\ 0 & 1 & e^{\frac{\pi j}{2}} & 0 \\ 0 & -e^{-\frac{\pi j}{2}} & 1 & 0 \\ 0 & 1 & 0 & e^{\frac{\pi j}{2}} \\ 0 & -e^{-\frac{\pi j}{2}} & 0 & 1 \\ 0 & 0 & 1 & e^{\frac{\pi j}{2}} \\ 0 & 0 & -e^{-\frac{\pi j}{2}} & 1 \end{bmatrix}. \quad (3.5)$$

\mathbf{S} leaves the bright output untouched (i.e., a positive real coefficient means that the light is not phase-shifted between the input and output), and further splits the nulled outputs by selectively introducing $\pm\pi/2$ phase shifts. The overall effect of the combiner is now described by a four-input/seven-output (4×7) nuller response matrix, noted $\mathbf{M}_{4 \times 7}$:

$$\mathbf{M}_{4 \times 7} = \mathbf{S} \cdot \mathbf{N} = \frac{1}{4} \times \begin{bmatrix} 2 & 2 & 2 & 2 \\ 1 + e^{\frac{\pi j}{2}} & 1 - e^{\frac{\pi j}{2}} & -1 + e^{\frac{\pi j}{2}} & -1 - e^{\frac{\pi j}{2}} \\ 1 - e^{-\frac{\pi j}{2}} & -1 - e^{-\frac{\pi j}{2}} & 1 + e^{-\frac{\pi j}{2}} & -1 + e^{-\frac{\pi j}{2}} \\ 1 + e^{\frac{\pi j}{2}} & 1 - e^{\frac{\pi j}{2}} & -1 - e^{\frac{\pi j}{2}} & -1 + e^{\frac{\pi j}{2}} \\ 1 - e^{-\frac{\pi j}{2}} & -1 - e^{-\frac{\pi j}{2}} & -1 + e^{-\frac{\pi j}{2}} & 1 + e^{-\frac{\pi j}{2}} \\ 1 + e^{\frac{\pi j}{2}} & -1 - e^{\frac{\pi j}{2}} & 1 - e^{\frac{\pi j}{2}} & -1 + e^{\frac{\pi j}{2}} \\ 1 - e^{-\frac{\pi j}{2}} & -1 + e^{-\frac{\pi j}{2}} & -1 - e^{-\frac{\pi j}{2}} & 1 + e^{-\frac{\pi j}{2}} \end{bmatrix}. \quad (3.6)$$

In order to identify the output combinations of $\mathbf{M}_{4 \times 7}$ that would result in self-calibrating observable quantities, which are referred to as kernel-nulls, [Martinache & Ireland \(2018\)](#) proposed to study the properties of a second-order derivative matrix \mathbf{A} . This 6×6 matrix is analogous to the phase transfer matrix introduced by [Martinache \(2010\)](#) and records the response of the nuller to the six second-order terms shown in Eq. (3.4). Linear combinations of rows of \mathbf{A} that equal zero will cancel out the second-order terms caused by small atmospheric piston residuals. These linear combinations are summarised by a left-hand operator \mathbf{K} , that results in a three-element kernel output vector: $\kappa(t) = \mathbf{K} \cdot I(t)$, where $I(t)$ is a six-component vector describing the raw output effectively recorded by the nuller (see Eq. (2.4)). For this ideal nuller, the solution is quite simple and \mathbf{K}

is given as:

$$\mathbf{K} = \begin{bmatrix} 1 & -1 & 0 & 0 & 0 & 0 \\ 0 & 0 & 1 & -1 & 0 & 0 \\ 0 & 0 & 0 & 0 & 1 & -1 \end{bmatrix}. \quad (3.7)$$

A kernel output is therefore simply the pairwise difference between consecutive raw outputs (1–2, 3–4, and 5–6). On a less ideal nuller, \mathbf{K} would generally be found as the product of the SVD of \mathbf{A} , using the methodology of [Martinache \(2010\)](#). [Laugier et al. \(2020\)](#) investigated the properties of $\mathbf{M}_{4 \times 7}$ and found that the kernel forming combinations can be identified by examining the complex matrix plots (CMPs) of the combiner.

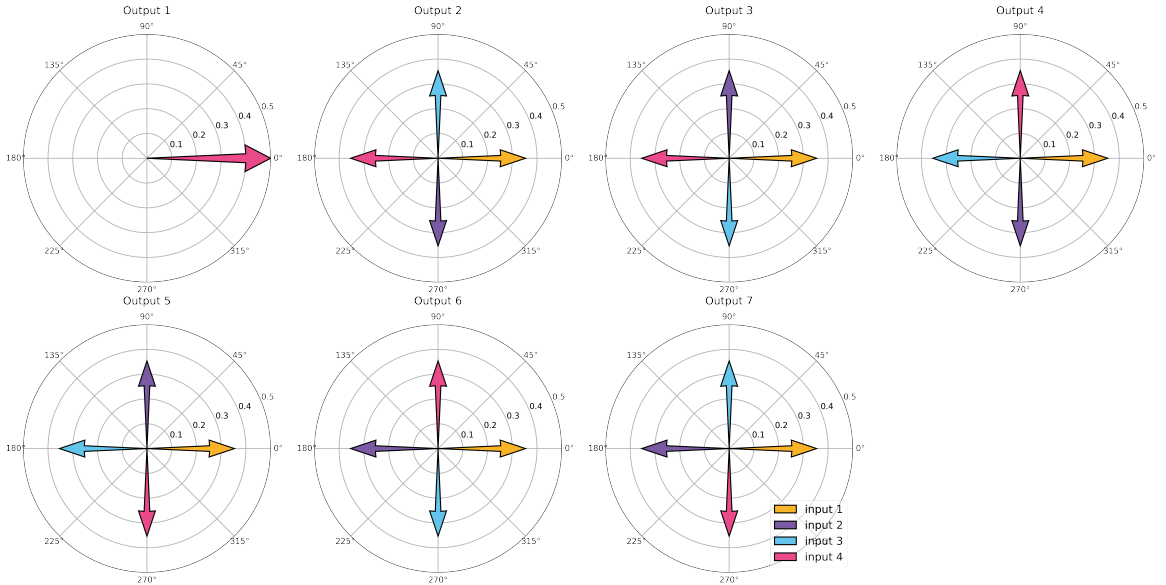


Figure 15: Complex matrix plots describing the theoretical $\mathbf{M}_{4 \times 7}$ of a four-input/seven-output (4×7) kernel-nuller. The phase of each input is represented by a colored arrow whose length encodes the amplitude. At each output, the resulting electric field is the sum of all arrows. Since one can only record the intensity (absolute square), the nuller is insensitive to any global phase shift applied to an output (or row of $\mathbf{M}_{4 \times 7}$), which would correspond to an overall rotation of the arrows in a complex matrix plot. Only relative phase offsets introduced by the device between the inputs matter, and the convention here is to take input 1 as the phase reference, explaining why all yellow arrows remain aligned with the real axis of the complex plane. Four in-phase input signals combine to produce a bright output (output 1). For the six distinct nulled outputs (output 2–7), pairs of inputs along each nulling baseline are combined with phase shifts that are multiples of $\pi/2$. For instance, to produce output 2, input 1 is combined with input 4 and input 2 is combined with input 3. Similar inspections can also be made for the subsequent outputs.

From the CMPs of $\mathbf{M}_{4 \times 7}$ presented in Fig. 15, one can observe that the nulled outputs are analogous to the outputs generated with a double Bracewell (see Fig. 12), though in this architecture the amplitude is reduced due to additional splitting. Figure 15 also shows that outputs 2–3, 4–5, and 6–7 are mirror images (or complex conjugates) of each other. By identifying the conjugate pairs from the CMPs, Laugier et al. (2020) describes the robustness of kernel-nulls, whose nomenclature I adopt here:

If \mathbf{m}_1 and \mathbf{m}_2 are a conjugate pair of nulled rows of \mathbf{M} :

$$\mathbf{m}_2 = \mathbf{m}_1^*. \quad (3.8)$$

A kernel-null $\kappa(\mathbf{u})$ is therefore a difference of the two measured intensities:

$$\kappa(\mathbf{u}) = |\mathbf{m}_1 \mathbf{u}|^2 - |\mathbf{m}_2 \mathbf{u}|^2 = \mathbf{m}_1 \mathbf{u} (\mathbf{m}_1 \mathbf{u})^* - \mathbf{m}_2 \mathbf{u} (\mathbf{m}_2 \mathbf{u})^*. \quad (3.9)$$

Applying Eq. (3.8) and Eq. (3.9) gives:

$$\kappa(\mathbf{u}) = \mathbf{m}_1 \mathbf{u} (\mathbf{m}_1 \mathbf{u})^* - \mathbf{m}_1^* \mathbf{u} (\mathbf{m}_1^* \mathbf{u})^*. \quad (3.10)$$

Considering the approximation in Eq. (3.2):

$$\kappa(\mathbf{u}) = \mathbf{m}_1 (\mathbf{a} + j\boldsymbol{\varphi}) (\mathbf{m}_1 (\mathbf{a} + j\boldsymbol{\varphi}))^* - \mathbf{m}_1^* (\mathbf{a} + j\boldsymbol{\varphi}) (\mathbf{m}_1^* (\mathbf{a} + j\boldsymbol{\varphi}))^*, \quad (3.11)$$

where \mathbf{a} is a vector of ones. Since $\mathbf{m}_1 \mathbf{a} = 0$ and $\mathbf{m}_1^* \mathbf{a} = 0$, the remaining terms are the ones containing only the imaginary perturbation term $j\boldsymbol{\varphi}$:

$$\kappa(\mathbf{u}) = (\mathbf{m}_1 j\boldsymbol{\varphi}) (\mathbf{m}_1 j\boldsymbol{\varphi})^* - (\mathbf{m}_1^* j\boldsymbol{\varphi}) (\mathbf{m}_1^* j\boldsymbol{\varphi})^*. \quad (3.12)$$

Distributing the conjugate operator gives:

$$\kappa(\mathbf{u}) = -\mathbf{m}_1 j\boldsymbol{\varphi} \mathbf{m}_1^* j\boldsymbol{\varphi} + \mathbf{m}_1^* j\boldsymbol{\varphi} \mathbf{m}_1 j\boldsymbol{\varphi}, \quad (3.13)$$

giving $\kappa(\mathbf{u}) = 0$, owing to commutativity. Equation (3.13) shows that the difference of a conjugate pair of nulled outputs will produce a kernel-null that is robust to small fringe tracking phase errors. This property can also be applied to small amplitude photometric fluctuations, whose impact is modelled using the framework outlined for the phase. However, photometric fluctuations of the inputs can be independently measured via photometric taps.

To demonstrate the robustness of kernel-nulls, Martinache & Ireland (2018) performed a series of simulated observations with a kernel-nuller at the focus of the VLTI 4-UT (at zenith) configuration. The simulation included an off-axis

3 kernel-nulling for the direct detection of exoplanets

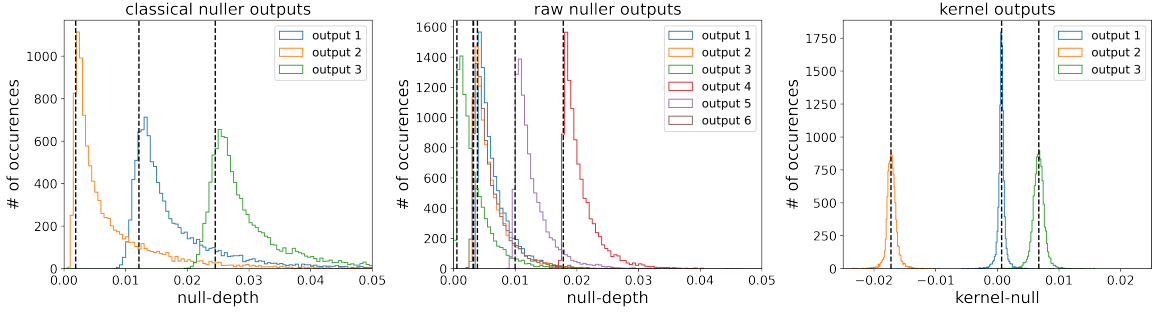


Figure 16: Statistical distribution of the four-input/seven-output (4×7) kernel-nuller outputs during the observation of an off-axis companion (for a contrast $c = 10^{-2}$, and located at $\alpha = +4.8$ mas, $\delta = +1.8$ mas) in the presence of 50 nm RMS residual piston excursions drawn from a Gaussian distribution. Each sub-figure (from left to right) features the distribution of the outputs at the different stages: the classical nuller \mathbf{N} , raw nuller $\mathbf{M}_{4 \times 7}$ and kernel outputs κ . The dashed lines mark the expected location of the astrophysical null – and subsequent kernel-null – in the absence of phase perturbations. Plot from [Martinache & Ireland \(2018\)](#).

companion located at an optimal location of $\alpha = +4.8$ mas, $\delta = +1.8$ mas (for a contrast $c = 10^{-2}$). Figure 16 presents the results of these simulations (a total of 10^4 acquisitions per simulation) that are in the presence of 50 nm residual piston excursions. Each sub-figure features the distribution of the outputs at the different stages: the classical nuller \mathbf{N} , raw nuller $\mathbf{M}_{4 \times 7}$, and kernel outputs κ . We see that the null-depth distributions for both the classical and raw nuller outputs are asymmetric, trailing off more sharply on one side than the other. On-sky observations with PFN and GLINT exhibit such skewed distributions that rely on the NSC procedure I described in Chapter 2 to deduce the astrophysical null-depth. By comparison, the self-calibrating properties of the kernel-null are apparent as the distribution is symmetric with relatively straightforward statistics which allow for a direct interpretation. It is this reality that motivated the kernel-nuller architecture, designed so that at any instant, simultaneously recorded values of the nulled outputs can be combined to form kernel-nulls, disentangling genuine astrophysical signals from seeing-induced light leakage.

Besides the expected multiplication of outputs going from \mathbf{N} to $\mathbf{M}_{4 \times 7}$, a major difference lies in the symmetry properties of the outputs in response to the presence of off-axis features in the interferometric field of view. The classical nuller features transmission maps that are symmetric relative to the on-axis reference. But, the raw nuller transmission maps are asymmetric: allow to discriminate a positive from a negative offset position, thus providing a stronger constraint on the position of a companion around a bright star from a single observation. The kernel output maps that consist of linear combinations of asymmetric transmis-

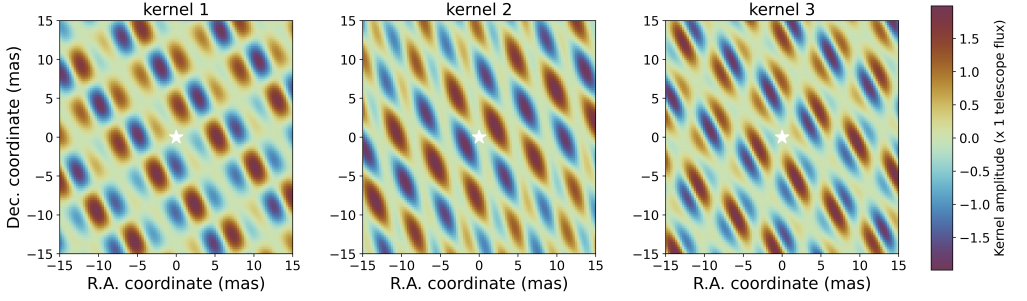


Figure 17: Kernel output maps of a four-input/seven-output (4×7) kernel-nuller. These maps have been computed for a wavelength of $3.6\mu\text{m}$ with the VLTI 4-UT array for a pointing exactly at zenith. To better illustrate the effects of nulling close to the central star, the field of view of a single snapshot in these maps has been set by the shortest ($B = 46.6$ meter) baseline of the array ($\lambda/B \approx 15$ mas). A kernel output is simply the difference between the two nuller outputs for which the same pairs of inputs are nulled with each other (output 2–3, 4–5, and 6–7 in Fig. 15). Taking the difference of output values means that unlike raw photometric-like outputs, kernel outputs can take negative values. This is shown on the color scale on the right of the map where the transmission is expressed in units of kernel amplitude. A white star in each map marks the location of the central star where the transmission, by design, is equal to zero.

sion maps are also asymmetric as shown in Fig. 17. Whereas raw outputs are a measure of flux, which is always positive, kernel outputs can take negative values. These outputs are optimal for the observation of high-contrast non-symmetrical features, in particular, exoplanets. Meanwhile, the classical nuller outputs could be used to study brighter symmetrical features such as exozodi, perhaps with the aid of NSC.

Laugier et al. (2020) describes the asymmetry of the kernel outputs by considering two electric field vectors \mathbf{u} & \mathbf{u}' from sources located at symmetric positions in the field of view, thereby:

$$\mathbf{u}' = \mathbf{u}^*. \quad (3.14)$$

For a conjugate pair of nulled rows \mathbf{m}_1 and \mathbf{m}_2 , and substituting Eq. (3.14) into Eq. (3.9):

$$\kappa(\mathbf{u}) = \mathbf{m}_1 \mathbf{u}'^* (\mathbf{m}_1^* \mathbf{u}') - \mathbf{m}_2 \mathbf{u}'^* (\mathbf{m}_2^* \mathbf{u}'). \quad (3.15)$$

Following the substitution of Eq. (3.8):

$$\kappa(\mathbf{u}) = \mathbf{m}_2^* \mathbf{u}'^* (\mathbf{m}_2 \mathbf{u}') - \mathbf{m}_1^* \mathbf{u}'^* (\mathbf{m}_1 \mathbf{u}'). \quad (3.16)$$

Hence the response is asymmetric:

$$\kappa(\mathbf{u}) = -\kappa(\mathbf{u}'). \quad (3.17)$$

2 Simplified kernel-nuller architecture

Utilising the analytical descriptions of the properties of kernel-nulls (i.e., Eq. (3.13) & Eq. (3.17)), Laugier et al. (2020) proposed a method to construct a kernel-nuller matrix for an arbitrary number of apertures. Such a matrix features pairs of so-called enantiomorph (or asymmetric) outputs that form a kernel-null, and is designed to produce the maximum number of nulled outputs n_{nulled} :

$$n_{\text{nulled}} = (n - 1)!, \quad (3.18)$$

where, n is the number of apertures. The number of nulled outputs that would result from the application of this scheme rapidly grows with an increase in n . For $n > 4$, some of the n_{nulled} outputs are redundant and would not bring any new constraint on an observed target. To verify this, we can examine the case of a five-input kernel-nuller with $n_{\text{nulled}} = 24$. For an arbitrary kernel-nuller matrix, the number of independent kernel-nulls n_{kn} is given by the following expression shown in Laugier et al. (2020) as:

$$n_{\text{kn}} = \frac{(n - 1)(n - 2)}{2}. \quad (3.19)$$

Therefore, $n_{\text{kn}} = 6$ for a five-input kernel-nuller. Since kernel-nulls are a linear combination of a pair of outputs, the number of independent nulled outputs for this nuller would be given as: $2 \times n_{\text{kn}} = 12$. Indeed, one can choose to only retain the independent nulled outputs that preserve n_{kn} (i.e., $n_{\text{nulled}} - n_{\text{kn}}$), and the faint signal of a companion is then split over a minimum of 13 outputs (including the bright output). However, a kernel-nuller does not need to be complete: solutions can be found with a reduced number of outputs that nevertheless result in the formation of at least one self-calibrating observable (the double Bracewell is one such example). An $n \times n$ kernel-nuller matrix is a simplified architecture that maximises the throughput with the minimum number of outputs, and only requires a single stage.

The following example of a four-input/four-output (4×4) kernel-nuller demonstrates how one can create an $n \times n$ complex matrix: we begin by creating a 4×4 array \mathbf{A} (see Eq. (3.20)), where our convention will be to take input one as the phase reference and output one as the bright output, explaining why the first column and row of \mathbf{A} contains 0, respectively. The second row has equally spaced

values that are multiples of 1, the third with values that are multiples of 2, and the fourth includes values that are multiples of 3. We then compute the modulo of \mathbf{A} to produce an array whose values will be applied as phase coefficients:

$$\mathbf{A} = \begin{bmatrix} 0 & 0 & 0 & 0 \\ 0 & 1 & 2 & 3 \\ 0 & 2 & 4 & 6 \\ 0 & 3 & 6 & 9 \end{bmatrix} (\text{mod}4) = \begin{bmatrix} 0 & 0 & 0 & 0 \\ 0 & 1 & 2 & 3 \\ 0 & 2 & 0 & 2 \\ 0 & 3 & 2 & 1 \end{bmatrix}. \quad (3.20)$$

Therefore, the nuller response matrix \mathbf{M} has complex coefficients in row r and column k defined by:

$$\mathbf{M}_{r,k} = \frac{1}{\sqrt{n}} e^{\frac{2\pi j}{n} A_{r,k}}. \quad (3.21)$$

A 4×4 kernel-nuller is then computed as:

$$\mathbf{M}_{4 \times 4} = \frac{1}{2} \times \begin{bmatrix} 1 & 1 & 1 & 1 \\ 1 & e^{\frac{\pi j}{2}} & -1 & e^{\frac{3\pi j}{2}} \\ 1 & -1 & 1 & -1 \\ 1 & e^{\frac{3\pi j}{2}} & -1 & e^{\frac{\pi j}{2}} \end{bmatrix}. \quad (3.22)$$

According to Eq. (2.3), $\|V\|^2 = \|U\|^2$ if the interferometric combinations preserve total flux, which means that \mathbf{M} must be a complex unitary matrix. To prove that $\mathbf{M}_{4 \times 4}$ is indeed unitary, one can verify that it satisfies the following condition:

$$\mathbf{M}_{4 \times 4}^H \cdot \mathbf{M}_{4 \times 4} = \mathbf{I}, \quad (3.23)$$

where $\mathbf{M}_{4 \times 4}^H$ is the conjugate transpose (or Hermitian) and \mathbf{I} is the identity matrix. This condition will be met for any derived $n \times n$ matrix. If n is odd, then the nuller will produce $(n - 1)/2$ independent kernel-nulls (or n_{kn}). When n is even, $n_{\text{kn}} = (n - 2)/2$, with a classical Bracewell null generated on one of the outputs. This output will consist of $n/2$ apertures with phase 0, and $n/2$ apertures having a phase of π . The matrix \mathbf{M} obtained with Eq. (3.21) represents an interferometric recombiner for which a conjugate pair of nulled rows \mathbf{m}_1 and \mathbf{m}_2 can be subtracted to form a kernel-null κ .

3 3x3 kernel-nuller

A three-input/three-output (3×3) combiner operates the minimum number of sub-apertures required to implement kernel-nulling, and is derived with Eq. (3.21) as:

$$\mathbf{M}_{3 \times 3} = \frac{1}{\sqrt{3}} \begin{bmatrix} 1 & 1 & 1 \\ 1 & e^{\frac{2j\pi}{3}} & e^{\frac{4j\pi}{3}} \\ 1 & e^{\frac{4j\pi}{3}} & e^{\frac{2j\pi}{3}} \end{bmatrix}. \quad (3.24)$$

Input beam combinations performed by this nuller (see Fig. 18) result in one bright and two nulled outputs, which by subtraction produce one self-calibrating observable. Utilising this architecture, Cvetojevic et al. (2022) experimentally demonstrated (at $1.55 \mu\text{m}$ and with a spectral resolution of 5.2 nm over a $0.55 \mu\text{m}$ bandwidth) the first successful creation of a kernel-null with a device manufactured out of a single multimode interference (MMI, see Chapter 5) coupler. OPDs either internal or external to the MMI can lead to some amount of flux leakage, and therefore a finite extinction in the nulled outputs. To compensate for these phase perturbations, Cvetojevic et al. (2022) employed a deformable mirror to locate the input beam OPD offset values (also referred to as phase set-point) that minimise the amount of on-axis light trickling down the different nulled outputs. At the phase set-point of the device, the intensity ratio of a nulled output over the bright output (or instrumental null-depth) was measured as: $n_1 = 2.397 \times 10^{-3} \pm 6 \times 10^{-6}$ (nulled output 1) and $n_2 = 1.849 \times 10^{-3} \pm 6 \times 10^{-6}$ (nulled output 2). The 0.548×10^{-3} imbalance between the outputs was attributed to unavoidable optical losses through the device and a misalignment between the chip output waveguide/fibre array interface in the experimental setup. As the accuracy of the set-point was better than 10 nm (see Fig. 11 in Cvetojevic et al. 2022), OPD set-point induced bias was deemed negligible in comparison to the effect of misalignment.

In reality, a nuller will not reside at the set-point due to phase errors induced by the atmosphere or optics. Current levels of VLTI/GRAVITY fringe-tracker residuals are ~ 200 nm on the UTs and ~ 100 nm for the ATs (see Lacour et al. 2019). Figure 19a shows the null-depth distributions at the two nulled outputs when the input beams experience OPD fluctuations drawn from a Gaussian distribution with a 100 nm standard deviation. At any instant t , a kernel-null is computed as $\kappa(t) = n_1(t) - n_2(t)$, which results in the distribution shown in Fig. 19b. One can compute the median of this symmetric distribution (marked by the black vertical

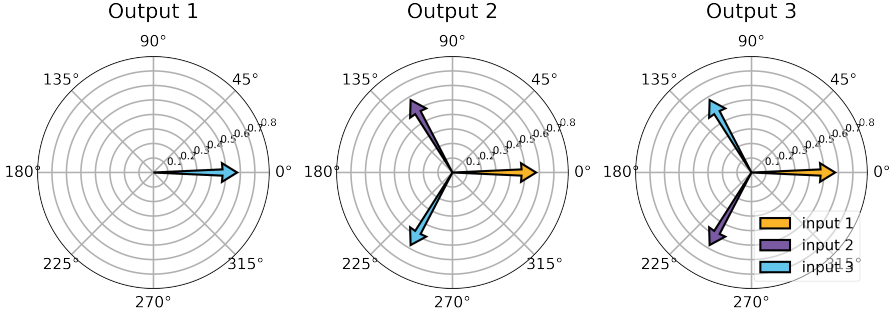


Figure 18: Complex matrix plots describing the theoretical $\mathbf{M}_{3 \times 3}$ of a three-input/three-output (3×3) kernel-nuller. The phase of each input is represented by a colored arrow whose length encodes the amplitude. At each output, the resulting electric field is the sum of all arrows. Since one can only record the intensity (absolute square), the nuller is insensitive to any global phase shift applied to an output (or row of $\mathbf{M}_{3 \times 3}$), which would correspond to an overall rotation of the arrows in a complex matrix plot. Only relative phase offsets introduced by the device between the inputs matter, and the convention here is to take input 1 as the phase reference, explaining why the first column of $\mathbf{M}_{3 \times 3}$ only contains 1, or equivalently, why all yellow arrows remain aligned with the real axis of the complex plane. Output 1 (bright output) is an in-phase constructive recombination of the inputs. Outputs 2 & 3 both result in nulls (with the sum of the three arrows leading back to zero), though they differ in the applied input phase shifts that are multiples of $\pi/3$.

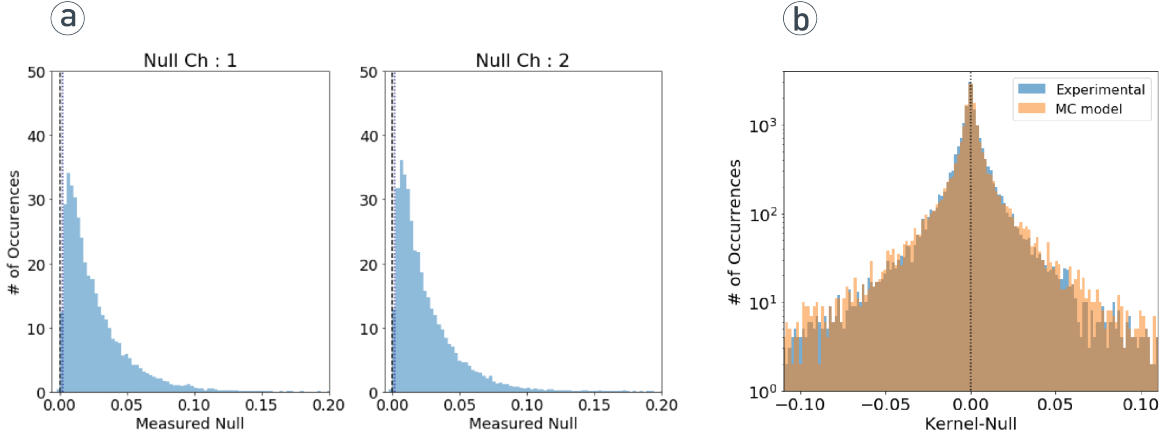


Figure 19: **a)** Statistical distribution of the experimentally measured instrumental null-depth at the nulled outputs (n_1 & n_2) of the 3×3 kernel-nuller at $1.55 \mu\text{m}$ under 100 nm RMS residual piston for an unresolved on-axis source. The instrumental null (marked by the blue vertical dashed line) is far removed from the distribution mean, which is heavily biased by the phase perturbations. On-sky observations with PFN and GLINT exhibit such skewed distributions that rely on the NSC procedure described in Chapter 2 to deduce the astrophysical null-depth. Plot from Cvetojevic et al. (2022). **b)** Statistical distribution of the subsequent kernel-null (κ) distribution (i.e., $\kappa(t) = n_1(t) - n_2(t)$). One can compute the median of this symmetric distribution (marked by the black vertical dashed line) to estimate the experimental kernel-null: $\kappa = -6.5 \times 10^{-5} \pm 1.2 \times 10^{-4}$. The Monte Carlo simulations of an idealised 3×3 kernel-nuller under 100 nm RMS show a close fit with the experimental result. Plot from Cvetojevic et al. (2022).

dashed line) to estimate the experimental kernel-null: $\kappa = -6.5 \times 10^{-5} \pm 1.2 \times 10^{-4}$. The Monte Carlo simulations of an idealised 3×3 kernel-nuller under 100 nm RMS show a close fit with the experimental result.

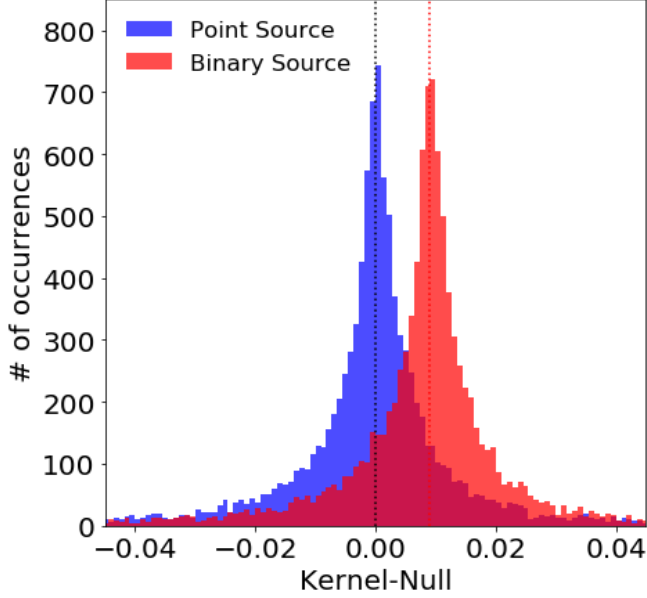


Figure 20: Statistical distribution of the experimental kernel-null for an unresolved on-axis source and a simulated binary companion under 100 nm RMS residual piston. The binary source consists of the on-axis signal (κ marked by the blue vertical dashed line), and the signal of a 10^{-2} contrast companion at a separation of 2.32 mas. As the flux of the off-axis companion is interfered constructively in the nulled outputs, this will result in an offset of the binary source distribution when compared to the point source. The estimated experimental kernel-null of the binary source: $\kappa_b = 1.06 \times 10^{-2} \pm 8.1 \times 10^{-4}$ is marked by the red vertical dashed line. Plot from Cvetojevic et al. (2022).

Cvetojevic et al. (2022) further demonstrated the kernel-null behaviour in the presence of a 10^{-2} contrast companion at a separation of 2.32 mas. The companion was simulated by co-adding a series of data-frames between the phase set-point (on-axis source) and the off-set values of a companion that corresponded to a maximum kernel response, which is a direct translation of the companion’s contrast. Frames alternating between these two off-set positions were acquired under 100 nm RMS. Figure 20 shows that determining the astrophysical kernel-null is quite straightforward as the off-axis distribution will appear shifted from an on-axis kernel-null distribution. The kernel-null for the companion’s signal was measured to be $\kappa_b = 1.06 \times 10^{-2} \pm 8.1 \times 10^{-4}$.

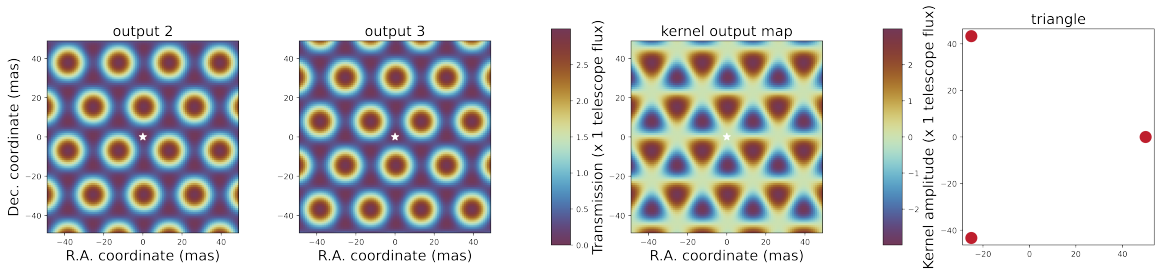


Figure 21: Three-input/three-output (3×3) kernel-nuller transmission maps —and subsequent kernel output map— computed for a wavelength of $9.6 \mu\text{m}$, in an equilateral triangular array for a single snapshot pointing. The field of view of a single snapshot in these maps can be set by the shortest ($B = 50$ meter) baseline of the array ($\lambda/B \approx 38 \text{ mas}$). However, to better illustrate the distinctness of each output response, I have extended this to ± 50 mas. The transmission maps of output 2 & 3 differ from one another, and this diversity in the output response provides a constraint on the properties of a potential companion in the vicinity of a much brighter star. Both maps share the same color scale where the transmission is expressed in units of the planet flux. Taking the difference of the two outputs produces the kernel output map, which contains positive and negative values by construction (shown by the color scale on the right of the map where the transmission is expressed in units of kernel amplitude). A white star in each map marks the location of the central star where the transmission, by design, is equal to zero. The coordinate positions of the three telescopes arranged in an equilateral triangle configuration are shown on the far right. These coordinates are computed as $x = B \cos \theta$ and $y = B \sin \theta$, where $B = 50\text{-m}$ and $\theta = 0, \frac{2\pi}{3}, \frac{4\pi}{3}$.

Besides the double Bracewell/X-array, the Three Telescope Nuller (TTN; [Karlsson et al. 2004](#)) was studied extensively (i.e., launch requirements, payload spacecraft, and ground segment) for the ESA/Darwin mission. The three apertures of the TTN are deployed in an equilateral triangle configuration with relative phase offsets: $0, \frac{2\pi}{3}, \frac{4\pi}{3}$, that cancel the on-axis light. Beam recombination is achieved by coupling the light from the telescopes into a single-mode waveguide. A single output TTN only detects the planetary signal half of the time, for which [Karlsson et al. \(2004\)](#) reported a mean (15.2%) and maximum (40%) modulation efficiency that was inferior to the double Bracewell/X-array (mean = 25.6% & max = 80%). However, by creating a second output, the modulation efficiency (mean = 28% & max = 74.6%) of the TTN was improved. Indeed, a 3×3 kernel-nuller replicates the properties of a dual output TTN, which is why I have computed the transmission maps —and subsequent kernel output map— presented in Fig. 21. Here, one can detect a threefold symmetry around the central null that could lead to undesirable imaging properties as the interferometer would be unable to separate the contributions of planets lying at similar angular radii with $\frac{2\pi}{3}$ offsets. Although such an interferometer only yields a second-order (θ^2) null, the complexity and cost of a space mission is reduced. With adjustable aperture separations, as would be the case with spacecraft formation flying, the constraints on the null could be

relaxed because the transmission map can be tuned for each target.

4 4x4 kernel-nuller

In this section, I will further describe the properties of the $M_{4 \times 4}$ solution presented in Sect. 2. The top panel of Fig. 22 shows the CMPs (summarised by Eq. (3.22)) that model the nuller and the transformations it operates on the input electric fields (represented by coloured arrows) in the complex plane. Four in-phase input signals combine to produce a bright output (output 1). Output 2 & 4 both result in nulls (with the sum of the four arrows leading back to zero), though they differ in the applied input phase shifts that are multiples of $\pi/2$. These outputs, which are analogous to the double Bracewell outputs shown in Fig. 12 are mirror images (or complex conjugates) of each other, an attribute that allows them to form a kernel-null. Output three of the device is a classical Bracewell null, where an equal fraction of input 2 and 3 are π phase-shifted so as to destructively interfere with the same fraction of input 1 and 4.

The middle panel of Fig. 22 presents the transmission maps for this four-input combiner. About the centre of the field, output map 2 & 4 are asymmetric. For transmission maps, this asymmetry is a desirable trait as it allows for the elimination of centro-symmetric astrophysical features that would otherwise hide a planetary companion. On the contrary, the symmetry displayed by output map 3 makes it ideal for the study of such features (i.e., exozodi or debris disks). Indeed, mid-infrared observations with the KIN and LBTI have demonstrated the potential of Bracewell nulling in probing warm ($T \sim 300$ K) exozodi located in the habitable zone of stars. However, both implementations of on-sky nulling relied on NSC, whose model fitting would be fairly complex to implement with a 4×4 nuller as it scales exponentially with an increase of inputs and combinations.

Output three could also be employed as a reference to calibrate the final output of the interferometer, akin to the bright output in coherent calibration (see Lane et al. 2006). This concept, which was applied to the double Bracewell (whose bright outputs would otherwise remain unused), exploits the fact that flux leakage through the null is coherent with starlight, but not with the planet light. Therefore, one can use a bright output as a reference beam and combine it with a fraction of the nulled output. Such mixing –with a controlled relative phase shift– yields an interferometric fringe, whose amplitude is a direct measure of the starlight leaking through the nulled output. Simulations shown by Lane et al. (2006) indicate that coherent calibration can significantly relax the control requirements needed to provide a deep on-axis null.

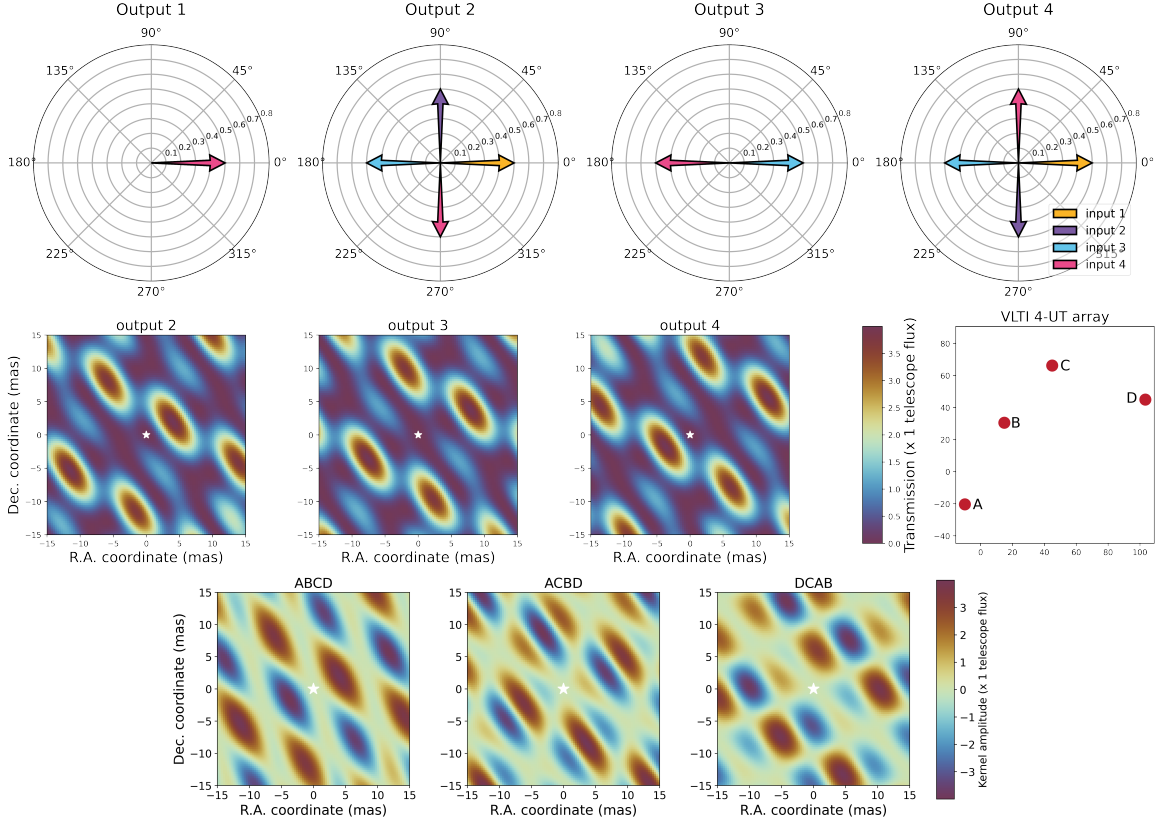


Figure 22: **Top panel:** Complex matrix plots describing the theoretical $M_{4 \times 4}$ of a four-input/four-output (4×4) kernel-nuller. The phase of each input is represented by a coloured arrow whose length encodes the amplitude. At each output, the resulting electric field is the sum of all arrows. Output 1 (bright output) is an in-phase constructive recombination of the inputs. Outputs 2 & 4 both result in nulls (with the sum of the four arrows leading back to zero), though they differ in the applied input phase shifts that are multiples of $\pi/2$. One can also observe that these outputs are mirror images of each other, an attribute that allows them to form a kernel-null. Output 3 is a classical Bracewell null (two arrows with a zero phase shift and two of equal amplitude with a π phase shift). **Middle panel:** 4×4 kernel-nuller transmission maps computed for a wavelength of $3.6 \mu\text{m}$ over a ± 15 mas field of view, with the VLT 4-UT array for a pointing exactly at zenith. To better illustrate the effects of nulling close to the central star, the field of view of a single snapshot in these maps has been set by the shortest ($B = 46.6$ metre) baseline of the array ($\lambda/B \approx 15$ mas). The transmission maps all differ from one another and this diversity in the output response provides a constraint on the properties of a potential companion in the vicinity of a much brighter star. All three maps share the same colour scale where the transmission is expressed in units of the planet flux. A white star in each map marks the location of the central star where the transmission for all nulled channels, by design, is equal to zero. The coordinate positions of the VLT four 8-m diameter unit telescopes (UTs), which are labelled A-B-C-D, are shown on the far right. **Bottom panel:** Kernel output maps computed for three different input beam permutations. The order of the inputs is shown above each map, which corresponds to the labelling of the UTs (see *Middle Panel*). Taking the difference of output values (shown by the colour scale on the right of the map where the transmission is expressed in units of kernel amplitude) means that unlike raw photometric-like outputs, kernel outputs can take negative values (shown by the colour scale on the right of the map where the transmission is expressed in units of kernel amplitude). A white star in each map marks the location of the central star where the transmission, by design, is equal to zero.

Compared with the double Bracewell (see Fig. 14), a 4×4 kernel-nuller exhibits the same modulation efficiency for off-axis features with the non-redundant baselines of the VLTI 4-UT configuration. But only one kernel output is generated in this simplified architecture, which corresponds to one of the 4×7 kernel outputs (see Fig. 17). However, in addition to the overall geometry of the array, the order by which the four input beams are recombined into the nuller will impact the imaging properties of the system. The bottom panel of Fig. 22 shows the kernel outputs that would be generated for three different input beam permutations. By observing with these permutations, a 4×4 nuller can still produce the different kernel outputs of the original design.

Considering that the NOTT double Bracewell nuller will be operated on the VLTI, the detection and characterisation of the thermal emission from young giant exoplanets with a 4×4 kernel-nuller is a feasible prospect. Besides, it could also serve as a technological pathway for the more advanced 4×7 combiner, whose contrast detection limits have been investigated with the VLTI. To achieve a spectral resolution $R \sim 50$, the analysis by Ireland (2020) shows that reaching a contrast better than $c = 10^{-5}$ over a one-hour integration with the ATs requires the targets to be brighter than $M = 9$ in the science band-pass. For the UTs, Martinache & Ireland (2018) determined the achievable contrast curves, which suggest that even with 150 nm RMS fringe tracking performance, a contrast better than $c = 10^{-5}$ can be attained for targets brighter than $M = 6$.

In addition to demonstrating technological readiness of the 4×7 design, a 4×4 kernel-nuller could provide a proof of concept for a future space mission as its simplified architecture may be compatible with the cubesat platform. ESA's PROBA-3 mission (current launch date: 2024) will feature two cubesats whose positioning accuracy (millimetre and arc second precision) will exceed the requirements for a space-based nulling interferometer (centimetre and arc minute range for TPF-I). If successful, the PROBA-3 formation flying model can be extended to a 6:1 X-array, which is more robust against systematic noise than a 2:1 X-array. With this so-called stretched X-array, I have computed the kernel output map for the 4×4 nuller and the modulation map of the double Bracewell (see Fig. 23). The asymmetric response of the double Bracewell is well defined by a series of bright and dark stripes that correspond to a high modulation efficiency. Meanwhile, the angular resolution is severely diminished in the kernel output map, and the kernel amplitude is of the order 10^{-16} . In this scenario, the inferior performance of the kernel-nuller is due to the redundant baselines provided by the rectangular geometry of the X-array. A kernel-nuller architecture requiring the simultaneous nulling of multiple baselines entails the use of non-redundant baselines.

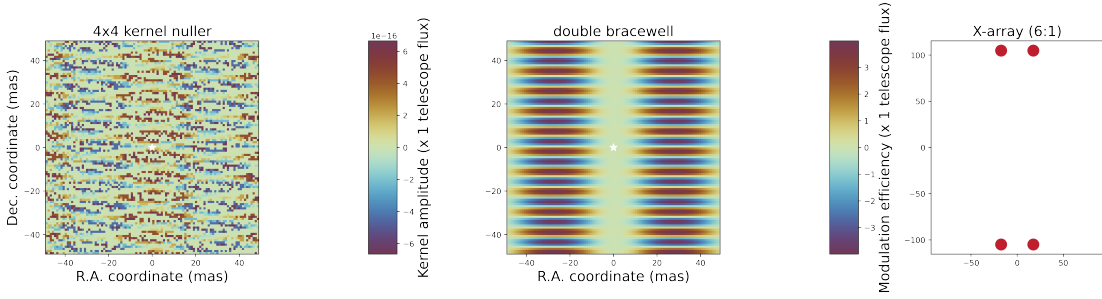


Figure 23: **Left panel:** Kernel output map of a four-input/four-output (4×4) kernel-nuller computed for a wavelength of $9.6\mu\text{m}$ in an X-array (6:1 aspect ratio) configuration for a single snapshot pointing. To better illustrate the effects of nulling close to the central star, the field of view (FOV) of a single snapshot in these maps can be set by the shortest ($B = 35$ meter) baseline of the array ($\lambda/B \approx 54$ mas). Here, I limit the FOV to ± 50 mas. The color scale on the right of the map shows the transmission, which is expressed in units of kernel amplitude. A white star in the map marks the location of the central star where the transmission, by design, is equal to zero. **Middle panel:** Double Bracewell modulation map computed for a wavelength of $9.6\mu\text{m}$ over a ± 50 mas FOV in an X-array (6:1 aspect ratio) configuration for a single snapshot pointing. The color scale on the right of the map shows the transmission, which is expressed in units of modulation efficiency. **Right panel:** The telescope coordinate positions for the X-array (6:1 aspect ratio) configuration. These coordinates have been computed with the formulation presented in Sect. 3.3, with a nulling baseline $B = 35\text{-m}$ and aspect ratio $q = 6$.

Utilising the nulling baseline $B = 35\text{-m}$ and aspect ratio $q = 6$ of the X-array shown in Fig. 23, one can compute a kite-shaped array with (x, y) telescope coordinate positions shown in Hansen et al. (2022) as:

$$x = 0.5B\sqrt{1 + q^2} \cos \theta \quad y = 0.5B\sqrt{1 + q^2} \sin \theta, \quad (3.25)$$

where $\theta = \frac{\pi}{2} - \beta, \frac{\pi}{2}, \frac{\pi}{2} + \beta, \frac{3\pi}{2}$, and $\beta = 2 \arctan(1/q)$. The non-redundant baselines provided by a kite array allow for a good overall response on the outputs of the 4×4 kernel-nuller and the double Bracewell (see Top and Middle Panel of Fig. 24). Although the kernel-nuller exhibits a higher signal amplitude (see Bottom Panel of Fig. 24) for a hypothetical planet at a separation of 50 mas, additional trade-off studies are needed to further validate the choice of array configuration.

3 kernel-nulling for the direct detection of exoplanets

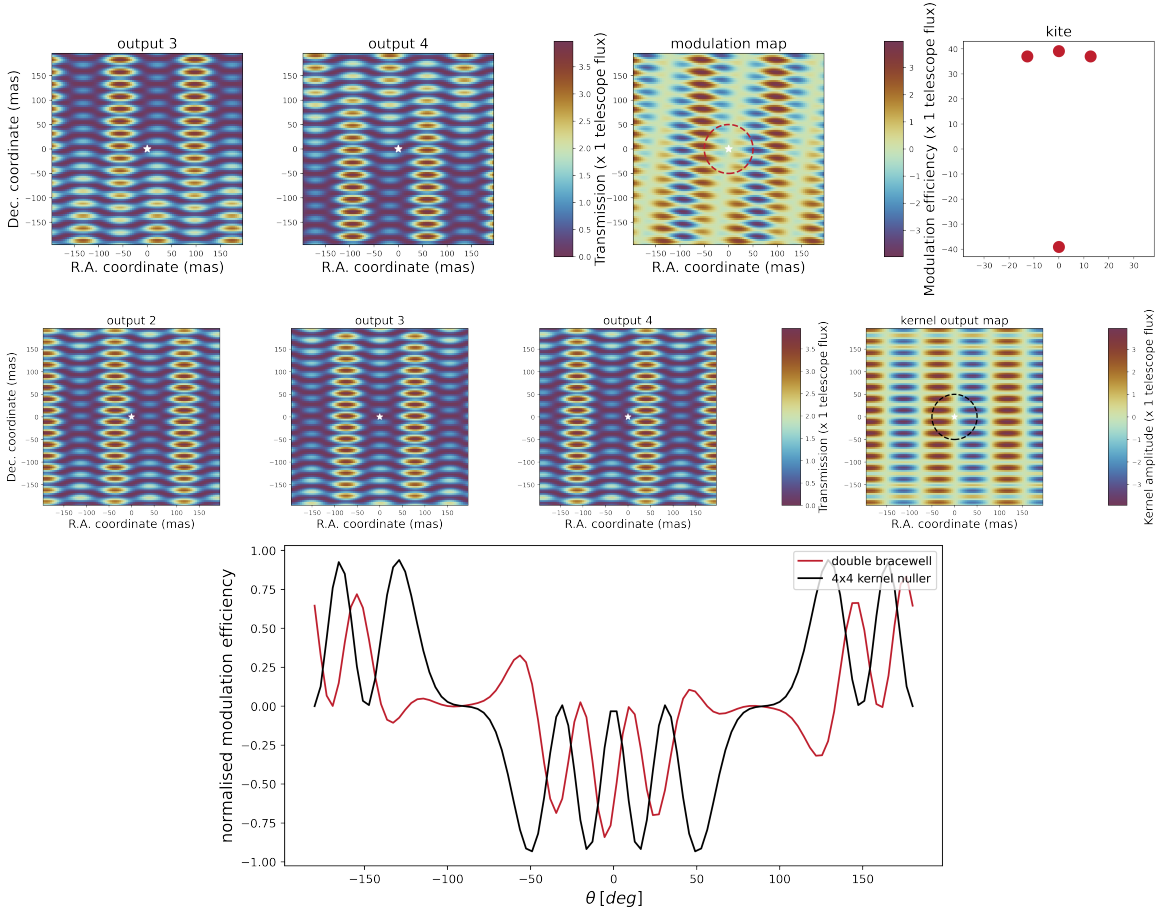


Figure 24: **Top panel:** Double Bracewell nuller transmission maps –and subsequent modulation map– computed for a wavelength of $9.6\mu\text{m}$ over a ± 200 mas field of view, with a kite array for a single snapshot pointing. When the interferometer goes through a 360° rotation while pointing to the star, a hypothetical planet describes a circle with radius 50 mas in the transmission plane, as indicated with the red coloured dashed lines in the modulation map. A white star in each map marks the location of the central star where the transmission, by design, is equal to zero. The telescope coordinate positions for a kite array are shown on the far right. **Middle panel:** Four-input/four-output (4×4) kernel-nuller transmission maps –and subsequent kernel output map– computed for a wavelength of $9.6\mu\text{m}$ over a ± 200 mas field of view, with a kite array for a single snapshot pointing. A hypothetical planet describes a circle with radius 50 mas in the transmission plane, as indicated with the black coloured dashed lines in the kernel output map. **Bottom panel:** Normalised modulation efficiency –by total flux– as a function of rotation angle θ for a planet (at 50 mas) detected with a double Bracewell and 4×4 kernel-nuller. As the nulling interferometer rotates around the line-of-sight, the modulation/kernel output map centred on the star rotates with it. As the map rotates, the bright and dark regions in the map sweep across the position of the planet, modulating its signal. The horizontal axis (Dec = 0) in the modulation/kernel output map is the reference axis for θ .

5 5x5 kernel-nuller

The question of the existence and distribution of life elsewhere in the cosmos could be answered with a space-based nulling interferometer. In Chapter 2 I have described how this enterprise was pursued with the Darwin and TPF-I missions. Due to technical challenges, and a limited scientific study of the exoplanet population, these missions did not proceed. Since then, however, our knowledge of exoplanets has significantly increased, and vast progress has been made in several key technologies. To this effect, the Large Interferometer For Exoplanets (LIFE; [Quanz et al. 2022](#)) is currently being developed to achieve the goals set out during the Darwin/TPF-I era, which include the detection and characterisation of temperate, terrestrial exoplanets in the mid-infrared (4 – 18.5 μm).

In an ideal nulling interferometer, the integration times required for planet detection and characterisation will mainly depend on the strength of the planetary signal and the level of photon noise. One can therefore use the signal to noise ratio (SNR) to determine the detectability of a planet or the extent to which it can be characterised in a particular integration time. For the LIFE mission, [Hansen et al. \(2022\)](#) built a model designed to derive the SNR of a large sample of simulated planets for four different nulling architectures: a 3×3 kernel-nuller (in an equilateral triangle array – see Fig. 21), the double Bracewell (X-array – see Fig. 13 & Fig. 23), 4×7 kernel-nuller (kite array – see Fig. 24), and a 5×5 kernel-nuller (pentagonal array with baseline scaling $\Gamma_B = 0.66, 1.03 \text{ \& } 1.68$). Figure 25 shows a graphical representation of the five-input combiner (computed via Eq. (3.21)) that is summarised by this matrix:

$$\mathbf{M}_{5 \times 5} = \frac{1}{\sqrt{5}} \times \begin{bmatrix} 1 & 1 & 1 & 1 & 1 \\ 1 & e^{\frac{2\pi j}{5}} & e^{\frac{4\pi j}{5}} & e^{\frac{-4\pi j}{5}} & e^{\frac{-2\pi j}{5}} \\ 1 & e^{\frac{4\pi j}{5}} & e^{\frac{-2\pi j}{5}} & e^{\frac{2\pi j}{5}} & e^{\frac{-4\pi j}{5}} \\ 1 & e^{\frac{-4\pi j}{5}} & e^{\frac{2\pi j}{5}} & e^{\frac{-2\pi j}{5}} & e^{\frac{4\pi j}{5}} \\ 1 & e^{\frac{-2\pi j}{5}} & e^{\frac{-4\pi j}{5}} & e^{\frac{4\pi j}{5}} & e^{\frac{2\pi j}{5}} \end{bmatrix}. \quad (3.26)$$

[Hansen et al. 2022](#) provides a full description of the photon noise-limited SNR model, including the various sources of noise. Here, I present a summary of this model, adopting the same nomenclature – the SNR is computed for each i th spectral channel and j th kernel-null as:

3 kernel-nulling for the direct detection of exoplanets

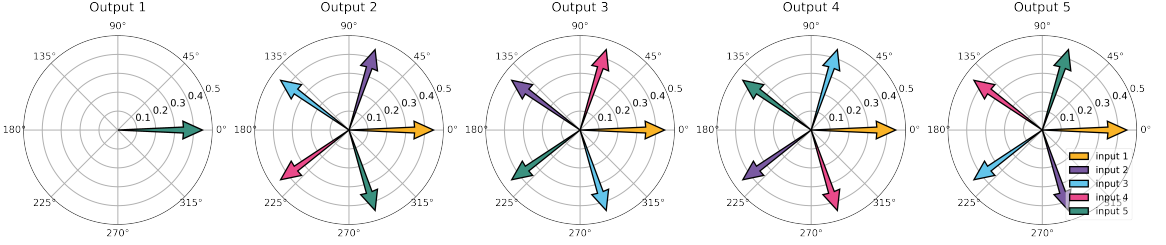


Figure 25: Complex matrix plots describing the theoretical $M_{5 \times 5}$ of a five-input/five-output (5×5) kernel-nuller. The phase of each input is represented by a coloured arrow whose length encodes the amplitude. Since one can only record the intensity (absolute square), the nuller is insensitive to any global phase shift applied to an output (or row of $M_{5 \times 5}$), which would correspond to an overall rotation of the arrows in a complex matrix plot. Only relative phase offsets introduced by the device between the inputs matter, and the convention here is to take input 1 as the phase reference, explaining why the first column of $M_{5 \times 5}$ only contains 1, or equivalently, why all yellow arrows remain aligned with the real axis of the complex plane. At each output, the resulting electric field is the sum of all arrows. Output 1 (bright outputs) is an in-phase constructive recombination of the inputs. Outputs 2, 3, 4 & 5 all result in nulls (with the sum of the five arrows leading back to zero), though they differ in the applied input phase shifts that are multiples of $2\pi/5$.

$$SNR_{i,j} = \sqrt{\frac{\eta t}{2}} \frac{F_{\text{signal},i,j} A}{\sqrt{F_{\text{leakage},i,j} A + F_{\text{exozod},i,j} A + a P_{\text{zod},i,j}}}, \quad (3.27)$$

where η is the interferometer throughput, t is the integration time, $F_{\text{signal},i,j}$ is the planet flux, A is the telescope area, $F_{\text{leakage},i,j}$ is the stellar leakage flux, $F_{\text{exozod},i,j}$ is the exozodiacal flux, a is a scaling factor for the zodiacal light ($a = 0.5$ for the 4×7 kernel-nuller and $a = 1$ for the other combiners), and $P_{\text{zod},i,j}$ is the zodiacal power. A $1/\sqrt{2}$ factor is applied on account of taking the nulled output difference to acquire the kernel signal. The distinct spectral channel and kernel-null SNRs are then combined with the formalism developed by [Lay \(2004\)](#):

$$SNR_{\text{tot}} = \sqrt{\sum_{i,j} SNR_{i,j}^2}. \quad (3.28)$$

For the four nulling architectures, including the different baseline scalings of the 5×5 kernel-nuller, [Hansen et al. \(2022\)](#) performed exoplanet detection simulations at three reference wavelengths ($\lambda_B = 10, 15 \text{ \& } 18 \mu\text{m}$), with $\eta = 5\%$, and $t = 5$ hr. The telescope diameter is scaled such that each nulling architecture has the same total area as four 2-m diameter telescopes. In these simulations, a planet is deemed to be detected if the total SNR (i.e., Eq. (3.28)) over the various wavelengths is > 7 . For habitable zone planets, a 5×5 kernel-nuller (with $\Gamma_B = 1.68$) is the most effective at $10 \mu\text{m}$, while a 5×5 (with $\Gamma_B = 1.03$) delivers the best

performance at $15\mu\text{m}$, and $18\mu\text{m}$ — where the highest planet detections for all architectures occur. At this wavelength, the peak average count for temperate, terrestrial planets (i.e., $R < 1.5R_{\oplus}$ and $250\text{K} < T < 350\text{K}$) is ~ 2.2 (5×5 with $\Gamma_{\text{B}} = 1.03$), and the lowest is ~ 1.7 (3×3 kernel-nuller).

Utilising the same parameters (where $\eta = 5\%$, $t = 5$ hr, $\lambda_{\text{B}} = 18\mu\text{m}$, and A is conserved) for the characterisation mode, a 5×5 (with $\Gamma_{\text{B}} = 0.66$ & 1.03) has an SNR that is ~ 1.2 times higher than the double Bracewell and 4×7 , while it is ~ 1.5 times higher than a 3×3 kernel-nuller. The SNR is set to zero for baselines outside of the 5 to 600-m range, which was the case here for the 5×5 (with $\Gamma_{\text{B}} = 1.68$). Considering that the aperture separations are adjustable with spacecraft formation flying, the different baseline scalings of the five-input combiner can be adopted for either exoplanet detection or characterisation.

Although a 5×5 kernel-nuller (in a pentagonal array) offers a higher scientific yield than the other nulling architectures, its transmission maps —and subsequent kernel output maps— exhibit a five-fold symmetry around the central null (see First and Second panel of Fig. 26). This could result in undesirable imaging properties as the interferometer would be unable to separate the contributions of planets lying at similar angular radii with $\frac{2\pi}{5}$ offsets. By changing the geometry of the array to an ellipse, as described by [Mennesson & Mariotti \(1997\)](#), the central symmetry is broken for the respective maps (see Third and Fourth panel of Fig. 26). Indeed, an elliptical array may lead to an easier distinction between the signals emitted by planets, but this necessitates a comprehensive image reconstruction analysis with multiple companions in the field of view. For such an arbitrary high-contrast scene, the image can be reconstructed using a variety of inverse model techniques such as SQUEEZE ([Baron et al. 2010](#)) or MACIM ([Ireland et al. 2006](#)).

Two kernel outputs are generated by a 5×5 kernel-nuller, and in the Top and Bottom panel of Fig. 27, one can observe that the circular array exhibits a higher modulation frequency for a hypothetical planet at a separation of 55 mas. Nevertheless, by stretching the array from a circle to an ellipse, the stretch and fit ([Lay 2006](#)) technique could be applied in order to determine which geometry —with different baseline scalings— is more robust to systematic noise. Besides, the SNR model of [Hansen et al. \(2022\)](#) should take into account the effects of systematic noise.

3 kernel-nulling for the direct detection of exoplanets

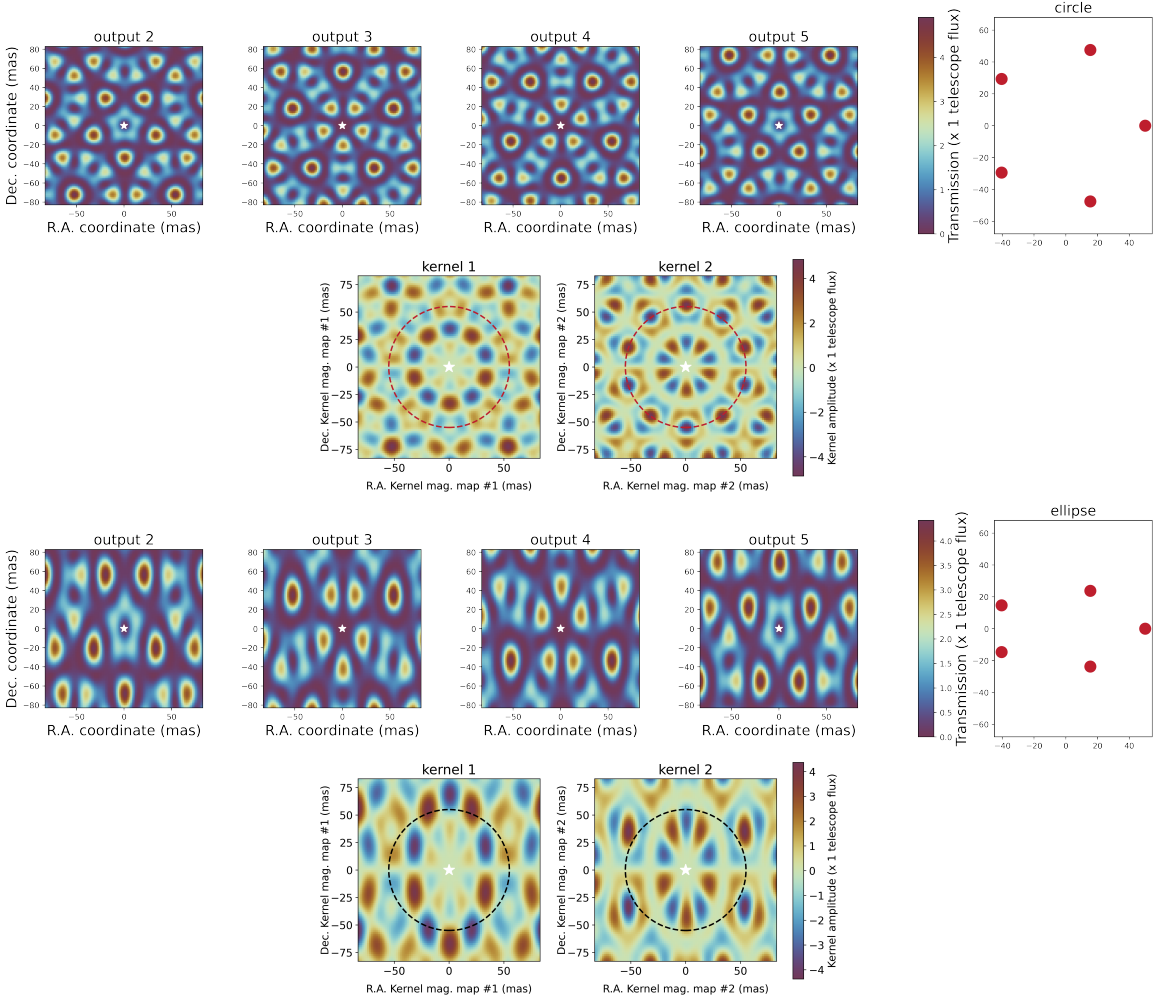


Figure 26: **First panel:** Five-input/five-output (5×5) kernel-nuller transmission maps computed for a wavelength of $9.6\mu\text{m}$, in a circular array for a single snapshot pointing. The field of view of a single snapshot in these maps can be set by the shortest ($B = 50$ meter) baseline of the array ($\lambda/B \approx 38 \text{ mas}$). However, to better illustrate the symmetrical properties of the interferometer, I have extended this to $\pm 85 \text{ mas}$. A white star in each map marks the location of the central star where the transmission for all nulled channels, by design, is equal to zero. The coordinate positions of the five telescopes arranged in a regular pentagonal configuration are shown on the far right. These coordinates are computed as $x = B \cos \theta$ and $y = B \sin \theta$, where $B = 50\text{-m}$ and $\theta = 0, \frac{2\pi}{5}, \frac{4\pi}{5}, \frac{6\pi}{5}, \frac{8\pi}{5}$. **Second panel:** 5×5 kernel output maps computed in a circular array. A kernel output is simply the difference between the two nuller outputs for which the same pairs of inputs are nulled with each other (i.e., output 2–5, 3–4). When the interferometer goes through a 360° rotation while pointing to the star, a hypothetical planet describes a circle with radius 55 mas in the transmission plane, as indicated with the red coloured dashed lines in the maps. **Third panel:** 5×5 kernel-nuller transmission maps computed in an elliptical array. The coordinate positions of the five telescopes arranged in an elliptical array are shown on the far right. These coordinates are computed as $x = B \cos \theta$ and $y = C \sin \theta$, where $B = 50\text{-m}$, $C = 25\text{-m}$ and $\theta = 0, \frac{2\pi}{5}, \frac{4\pi}{5}, \frac{6\pi}{5}, \frac{8\pi}{5}$. **Fourth panel:** 5×5 kernel output maps computed in an elliptical array. A hypothetical planet describes a circle with radius 55 mas in the transmission plane, as indicated with the black coloured dashed lines in the maps.

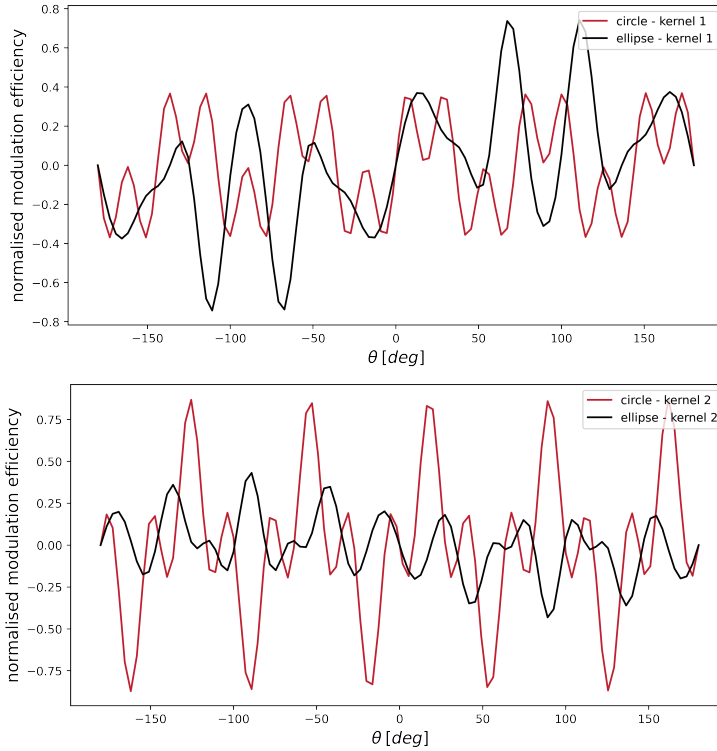


Figure 27: Normalised modulation efficiency —by total flux— as a function of rotation angle θ for a planet (at 55 mas) detected with a circular and elliptical array. As the 5×5 kernel-nuller rotates around the line-of-sight, the modulation map centred on the star rotates with it. As the map rotates, the bright and dark regions in the map sweep across the position of the planet, modulating its signal. The horizontal axis (Dec = 0) in the kernel output maps shown in Fig. 26 is the reference axis for θ . **Top panel:** Normalised modulation efficiency for kernel 1. **Bottom panel:** Normalised modulation efficiency for kernel 2.

6 Summary

Kernel-nulling, which follows the basic concept devised by [Bracewell \(1978\)](#), enables a reliable high-contrast imaging solution that is independent of the quadratic error terms induced either by fluctuations in the amplitude or phase, but not a combination thereof. In the paper that introduced this nulling architecture and data reduction technique, [Martinache & Ireland \(2018\)](#) proposed a four-input kernel-nuller designed to produce a complete set of six high-contrast (nulled) outputs, that give access to three self-calibrating observable quantities (a.k.a., kernel-nulls). The properties of the original two-stage 4×7 design (including the bright output) were examined by [Laugier et al. \(2020\)](#), and generalised for an

arbitrary number of apertures via graphical and analytical representations of a kernel-nuller matrix.

Laugier et al. (2020) describe a method to design a kernel-nuller matrix, which results in as many kernel-nulls as the number of independent closure-phases provided by the interferometric array. However, a kernel-nuller does not need to be complete: solutions can be found with a reduced number of outputs that nevertheless result in the formation of at least one self-calibrating observable (the double Bracewell is one such example). An $n \times n$ (where n is the number of apertures) kernel-nuller matrix is a simplified architecture that maximises the throughput with the minimum number of outputs, and only requires a single stage.

A simplified architecture (3×3 combiner) was utilised by Cvetojevic et al. (2022) to experimentally validate the first successful creation of a kernel-null with a device manufactured out of a single multimode interference coupler. This investigation was performed on the kernel test bench, whose deformable mirror was used to inject signals from both an unresolved point-source and a binary source analogue. A kernel-null was yielded with up to 200 nm RMS wavefront error, and its behaviour was demonstrated in the presence of a 10^{-2} contrast companion at a separation of 2.32 mas.

Measuring the mid-infrared spectrum of a temperate, terrestrial exoplanet's direct thermal emission would be an exceptional astronomical breakthrough that could lead to further discoveries. A space-based nulling interferometer, which will be deployed for the LIFE mission, is a promising approach to pursue this endeavour. According to Hansen et al. (2022), LIFE would obtain a higher scientific yield with a 5×5 kernel-nuller (in a pentagonal array) than with a 3×3 kernel-nuller (equilateral triangle array), the double Bracewell (X-array), or a 4×7 kernel-nuller (kite array).

This thesis work evaluates the astrophysical potential of the 4×7 kernel-nuller as the prime high-contrast imaging mode of the VLTI (see Chapter 4), and investigates the spectral behaviour of a 4×4 kernel-nuller (see Chapter 7).

Chapter 4

High-contrast detection of exoplanets with a kernel-nuller at the VLTI

This chapter was published as a peer-reviewed article in *Astronomy & Astrophysics*.


ASPRO2 (developed by the Jean-Marie Mariotti Centre¹) is widely used by astronomers to prepare for long-baseline interferometric observations at facilities such as the VLTI and CHARA. By specifying the instrument and the target's physical properties, one can determine the optimal array configuration for the desired observation. Indeed, this Java simulator, which employs (u, v) plots to compute visibility and phase measurements, is only applicable to conventional optical interferometry and no such tool exists for nulling interferometry.

To answer the nulling requirement for an observation preparation tool, I developed a Python simulation that applies the same coordinate transformation matrix used for (u, v) plots, but modified to only take into account baseline projection effects, which introduce diversity in the response of a nuller as a function of time. A sensitivity map known as the nuller global throughput map is generated from the simulation, and can be used to predict the probability of exoplanet detection in the nuller's field of view for a particular target. As the VLTI offers different array configurations, I utilised this map to assess their characteristics for a kernel-nuller exoplanet discovery observing program that exploits the synergy between astrometry and direct imaging.

Although the simulation tool was primarily developed for the 4×7 kernel-nuller at the VLTI, it can be applied to the family of kernel-nullers and at other observing facilities. In the appendix, I present similar plots shown in this chapter for a 6×6 combiner at the CHARA array.

¹<https://www.jmmc.fr>

High-contrast detection of exoplanets with a kernel-nuller at the VLTI

Peter Marley Chingaïpe¹ , Frantz Martinache¹, Nick Cvetojevic¹, Roxanne Ligi¹, David Mary¹, Mamadou N'Diaye¹, Denis Defrère², and Michael J. Ireland³

¹ Laboratoire Lagrange, Université Côte d'Azur, Observatoire de la Côte d'Azur, CNRS, Parc Valrose, Bât. H. Fizeau, 06108 Nice, France

e-mail: peter.chingaïpe@oca.eu

² Institute of Astronomy, KU Leuven, Celestijnenlaan 200D, 3001 Leuven, Belgium

³ Research School of Astronomy and Astrophysics, College of Science, Australian National University, Canberra 2611, Australia

Received 10 February 2023 / Accepted 24 April 2023

ABSTRACT

Context. The conventional approach to direct imaging is to use a single aperture coronagraph with wavefront correction via extreme adaptive optics (AO). Such systems are limited to observing beyond an inner working angle (IWA) of a few λ/D . Nulling interferometry with two or more apertures will enable detections of companions at separations at and beyond the formal diffraction limit.

Aims. In this paper, we evaluate the astrophysical potential of a kernel-nuller as the prime high-contrast imaging mode of the Very Large Telescope Interferometer (VLTI).

Methods. By taking into account baseline projection effects induced by Earth rotation, we introduce some diversity in the response of the nuller as a function of time. This response is depicted by transmission maps. We also determine whether we can extract the astrometric parameters of a companion from the kernel outputs, which are the primary intended observable quantities of the kernel-nuller. This then leads us to comment on the characteristics of a possible observing program for the discovery of exoplanets.

Results. We present transmission maps for both the raw nuller outputs and their subsequent kernel outputs. To further examine the properties of the kernel-nuller, we introduce maps of the absolute value of the kernel output. We also identify 38 targets for the direct detection of exoplanets with a kernel-nuller at the focus of the VLTI.

Conclusions. With continued upgrades of the VLTI infrastructure, which will reduce fringe tracking residuals, a kernel-nuller would enable the detection of young giant exoplanets at separations <10 AU, where radial velocity and transit methods are more sensitive.

Key words. instrumentation: interferometers – planets and satellites: detection – instrumentation: high angular resolution

1. Introduction

A resurgence has been seen in recent years of the use of nulling interferometry as a way of detecting and characterising exoplanets on account of new innovative concepts and advances in technology. Mature infrastructure for long-baseline interferometry is enabling the implementation of nulling architectures. These include the Very Large Telescope Interferometer (VLTI) and the Centre for High Angular Resolution Astronomy (CHARA), which routinely combine four and six telescopes, respectively. Current active endeavours in nulling interferometry for extrasolar planets are the NOTT project (formerly Hi-5, Defrère et al. 2018) and LIFE (Quanz 2019).

Towards the end of the 1970s, Bracewell & MacPhie (1979) introduced the concept of a two-telescope space-based nulling interferometer, referred to as the Bracewell interferometer. Later on, Angel & Woolf (1997) combined two Bracewell interferometers, thus achieving greater suppression of the on-axis source and superior (u, v) coverage. Also drawing from Bracewell's idea, Guyon et al. (2013) improved the attenuation of the on-axis source by optimising the recombination process of a nuller. This recombination process serves to reject the light from an on-axis source (normally a star) by means of coherent destructive interference between the optical beams while retaining as much of the light emanating from faint sources in close proximity to the

central star as possible. At infrared wavelengths, the flux ratio between the star and the planet is more favourable than in the visible domain, which makes nulling interferometers particularly attractive for the detection of light from exoplanets.

We turn to a nulling architecture and data reduction technique that follows the basic concept devised by Bracewell (1978) and offers a reliable high-contrast imaging solution that is robust to small instrumental perturbations. This architecture, called kernel-nulling, was proposed by Martinache & Ireland (2018) and is designed to exploit the use of a four-telescope interferometer. The two-stage kernel-nuller architecture produces three observable quantities, which are accordingly referred to as kernel-nulls. Akin to kernel-phases (Martinache 2010), which are an extension of closure phases (Jennison 1958), kernel-nulls are independent of the quadratic error terms induced either by fluctuations in the amplitude or phase, but not a combination thereof. According to Lay (2004), the amplitude-phase cross terms are expected to be the dominant contributor to contrast detection limits. In combination with a photometric monitoring of the input beams, a kernel-nuller makes it possible to disentangle genuine weak astrophysical signals from spurious residual instrument-induced light leakage, enabling higher contrast detections in the presence of residual fringe-tracking errors. Imperfections in the manufacturing and chromatic effects that would result in systematic errors can be compensated for

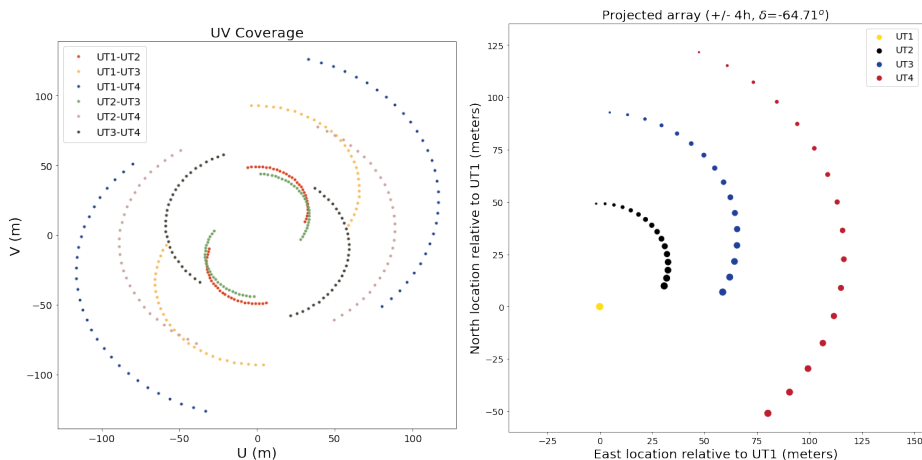


Fig. 1. Evolution of the (u, v) plane coverage (*left panel*) and the projected array (*right panel*) of the four VLTI UTs observing the target HIP 107773 over a ± 4 h range of hour angle. In the left figure we see the 2D projection of the six baselines of the four UTs on a plane perpendicular to the direction of the target. As the Earth rotates, the baselines formed by pairs of telescopes sample the complex visibility function at spatial frequencies labelled with coordinates u and v , sweeping out tracks that are rather circular on account of the favourable celestial location. In the right figure we see the projected geometry of the interferometric array relative to UT1, which is chosen as a reference. The locations of UT2, UT3, and UT4 from the point of view of the source appear to move around to UT1 in a clockwise direction.

with a tunable recombiner that would follow the adaptive-nuller concept introduced by Lay et al. (2003).

In the paper that introduced the concept of kernel-nuller, Martinache & Ireland (2018) computed transmission maps for a hypothetical snapshot scenario at zenith that did not attempt to account for the Earth rotation and its impact on the observable quantities. In this work, we take into account the Earth’s rotation, describing how it affects such maps and actually improves the detectability of off-axis companions. We also show how recorded series of kernel-nulls can be translated into constraints on the properties of a target. As the transmission maps are dependent on the layout of the telescopes and the pointing of the target, this study leads us to comment on the characteristics of a possible observing program for the discovery of exoplanets with a kernel-nuller at the focus of the VLTI.

2. The response of a nulling interferometer

A conventional constructive interferometer coherently recombines the optical beams from two or more telescopes to measure the so-called complex visibility of an astronomical scene. Baselines formed by pairs of telescopes sample the complex visibility function at spatial frequencies labelled with coordinates u and v . The accumulation of sufficient complex visibility measurements eventually leads to enough constraints that an image or a parametric representation of the astronomical scene can be reconstructed by virtue of the Van Cittert–Zernike theorem.

Optical interferometers use a sparse array of telescopes, which leads to an incomplete (u, v) plane coverage in the snapshot mode. Observing facilities therefore take advantage of aperture synthesis techniques first developed for radio astronomy in the late 1940s that have since been elaborated for the optical regime (see Labeyrrie et al. 2006 for an analysis on aperture synthesis for optical interferometry) to improve the (u, v) plane coverage by making use of the Earth’s rotation. As the Earth rotates, the projected baseline vector – as seen from the

source – and the corresponding spatial frequencies vary with time, sweeping out tracks in the (u, v) plane. Such tracks are conveniently summarised by a (u, v) coverage plot (left panel of Fig. 1) whose overall density and distribution are good diagnoses of the richness of the observation.

The information collected by a nuller is used in a different manner. In nulling interferometry, the requirement to redirect away the on-axis stellar light implies that the complex visibility of the source brightness distribution is in general not directly accessible. A four-beam nuller records the observed flux of a faint off-axis source acquired by a finite number of nulled outputs after the light from an on-axis source has been optically redirected toward one or more bright outputs. Even in ideal observing conditions, the link between the nulled outputs and the astronomical source is no longer described by a direct, linear relation such as the Van Cittert–Zernike theorem and the subsequent interpretation requires additional care.

2.1. Nuller output transmission maps

The most direct way to describe the non-trivial effect of a nuller recombining more than two telescopes is to compute transmission maps describing the response of the different outputs to the presence of a test point source over the field of view (FOV) of the interferometer. These transmission maps predict what fraction of the total flux of an off-axis source will find its way through the nuller, trickling down the different outputs.

An example of such a transmission map is represented in Fig. 2 for the kernel-nuller architecture described by Martinache & Ireland (2018); it was computed with the four unit telescopes (UTs) of the VLTI in the L -band ($\lambda = 3.6 \mu\text{m}$) for a hypothetical scenario of a pointing exactly at zenith. To better illustrate the effects of nulling close to the central star, the FOV of a single snapshot in these maps has been set by the shortest ($b = 46.6$ m) baseline of the array ($\lambda/b \approx 15$ mas). The recent experimental demonstration of a 3×3 kernel-nuller (Cvetojevic et al. 2022)

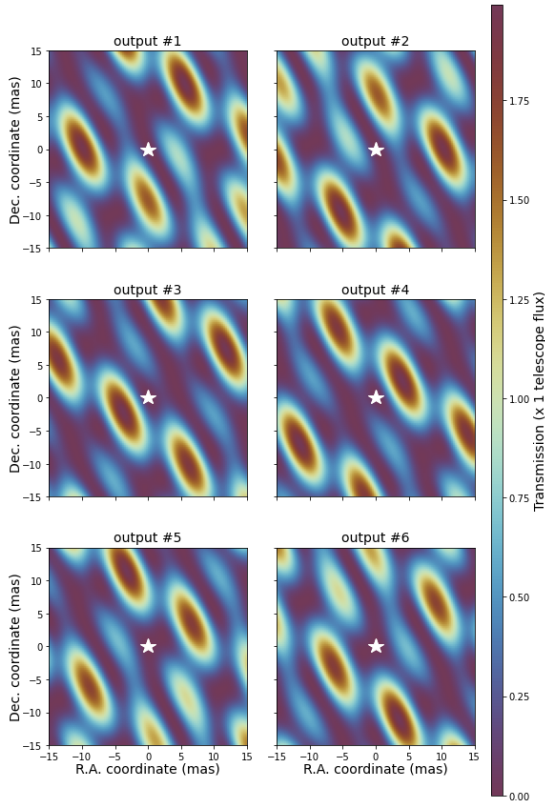


Fig. 2. Nuller output transmission maps of a kernel-nuller at the focus of the four VLTI UTs, observing a ± 15 mas FOV surrounding the target HIP 107773. The figure shows the maps of the six nuller outputs for a pointing exactly at zenith. We see that these maps differ from one another and this diversity in the output response provides a constraint on the properties of a potential companion in the vicinity of a much brighter star. A white star in each map marks the location of the central star where the transmission for all channels is equal to zero, by design. About the centre of the field, the maps are asymmetrical. For transmission maps, this asymmetry is a desirable trait as it allows for the elimination of centro-symmetric astrophysical features that would otherwise hide a planetary companion. With four input beams being split into six outputs, we expect an average planet flux of $4/6$ ($=0.66$) per channel. All six maps share the same colour scale where the transmission peaks at approximately two times the planet flux collected by a single aperture.

had a spectral resolution of 5.2 nm over a $0.55 \mu\text{m}$ bandwidth, which we adopt for this investigation.

At a glance, we can see that these maps are not uniform and differ from one another. Other than the common on-axis transmission hole, which is the very purpose of the nuller, each map features bumps and gaps at distinct locations imposed both by the arrangement of the telescopes on the ground and by the inner details of the recombiner itself. Differences in these maps are a desirable feature: the measurement brought by each output is a new piece of information that will constrain the spatial distribution of intensity of the target astrophysical scene. Furthermore, a noteworthy feature of this particular architecture of nuller is that it produces as many distinct outputs as the total number of

baselines of the interferometer. However, the sparse nature of the interferometer also means that the monochromatic nuller output transmission maps are periodic. A blind snapshot observation with a nuller may very well by chance lead to the direct detection of the flux of an off-axis source, but will not suffice to unambiguously locate the source in the FOV. In this work, exactly as in aperture synthesis of constructive interferometry, we take advantage of the diversity brought by the rotation of the Earth and its effect on the different outputs, and their time-evolving and pointing-dependent transmission maps.

2.2. Projected interferometric array

Instead of having to keep track of the evolving (u, v) coordinates of the six baselines in the plane perpendicular to the line of the interferometric pointing (see the left panel of Fig. 1), in the computation of the nulled output transmission maps, we only have to keep track of the projected geometry of the interferometric array relative to one subaperture arbitrarily chosen as a reference. We can use the same coordinate transformation matrix (see e.g. Ségransan 2007) that computes the instantaneous (u, v) coordinates of an interferometer located at the mean latitude l and pointing at declination δ and hour angle h :

$$\begin{pmatrix} u \\ v \end{pmatrix} = \begin{pmatrix} -\sin(l) \sin(h) & \cos(h) \\ \sin(l) \cos(h) \sin(\delta) + \cos(l) \cos(\delta) & \sin(h) \sin(\delta) \end{pmatrix} \begin{pmatrix} B_{\text{north}} \\ B_{\text{east}} \end{pmatrix}, \quad (1)$$

but only to compute the apparent location of the three subapertures of the VLTI, which from the point of view of the source appear to move around to the reference subaperture. The right panel of Fig. 1 shows how this projected interferometric array evolves over time, with UT1 chosen as a reference, and compares it to the usual (u, v) coverage plot visible to the left. These telescope coordinate tracks were computed over an hour angle range of ± 4 h for the specific example of HIP 107773, which is located at a favourable celestial location ($\delta = -64^{\circ}42'45''$) for the VLTI ($l = -24^{\circ}24'37''$) and results in rather circular tracks. We will repeatedly use this example in order to demonstrate the effect this has on the outputs of a kernel-nuller at the focus of the VLTI.

2.3. Time-evolving output transmission maps

At any instant, using the matrix transform of Eq. (1), we can compute the apparent (x, y) coordinates of the UTs relative to UT1. To compute the output transmission maps across the FOV, we need to keep track of the value of the electric field emitted by an off-axis test source of right ascension and declination offset (α, δ) , that is collected by the different subapertures and possibly affected by some amount of residual piston ρ . For this point source, the four-element vector U (commensurate with the number of UTs) of complex amplitudes at the aperture entrance with wavelength λ is:

$$U(\alpha, \delta) \propto e^{(-2\pi i/\lambda)(\rho + (x\alpha + y\delta))}. \quad (2)$$

Having taken UT1 as the spatial reference, it is natural to also select it as the phase reference so that the phases of the different electric fields sampled by the other UTs are measured relative to this reference. The piston values are also quoted relative to UT1. The coherent interferometric combinations performed between the subapertures are fully described by a complex matrix \mathbf{M} , which links the input complex amplitudes of the off-axis test

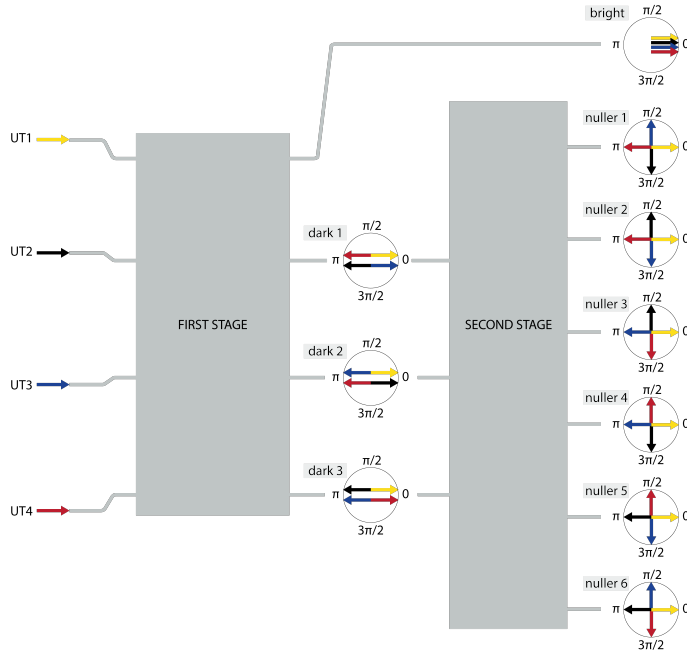


Fig. 3. Schematic representation of the two-stage kernel-nuller architecture. Light from the four VLTI UTs is coupled into the first 4×4 stage, which produces four outputs. Four in-phase ($\varphi = 0$) signals interfere constructively to produce a bright output (where most of the on-axis starlight is directed). For the three dark outputs, a phase shift ($\varphi = \pi$) is applied to the signal from two out of the four inputs. This means that when the light is combined, one input is out of phase from the other and so destructive interference occurs, leaving no starlight. At each stage of the four-beam combination, the different input (represented by coloured arrow) phase shifts applied to obtain the respective outputs are shown with complex matrix plots (Laugier et al. 2020). The second 3×6 stage performs six possible pairwise combinations of the dark outputs, with a phase shift ($\varphi = \frac{\pi}{2}$) introduced on one of the outputs. From the complex matrix plots of these six nulled outputs, we can see that pairs (nuller 1–2, 3–4, and 5–6) of outputs are mirror images of each other, an attribute that allows them to form a kernel-null.

source to the complex amplitudes of the nulled output. A detector records the intensity (i.e. square modulus) of the complex amplitude. We refer to the two-dimensional response of the nulled outputs at time t as nulled output transmission maps:

$$\tau(\alpha, \delta, t) = |\mathbf{M} \cdot U(\alpha, \delta, t)|^2, \quad (3)$$

and we use them extensively to comment on the properties of several observing scenarios with the kernel-nuller. At any instant, for an astrophysical scene described by a (usually unknown) function $O(\alpha, \delta)$, the raw output effectively recorded by the nulled will be the six-component vector:

$$I(t) = \int \tau(\alpha, \delta, t) \cdot O(\alpha, \delta) d\alpha d\delta. \quad (4)$$

Kernel outputs, noted κ , which are the primary intended observable quantities for the kernel-nuller, are linear combinations of simultaneous raw outputs. These combinations are summarised by a left-hand operator \mathbf{K} , which results in the three-element vector: $\kappa(t) = \mathbf{K} \cdot I(t)$. In Sect. 4.1, we see how to go from a record of raw outputs $I(t)$ or kernel outputs $\kappa(t)$ back to a description of the object $O(\alpha, \delta)$. To comment on some specific properties of the kernel-nuller, it is also useful to look at how the kernel outputs respond to the presence of an off-axis point source. We therefore also introduce kernel output maps $\kappa_M(\alpha, \delta, t)$, which are directly computed as:

$$\kappa_M(\alpha, \delta, t) = \mathbf{K} \cdot \tau(\alpha, \delta, t). \quad (5)$$

3. Simulated kernel-nulling observations at the VLTI

In this section, we present simulated monochromatic kernel-nulling L -band ($\lambda = 3.6 \mu\text{m}$) observations of the aforementioned target HIP 107773 at the focus of the four VLTI UTs. The simulated observing sequence consists of nine equally spaced pointings over the $\pm 4\text{h}$ range of hour angle. Below, we discuss the output and the properties of the baseline kernel-nuller design of Martinache & Ireland (2018).

Figure 3 is a schematic representation of this two-stage nulled architecture, which shows the four-UT beam combination that results in six nulled outputs, with the different phase shifts applied at each stage. In the first 4×4 stage, four in-phase signals from the UTs are combined to produce a bright output (bright in Fig. 3). For the three distinct dark outputs (dark 1–3 in Fig. 3), pairs of UTs along each nulling baseline are combined with a π phase shift on one of the input signals. To produce dark output 1, UT1 (set as the phase reference) is combined with UT4 and UT2 is combined with UT3. The combination of UT1-UT3 and UT2-UT4 yields ‘dark output 2’ whereas UT1-UT2 and UT3-UT4 generates ‘dark output 3’. The second 3×6 stage leaves the bright output untouched and performs six possible pairwise combinations of the dark outputs. By introducing a $\frac{\pi}{2}$ phase shift on one of the outputs, each dark output is split into two asymmetric responses, which is analogous to phase chopping (Angel & Woolf 1997; Lay 2004; Mennesson et al. 2005). The overall

effect of the recombiner taking four UTs and producing six nuller outputs (nuller 1–6 in Fig. 3) is described by a 6×4 complex matrix \mathbf{M} , which we use to compute the response of these outputs (see Eq. (3)):

$$\mathbf{M} = \frac{1}{4} \times \begin{bmatrix} 1+j & 1-j & -1+j & -1-j \\ 1+j & -1+j & 1-j & -1-j \\ 1+j & 1-j & -1-j & -1+j \\ 1+j & -1+j & -1-j & 1-j \\ 1+j & -1-j & 1-j & -1+j \\ 1+j & -1-j & -1+j & 1-j \end{bmatrix}. \quad (6)$$

This nuller is also associated with a kernel matrix \mathbf{K} , which when applied to the raw outputs of the nuller produces observable quantities called kernel outputs that are intrinsically more robust to fringe tracking residuals:

$$\mathbf{K} = \begin{bmatrix} 1 & -1 & 0 & 0 & 0 & 0 \\ 0 & 0 & 1 & -1 & 0 & 0 \\ 0 & 0 & 0 & 0 & 1 & -1 \end{bmatrix}. \quad (7)$$

For this design, a kernel output is therefore simply the difference between the two nuller outputs for which the same pairs of telescopes are nulled with each other (nuller 1–2, 3–4, and 5–6 in Fig. 3). Due to the asymmetric response of the nuller outputs (e.g. nuller 1–2 in Fig. 3), a centro-symmetric signal is eliminated by the subtraction. A difference of output values also means that unlike raw photometric-like outputs, kernel outputs can take negative values. To further comment on the properties of the kernel-nuller, it is useful to examine the absolute value of the kernel output. In addition to monitoring the evolution of the nuller output transmission maps $\tau(\alpha, \delta, t)$ in Sect. 3.1 and the global nuller throughput in Sect. 3.2, we therefore also look at kernel magnitude maps $|\kappa_M(\alpha, \delta, t)|$ (in Sect. 3.3).

3.1. Nuller output transmission maps with time

The optimal configuration for a nuller is when the bright target is positioned at the centre of the transmission map and the off-axis feature is situated in an area that is mostly driven towards the nulled outputs. As the location of the off-axis feature may be unknown, its detection in a snapshot is not guaranteed. Even in the case where some signal is detected, we cannot directly identify where the flux is coming from, because the signal is the result of an integral over the FOV (see Eq. (4)). This is why [Bracewell \(1978\)](#) proposed to rotate the interferometer: the on-axis bright star remains nulled, while off-axis features travel through the transmission maps, resulting in intensity modulations on the different outputs that can later be interpreted.

With a ground-based long-baseline interferometer, the scenario is different. For any pointing, in addition to the expected rotation of the transmission pattern manifest in Fig. 4, the different baselines stretch and shrink over the course of the transit. This is made evident by the transmission patterns, which have a broad appearance when the projected baselines are short (Col. 1 in the first block of Fig. 4) and appear narrow when the baselines are long at transit (Col. 5 in the first block of Fig. 4). As the source moves away from transit, the baselines begin to shorten again and we notice a progressive increase in the size of the transmission patterns.

From the time-averaged transmission maps shown in the second block of Fig. 4, we can confirm that the raw outputs do indeed work in pairs. If we isolate the time-averaged outputs 1 and 2, we see that the resulting dark spiral tracks in output 2

occupy the previous locations of bright spiral tracks in output 1 and vice versa. The same applies for outputs 3 and 4, and outputs 5 and 6. Consequently, a potential off-axis source located at the point of maximum transmission of one map would not give any signal through the other map. Thus, if we alternately detect a pair of outputs, the signal of an off-axis source can be further modulated and therefore retrieved.

The optimal sensitivity for each of these pairs of outputs occurs at slightly different angular separations in right ascension offset: ± 10 mas for outputs 1 and 2, ± 3 mas for outputs 3 and 4 and ± 6 mas for outputs 5 and 6. This is in line with the length of the shortest nulling baselines used for each pair of outputs, the shortest one being used for outputs 1 and 2 (UT2–UT3 = 46.6-m) and the longest one for outputs 3 and 4 (UT2–UT4 = 89.4-m). On average, over the entire ± 4 h observing window, these lead to a relatively uniform sensitivity. At any instant, the individual nuller outputs have an average throughput of approximately one-sixth of the total flux collected by four telescopes.

3.2. Nuller global throughput map with time

To assess the efficiency of the nuller at any given time for a specific observing scenario, it is useful to monitor the evolution of the overall throughput. Adding together the six nuller output transmission maps at any instant yields a new map, which we refer to as the nuller global throughput map (third block of Fig. 4). In the absence of prior information (ephemeris) about the location of a potential off-axis companion, the throughput map (time averaged over the planned observing window) can be used to predict the probability of detection. Located at the centre of these maps is an on-axis null, which upon observation is seen to go through a $\sim 90^\circ$ clockwise rotation over the ± 4 h range of hour angle. Replicas of the on-axis null (transmission holes) are visible in the throughput map. The layout of the four VLTI UTs generally favours detections in the top-right and bottom-left corners of the maps; however, Earth rotation eventually results in a more uniform coverage of the throughput map, as shown in the fourth (bottom-right) block of Fig. 4.

The extent of the maps we present above is limited to the FOV provided by the shortest snapshot baseline. The effective FOV extends to the diffraction limit of a UT ($\lambda/d \approx 90$ mas): any structure located within this FOV will be coupled into the recombiner and it is therefore relevant to look at what is happening for an extended FOV.

Panel a of Fig. 5 reproduces the throughput map for a snapshot observation at zenith, over an extended ± 30 mas FOV. The angular separation at which the on-axis null first reaches half of the peak throughput can be used as an approximation of the inner working angle (IWA). For the scenario at zenith, the peak throughput recorded is ~ 3.9 , which gives an IWA of ± 4 mas in right ascension offset and ± 6 mas in declination offset. The periodic response of the nuller in this monochromatic scenario is made obvious with the numerous replicas of the on-axis null – that would hide the signal of a companion – repeating every 15 mas. As the size of the observing window progressively increases, the transmission holes eventually fill in, with the nuller exhibiting a more homogeneous throughput after an eight-hour observation period (panel e of Fig. 5). The peak throughput at this range of hour angle is ~ 3.7 and the IWA is observed to be ± 4 mas in right ascension and declination offset. Earth rotation does change things somewhat for a suitable target such as HIP 107773, but less favourable scenarios at higher declination angles will retain some transmission holes in the throughput maps even with a sufficiently wide observing window.

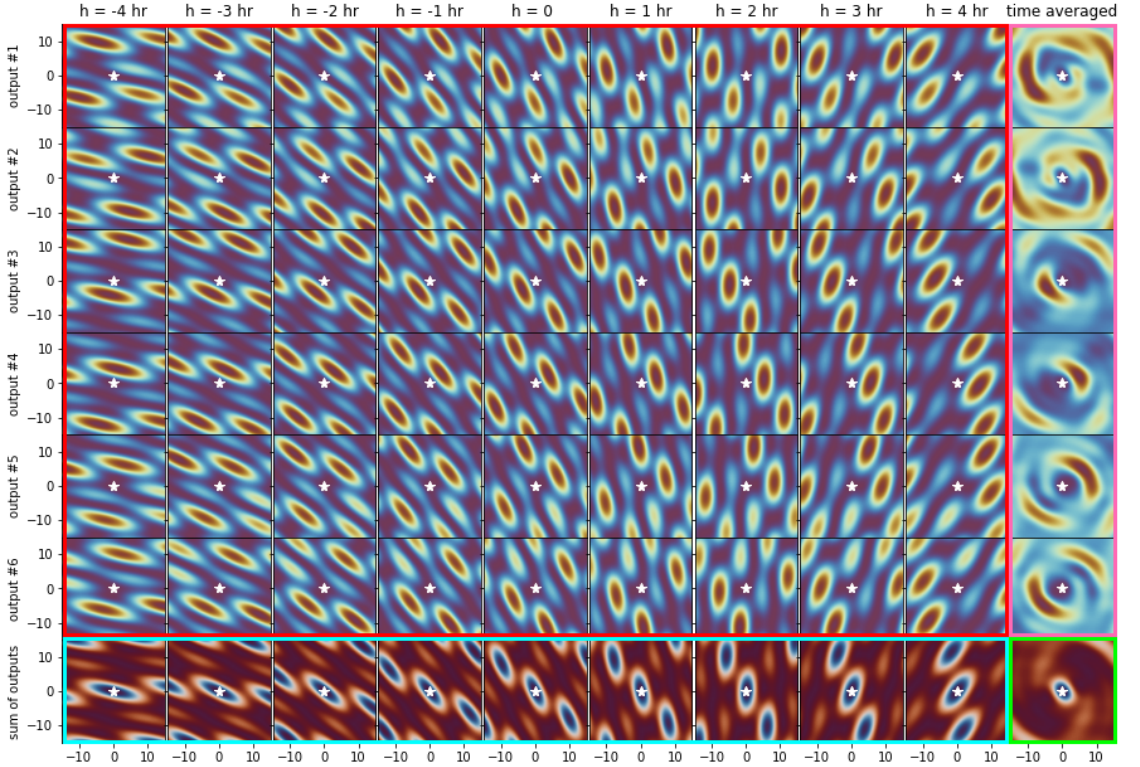


Fig. 4. Evolution of the nuller output transmission maps of a kernel-nuller at the focus of the four VLTI UTs, observing the ± 15 mas FOV surrounding the target HIP 107773. The figure shows four blocks of maps altogether, which provide insights into the behaviour of the nulled outputs. The first block (red contour, top left) of 54 maps shows how the transmission maps of the six nuller outputs evolve over a 4 h observing period centred on the target transit time ($h = 0$). These maps all share the same colour scale as Fig. 2 and show that at any instant, the transmission for at least part of the FOV per output can reach up to the totality of the flux collected by two telescopes. We can see the transmission patterns gradually rotating in a clockwise direction with time, scanning the FOV to intercept the light of any off-axis feature of the astrophysical scene. A white star in each plot marks the location of the central star where the transmission for all channels is equal to zero, by design. The second block (pink contour, rightmost column) of six maps shows the time-average of each nuller output transmission map, using the same colour scales and conventions. Looking at these, we can visually confirm that the outputs do indeed work in pairs characterised by asymmetric responses. The third block (blue contour, bottom row) of nine maps shows how at any instant, the sum of all output maps is spatially distributed. This series of images uses the same colour scale as Fig. 5. Summing the outputs shows that the overall instantaneous sensitivity of the nuller is much more uniform over the FOV, even if it nevertheless systematically features off-axis replicas of the on-axis null, which are referred to as transmission holes. The fourth block (green contour, single bottom right map) shows the time-averaged global throughput, which reveals that with a sufficiently wide observing window, the FOV is uniformly covered, and the nuller will be able to capture the light of a companion regardless of where it may reside.

3.3. Kernel magnitude maps with time

The primary motivation for the kernel-nuller is the production of observable quantities called kernel-nulls, which are less sensitive to residual piston fluctuations. We show above that for this specific architecture, kernel outputs are simply the pairwise difference between consecutive raw outputs (1–2, 3–4, and 5–6). Whereas raw outputs are a measure of flux, which are always positive, kernel outputs can take negative values (see Fig. 7). Therefore, in order to make quantitative observations about the detectability by a kernel-nuller, we look at kernel magnitude maps.

The kernel magnitude maps presented in the first block of Fig. 6 are analogous to the nuller output transmission maps; however, some differences between the respective maps are apparent. By virtue of taking the norm of the kernel output, we observe a

symmetry about the centre of the field in the magnitude maps and we also detect an increased number of transmission patterns. This means that for a given observation period, a potential companion will travel through more successive bright and dark regions in the magnitude maps, thus generating higher harmonics in the detected signal, which can give a stronger constraint on the position of the companion. In Sect. 4.1, we show how this signal can be used to give a description of a companion around a bright star.

From the time-averaged magnitude maps shown in the second block of Fig. 6, we observe that the kernel outputs display a more homogeneous sensitivity in the FOV relative to the raw outputs. Each output reaches its optimal sensitivity at varying positions in right ascension offset: with output 1 at ± 10 mas, output 2 at ± 3 mas, and output 3 at ± 6 mas. In the third block of Fig. 6 we show computed throughput maps, which are referred to

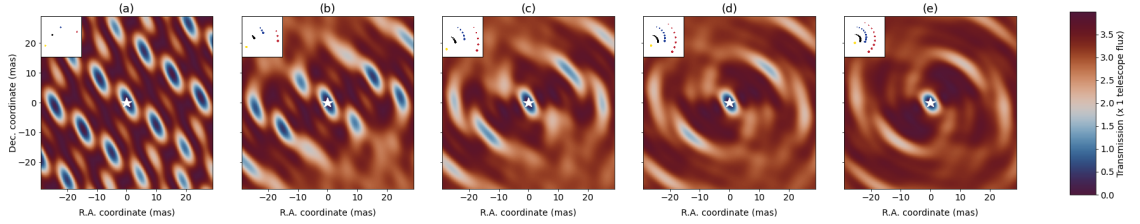


Fig. 5. Nuller global throughput maps at various observation periods of a kernel-nuller at the focus of the four VLTI UTs, observing the ± 30 mas FOV surrounding the target HIP 107773. The throughput maps allow us to assess the overall off-axis efficiency of a nulling observing sequence. In panel a, we see the throughput map for a single snapshot pointing at zenith. For the following maps, we computed the throughput maps at each pointing and then co-added the maps over the range of hour angle: panel b is the throughput map for three equally spaced pointings over a ± 1 h range of hour angle, panel c is that for five equally spaced pointings over ± 2 h, panel d for seven equally spaced pointings over ± 3 h, and panel e for nine equally spaced pointings over ± 4 h. The pointings of the projected array are shown inset in each throughput map. A white star in each map marks the location of the central star where the rejection by the nuller is optimal, as shown by the on-axis null. The five maps share the same colour bar where the transmission is expressed in units of the planet flux.

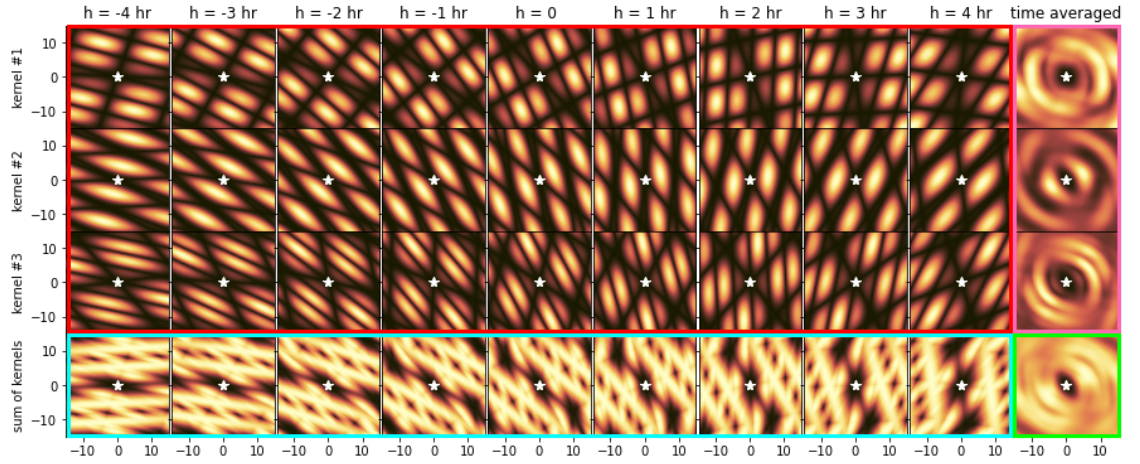


Fig. 6. Evolution of the kernel magnitude maps of a kernel-nuller at the focus of the four VLTI UTs, observing the ± 15 mas FOV surrounding the target HIP 107773. The figure shows four blocks of maps altogether, which provide insights into the behaviour of the kernel outputs. The first block (red contour, top left) of 54 maps shows how the magnitude maps of the three kernel-nuller outputs evolve over a ± 4 h observing period centred on the target transit time ($h = 0$). We can see the transmission patterns gradually rotating in a clockwise direction with time, scanning the FOV to intercept the light of any off-axis feature of the astrophysical scene. A white star in each plot marks the location of the central star where the transmission for all channels is equal to zero, by design. The second block (pink contour, rightmost column) of three maps shows the time-averaged of each kernel output magnitude map. The third block (blue contour, bottom row) of nine maps shows how at any instant, the sum of all kernel magnitude maps is spatially distributed. Summing the kernel outputs shows that the overall instantaneous sensitivity of the nuller is much more uniform over the FOV, even if it nevertheless systematically features off-axis replicas of the on-axis null, which are referred to as transmission holes. The fourth block (green contour, single bottom-right map) shows the time-averaged global throughput, which reveals that with a sufficiently wide observing window, the FOV is uniformly covered, and the nuller will be able to capture the light of a companion regardless of where it may reside. All maps share the same colour scale where the transmission is expressed in units of the kernel amplitude collected by one telescope.

as kernel global throughput maps and we observe from the time-averaged throughput map shown in the fourth block of Fig. 6 that with a sufficiently wide observing window, the FOV is uniformly covered.

4. Translation of kernel-nuller signals

In this section, we show how the signals acquired by a kernel-nuller can be exploited to build up a useful two-dimensional representation of a target of interest. Section 2 introduced the formalism required to account for the effect of Earth rotation on the raw outputs $I(t)$ produced by the nuller and their subsequent kernel outputs $\kappa(t)$. Equation (4) in particular describes

how, in the presence of Earth rotation, the object function $O(\alpha, \delta)$ describing the target becomes encoded in temporal fluctuations of the recorded raw outputs $I(t)$. To illustrate this effect, we performed a simulated observing sequence of HIP 107773 consisting of 17 equally spaced pointings over a ± 4 h range of hour angle. The simulation includes an off-axis companion conveniently located at $\alpha = +5.0$ mas, $\delta = +5.0$ mas (for a contrast $c = 10^{-3}$), where (according to Figs. 4 and 6) the sensitivity of the four-UT configuration of the VLTI is expected to be optimal. The presence of the companion induces a modulation of the different outputs of the nuller and their subsequent kernels, represented in the left and right panels of Fig. 7, respectively. If the action of the nuller were uniform, each channel would register

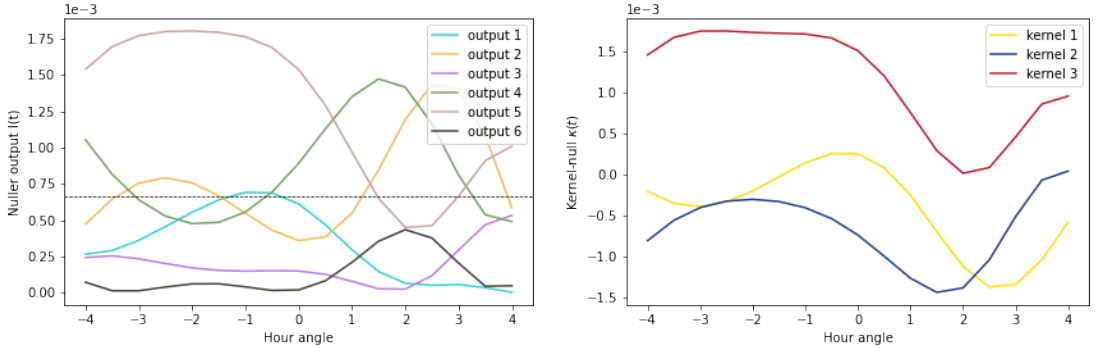


Fig. 7. Modulation of the raw null (*left panel*) and the kernel-null (*right panel*) induced by a single off-axis companion located at $\alpha = +5.0$ mas, $\delta = +5.0$ and with a contrast of $c = 10^{-3}$. This simulated kernel-nulling observation of HIP 107773 at the focus of the four VLTI UTs was in the absence of perturbations. The figures show that there is no redundancy in the kernel-nuller architecture as each of the six raw outputs and each of the three kernel outputs produces a different signal over the ± 4 h range of hour angle. Whereas the raw outputs are all positive, the kernel outputs can take negative values. If the action of the nuller was uniform, each channel would register a constant and uniform amount of flux, which in the units of the *left panel* would be $2/3 \times 10^{-3}$ (as shown by the dashed line).

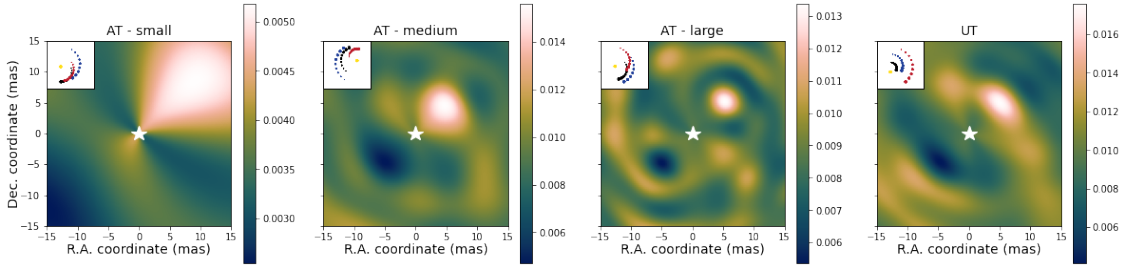


Fig. 8. Collinearity maps for different four-telescope VLTI interferometric array configurations over a ± 15 mas FOV. These maps were computed from the data-set acquired from simulated kernel-nulling observations of HIP 107773 over a ± 4 h range of hour angle. For these simulations in the absence of perturbations, an off-axis companion with a contrast of $c = 10^{-3}$ was placed at $\alpha = +5.0$ mas, $\delta = +5.0$. For the small (A0-B2-D0-C1) configuration of the ATs, we observe a maximum of collinearity confined to the top right of the map. Owing to the low spatial resolution provided by this array, we cannot infer the exact location of the companion. The collinearity map is improved with the use of the medium (K0-G2-D0-J3) AT configuration. Here, we see a broad maximum of collinearity around the location of the companion. The longer baselines provided by the large (A0-G1-J2-J3) AT configuration and the UTs will result in a higher spatial resolution. This is made evident in the collinearity maps computed with these array configurations by a narrower maximum of collinearity around the location of the companion. The scale on the right of each collinearity map denotes the amplitude of the companion signal, which is proportional to its contrast. The pointings of the projected array are shown inset in each collinearity map. A white star in each map marks the location of the central star where the rejection by the nuller is optimal.

a constant and uniform amount of flux, which in the units of the left panel of Fig. 7 would be $2/3 \times 10^{-3}$. In this favourable location, some outputs can record up to twice that amount.

4.1. Collinearity map

To decode these temporal fluctuations of the nuller measurements and turn them back into constraints on the spatial structure of the object, we can correlate the sequence of signals $I(t)$ acquired during an observation with the response of the nuller $\tau(\alpha, \delta, t)$ computed for the target over the same observation window, which produces a 2D map:

$$C_I(\alpha, \delta) = \frac{\int I(t) \cdot \tau(\alpha, \delta, t) dt}{\int \tau(\alpha, \delta, t) dt} \quad (8)$$

This procedure is identical to the concept of a 2D binary model collinearity map, as used by Laugier et al. (2019) and Martinache et al. (2020) in the context of kernel-phase interferometry. The

recorded signals $I(t)$ or their kernel outputs $\kappa(t)$ are effectively projected onto a 2D grid of possible binary models. Assuming that we get enough diversity over time in the signal, and a nuller transmission response that is unambiguous – as is the case with a kernel-nuller producing asymmetric outputs – the resulting map can serve as a first estimate of the object function $O(\alpha, \delta)$ (see Sect. 2) from which the bright on-axis source has been removed. Collinearity maps can be constructed from the raw nuller outputs (Eq. (8)) as well as from the kernel of these outputs:

$$C_\kappa(\alpha, \delta) = \frac{\int \kappa(t) \cdot \kappa_M(\alpha, \delta, t) dt}{\int \kappa_M(\alpha, \delta, t) dt}, \quad (9)$$

as described in Sect. 3, which now include an off-axis companion (presented in Fig. 7) located at $\alpha = +5.0$ mas, $\delta = +5.0$ mas and with a contrast $c = 10^{-3}$. One can verify that the sensitivity of the nuller with the raw outputs and kernel outputs is optimal at these coordinates with the throughput maps presented in the bottom right of Figs. 4 and 6.

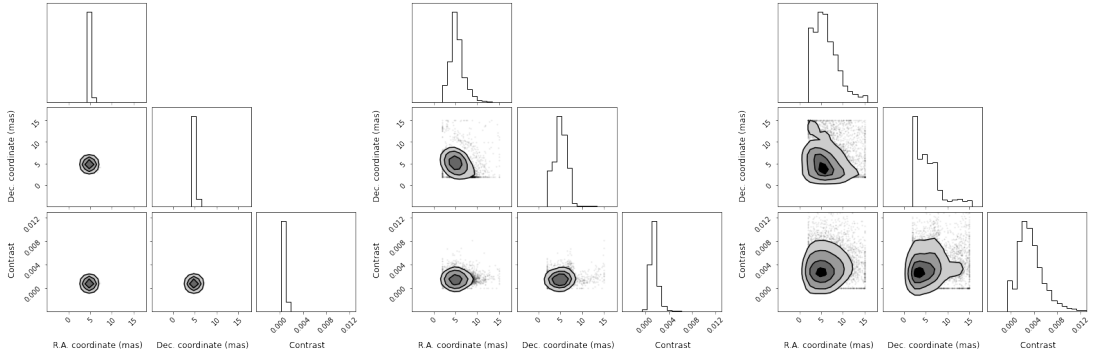


Fig. 9. Corner plots of the distribution of fitted values in position (α , δ) and contrast c for an off-axis companion located at $\alpha = +5.0$ mas, $\delta = +5.0$ mas and with a contrast $c = 10^{-3}$. The figures show the distributions of the respective parameters with varying piston residual size. *Left panel:* at 50 nm, we see well-distributed values around the coordinate locations of the companion with $\sigma_{\text{RA}} = 0.22$ mas and $\sigma_{\text{Dec}} = 0.25$ mas. *Middle panel:* at 100 nm, we begin to see some flux leakage from the null particularly in the δ distribution with $\sigma_{\text{RA}} = 2.01$ mas and $\sigma_{\text{Dec}} = 2.26$ mas. *Right panel:* at 150 nm, the piston-induced leaked intensity is more pronounced for both α and δ with $\sigma_{\text{RA}} = 4.11$ mas and $\sigma_{\text{Dec}} = 4.30$ mas. Each four-UT MC simulated data-set consists of 10^4 series of kernel outputs acquired in the presence of a controlled amount of residual phase noise.

The fidelity of the collinearity map is dependent on the spatial resolution provided by the interferometric array. The larger the baselines of the array, the higher the spatial resolution, which improves the accuracy of the estimate of $O(\alpha, \delta)$. For observations with four telescopes, the VLTI can operate with the 8m UTs or with the 1.8m auxiliary telescopes (ATs). Whilst the positions of the UTs are fixed, the ATs are relocatable and can be moved to a number of different stations. This way, observations on several different baselines can be carried out. The list of AT quadruplets offered in P110 (1 October 2022 – 31 March 2023) are:

- small, consisting of stations A0-B2-D0-C1, with baseline lengths of between 11.3 and 33.9 m.
- medium, consisting of stations K0-G2-D0-J3, with baseline lengths of between 39.99 to 104.3 m.
- large, consisting of stations A0-G1-J2-J3, with baseline lengths of between 58.2 and 132.4 m.

Figure 8 shows the result of the computation of several collinearity maps $C_1(\alpha, \delta)$ over a grid of possible locations, covering a ± 15 mas FOV for the three AT configurations and the UTs. As expected, the shorter baselines of the small configuration are of low spatial resolution, and therefore we see in the collinearity map of this array that $O(\alpha, \delta)$ is estimated over a wide region encompassing ~ 15 mas in right ascension and declination offset. The large configuration offers the longest baselines and in the map of this array we observe a narrower spatial structure of $O(\alpha, \delta)$ meaning that we can more accurately infer the location of the companion. The collinearity maps derived with the medium, large, and UT configurations suggest that the use of these arrays can allow us to effectively demodulate the signal of the companion. In these maps, a maximum of collinearity can be observed where the companion is expected, and as the amount of flux present in the different outputs is proportional to the brightness of the companion, when properly normalised, the maximum of collinearity matches the contrast of the companion.

4.2. Extracting astrometric parameters of an off-axis companion

The location of the point of maximum collinearity in the map shown in Sect. 4.1 of the four-UT configuration can be used as a first estimate of the position (α , δ) and contrast c of the actual

companion. This first estimate can then serve as the starting point in a parametric χ^2 minimisation procedure where the data (real or simulated) are compared to the parametric model of a binary object. The introduction of piston phase affects the fidelity of the fit. To estimate how these residual fringe-tracker errors affect our relative astrometry, we use Monte Carlo (MC) simulations. Each MC simulated data-set consists of 10^4 series of kernel outputs acquired in the presence of a controlled amount of residual phase noise. We use the `lmfit` Python package (Newville et al. 2016), which is an implementation of the Levenberg-Marquardt algorithm to find the best fitting binary parameters and look at how they are distributed. Here, χ^2 is a measure of the mean-squared difference between the measured kernel values $\kappa(t)$ and the corresponding values for the model $\kappa_B(\alpha, \delta, c, t)$:

$$\chi^2(\alpha, \delta, c) = \sum_t \frac{|\kappa(t) - \kappa_B(\alpha, \delta, c, t)|^2}{\sigma^2}, \quad (10)$$

where σ^2 is the variance of the piston phase in $\kappa(t)$. Figure 9 shows the result of some of these MC simulations for 50, 100, and 150 nm of fringe-tracking residuals. To put these values into context, current levels of VLTI/GRAVITY fringe-tracker residuals are ~ 200 nm on the UTs, though the GRAVITY+ upgrade will aim to decrease this to below 100 nm RMS. When deployed on telescopes, a nuller is extremely sensitive to such phase perturbations even after adaptive optics (AO) or fringe-tracker correction. The self-calibrating observables derived from a kernel-nuller attempt to alleviate this and we observe from the right panel of Fig. 9 that even with 150 nm piston induced error, the variance in the respective astrometric parameters is still relatively low.

5. Kernel-nuller exoplanet discovery observing program

Over the past decade, the majority of the directly imaged exoplanets found so far were discovered from ‘blind’ surveys where targets are selected based on age and distance from Earth. These detections have mostly been in the near-infrared using 8m ground-based telescopes coupled with extreme AO and coronagraphy. The most recent blind direct imaging surveys such

as Gemini-GPIES (Nielsen et al. 2019) and SPHERE-SHINE (Chauvin et al. 2017) have shed light on the occurrence rates of giant planets of between 10 and 100 AU and the formation mechanisms involved. However, these surveys have yielded few planet detections; for instance, the GPIES survey detected 9 companions from the approximately 300 stars imaged. The planetary mass companions around three of the imaged stars (HR 8799; Marois et al. 2008, β Pic; Lagrange et al. 2009, HD 95086; Rameau et al. 2013) were already known prior to the survey. Young stars (<100 Myr) have been natural targets for both the GPIES and SHINE surveys as their young age corresponds to bright young exoplanets, thus reducing the contrast ratio required for successful observations. The close distance of these surveys (~100 pc) should allow for exoplanet detections at closer separations to their host stars, although the exoplanets detected have been at wide separations (>20 AU) typically because the Gemini and SPHERE imaging systems are limited to observing beyond an IWA of a few λ/d (92 AU at ~111 pc). Indirect observation methods such as radial velocity and primary transit are more sensitive at close (<10 AU) separations, though here the presence of the planets is inferred, whereas direct imaging provides the photons from the planets themselves. The angular resolution provided by long-baseline interferometry and an on-axis high-contrast imaging mode will enable the direct detection of planetary companions in a region of the parameter space that has so far only been covered by indirect detection methods.

5.1. Combining astrometry and interferometry

For increased efficiency, an interferometric direct detection survey of extrasolar companions should target objects that are already suspected of harbouring one or more low-mass companions. With the aid of the unprecedented accuracy of *Gaia* (Gaia Collaboration 2016) astrometric measurements and its sensitivity to substellar companions, new techniques such as the proper motion anomaly (PMA, Kervella et al. 2019, 2022), the $\delta\mu$ method (Fontanive et al. 2019; Bonavita et al. 2020, 2022), and astrometric accelerations (Brandt 2018; Brandt et al. 2019; Brandt 2021) demonstrate how dynamical evidence – which previously only gave access to stellar companions – can now provide access to substellar companions. These techniques are all based on changes in stellar proper motions measured between two different astrometric catalogues covering long time baselines. The proper motion values measured between the catalogues should be identical for an isolated star. However, the tug of a companion will cause the position of the star to deviate slightly from what would be expected if it was isolated. This will result in a difference in proper motion measurements between the catalogues and can therefore be interpreted as an indication of the presence of an unseen companion around a single star.

The COPAINS survey (Fontanive et al. 2019; Bonavita et al. 2022) conducted with SPHERE/VLT is a recent example of the successful use of this $\delta\mu$ method, and led to the detection of 10 companions (6 of stellar mass and 4 brown dwarfs) out of a target sample of 25. In this section, we consider such a targeted approach for a discovery observing program with a kernel-nulling recombiner at the focus of the VLTI.

5.2. Target selection

We use the PMA catalogue (Kervella et al. 2022) of HIPPARCOS and *Gaia* EDR3 astrometry for ~11 000 stars as a proxy for giant planetary companions (1–13 M_{Jup}). As the VLTI is located in the southern hemisphere, we only consider targets from the

PMA catalogue with $\text{dec} < 16^\circ$. The sensitivity of the PMA technique to substellar companions decreases with the distance to the target, and therefore we restrict our target list to stars located within 100 pc ($\varpi > 10$ mas) of the Sun. The sensitivity of the PMA technique will also decrease as the mass of the primary star m_\star increases. We therefore impose a conservative range of $M_\odot < m_\star < 1.2 M_\odot$ on the primary mass, which has been estimated via various references in Kervella et al. (2019). As an indicator of binarity, we follow the approach of Kervella et al. (2022) and consider all the targets with an EDR3 PMA $S/N > 3$ to be probable companion-hosting stars. Assuming a circular orbit of radius r for the companion, its mass m_p is related to the PMA signal $\Delta\mu$ by the following expression shown in Kervella et al. (2019) as:

$$\frac{m_p}{\sqrt{r}} = \sqrt{\frac{m_\star}{G}} v_1 = \sqrt{\frac{m_\star}{G}} \left(\frac{\Delta\mu}{\varpi} \times 4740.47 \right), \quad (11)$$

where G is the gravitational constant, v_1 the tangential orbital velocity of the primary, and ϖ its parallax. The m_p values are estimated in the PMA catalogue at an orbital separation of 5 AU. In this scenario, we select the targets for which the astrometric signature is compatible with the presence of giant planetary mass companions. We then apply the Banyan Σ algorithm (Gagné et al. 2018) to this list of targets in order to determine their membership probability to young stellar associations. The Bayesian probability reported by Banyan Σ is based on the stellar coordinates, proper motion, radial velocity, and distance of the targets. We identify 38 targets as having a probability >95% of belonging to a young association and we show a sample of these in Table 1.

Now that we have an estimate of the age of the giant planetary companions potentially orbiting these targets, we can use isochrones from an evolutionary model to provide us with the photometric properties of the planet as a function of age. To do this we used species (Stolker et al. 2020), which is a toolkit developed for the spectral and photometric analysis of directly imaged exoplanets. Several evolutionary models are supported by species and for this analysis we use the AMES-Cond model. The AMES-Cond isochrones shown in Fig. 10 assume a hot start (i.e. high initial entropy) for the planet and one can use them to estimate its temperature T_p and surface gravity g . With these parameters, we can estimate the L -band planet/star flux ratio for self-luminous planets assumed to have a blackbody spectrum as:

$$c = \left(\frac{R_p}{R_\star} \right)^2 \frac{T_p}{T_\star}, \quad (12)$$

where R_p is the planetary radius that is derived from g , R_\star the stellar radius (see Table 1), and T_\star the star's effective temperature, which is approximated from its spectral type. Figure 11 shows how the 38 identified companion candidates are distributed in an angular separation–contrast plot. To achieve a spectral resolution $R \sim 50$, the analysis by Ireland (2020) shows that reaching a contrast better than $c = 10^{-5}$ over a one-hour integration with the ATs requires the targets to be brighter than $M = 9$ in the science band-pass (here the L -band). Moreover, the ability to observe the different targets is also dependent on the performance of the upstream AO system NAOMI (Woillez et al. 2019), which has a limiting magnitude of $R = 12$. We cross-matched our sample of targets with the USNO-B catalogue (Monet et al. 2003) to find the corresponding R -band magnitudes. We can confirm that all our 38 targets are bright enough to be observed by the VLTI ATs and lead to sensitive

Table 1. Ten of the 38 identified targets for the kernel-nuller discovery observing program, derived from the proper motion anomaly (PMA, Kervella et al. 2022) catalogue of HIPPARCOS and *Gaia* EDR3 astrometry.

| HIP | R (mag) | K (mag) | SpT | ϖ (mas) | $\Delta v_{T,G3}$ (m s ⁻¹) | m_* (M_\odot) | R_* (R_\odot) | m_p (M_{Jup}) | Sep. (mas) | log(<i>c</i>) | Assoc. | Age (Myr) |
|-------|------------|------------|-------|-------------------|---|------------------------|------------------------|------------------------|---------------|-----------------|--------|--------------|
| 1481 | 7.13 | 6.15 | F8V | 23.35 | 22.13 | 1.16 | 1.12 | 2.55 | 116.78 | -6.78 | THA | 45 |
| 14157 | 7.92 | 6.55 | K0V | 19.45 | 69.06 | 0.94 | 1.24 | 7.12 | 97.23 | -6.87 | CARN | 200 |
| 16544 | 8.30 | 7.09 | G2V | 19.13 | 43.98 | 1 | 0.94 | 4.75 | 95.67 | -5.77 | BPMG | 24 |
| 17338 | 8.69 | 7.20 | G8V | 17.57 | 50.75 | 1 | 1.03 | 5.48 | 87.87 | -5.99 | OCT | 35 |
| 30034 | 8.60 | 6.98 | K1V | 19.94 | 65.45 | 0.86 | 1.04 | 6.13 | 99.73 | -5.99 | CAR | 45 |
| 30314 | 6.15 | 5.04 | G1V | 41.89 | 12.52 | 1.08 | 1.07 | 1.40 | 209.44 | -7.32 | ABDMG | 149 |
| 50032 | 8.58 | 7.06 | K2V | 24.33 | 27.26 | 0.90 | 0.8 | 2.69 | 121.65 | -5.49 | UCL | 16 |
| 53837 | 7.16 | 6.05 | G2V | 30.03 | 15.46 | 1.08 | 0.95 | 1.73 | 150.16 | -6.14 | LCC | 15 |
| 78264 | 8.19 | 7.21 | F7V | 14.43 | 50.50 | 1.16 | 1.1 | 5.82 | 72.16 | -5.83 | UCL | 16 |
| 81295 | 9.35 | 8.24 | G3/5V | 11.09 | 101.70 | 1.06 | 0.94 | 11.29 | 55.47 | -4.89 | UCL | 16 |

Notes. The table includes the stellar R and K magnitudes, spectral type, parallax (ϖ), $\Delta v_{T,G3}$, which is the norm of the tangential PMA vector converted to linear velocity using the *Gaia* EDR3 parallax, m_* , the mass of the primary star, R_* the stellar radius, and m_p the mass of a companion assuming a 5 AU orbit. The angular separation estimate is given by the ratio between the semi-major axis (assumed to be 5 AU) and the distance to the system. The estimated contrast *c* of the companion is given as log(*c*). The full names of the young stellar associations listed are AB Doradus (ABDMG), β Pictoris (β PMG), Carina (CAR), Carina-Near (CARN), Lower Centaurus Crux (LCC), Octans (OCT), Tucana-Horologium Association (THA), and Upper Centaurus Lupus (UCL). The ages of the young associations are from Gagné et al. (2018).

contrast-detection limits. Table 1 lists the properties of 10 of the 38 identified targets for the kernel-nuller discovery observing program.

5.3. Kernel-nulling at the VLTI

Considering that telescope time is limited, using the UTs for kernel-nulling observations would only be warranted in the context of an exoplanet characterisation program. We know from the collinearity maps shown in Sect. 4.1 that the medium and large AT configurations are both capable of providing the spatial resolution needed for exoplanet detection on account of their long baselines. To request an imaging program with the VLTI ATs, ESO¹ requires a user to select a minimum of two configurations. Thus, we opt for the medium and large AT quadruplets for our discovery observations.

The single-mode (diffraction-limited) FOV of the ATs for *L*-band observations extends to ~ 400 mas. This outer working angle (OWA) adequately covers the expected range of angular separation for the 38 companion candidates represented in Fig. 11. The large AT quadruplet configuration features a maximum baseline length of 132.4m, which sets an IWA of 5.4 mas (6.9 mas for the medium). The IWA and OWA constraints suggest that the kernel-nuller can detect giant planets on orbits ranging from 0.24 to 18 AU (0.31–18 AU for the medium) for an object located at a distance of ~ 45 pc (median distance of identified companion candidates).

An observer in charge of the planning of this program can use the kernel global throughput map we present in Sect. 3.3 to predict the probability of detection at the expected location of a potential companion. Figure 12 shows the maps computed with the medium and large AT configurations for one of the identified targets: HIP 116748 ($c \sim 10^{-6}$). A companion orbiting at 5 AU from this host star would be located at an angular separation of ~ 113 mas. Over the course of a one-hour observation, the throughput maps go through a $\sim 10^\circ$ rotation. The average throughput of the nuller across the FOV reaches ~ 3 : the planet

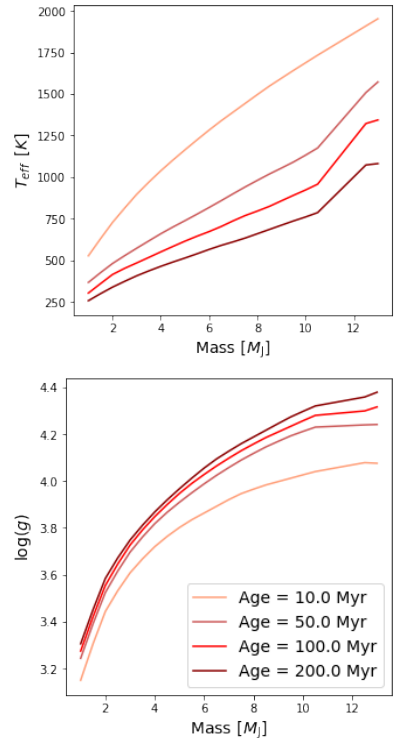


Fig. 10. AMES-Cond isochrones computed with a cloudless atmosphere as a boundary condition of the interior structure. *Top panel:* evolution of the effective temperature T_{eff} of giant planetary companions as a function of mass for different ages. *Bottom panel:* evolution of the surface gravity $\log(g)$ of giant planetary companions as a function of mass for different ages. The surface gravity g is in cgs units.

¹ <https://www.eso.org/sci/facilities/paranal/telescopes/vlti/configuration/P111.html>

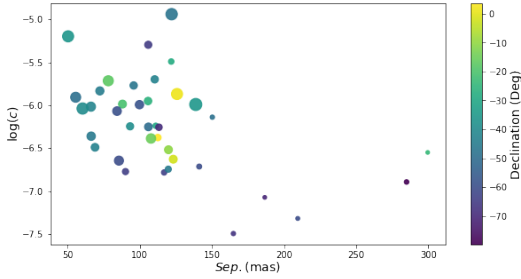


Fig. 11. Identified companion candidates to the targets identified for the kernel-nuller discovery observing program. These 38 targets are derived from the PMA catalogue (Kervella et al. 2022) of HIPPARCOS and *Gaia* EDR3 astrometry. The companion contrast c is presented as a function of the angular separation, which is given by the ratio between the semi-major axis (assumed to be 5 AU) and the distance to the system. The colour of the markers indicates the declination angle of the target system and the size depicts the mass of the companion (M_{up}).

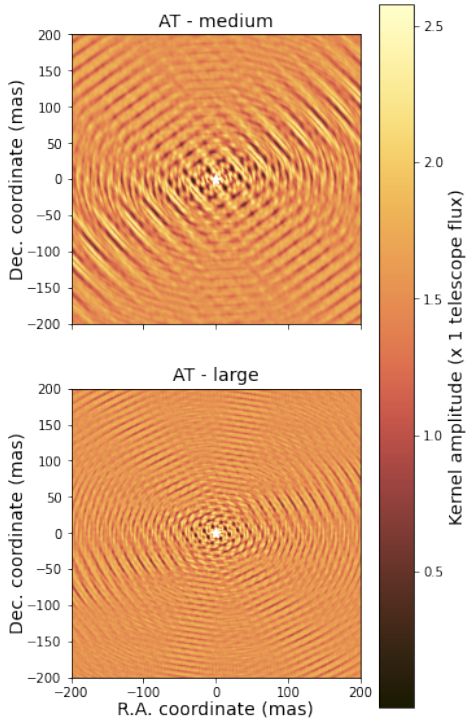


Fig. 12. Kernel global throughput maps of a kernel-nuller at the focus of the four VLTI ATs, observing the ± 200 mas FOV surrounding the target HIP 116748 for 1 h. *Top panel:* throughput map computed with the medium (K0-G2-D0-J3) AT configuration. *Bottom panel:* throughput map computed with the large (A0-G1-J2-J3) AT configuration. Both maps use the same colour scale, where the transmission is expressed in units of the kernel amplitude collected by one telescope. A white star in each map marks the location of the central star where the rejection by the nuller is optimal.

flux collected by three out of the four sub-apertures contributes to the detection of about 2300 photons (assuming an overall

efficiency of $\sim 3.2\%$ as reported by Laugier et al. 2023). The corresponding average magnitude of the kernel-null (see Fig. 12) is approximately 1.55. Both configurations provide a good detection completeness at the estimated location of the companion. For targets at higher (less favourable) declinations ($> -30^\circ$), the large configuration should be prioritised.

Figure 11 shows that the average expected contrast ratio for the identified companion candidates is $c \sim 10^{-6}$. According to Ireland (2020), reaching this level of contrast puts some very stringent requirements on the quality of the fringe tracking (~ 3 nm RMS) and the stability of the intensity fluctuations (0.01% RMS). These requirements are certainly challenging but achieving them would enable key science goals such as the detection of young giant exoplanets at separations of < 10 AU and the atmospheric characterisation of their atmospheres with a moderate spectral resolution ($R \sim 50$). A detailed analysis of the systematic errors introduced by the non-ideal nature of a nuller is beyond the scope of this paper. However, this could be the subject of a future publication as it is required in order to draw more definitive conclusions as to the sensitivity limits of our approach.

The infrastructure of the VLTI is currently on a transformative upgrade path: moving from the first generation FINITO fringe tracker (Le Bouquin et al. 2008) to that of GRAVITY (Lacour et al. 2019) has successfully reduced the fringe-tracking residuals on the ATs from ~ 150 to ~ 100 nm RMS, and other upgrades of the VLTI infrastructure are on their way. High-contrast detection of planetary companions using nulling is the objective of the NOTT instrument (Laugier et al. 2023); one of the modules of the planned Asgard instrument suite to be installed at the focus of the VLTI in 2025. The Asgard suite also includes HEIMDALLR (Ireland et al. 2018); a high-precision fringe tracker and injection stabilisation module. A HEIMDALLR prototype (Cvetojevic et al., in prep.) was tested in the laboratory and it was demonstrated that for targets brighter than $K = 11$, closed-loop fringe-tracking residuals can be brought down to ~ 4 nm RMS. To assess ultimate sensitivity, further analysis of the longitudinal dispersion between the K - and the L -band will be required. Assuming that the Asgard shared infrastructure fully addresses these effects and the operational challenges of non-common path aberrations, this ambitious program remains achievable with the VLTI.

6. Conclusions

The analysis performed in this paper shows that by taking into account baseline projection effects induced by Earth rotation, we introduce some diversity in the response of a nuller as a function of time. This response is depicted by transmission maps, which we show for both the raw nuller outputs and their subsequent kernel outputs – which are the primary intended observable quantities of the kernel-nuller. To further comment on the properties of the kernel-nuller, we examine the absolute value of the kernel output and present maps of this absolute value, which we call kernel magnitude maps. With enough evolution of the response of the nuller, we show that the so-called blind spots that we see in the snapshot throughput maps are eventually filled in.

The collinearity maps we present show that the increased diversity in the response results in a predictable modulation of the output of the nuller if a potential off-axis companion is present at a specific location. These maps are different for the various four-telescope arrays offered at the VLTI on account of their varying baseline lengths. The location of maximum

collinearity in these maps can be used as a first estimate of the position (α, δ) and contrast c of the actual companion, which can then serve as the starting point in a parametric χ^2 minimisation procedure. While we have been able to infer the position of a single companion with the collinearity map, this investigation could be extended to multiple companions in the FOV. For such an arbitrary high-contrast scene, the image can be reconstructed using a variety of inverse model techniques such as SQUEEZE (Baron et al. 2010) or MACIM (Ireland et al. 2006).

We assessed the characteristics of a kernel-nuller discovery observing program for the direct imaging of exoplanets. By exploiting the synergy between astrometry and direct imaging, we show the target-selection process for this program. The complete analysis of the targets identified is beyond the scope of this paper as we would also need to take into account other indicators of binarity such as the renormalised unit weight error (RUWE; Lindegren et al. 2021) and determine whether or not the potential giant planetary mass companions identified are gravitationally bound to their host star. Additionally, the possible positions of the companion generating the astrometric signature can be further limited by using $\Delta v_{T,G3}$, as shown by Bonavita et al. (2022). Furthermore, with all subsequent *Gaia* data releases, the sensitivity of the PMA technique will continue to improve.

Acknowledgements. This project has received funding from the European Research Council (ERC) under the European Union's Horizon 2020 research and innovation program (grant agreement CoG – 683029). DD acknowledges the support from the ERC under the European Union's Horizon 2020 research and innovation program (grant agreement CoG – 866070).

References

- Angel, J. R. P., & Woolf, N. J. 1997, *ApJ*, 475, 373
- Baron, F., Monnier, J. D., & Kloppenborg, B. 2010, *SPIE Conf. Ser.*, 7734, 77342I
- Bonavita, M., Fontanive, C., Desidera, S., et al. 2020, *MNRAS*, 494, 3481
- Bonavita, M., Fontanive, C., Gratton, R., et al. 2022, *MNRAS*, 513, 5588
- Bracewell, R. N. 1978, *Nature*, 274, 780
- Bracewell, R. N., & MacPhie, R. H. 1979, *Icarus*, 38, 136
- Brandt, T. D. 2018, *ApJS*, 239, 31
- Brandt, T. D. 2021, *ApJS*, 254, 42
- Brandt, T. D., Dupuy, T. J., & Bowler, B. P. 2019, *AJ*, 158, 140
- Chauvin, G., Desidera, S., Lagrange, A. M., et al. 2017, in *SF2A-2017: Proceedings of the Annual meeting of the French Society of Astronomy and Astrophysics*, eds. C. Reyli , P. Di Matteo, F. Herpin, et al., 331
- Cvetojevic, N., Martinache, F., Chingaipe, P., et al. 2022, arXiv e-prints [arXiv:2206.04977]
- Defr re, D., Absil, O., Berger, J. P., et al. 2018, *Exp. Astron.*, 46, 475
- Fontanive, C., Mu i , K., Bonavita, M., & Biller, B. 2019, *MNRAS*, 490, 1120
- Gagn , J., Mamajek, E. E., Malo, L., et al. 2018, *ApJ*, 856, 23
- Gaia Collaboration (Prusti, T., et al.) 2016, *A&A*, 595, A1
- Guyon, O., Mennesson, B., Serabyn, E., & Martin, S. 2013, *PASP*, 125, 951
- Ireland, M. 2020, *SPIE Conf. Ser.*, 11203, 112030U
- Ireland, M. J., Monnier, J. D., & Thureau, N. 2006, *SPIE Conf. Ser.*, 6268, 62681T
- Ireland, M. J., Defr re, D., Martinache, F., et al. 2018, *SPIE Conf. Ser.*, 10701, 107011I
- Jennison, R. C. 1958, *MNRAS*, 118, 276
- Kervella, P., Arenou, F., Mignard, F., & Th venin, F. 2019, *A&A*, 623, A72
- Kervella, P., Arenou, F., & Th venin, F. 2022, *A&A*, 657, A7
- Labeyrie, A., Lipson, S. G., & Nisenson, P. 2006, *An Introduction to Optical Stellar Interferometry* (Cambridge University Press)
- Lacour, S., Dembet, R., Abuter, R., et al. 2019, *A&A*, 624, A99
- Lagrange, A. M., Gratadour, D., Chauvin, G., et al. 2009, *A&A*, 493, A21
- Laugier, R., Martinache, F., Ceau, A., et al. 2019, *A&A*, 623, A164
- Laugier, R., Cvetojevic, N., & Martinache, F. 2020, *A&A*, 642, A202
- Laugier, R., Defr re, D., Woillez, J., et al. 2023, *A&A*, 671, A110
- Lay, O. P. 2004, *Appl. Opt.*, 43, 6100
- Lay, O. P., Jeganathan, M., & Peters, R. 2003, *SPIE Conf. Ser.*, 5170, 103
- Le Bouquin, J. B., Bauvri, B., Haguenaue, P., et al. 2008, *A&A*, 481, 553
- Lindegren, L., Klioner, S. A., Hern andez, J., et al. 2021, *A&A*, 649, A2
- Marois, C., Macintosh, B., Barman, T., et al. 2008, *Science*, 322, 1348
- Martinache, F. 2010, *ApJ*, 724, 464
- Martinache, F., & Ireland, M. J. 2018, *A&A*, 619, A87
- Martinache, F., Ceau, A., Laugier, R., et al. 2020, *A&A*, 636, A72
- Mennesson, B., L ger, A., & Ollivier, M. 2005, *Icarus*, 178, 570
- Monet, D. G., Levine, S. E., Canzian, B., et al. 2003, *AJ*, 125, 984
- Newville, M., Stensitzki, T., Allen, D. B., et al. 2016, *Astrophysics Source Code Library* [record ascl:1606.014]
- Nielsen, E. L., De Rosa, R. J., Macintosh, B., et al. 2019, *AJ*, 158, 13
- Quanz, S. 2019, in *EPSC-DPS Joint Meeting 2019*, EPSC-DPS2019-327
- Rameau, J., Chauvin, G., Lagrange, A. M., et al. 2013, *ApJ*, 772, L15
- S gransan, D. 2007, *New A Rev.*, 51, 597
- Stolker, T., Quanz, S. P., Todorov, K. O., et al. 2020, *A&A*, 635, A182
- Woillez, J., Abad, J. A., Abuter, R., et al. 2019, *A&A*, 629, A41

Chapter 5

Photonics

An integrated optics chip, which is the optical equivalent of a microelectronic circuit, had been fabricated prior to my arrival in Nice. It contains 12 distinct kernel-nulling arrangements that allow us to experimentally validate different methods of routing, phase delays, and beam combination. The kernel-nullers on the chip are manufactured out of a device known as a multimode interference (MMI) coupler. MMIs are only beginning to emerge in astronomical instrumentation, and are an alternative to conventional waveguiding photonic components, whose application in astronomy I review in this chapter.

The so-called astrophotonics has led to the GRAVITY beam combiner that — in dual-field mode— enables astrometry and *K*-band spectroscopy of exoplanets. Akin to GRAVITY, the GLINT integrated optics nuller employs pairwise beam combination —with directional couplers— where one interferometric baseline is nulled at a time. But a kernel-nuller cannot operate in this approach, hence the use of an MMI which simultaneously nulls multiple baselines. These devices allow for simple and compact kernel-nulling arrangements on a 16-mm × 16-mm photonic chip. I conclude the chapter by describing this chip and its respective components.

1 A brief introduction to astrophotonics

Photonics is the use of materials to manipulate light, which involves its emission, transmission, processing and detection. The origin of this branch of optics can be traced back to the 1960s with the invention of the laser and advances in the application of optical fibres (see Fig. 28) for light propagation. These cylindrical photonic waveguides consist of a core (central region of fibre where light travels) surrounded by a transparent cladding material with a lower refractive index. Light is confined to the core by the principle of total internal reflection. The core is typically made of glass or plastic, and the amount of light entering a fibre is proportional to its diameter. Depending on this diameter, the index contrast

between the core/cladding, and cladding structure, optical fibres can either be single-mode or multimode. A typical single-mode fibre—for the 1550 nm region—has a core diameter between 8 – 10.5 μm , and a cladding diameter of 125 μm . The single spatial mode transmitted by the fibre is characterised by a Gaussian profile. Multimode fibres have a much larger core diameter (50 – 100 μm), and support 100s - 1000s of modes.

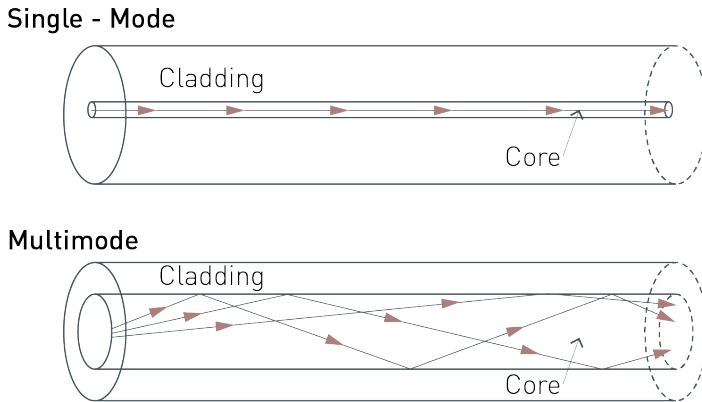


Figure 28: Single-mode (*Top*) and graded-index multimode (*Bottom*) optical fibres that transmit light (propagation direction depicted by arrows) from one end to the other. These cylindrical photonic waveguides have a central core surrounded by a cladding with a slightly lower ($\sim 1\%$) refractive index. In the case of silica fibres, the cladding often consists of pure silica (SiO_2), while the core is doped (e.g. with germania (GeO_2)) in order to achieve an increased index of refraction. As the core has a higher refractive index than the cladding, light will be confined to it if the angular condition for total internal reflectance is met. The electric field distributions of light propagating in the core are generally referred to as modes. Depending on the number of modes that are supported in a core, which is determined by the fibre geometry and composition, optical fibres are specified as single-mode or multimode.

Experimental investigations by Charles Kuen Kao combined fibres of very pure glass with lasers, and demonstrated that high-loss in fibres arose from glass impurities. This groundbreaking development in photonics, which was awarded one half of the 2009 Nobel Prize in Physics, formed the basis of the telecommunications revolution of recent decades by enabling the efficient transmission of information over long distances. The subsequent demand and investment in the industry has led to the maturation of waveguiding photonic components that are widely used in various fields, including astronomy. Indeed, the overwhelming majority of these components are optimised for operations in the optical communication bands: *O*-band (1.26 – 1.36 μm) & *C*-band (1.53 – 1.565 μm) – whose wavelengths overlap with the astronomical near-infrared. Consequently, numerous applications of photonics (i.e., astrophotonics) that overcome the deficiencies

of conventional bulk optics instrumentation have been developed. These include integral field units (IFUs; see Sect. 1.1) comprised of optical fibres and charge-coupled devices (CCDs). The invention of the CCD concept by Willard S. Boyle and George E. Smith was awarded the other half of the 2009 Physics Nobel Prize.

1.1 Integral field units

In the early years of photonics, the quality of commercially available fibres was insufficient for long data transmission, but the influence of the telecommunications industry rapidly increased their optical properties (i.e., improvement in mechanical reliability, polarisation control or transparency). To determine the performance of such fibres, [Angel et al. \(1977\)](#) made laboratory measurements—in the UV and visible—of fused silica fibres manufactured by Valtec Corporation. Over ~ 20 -m lengths, the fibres were found to show a high transmission in the $0.3 - 2\mu\text{m}$ spectral range, which would make them ideal to link arrays of telescopes (see the Fibre-Linked Optical Array Telescope (FLOAT); [Angel et al. 1977](#)). Besides demonstrating the practicality of the FLOAT concept, [Hubbard et al. \(1979\)](#) obtained the first astrophotonic spectrum (of NGC 4151) via a single fused silica fibre ($125\mu\text{m}$ diameter and 20-m length) connecting the 91-cm Steward telescope to a spectrograph located in a laboratory below the observing floor.

The favourable investigations of single optical fibres led to the pioneering multi-object spectrograph, whose system consisted of three alternating sets of 37 fused silica fibres housed in boxes. Owing to the tangle of fibres inside a box, the spectrograph was called Medusa ([Hill et al. 1980](#)). Pre-drilled 3-mm thick aluminium aperture plates were mounted on each box, with short lengths of $300\mu\text{m}$ —in diameter—fibres glued into the aperture holes corresponding to object positions in the focal plane of the 2.3-m Steward telescope on Kitt Peak. This interchangeable aperture plate scheme allowed for the sampling of different parts of the field of view, and from a single exposure of the cluster Abell 1904, the redshifts of 26 individual galaxies were determined. Such a device which segments the image of the target in the focal plane by way of a fibre array is generally referred to as an IFU.

IFUs have paved the way for an era of large-scale galactic surveys. Indeed, the most detailed three-dimensional maps of the cosmos are attributed to the Sloan Digital Sky Survey (SDSS; [York et al. 2000](#)), whose IFU is analogous to Medusa. But besides a fibre array, IFUs can use other techniques to divide the field of view. The SINGle Faint Object Near-IR Investigation (SINFONI; [Eisenhauer et al. 2003](#))

on the VLTI operates an image slicer technique (see Fig. 29). Here, a stack of 32 plane mirrors divides a two-dimensional image into 32 smaller components. A second set of 32 mirrors, the so-called big slicer, re-positions them into a one-dimensional pseudo-slit (i.e., in a line end-to-end). The SPectrograph for Infrared Faint Field Imaging (SPIFFI; Iserlohe et al. 2004) disperses the light from the slit into its separate wavelengths. All the slices at each wavelength are rearranged in a three-dimensional data cube, from which a reconstructed image –with two spatial and one spectral dimension– is produced.

Image slicing will also be utilised on the ELT’s High Angular Resolution Monolithic Optical and Near-infrared Integral field spectrograph (HARMONI; Thatte et al. 2010). Its Adaptive Optics Calibration Unit (AOCU; Schwartz et al. 2022) performs several functions that include: calibrating the wavefront sensors, and measuring non-common path aberrations. For multi-wavelength guidance, the unit employs photonic crystal fibres (PCFs; Birks et al. 1997). PCFs, typically made of pure fused silica, obtain their waveguide properties from an arrangement of very tiny and closely spaced air holes that surround the core (i.e., cladding region in Fig. 28), and go through the full length of the fibre. The comparatively large index contrast between air and glass, and the ability to vary the sizes and positions of the air holes gives PCFs a much broader range of index profiles than conventional optical fibres. However, PCFs can be highly non-linear and birefringent, which means that the refractive index of the fibre is dependent on the polarisation and propagation direction of light. Although they also exhibit unusual dispersion, polarisation-maintaining PCFs are single-mode over the entire transparency range of silica (0.3 – 2 μ m). A single-mode PCF is used to inject broadband light from a supercontinuum source into the kernel test bench that I present in Chapter 6.

Another technique for an IFU is with a microlens array, which is a one or two dimensional array of small lenses (lenslets) that is commonly used to enhance the coupling of light to optical fibres. A microlens was built for the Spectroscopic Areal Unit for Research on Optical Nebulae (SAURON; Bacon et al. 2001): an IFU on the 4.2-m William Herschel Telescope located in La Palma. The SAURON lenslet array is fabricated from fused silica and consists of over 1600 lenslets. Each lenslet has a square shape (side length of 1.31-mm), whose light, after a collimator, is dispersed by a grism (combination of a prism and grating). A CCD camera then images the resulting spectra. Indeed, all photonics-based devices encounter the difficulty of coupling light into a waveguide, which is why sometimes, fibre array IFUs are used in combination with a microlens (see Fig. 30). However, extreme AO is still needed to reduce coupling losses.

5 *kernel-nulling for the direct detection of exoplanets*

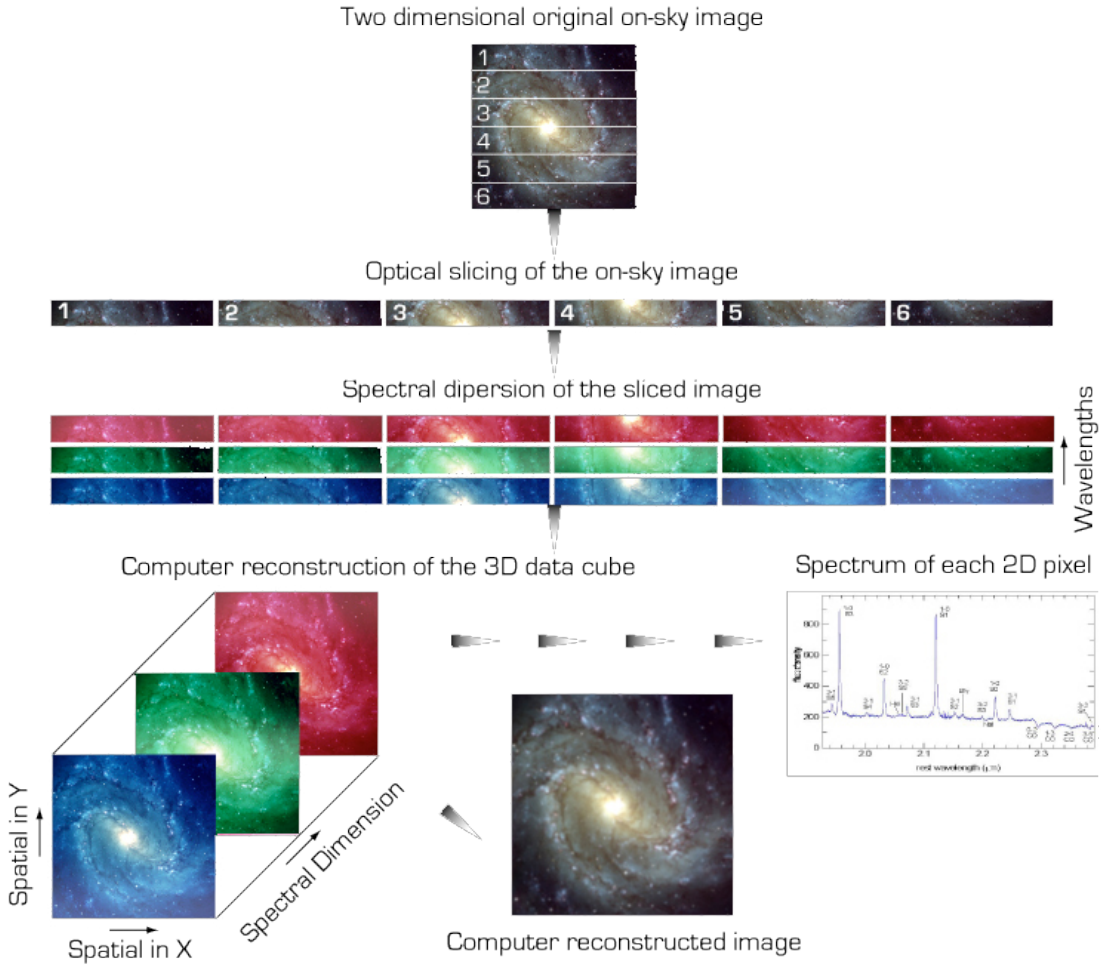


Figure 29: Principle of an image slicer integral field unit (IFU). A two-dimensional image is divided into smaller components (via optical slicing), and re-positioned into a one-dimensional pseudo-slit (i.e., in a line end-to-end). A spectrograph disperses the light from the slit into its separate wavelengths. All the slices at each wavelength are rearranged in a three-dimensional data cube, from which a reconstructed image—with two spatial and one spectral dimension—is produced. Image from <http://eso.org/>.

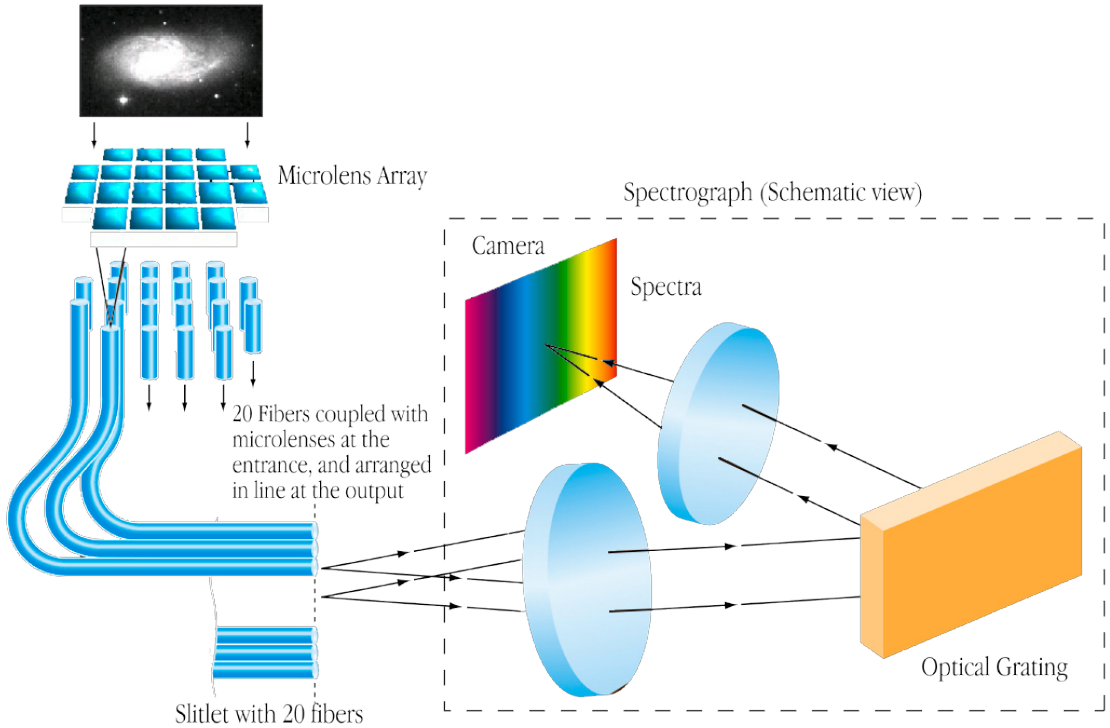


Figure 30: Principle of a microlens-fibre coupled integral field unit (IFU). A microlens array is a one or two dimensional array of small lenses (lenslets) that efficiently couple the light into optical fibres. The coupled light from the fibres is incident on a lens that collimates the light, i.e., light rays within the beam are parallel to each other after passing the lens, which makes it easier to accurately distinguish the various spectral components separated on diffraction from the grating. A focusing lens directs the dispersed light from the grating towards a detector. Image from <http://eso.org/>.

To mitigate the extreme AO requirement while preserving a high throughput, single-mode spectrographs fed by a photonic lantern (PL; Leon-Saval et al. 2005) have been proposed (e.g., the Photonic Integrated Multi-Mode Spectrograph (PIMMS); Bland-Hawthorn et al. 2010). PLs are tapered optical fibres that adiabatically (i.e., in a gradual way) transform a multimode optical fibre into a collection of single-mode fibres. The numerous modes supported by a multimode fibre allows complex beam profiles to be efficiently coupled, while the output of a single-mode waveguide does not evolve with time or with input beam fluctuations, and so is extremely stable. If the number of single-mode fibres matches the number of spatial modes supported by a multimode fibre, there will be a low loss transition (from multimode to single-mode) that can provide diffraction-limited performance to a spectrograph on a telescope with an inferior AO.

1.2 Interferometric beam combiners

The spatial filtering properties provided by single-mode fibres can also be exploited with interferometric beam combiners (see [Froehly 1981](#)). Not only do these fibres reduce the effect of atmospheric turbulence leading to accurate visibility measurements, but they also allow for uncomplicated optical layouts with simple alignment procedures especially if more than two apertures are employed. The Fibre Linked Unit for Optical Recombination (FLUOR; [Coudé du Foresto & Ridgway 1992](#)), which was conceived as a two-input beam combiner, established the use of single-mode fibres for interferometry when fluoride glass fibres became available in the $2 - 4\mu\text{m}$ range. These fibres manufactured by Le Verre Fluoré had a numerical aperture (0.23) and core diameter ($6.5\mu\text{m}$) that made them ideal for single-mode operation at wavelengths $> 1.95\mu\text{m}$.

Figure 31 provides a visual representation of the FLUOR recombination device, which implemented three *X*-couplers to simultaneously obtain two interferometric and two photometric outputs. The *X*-couplers were made by bringing two fibre cores in close proximity without contact so that the evanescent fields of the mode (the part of the electric field that extends outside the core) interact. A directional coupler that has waveguides in contact is referred to as a zero-gap coupler. If there is light in only one input fibre (or waveguide), then an *X*-coupler will act as a *Y*-coupler, which was the case for two of the *X*-couplers (*X*1 & *X*2) used in FLUOR. Dispersion compensating fibre segments were inserted between the '*Y*-couplers' and the *X*-coupler, with their lengths adjusted in such a way that the differential dispersion between each arm of the interferometer was as small as possible. Optical fibre dispersion, which includes modal dispersion, chromatic dispersion and polarisation mode dispersion, describes the process of how an input signal broadens or spreads out as it propagates from one end of the fibre to the other. This effect reduces the sensitivity of the interferometer as the longer integration time increases the noise accumulated on a detector. By optimising the waveguide structure (core diameter and the index contrast between the core/cladding), [Coudé du Foresto et al. \(1995\)](#) showed that fluoride glass fibre dispersion is reduced by more than two orders of magnitude in the $2 - 2.7\mu\text{m}$ range.

FLUOR transformed a pair of 80-cm telescopes — separated by a 5.5-m baseline— into an astronomical interferometer, and with the *K*-band observations of α Orionis and α Tauri, the device demonstrated for the first time the coherent recombination of stellar signals by guided optics. Originally located at the Kitt Peak National Observatory in Arizona, FLUOR was later moved to the Infrared and

Optical Telescope Array (IOTA; [Carleton et al. 1994](#)) on Mt. Hopkins. IOTA comprised of three 45-cm diameter telescopes that could be positioned at 17 stations on an L-shaped track: the north-east arm was 35-m long, and the south arm, which makes an approximate angle of 45° with the north-east, had a length of 15-m. It operated with 2 telescopes from 1995, and 3 telescopes from February 2002 to the end of June 2006. FLUOR has been operating at the CHARA Array since 2002, and after a program of upgrades (known as Jouvence of FLUOR), the instrument is now called JouFLU ([Scott et al. 2013](#)).

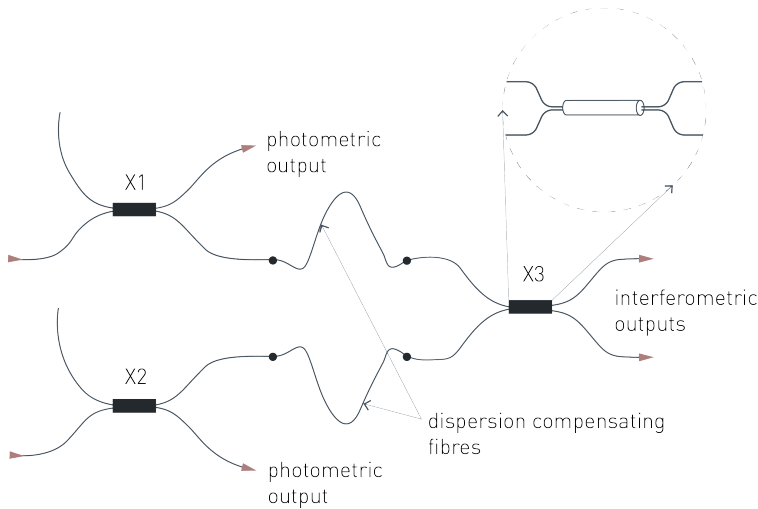


Figure 31: Schematic representation of the 2-input/4-output Fibre Linked Unit for Optical Recombination (FLUOR; [Coudé du Foresto & Ridgway 1992](#)). This *K*-band fibre-fed interferometric beam combiner implemented three *X*-couplers and two dispersion compensating fibre segments to simultaneously obtain the interferometric signal and the photometric channels for calibration. The *X*-couplers were made by bringing two fibre cores in close proximity without contact so that the evanescent fields of the mode (the part of the electric field that extends outside the core) interact. If there is light in only one input fibre (or waveguide), then an *X*-coupler will act as a *Y*-coupler, which was the case for *X1* and *X2*. The *X*-coupler (shown inset) was manufactured by bringing by bringing two fibre cores in close proximity without contact (evanescent field mixing). Image adapted from [Coudé du Foresto, Perrin, et al. \(1997\)](#).

Single-mode fibres combine all six telescopes of the CHARA array (from $1.45 - 2.5\mu\text{m}$) with low ($R \sim 35, 150, \text{ or } 250$) spectral resolution on the Michigan In-fraRed Combiner (MIRC; [Monnier et al. 2004](#)), which is based on the heritage of FLUOR. [Baron et al. \(2014\)](#) observed two red supergiants (HD 14488 and HD 14142) with the milliarcsecond spatial resolution delivered by this multi-axial combiner. The same combination scheme —where focusing optics combine parallel beams in the image plane— is applied on the single-mode fibre-fed Astronomical Multi-BEam combineR (AMBER; [Petrov et al. 2007](#)). It utilises three VLTI UTs

or ATs to provide three visibilities and one closure phase with low ($R = 35$), moderate ($R = 1000$) and high ($R = 10000$) spectral resolutions in the near-infrared. Observations with AMBER enabled [Ohnaka et al. \(2017\)](#) to measure a vigorous atmospheric motion in the red supergiant star Antares.

Besides fibre optics, an interferometric beam combiner can also be made of a photonic integrated circuit (PIC; [Miller 1969](#)) that performs several functions (i.e., routing, beam splitting, and recombination) in a single component. PIC-based beam combiners, which were proposed in the 1990s (see [Kern et al. 1997](#)), exhibit a superior thermo-mechanical stability to that of their fibre optic counterparts owing to the shorter waveguides embedded on a microchip. Because the devices are robust to external parameters such as temperature and pressure, a cryostat implementation which reduces thermal emission is possible.

2 Integrated optics beam combiners

Integrated optics designed for telecommunication applications operate at wavelengths that correspond to the H -band atmospheric transmission window, which allowed for the development of several PIC beam combiner prototypes by Laboratoire d’Astrophysique de l’Observatoire de Grenoble. The laboratory characterisation (see [Berger et al. 1999](#), [Haguenauer et al. 2000](#)) of these 5-mm \times 40-mm photonic chips demonstrated high and stable contrasts ($\sim 96\%$ at $1.55\mu\text{m}$ and $\sim 92\%$ in the H -band) as well as a good optical throughput ($\sim 43\%$). This proof of concept led to the first PIC-based observations of stars (see [Berger et al. 2001](#)) that used two different H -band chips. The chip identified as LEMO was fabricated with the ion exchange process (see [Benech 1997](#)). Light from the two apertures of the IOTA array was coupled into this beam combiner (shown in [Fig. 32](#)) via 1-m polarisation-maintaining single-mode fibres. By adiabatically broadening the input waveguide, a direct Y -junction split each input into two separate waveguides: one output providing the photometric calibration signal, and the other coupled into a reverse Y -junction that combined the inputs to produce one interferometric output. Y -junctions are fairly simple to fabricate and are typically designed to produce an achromatic 50:50 splitting ratio. The other chip (referred to as LETI) employed a silica-on silicon (see [Mottier 1997](#)) technique and combined the inputs in an asymmetric directional coupler, which provides two interferometric outputs in phase opposition. Similar to the LEMO beam combiner, calibration signals of the flux variations were extracted with two direct Y -junctions.

Following its expansion to three telescopes, the IOTA array was used to investigate the three-input beam combiner on the Integrated Optics Near-infrared

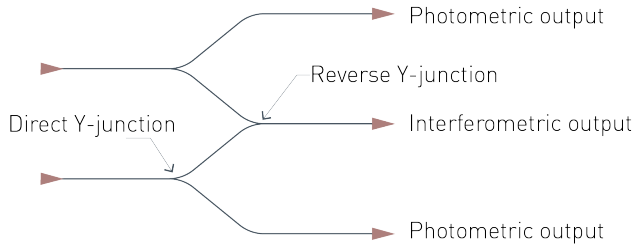


Figure 32: Two-input integrated optics beam combiner. The light from the telescopes is coupled into the photonic chip via polarisation-maintaining single-mode fibres. Two direct Y-junctions provide photometric calibration signals for each chip input, and a reverse Y-junction combines the inputs to produce one interferometric output. Image adapted from Berger et al. (1999).

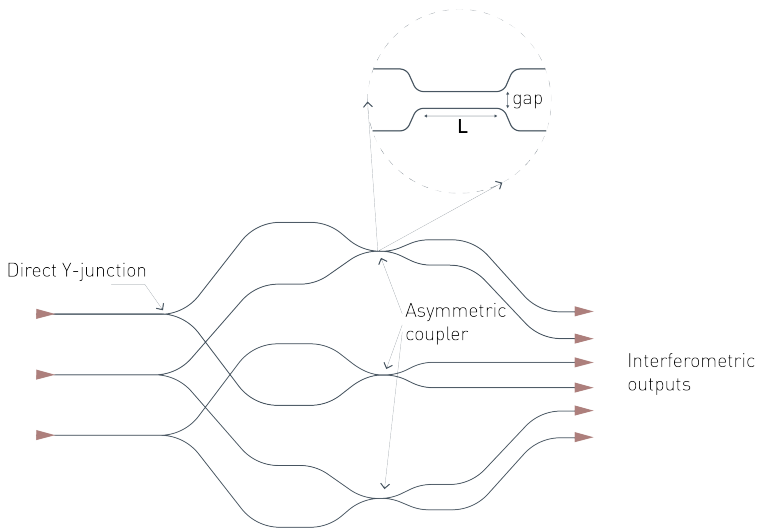


Figure 33: Three-input IONIC beam combiner. Each input is split with a Y-junction, resulting in six waveguides fed into three asymmetric couplers that enable a pairwise combination of the three possible interferometric baselines. With such a combination scheme, the photometry can be calibrated without photometric channels. An asymmetric coupler (shown inset) is realised by bringing two single-mode waveguides in close proximity along a certain interaction length L . If there is light present in both waveguides, they will interfere in the interaction region. This interference can be controlled by careful design of the physical and optical properties of the waveguides, the wavelength, the gap between the waveguides (also referred to as the waveguide separation h), and L . While any splitting ratio can be achieved, typically 50:50 is used to maximise the resulting fringe contrast. In such a coupler, there will be a π phase offset between the two outputs. Image adapted from Berger et al. (2003).

Interferometric Camera (IONIC; Berger et al. 2003, Rousset-Perraut et al. 1999). Figure 33 shows a schematic of the IONIC beam combiner waveguide circuitry, whose inputs are split with Y-junctions, resulting in six waveguides fed into three asymmetric couplers that allow for a pairwise combination of the three possible interferometric baselines. With such a combination scheme, the photometry can be calibrated without photometric channels by computing a photometric matrix (akin to the transfer matrix in Coudé du Foresto, Ridgway & Mariotti 1997). An observation with this silica-on silicon chip measured visibility closure phases of 12 Boötis in the H -band.

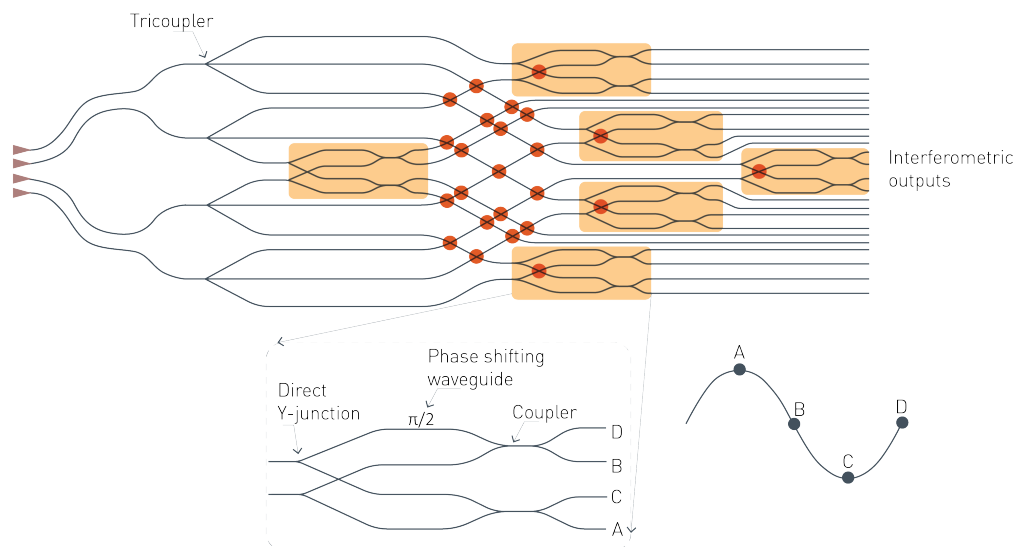


Figure 34: **Top:** Schematic of the 4-input/24-output PIONIER beam combiner waveguide circuitry. For each injected beam, the light propagates through single-mode waveguides and is divided by a succession of tricouplers, Y-junctions, and couplers — which provide two interferometric outputs in phase opposition. A so-called ABCD unit that implements the pairwise combination is highlighted in orange. Waveguide crossings that can introduce cross-talk are marked with a red dot. **Bottom Left:** In one arm of each telescope pair, a phase-shifting waveguide modifies the phase of the propagating beam by $\pi/2$. This means that for each of the six possible interferometric baselines, there are four outputs corresponding to a phase-shift between the two beams of $0, \pi/2, \pi,$ and $3\pi/2$. The phase-shifting function is based on the variation of the effective index (i.e., index encountered by the fundamental mode propagating in the waveguide) with the waveguide diameter. Enlarging one of the two parallel waveguides —of the same physical length— creates a difference in the effective index and leads to an optical path difference between them. By recording the four phase states, one can retrieve the visibility amplitude and phase via the ABCD method described in Colavita (1999). **Bottom Right:** Representation of the four relative phases achieved in the four outputs. Image adapted from Benisty et al. (2009).

The successful on-sky demonstrations of the different photonic chips at the IOTA array established that integrated optics had sufficient maturity to provide

efficient and reliable H -band beam combiners, which was further validated by the characterisation of a four-input chip. Here, [Benisty et al. \(2009\)](#) obtained a throughput of $\sim 65\%$ and an instrumental contrast $\geq 80\%$ (in the $1.54 - 1.66\mu\text{m}$ range). This silica-on silicon chip was later deployed in PIONIER ([Le Bouquin et al. 2011](#)) – a visitor instrument for the VLTI. Figure 34 shows a schematic of the PIONIER waveguide circuitry, where four tricouplers split the input light across 12 waveguides that are mixed pairwise by so-called ABCD units (highlighted in orange). The four outputs of each ABCD unit deliver four phase states in quadrature ($0, \pi/2, \pi,$ and $3\pi/2$) of one of the six possible interferometric baselines. By recording the four phase states (see bottom right of Fig. 34), one can retrieve the visibility amplitude and phase with the ABCD method described in [Colavita \(1999\)](#). PIONIER adopted the imaging module from IONIC, which facilitates the measurements of six visibilities and three independent closure phases with low ($R \sim 40$) spectral resolution. The instrument laid the foundations for the Multi AperTure mid-Infrared SpectroScopic Experiment (MATISSE; [Lopez et al. 2022](#)) and GRAVITY by enabling four-telescope operation of the VLTI’s UTs or ATs.

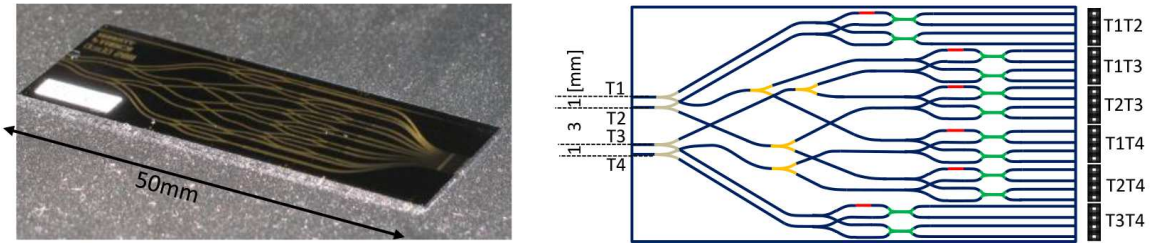


Figure 35: **Left:** Four-telescope integrated optics beam combiner of GRAVITY that is designed to exploit the four VLTI UTs or ATs in the K -band. This $50\text{-mm} \times 20\text{-mm}$ photonic chip was fabricated with a silica-on-silicon technique by CEA-LETI. **Right:** Schematic of the 4-input/24-output GRAVITY beam combiner waveguide circuitry. For each injected beam, the light propagates through single-mode waveguides (shown in blue) and is divided by a succession of Y-junctions (in grey and yellow) and couplers (in green) – which provide two interferometric outputs in phase opposition. In one arm of each telescope pair (T1 & T2, T1 & T3, T2 & T3, T1 & T4, T2 & T4, T3 & T4), a phase-shifting device (in red) modifies the phase of the propagating beam by $\pi/2$. This means that for each of the six possible interferometric baselines, there are four outputs corresponding to a phase-shift between the two beams of $0, \pi/2, \pi,$ and $3\pi/2$. The phase-shifting function is based on the variation of the effective index (i.e., index encountered by the fundamental mode propagating in the waveguide) with the waveguide diameter. Enlarging one of the two parallel waveguides – of the same physical length – creates a difference in the effective index and leads to an optical path difference between them. By recording the four phase states, one can retrieve the visibility amplitude and phase via the ABCD method described in [Colavita \(1999\)](#). In practice, the departure from ideal quadrature means that the so-called pixel-to-visibility matrix (P2VM; [Tatulli et al. 2007](#)), which enables one to estimate the complex visibility from the interference fringes recorded on the detector, is generally used. A calibration of the instrument provides the visibility-to-pixel (V2PM) matrix, whose inversion yields the P2VM matrix. Image from [Perraut et al. \(2018\)](#).

GRAVITY is equipped with two identical *K*-band beam combiners (see Perraut et al. 2018): one for fringe tracking (see Lacour et al. 2019) and the other for scientific observations. The left panel of Fig. 35 shows the 50-mm \times 20-mm GRAVITY photonic chip that is fabricated with a silica-on silicon technique. Light is injected into the chip via four fluoride fibres —manufactured by Le Verre Fluoré— with a numerical aperture (0.2 ± 0.02) and core diameter ($6.5 \mu\text{m}$) that makes them ideal for single-mode operation at wavelengths $> 1.88 \mu\text{m}$. Each input is split with direct *Y*-junctions (highlighted grey in the right panel of Fig. 35), which was a departure from the tricouplers employed on PIONIER. The optical design of the chip was also revised by shortening the length of the phase shifting waveguides (highlighted red) that were not fully achromatic in PIONIER. Furthermore, an increase in the index contrast between the core/outer layers enhanced light confinement and enabled the use of a stronger waveguide curvature. These optimisations reduced the length of the beam combiner (PIONIER chip measures 80-mm \times 8-mm), and thus the propagation losses. Compared to PIONIER, the GRAVITY chip features fewer waveguide crossings that can introduce cross-talk (see PIONIER waveguide crossings marked with a red dot in Fig. 34). Perraut et al. (2018) measured a cross-talk flux of less than 0.3% for GRAVITY, whereas Benisty et al. (2009) estimated it to be below $1.2\% \pm 0.4\%$ for PIONIER.

Design requirements (i.e., throughput $> 55\%$ and an instrumental contrast $> 95\%$ in polarised light) for the GRAVITY chip were derived from its primary science case, which was to accurately measure the dynamical processes around the supermassive black hole Sagittarius *A** (Genzel et al. 2010, GRAVITY Collaboration et al. 2018). Indeed, the instrument has delivered groundbreaking results in many different science areas with its classical ABCD beam combiner approach. This ABCD principle is adapted on the 6-input/60-output Stellar Parameters and Images with a Cophased Array (SPICA; Pannetier et al. 2022) fringe tracking chip that measures 82-mm \times 35-mm, has a throughput $> 60\%$, and an instrumental contrast $> 95\%$ for polarised light in the *H*-band.

Pairwise beam combining photonics is also implemented on the GLINT nuller, which is based on the heritage of an integrated pupil-remapping interferometer known as Dragonfly (Jovanovic et al. 2012). The first iteration of GLINT was a 2-input/4-output borosilicate glass (Schott AF-45) chip of 41-mm \times 10-mm \times 0.7-mm (length \times width \times height). Light from two sub-apertures —separated by a 5.5-m baseline— of the Subaru Telescope was injected into $10.75 \mu\text{m}$ single-mode waveguides within the chip. These waveguides were inscribed with the Ultrafast Laser Inscription (ULI) method which uses a femtosecond pulsed laser to create a positive refractive index change inside the medium. *Y*-junctions split

each input with $\sim 33\%$ of the light directed to a photometric output. A 50:50 directional coupler introduced a $\pi/2$ phase shift to produce one nulled and one bright output. Norris et al. (2020) measured a transmission of $86 \pm 1\%$ and waveguide propagation losses of $0.14 \pm 0.04\text{dB/cm}$ at $1.55\mu\text{m}$. An earlier prototype (GLINT South; Lagadec et al. 2018) of the two-input GLINT nuller was deployed on the 3.9-m Anglo-Australian Telescope.

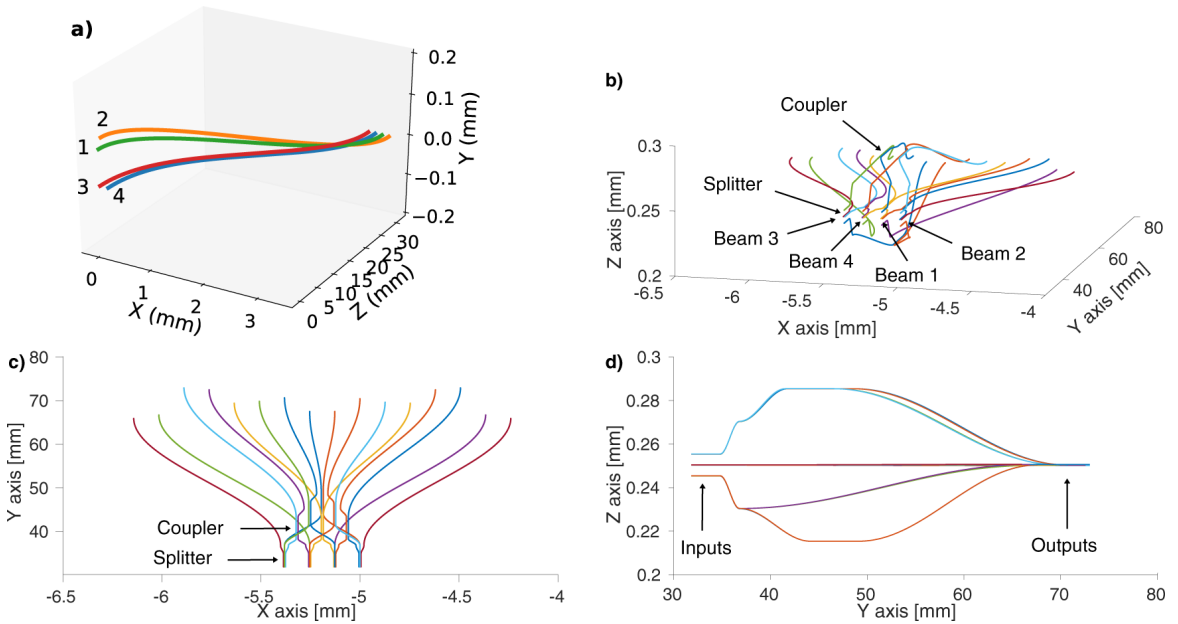


Figure 36: Schematics of the GLINT photonic nuller waveguide circuitry. This 4-input/16-output chip, which operates at $\sim 1.55\mu\text{m}$, is integrated into SCE_xAO at the Subaru Telescope and measures $75\text{-mm} \times 3.5\text{-mm} \times 2\text{-mm}$ (length \times width \times height). The single-mode waveguides are inscribed in a borosilicate glass (Schott AF-45) chip with the Ultrafast Laser Inscription (ULI) method. **a)** The chip inputs on the left of the figure are transformed from a 2D configuration —that matches the pupil sampling pattern— to a 1D configuration at the outputs on the right. All the waveguides have the same optical path length with input one shown in green, input two in orange, input three in red, and input four in blue. **b)** Perspective view of the chip waveguide circuitry. **c)** Plan view of the chip waveguide circuitry. Light injected into the 4 inputs (shown at the bottom of the figure) is divided by a succession of Y-junctions and couplers, resulting in 16 interferometric outputs: six outputs corresponding to six baselines (i.e., one nulled and one bright output per coupler) and four photometric outputs. **d)** Right-side view of the chip waveguide circuitry. Image from Martinod et al. (2021).

Figure 36c shows a waveguide circuitry schematic of the second version of GLINT, where four inputs (shown at the bottom of the figure) are divided by a succession of Y-junctions and couplers. This results in 16 interferometric outputs: six outputs corresponding to six baselines (i.e., one nulled and one bright output per coupler) and four photometric outputs — that are redirected into a

spectrograph via separate single-mode fibres. [Mennesson et al. \(2006\)](#) exploited the spatial filtering properties of single-mode fibres to improve the instrumental null-depth on the Palomar Fibre Nuller. The spectrally dispersed outputs of the four-input GLINT nuller are projected on a C-RED 2 InGaAs camera, which was an upgrade from the Femto OE-200-IN2 InGaAs-based detector used by [Norris et al. \(2020\)](#) for the two-input. Although both GLINT nullers yielded null-depth accuracies of $\sim 10^{-4}$ (with the aid of the NSC procedure I described in Chapter 2), the deployed Bracewell architecture cannot exploit the benefit of multi-aperture interferometry, which allows for a greater suppression of the on-axis source and the formation of self-calibrating observables.

An advanced approach to nulling interferometry was implemented with an integrated optics four-telescope double Bracewell nuller. This $0.36\text{-mm} \times 50\text{-mm}$ photonic chip featured three evanescent directional couplers, each producing π phase-shifted outputs. To determine the optimal coupler geometry (see inset of Fig. 33 for coupler geometry), [Errmann et al. \(2015\)](#) set the length L of the interaction region at 10-mm, and varied the waveguide separation h —between $17\mu\text{m}$ and $19\mu\text{m}$ —of the various couplers. By measuring their splitting ratios, the best approximation to the ideal 50:50 ratio was found with $h = 18\mu\text{m}$. Imbalance between the outputs was attributed to interference of the output signal with stray light, fabrication defects, and radiation losses in the ULI fabricated silica waveguides. These effects, coupled with phase fluctuations between the four inputs resulted in a null-depth of $\sim 8 \times 10^{-3}$ at $0.633\mu\text{m}$.

A double Bracewell architecture is also employed on a ULI fabricated gallium lanthanum sulphide (GLS) chip for the NOTT project (see [Sanny et al. 2022](#)). GLS is a chalcogenide glass with a wide transparency range ($0.5 - 9\mu\text{m}$), which will enable the NOTT instrument to characterise young giant planets in the L' -band down to the snow line of their host system. Besides Y-junctions and couplers, chalcogenide glass has also been used to fabricate multimode interference (MMI, [Soldano & Pennings 1995](#)) couplers. These ultra-compact photonic devices are widely used for beam splitting and recombining due to their large bandwidth, low insertion loss and high fabrication tolerance. [Kenchington Goldsmith, Cvetojevic, et al. \(2017\)](#) & [Kenchington Goldsmith, Ireland, et al. \(2017\)](#) investigated chalcogenide glass MMIs designed for mid-infrared nulling interferometry, and established that they provide a reasonable achromatic response over a ~ 300 nm bandwidth. Recently, [Cvetojevic et al. \(2022\)](#) experimentally validated the use of a single silicon nitride MMI as a 3-input/3-output kernel-nuller and verified its self-calibrating properties. This device is one of several components integrated on the kernel-nuller photonic chip that I will describe in Sect. 3.

3 Multimode interference coupler

The kernel-nuller photonic chip presented in Fig. 37a contains 12 different kernel-nulling arrangements that are composed of single or multiple MMI couplers. One of these arrangements is a four-input/four-output (4×4) MMI, which I characterised on the kernel test bench (see Chapter 7). To describe how an MMI operates, I will use this 4×4 combiner as an example.

Figure 37c shows the 4×4 MMI that implements the input phase offsets and beam combinations required by the complex matrix $M_{4 \times 4}$ (see Chapter 3). It is composed of identical access waveguides (single-mode) – positioned at the input and output of a central rectangular waveguide referred to as the MMI cavity. Tapers connect the access waveguides to the cavity that allows light to be tightly contained and steered through it. By expanding and contracting adiabatically (i.e., in a gradual way), the tapers minimise mode mismatch losses between the access waveguide mode and the multimode cavity. For the 4×4 MMI, the input tapers expand from $1 \mu\text{m}$ to $4.5 \mu\text{m}$ (in reverse for the outputs) over an $80 \mu\text{m}$ propagation length.

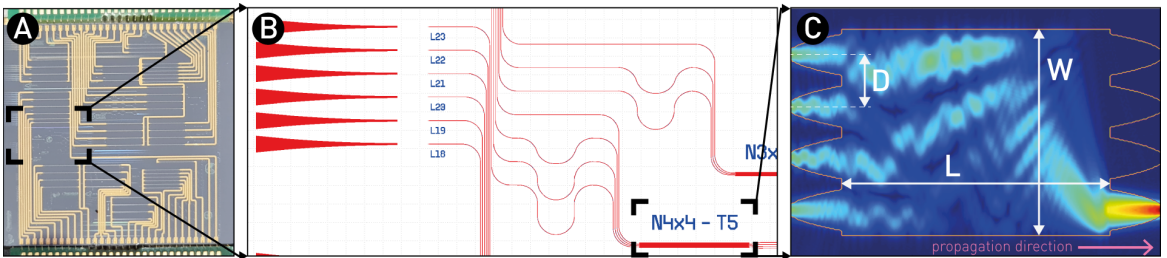


Figure 37: Kernel-nulling interferometry takes place entirely within the $16\text{-mm} \times 16\text{-mm}$ photonic chip shown in (A). The chip was fabricated with photo-lithography in silicon nitride (Si_3N_4), and contains 12 distinct kernel-nulling arrangements that allow us to experimentally validate different methods of routing, phase delays, and beam combination. An additional feature of the chip is active on-chip phase control, which is enabled by the electrodes shown in yellow. These electrodes heat up selected areas of the device, allowing for discrete tuning of the effective refractive indices of the modes travelling therein. Our focus here is on the 4×4 kernel-nuller shown in (B). In the top left of this figure we can see the input waveguide tapers (mode-converters) that efficiently convert the incident mode to the single-mode waveguide core size of $\sim 1 \mu\text{m}$. Output waveguide tapers convert the fundamental mode of the single-mode waveguide to the mode of standard SMF-28e optical fibre cables. The Si_3N_4 platform enables a low-loss, complex routing of the input waveguides into the four-input/four-output (4×4) multimode interference (MMI) coupler shown in (C). In this beam propagation simulation of the 4×4 MMI, light from four single-mode waveguides is launched into the central MMI cavity, which results in three nulled outputs and one bright output via the self-imaging effect.

When light is launched into the input waveguides, it excites multiple higher order modes in the Si_3N_4 cavity of the 4×4 MMI. The self-imaging principle, which

is the basis for MMI coupler operation, reproduces the input field excitation in single or multiple images at periodic lengths along the propagation direction. This phenomenon is based on the propagation properties of a cavity that is designed to support a large number of modes which encounter different effective refractive indices. Each mode propagates at a distinct velocity, acquiring different phases that results in constructive and destructive interference along the multimode cavity. At a particular cavity length, all the modes are in-phase and the total field is the same as the input, yielding the self-imaged condition shown at the bottom right of Fig. 37c. By properly placing the access waveguides, this image can be efficiently coupled into the bright output (where most of the on-axis light is directed), thus producing the desired behavior. Given a suitable interferometric baseline, the off-axis flux will reinforce (constructive interference) in the nulled outputs.

Depending on the length L and width W of the cavity, as well as the access waveguide separation D , different self-imaging arrangements (or a different $\mathbf{M}_{4 \times 4}$) can be obtained. For the MMI used in this work, the main design parameters are; $L = 440 \mu\text{m}$, $W = 20 \mu\text{m}$, and $D = 5 \mu\text{m}$. According to Besse et al. 1994, the optical bandwidth of MMI couplers is inversely proportional to L and to the number of access waveguides N , while the fabrication tolerances are independent of N but are proportional to D . Although the Si_3N_4 platform used for the 4×4 MMI has a high fabrication tolerance, manufacturing imperfections introduce variations from the main design parameters that can drive the multimode cavity away from exact self-imaging, and thus $\mathbf{M}_{4 \times 4}$ would deviate from the expected amplitude and phase values. Moreover, the presence of unavoidable optical losses means that the total output flux of a real MMI is less than the total input flux, and so we must determine $\mathbf{M}_{4 \times 4}$ experimentally (see Chapter 7).

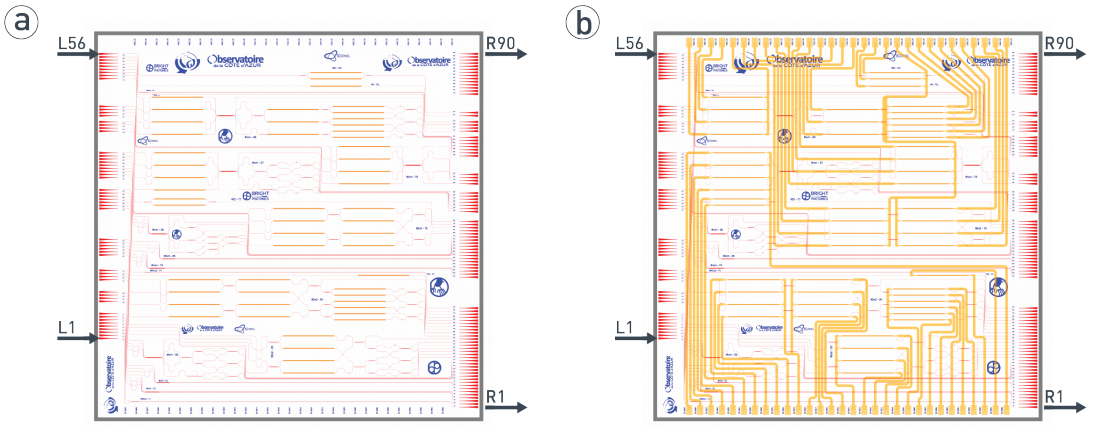


Figure 38: a) Waveguide circuitry of the kernel-nuller photonic chip that was fabricated with photo-lithography in silicon nitride (Si_3N_4). This $16\text{-mm} \times 16\text{-mm}$ chip has 56 inputs (labelled L56 - L1 on the left of the figure) and 90 outputs (labelled R90 - R1 on the right of the figure). b) Thermo-optic phase actuators integrated into the photonic chip can be applied to correct for OPD errors due to manufacturing imperfections or laboratory drift. These phase actuators situated in specific areas of the chip are controlled by electronic channels (the chip consists of 60). By applying a current via these channels, the yellow electrodes shown in the figure heat up, allowing for discrete tuning of the effective refractive indices of the modes travelling therein.

4 Photonic chip components

Figure 38a shows the waveguide circuitry of the kernel-nuller photonic chip that was fabricated with photo-lithography in silicon nitride (Si_3N_4). This Si_3N_4 platform enables a low-loss, complex routing of the waveguides on the $16\text{-mm} \times 16\text{-mm}$ chip. The 56 chip inputs (labelled L56 - L1 on the left of Fig. 38a) each have waveguide tapers (mode-converters) that efficiently convert the incident mode to the single-mode waveguide core size of $\sim 1\mu\text{m}$. At the 90 outputs (labelled R90 - R1 on the right of Fig. 38a), the tapers convert the fundamental mode of the single-mode waveguide to the mode of standard SMF-28e optical fibre cables. Thermo-optic phase actuators –integrated into the photonic chip– can be applied to correct for OPD errors due to manufacturing imperfections or laboratory drift. These phase actuators situated in specific areas of the chip are controlled by electronic channels (the chip consists of 60). By applying a current via the channels, the yellow electrodes shown in Fig. 38b heat up, allowing for discrete tuning of the effective refractive indices of the modes travelling therein.

The 20 different components (see Fig. 39 - Fig. 42) on the kernel-nuller photonic chip are arranged according to the input and output numbering shown

in Fig. 38a & b. Indeed, the most complex of these devices is the 4×7 kernel-nuller design of [Martinache & Ireland \(2018\)](#). However, one can detect that this solution requires fewer couplers and splitters than an ABCD combiner with the same number of inputs (see Fig. 34 and Fig. 35). Some of the 4×7 combiners (see Fig. 39e, Fig. 40g & Fig. 41o) include phase actuators on most of the waveguides, which would allow for the active reconfiguration of the nuller response matrix. Fig. 39e and Fig. 41o are two different implementations of the first and second stage of the 4×7 design. The smaller couplers used in the latter are less chromatic, which suggests a deeper broadband null.

Indeed, a simplified architecture is realised with the 4×4 solutions. Considering that these nullers can only produce one kernel-null, an interesting investigation would be to determine if the other kernel-nulls can be produced by tuning the phase actuators (see Fig. 39f & Fig. 40i). If this internal modulation can be implemented rapidly, it would also mean that the frequency of planetary signals can be much higher.

Future iterations of adaptive kernel-nullers can compensate for imbalances in the amplitude and phase by spectrally dispersing the light of each input into a number of wavelength channels with arrayed waveguide gratings (AWGs). Each channel will include a Mach-Zehnder interferometer (i.e., Fig. 39a) to control the amplitude and a phase shifter (i.e., Fig. 39b) to tune the phase. The channels would then be recombined into a single waveguide by another AWG before being fed into the nuller (see [Jovanovic et al. 2022](#) for photonic spectral shaper architecture).

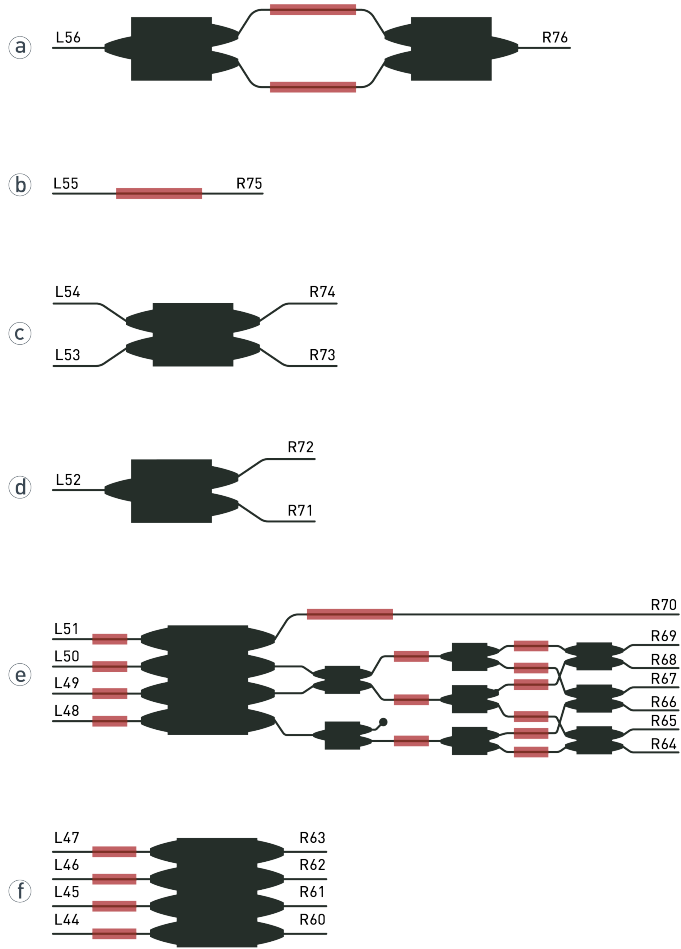


Figure 39: Kernel-nuller photonic chip components. **a)** Mach-Zehnder interferometer. This device is made up of a 1×2 MMI, and a 2×1 MMI. **b)** Phase-shifter. **c)** 2×2 MMI. **d)** 1×2 MMI. **e)** 4×7 kernel-nuller. This device is made up of a 4×4 MMI, four 1×2 MMIs, and four 2×2 MMIs. **f)** 4×4 MMI. For each device, the numbering on the left indicates the chip input port and the right denotes an output. Thermo-optic phase actuators integrated into *a*, *b*, *e* and *f* are highlighted red. The phase actuators modify the refractive index of the waveguide through a change in temperature induced by a small electrical charge.

5 kernel-nulling for the direct detection of exoplanets

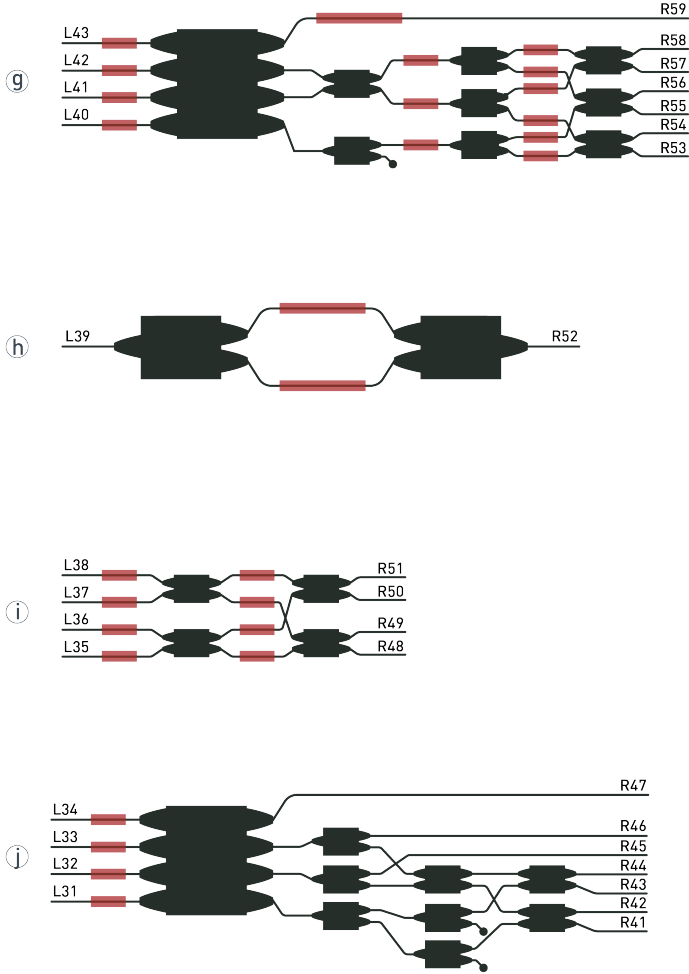


Figure 40: Kernel-nuller photonic chip components. **g)** 4×7 kernel-nuller. This device is made up of a 4×4 MMI, four 1×2 MMIs, and four 2×2 MMIs. **h)** Mach-Zehnder interferometer. This device is made up of a 1×2 MMI, and a 2×1 MMI. **i)** 4×4 kernel-nuller. This device is made up of four 2×2 MMIs. **j)** 4×7 kernel-nuller. This device is made up of a 4×4 MMI, four 1×2 MMIs, and three 2×2 MMIs. For each device, the numbering on the left indicates the chip input port and the right denotes an output. Thermo-optic phase actuators integrated into the respective devices are highlighted red. The phase actuators modify the refractive index of the waveguide through a change in temperature induced by a small electrical charge.

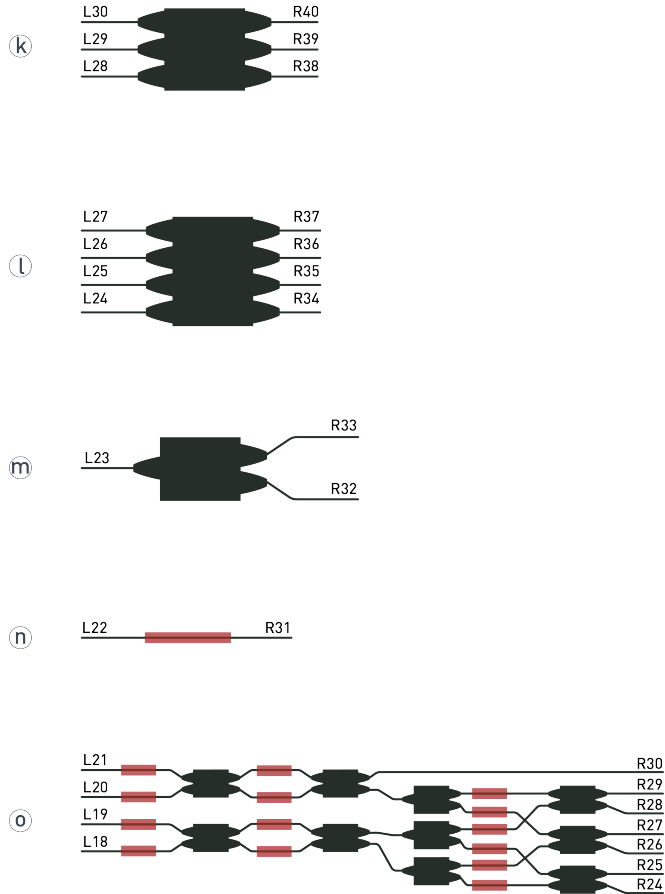


Figure 41: Kernel-nuller photonic chip components. **k)** 3×3 MMI. **l)** 4×4 MMI. **m)** 1×2 MMI. **n)** Phase-shifter. **o)** 4×7 kernel-nuller. This device is made up of three 1×2 MMIs and seven 2×2 MMIs. For each device, the numbering on the left indicates the chip input port and the right denotes an output. Thermo-optic phase actuators integrated into *n* and *o* are highlighted red. The phase actuators modify the refractive index of the waveguide through a change in temperature induced by a small electrical charge.

5 kernel-nulling for the direct detection of exoplanets

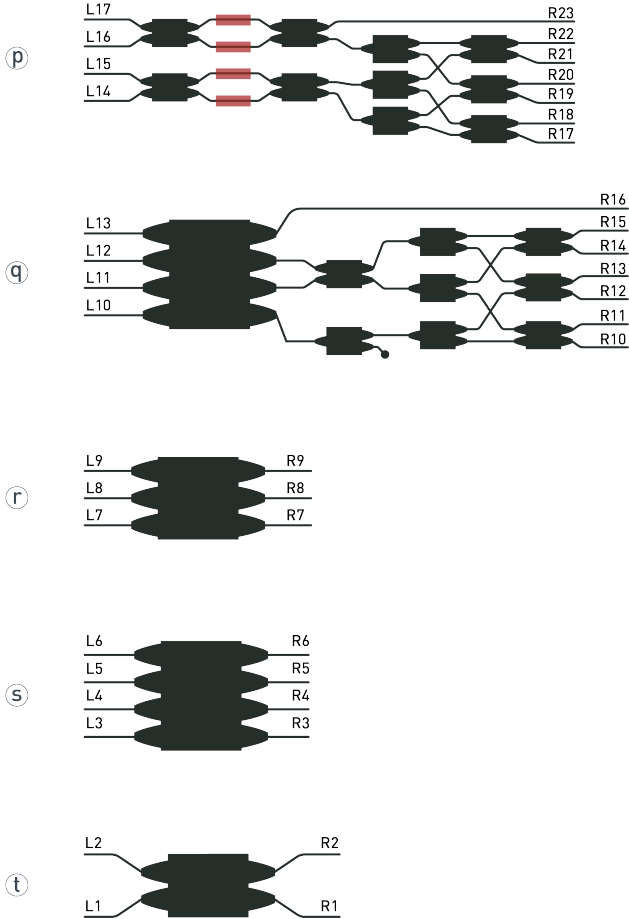


Figure 42: Kernel-nuller photonic chip components. **p)** 4×7 kernel-nuller. This device is made up of three 1×2 MMIs and seven 2×2 MMIs. Thermo-optic phase actuators integrated into the device are highlighted red. The phase actuators modify the refractive index of the waveguide through a change in temperature induced by a small electrical charge. **q)** 4×7 kernel-nuller. This device is made up of a 4×4 MMI, four 1×2 MMIs, and three 2×2 MMIs. **r)** 3×3 MMI. **s)** 4×4 MMI. **t)** 2×2 MMI. For each device, the numbering on the left indicates the chip input port and the right denotes an output.

5 Summary

Over the past few decades, the application of photonics to astronomy (or astrophotonics) has emerged as a technology for astronomical instrumentation, providing waveguiding components that direct, shape, and manipulate the light from telescopes. Indeed, photonics has primarily been driven by the telecommunications industry, and the overwhelming majority of these fibre or chip based components are optimised for operations in the optical communication bands. However, as these wavelengths overlap with the astronomical near-infrared, numerous astrophotonic devices that overcome the deficiencies of conventional bulk optics instrumentation have been developed.

Single-mode waveguides support one spatial mode, which means that the output of the device does not evolve with time or with input beam fluctuations, making them extremely stable. These spatial filtering properties are exploited with photonic crystal fibres and fibre bundle IFUs, which are sometimes used in combination with a microlens array owing to the difficulty in coupling light into the waveguide. Although extreme AO can mitigate coupling losses, modal conversion with photonic lanterns can relax the AO constraints while preserving a high throughput.

FLUOR pioneered the use of single-mode fibres with interferometric beam combiners. Here, three *X*-couplers and two dispersion compensating fibre segments were implemented to simultaneously obtain the interferometric signal and the photometric channels for calibration. The *X*-couplers were made by bringing two fibre cores in close proximity without contact so that the evanescent fields of the mode (the part of the electric field that extends outside the core) interact. If there is light in only one input fibre (or waveguide), then an *X*-coupler will act as a *Y*-coupler. Instruments such as MIRC (at CHARA) and AMBER (at the VLTI) have been based on the heritage of FLUOR.

Interferometric beam combiners can also be made of a photonic integrated circuit, where several functions (i.e., routing, beam splitting, and recombination) are performed in a single component. PIC-based beam combiners exhibit a superior thermo-mechanical stability than their fibre optic counterparts owing to the shorter waveguides embedded on a microchip. Because the devices are robust to external parameters such as temperature and pressure, a cryostat implementation that reduces thermal emission is possible. PIC beam combiners have been successfully implemented with PIONIER and GRAVITY at the VLTI.

Beam splitting and recombination can also be integrated into a single component known as an MMI. Rather than using a classical pairwise combination,

the multiple MMI inputs are allowed to interfere in a planar multimode waveguide section. By varying specific parameters of the device, the required intensity profile at its output can be produced. The kernel-nuller photonic chip contains 12 different kernel-nulling arrangements that are composed of single or multiple MMI couplers. One of these is a four-input/four-output (4×4) MMI, which I characterised on the kernel test bench (see Chapter 7) that integrates various photonic components such as single-mode fibres, a photonic crystal fibre, and a microlens array.

Chapter 6

Kernel test bench

In the previous chapters I have established the challenging nature of direct imaging and shown how ground-based long baseline interferometry can be complementary to other observation techniques in taking images of faint off-axis companions at very small angular separations. Indeed, I propose to search for young giant planets around nearby stars in well known young moving groups and associations with kernel-nulling interferometry. Thanks to a combination of single-mode fibres which provide spatial filtering properties, and photonic integrated circuits whose advantage over bulk-optics is stability and compactness, it is possible to experimentally demonstrate kernel-nulling. Here, I describe the kernel test bench that aids this endeavour, and present the spectrograph that I designed and integrated on this setup.

1 Experimental setup

Figure 43 shows the kernel test bench (located at the Lagrange Laboratory in Nice) that has been designed for the spectral characterisation of the kernel-nuller photonic chip presented in Chapter 5. Nulling interferometry is very sensitive to intensity, phase and polarisation mismatches between the beams to be combined, which is why the bench is installed in an ISO-7 (also known as class 10,000) clean-room — maintained at a temperature of $\sim 22^\circ\text{C}$, a relative humidity of $\sim 49\%$ and an air pressure of $\sim 44\text{ Pa}$. ISO-7 is one of the most common clean-room classes with particles smaller than $0.5\mu\text{m}$ in diameter not taken into consideration. The concentration of particles of size $\geq 0.5\mu\text{m}$ should be no more than 352,000 per m^3 . For particles $\geq 1\mu\text{m}$: 83,200 or lower, and for particles $\geq 5\mu\text{m}$: 2,930 or lower. Air cleanliness is achieved by passing the air through filters and the more often it passes through these filters, the fewer particles are left in the room.

Typically, an ISO-7 clean-room maintains 60-150 air changes per hour with a ceiling coverage of 15-25%, however, these air changes can lead to a drift in the alignment of the optical elements. According to [Chazelas et al. \(2006\)](#), in the

presence of instrumental drifts, the power spectral density of the null-depth has a so-called $1/f$ component, where f is the frequency. This means that the longer the time interval between instrument calibrations, the more noise there is at low frequency. During the experimental validation of a 3-input/3-output kernel-nuller, [Cvetojevic et al. \(2022\)](#) reported a drift that affected the translation stage holding the photonic chip. Here, a drift of up to 1 mrad from the central tip/tilt position of each chip input was measured over a 24 hour period. To overcome this drift, I applied an injection optimisation routine (see Sect. 2) and re-calibrated the instrument before any new set of measurements were taken.

Apart from the environmental conditions of the laboratory, the alignment of the optics can also be affected by floor vibrations that might arise from foot and vehicle traffic or building reverberations. The optics designed for complex interferometric applications such as kernel-nulling require sub-micron precision (a fraction of a wavelength), so much so that even small deviations in the arrangement of the elements might lead to futile data measurements. A vibration control platform (or optical table) is used to absorb such perturbations with minimum deflection, providing long-term stability in the alignment that is needed. For the kernel test bench, we employ a Newport RS 4000 optical tabletop featuring six tunable mass dampers that reduce the dynamic response of the table. The frequency of the dampers, which ranges from 25 to 525 Hz, is tuned to the frequencies of table resonances so that when these frequencies are excited, the dampers will resonate out of phase with the structural motion. This tabletop sits on four Newport S-2000 optical table supports that use pneumatic vibration isolators to reduce the ability of floor vibrations to cause vibrations in the tabletop. The height of these supports can be adjusted to compensate for uneven floors, thus allowing for a flat table surface.

The optical tabletop is made of 4.8-mm thick top and bottom sheets of steel, separated by a steel honeycomb core structure. This steel construction not only provides the required mechanical stability but also the thermal stability. Steel components expand and contract similarly, maintaining flatness during changes in temperature, which can be induced by localised heat sources such as a laser. Indeed, a Fianium WhiteLase Micro Supercontinuum laser is mounted on the tabletop shown in Fig. 43, however, this ultra-compact unit includes an integrated air cooling system that removes any excess heat. With a total output power of more than 0.2 W, the WhiteLase Micro generates light with a broad optical bandwidth ($0.4 \mu\text{m}$ to $2.2 \mu\text{m}$) in a photonic crystal fibre (PCF) by a process known as supercontinuum generation, which was first observed in the 1970s by [Alfano & Shapiro \(1970a\)](#) & [Alfano & Shapiro \(1970b\)](#). The pulsed picosecond oscillator driving the

6 kernel-nulling for the direct detection of exoplanets

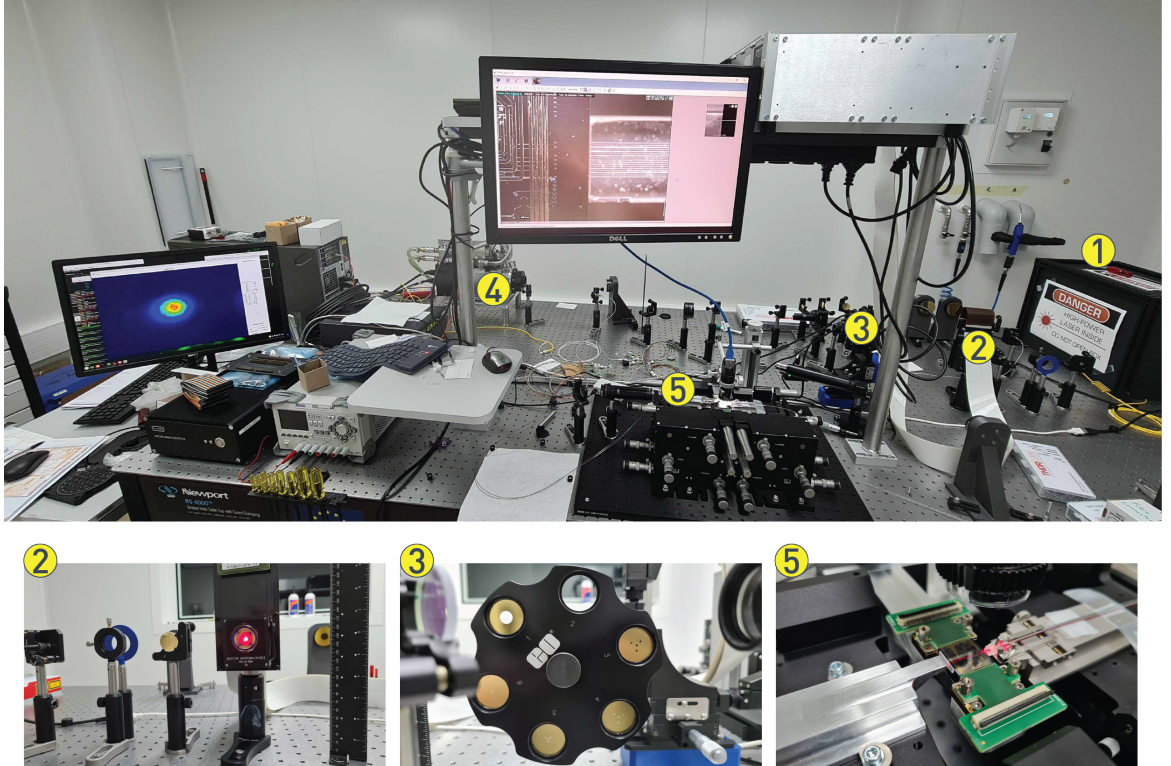


Figure 43: Kernel test bench located at the Lagrange Laboratory in Nice. 1) Calibration source box. Inside this box, light from the supercontinuum source is collimated with a fibre collimator. A computer controlled filter wheel housing several neutral density (ND) and bandpass filters is placed in the collimated beam. An ND filter is used to adjust the total flux output, which can be orders of magnitude too high for the detector. A bandpass filter transmits a well-defined wavelength band of light, while rejecting other unwanted radiation. Following the filter wheel, the beam is then re-injected into a single-mode photonic crystal fibre (PCF) that injects light into the bench. Owing to the spatial filtering properties of PCFs, any wavefront aberration induced by the filters is not transmitted into the bench. The Fianium WhiteLase Micro Supercontinuum laser (not shown) is located next to the calibration source box. 2) Boston Micromachines Hex-507 deformable mirror. 3) Mask wheel. 4) 320×256 pixel fast readout C-RED One camera. 5) A pair of high-precision Nanomax 6-axis flexure stages are used to align the microlens array and the output fibre array to the kernel-nuller photonic chip, which itself is on a 3-axis precision translation stage.

supercontinuum runs at a fixed repetition rate of 20 MHz, making it suitable for steady-state or lifetime measurements. However, owing to the spectral broadening processes involved, PCF supercontinuum sources experience fluctuations both in intensity (see [Corwin et al. 2003](#)), and in the arrival time (and thus relative phase) of different spectral components (see [Dudley & Coen 2002](#)). To mitigate this noise that can limit resolution or precision, I generally applied a warm-up time of ~ 1 hour.

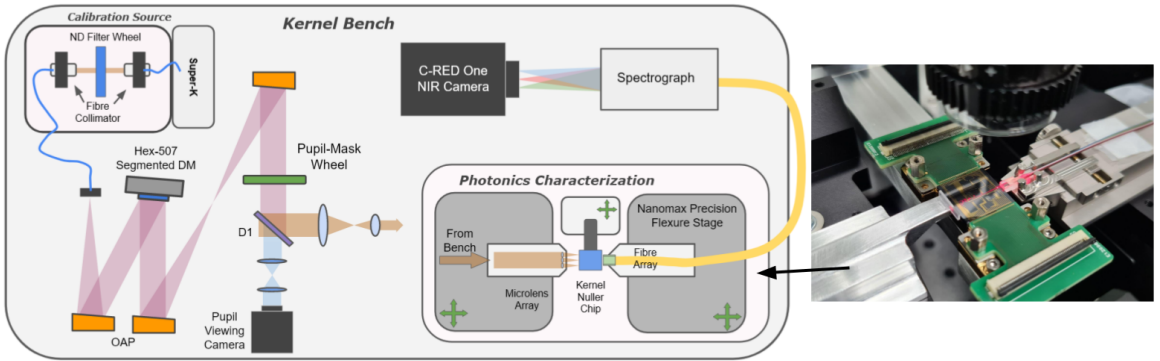


Figure 44: Schematic of the kernel test bench (shown in Fig. 43) that is used to spectrally characterise the kernel-nuller photonic chip (shown in right image).

Broadband light from the supercontinuum source is collimated with a fibre collimator (see calibration source box in Fig. 44). A computer controlled filter wheel housing several neutral density (ND) and bandpass filters is placed in the collimated beam. An ND filter is used to adjust the total flux output, which can be orders of magnitude too high for the detector. A bandpass filter transmits a well-defined wavelength band of light, while rejecting other unwanted radiation. Following the filter wheel, the beam is then re-injected into a single-mode PCF that injects light into the bench. A PCF allows for a much stronger mode confinement than conventional optical fibres, and owing to its spatial filtering properties, any wavefront aberration induced by the filters is not transmitted into the bench.

An off-axis parabolic mirror (OAP) reflects the beam onto the Boston Micro-machines Hex-507 deformable mirror (DM) shown in Fig. 43. The DM divides the beam into 169 hexagonal segments, each of which has individual tip-tilt (± 3 mrad) and piston ($\pm 2\mu\text{m}$) control with a modulation speed > 25 kHz. Tip-tilt is used to optimise the injection of the light into the chip input waveguides, which I describe with the optimisation routine in Sect. 2. Co-phasing is executed with the piston, and this is demonstrated when locating the set-point of the device (see Sect. 2).

Following the DM, the beam is reflected via a set of OAPs onto a mask wheel (see Fig. 43) that hosts numerous masks including a brass laser-cut mask consisting of four $620\ \mu\text{m}$ sized holes (commensurate with the four-input MMI presented in Chapter 5). This mask, which forms the primary pupil for the setup, blocks all but four active DM segments thus preventing unwanted light from entering the photonic chip and propagating through to the outputs. Stepper actuators are used to align these holes with the active DM segments, and this is monitored in real-time with the pupil viewing camera at visible wavelengths.

Immediately following the mask, a dichroic beam-splitter transmits the visible light ($< 1\ \mu\text{m}$) and reflects the near-infrared ($> 1\ \mu\text{m}$). A set of achromatic doublet lenses demagnify and re-image the pupil on the pupil viewing camera in the transmitted beam path. In the reflected path, the pupil from the bench is re-imaged onto a microlens array (MLA) via a pair of near-infrared achromatic doublets that reduce the mask-hole size from $620\ \mu\text{m}$ to $\sim 124\ \mu\text{m}$, matching the spacing and mode size of the chip input waveguides. It is noteworthy to mention that a linear polarizer is implemented between the DM and the chip inputs.

The MLA is aligned so that each of the four mask-holes overlap a single MLA lenslet of $127\ \mu\text{m}$ diameter. Four focal spots are formed at the chip inputs by the MLA, and the chip is translated so that the light is injected into the corresponding input waveguides. The light propagates through the chip towards the output waveguides where a fibre array is aligned, coupling the light into separate SMF-28e optical fibres and redirected to the spectrograph that I will describe in Sect. 3. Figure 43 shows the pair of high-precision Nanomax 6-axis flexure stages that are used to align the MLA and the output fibre array to the photonic chip, which itself is on a 3-axis precision translation stage. For each output, the dispersed light is binned into seventeen equally spaced spectral channels spanning the $1.4 - 1.6\ \mu\text{m}$ band-pass on a 320×256 pixel fast readout (C-RED One) camera. The 4-pixel spectral binning corresponds to a resolution of $9.5\ \text{nm}$.

2 Injection optimisation and phase set-point

Despite the sub-micron precision in the alignment of the experimental setup described in Sect. 1, it is pretty much impossible to perfectly align the chip inputs by hand. Therefore, prior to every experimental cycle, I performed an injection optimisation routine with the DM to find the optimal coupling location of the input waveguides. The DM scans (tip/tilt) each input of the four-input MMI presented in Chapter 5 over a ± 3 mrad range in increments of 0.2 mrad, and the output intensity is measured at the $1.55\ \mu\text{m}$ spectral channel. After the scan is

complete, a 2D Gaussian fit locates the central tip and tilt position for each input, which corresponds with the peak intensity measured at the outputs. Figure 45 shows a typical result of this optimisation routine.

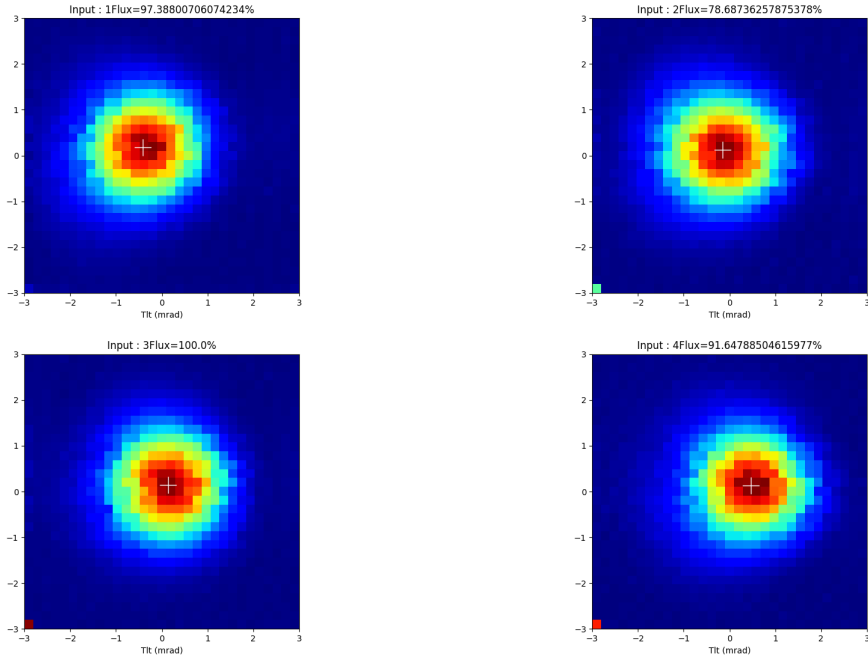


Figure 45: Optimal coupling location of the input waveguides of the four-input/four-output MMI. This injection optimisation routine is performed prior to every experimental cycle in order to compensate for misalignment in the experimental setup. The DM scans (tip/tilt) each input over a ± 3 mrad range in increments of 0.2 mrad, and the output intensity is measured at the $1.55 \mu\text{m}$ spectral channel. After the scan is complete, a 2D Gaussian fit locates the central tip and tilt position for each input, which corresponds with the peak intensity measured at the outputs.

Optical path differences (OPDs) between the four input beams will have an effect on the response of the device. These OPDs can be ascribed to physical path length differences through the setup, either internal or external to the MMI. Pennings et al. (1994) found that reflection, which is brought about by phase mismatch between inputs or internal resonance modes due to the occurrence of simultaneous self-images, can be significant even for MMI couplers with optimum transmission. The back reflection of the images into the access waveguides can thus lead to different optical path lengths. External to the device, OPD might arise in the alignment of the MLA with the photonic chip. Although some level of mismatch is inevitable, we can compensate for optical delays by locating the phase set-point that will bring the device as close as possible to a zero OPD state.

The set-point procedure I employ for the four-input/four-output MMI is similar to the OPD zeroing performed by [Cvetojevic et al. \(2022\)](#), although that was for a 2D parameter space. Here, it consists of OPD scans with the upstream DM where a ± 500 nm mechanical stroke (which translates into a ± 1000 nm OPD modulation) is simultaneously applied on input 2, 3 & 4 in increments of 50 nm. Input 1 is used as a reference and therefore left unmoved. At each DM step, the intensity on all four outputs is recorded at the $1.55 \mu\text{m}$ spectral channel. The data from the nulled outputs is merged into a 3D data cube (see right of Fig. 46) for a quick analysis that determines the DM command values that reproduce the specified design of the device shown in Fig. 37c. As the response of the MMI is wavelength periodic, increasing the DM stroke will locate multiple set-points that produce the same behaviour (minimum flux in the nulled outputs and a maximum in the bright). I utilise a higher resolution scan (DM step = 5 nm, DM range = ± 50 nm) to better constrain the final OPD offsets {input one: 0 nm, input two: +680 nm, input three: -440 nm, input four: +150 nm} that are used as a zero-point for all measurements.

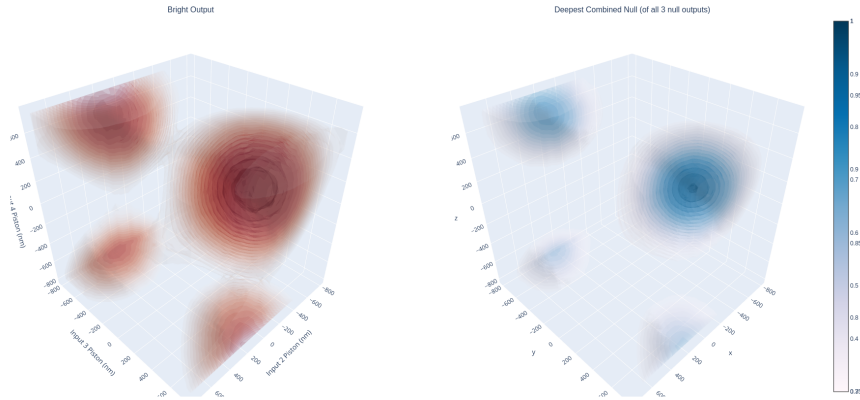


Figure 46: Four-input/four-output MMI phase set-point 3D data cubes. This set-point procedure consists of OPD scans with a deformable mirror (DM), where a ± 500 nm mechanical stroke is simultaneously applied on input 2, 3 & 4 of the MMI in increments of 50 nm. Input 1 is used as a reference and therefore left unmoved. At each DM step, the intensity on all four outputs is recorded at the $1.55 \mu\text{m}$ spectral channel, and the data from the nulled outputs is merged into the 3D data cube shown in the right figure (input 2:x-axis, input 3:y-axis, input 4:z-axis). From this, the piston values that produce the deepest null in these outputs are located simultaneously, and are coincident with the maximum intensity recorded in the bright output (see left figure). A higher resolution scan (step = 5 nm, range = ± 50 nm) is initiated from the primary piston values to better constrain the final OPD offsets {input one: 0 nm, input two: +680 nm, input three: -440 nm, input four: +150 nm} that are used as a zero-point for all measurements.

3 Spectrograph

I designed and built a multi-waveguide prism spectrograph tailored for the spectral characterisation of the kernel-nuller photonic chip presented in Chapter 5. The spectral range of interest ($1.2 - 1.8\mu\text{m}$) was initially defined by the operating wavelength range of the optical fibres that inject light into the spectrograph and the design central wavelength of the chip. However, designing a spectrograph is a non-linear process even though it may begin linearly. Indeed, one requires prior knowledge of the problem to be solved, including the reasoning behind the trade-offs in instrument design, which I attempt to clarify here. The reality is that after each step, it is likely that there will be some mismatch with constraints or goals. Perhaps resolution will be too low, read-out noise too high, or perhaps cost might be excessive. One then loops back to adjust some constraints in light of others. It is this dynamic back and forth among goals, parameters, and design that makes a recipe for spectrograph design impossible, or at least unnecessarily confining. In the following section, I present the optical elements of the spectrograph including their parameters that determine the final result ($\Delta\lambda = 9.5\text{ nm}$, $\lambda = 1.2 - 1.75\mu\text{m}$). Spot diagrams are used to evaluate the performance of the various elements, whose assembly is modelled with the aid of CAD design before integration and calibration on the kernel test bench.

3.1 Optical elements

Figure 47 shows a schematic diagram of the spectrograph whose basic principle is the following: the outputs of the photonic chip are coupled into SMF-28e optical fibre cables with a wavelength range of $1.26 - 1.625\mu\text{m}$. These fibres are single-mode approximately $0.05\mu\text{m}$ below to $0.2\mu\text{m}$ above the specified operating wavelength. They are individually placed on a V-grooved substrate with a pitch spacing of $127\mu\text{m}$, and are usually fixed into the grooves with epoxy and pressed by a glass cover. The mode field diameter (MFD), which is the diameter of the beam profile on exiting a single-mode fibre, is determined by the numerical aperture (i.e., measure of the light-gathering ability of an optical fibre) and cut-off wavelength ($< 1.26\mu\text{m}$). SMF-28e optical fibres operated above cut-off have a numerical aperture $NA = 0.14$, and at $1.55\mu\text{m}$, which is the design central wavelength of the kernel-nuller photonic chip, an MFD of $10.4 \pm 0.5\mu\text{m}$.

The so-called V-groove array that is mounted on a fibre holder directs the light towards a 2-inch near-infrared achromatic doublet lens of focal length L_C . Achromatic doublets are suitable for controlling chromatic aberrations and commonly used to achieve a diffraction-limited spot when using a monochromatic source.

6 kernel-nulling for the direct detection of exoplanets

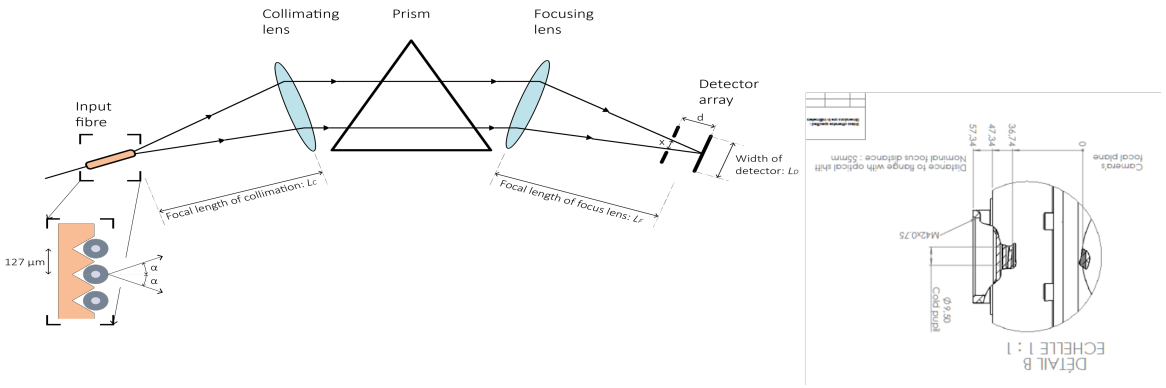


Figure 47: Schematic of a prism spectrograph. The outputs of the photonic chip are coupled into SMF-28e optical fibre cables individually placed on a V-grooved substrate with a pitch spacing of $127\ \mu\text{m}$. These fibre cables are usually fixed into the grooves with epoxy and pressed by a glass cover. Light emerges from the so-called V-groove array that is mounted on a fibre holder onto a collimating lens of focal length L_c . The collimated light is incident on an equilateral prism that disperses the light in the $1.2 - 1.8\ \mu\text{m}$ spectral range of interest. A focusing lens directs the dispersed light through the cold pupil ($x = 9.5\text{-mm}$ diameter) of a detector located at a focal length L_f . This length includes the flange focal distance d , which is shown in the image on the right for the 320×256 pixel fast readout C-RED One camera.

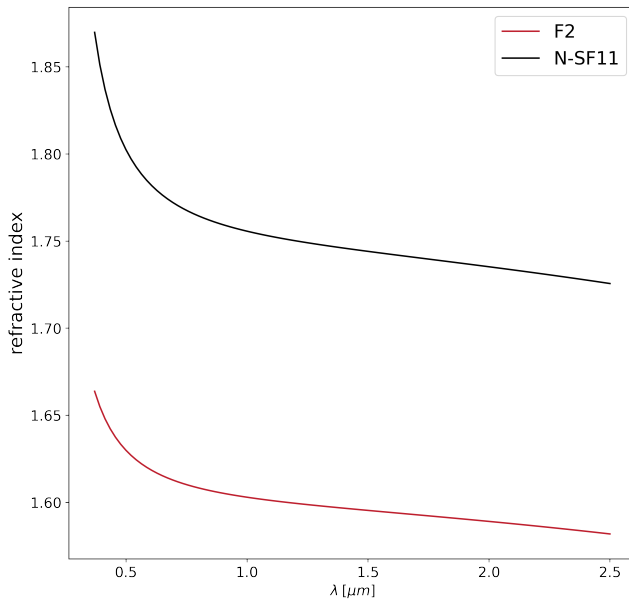


Figure 48: Refractive index as a function of wavelength for the F2 and N-SF11 prisms.

Here, the lens collimates the light, i.e., light rays within the beam are parallel to each other after passing the lens, which makes it easier to accurately distinguish the various spectral components separated on refraction from the prism. Given a range of lenses, the effective focal length of the collimating lens can be compared with the focal length required by the numerical aperture of an on-axis input fibre, and by a certain beam width w :

$$w = 2 \cdot L_C \cdot NA. \quad (6.1)$$

The longer the focal length, the larger the beam width that must not exceed the 2-inch lens diameter but also the 50-mm base length of the F2 equilateral dispersive prism on which the light is incident on. F2 is a flint glass that provides excellent performance in the visible and near-infrared spectral range and offers a high refractive index. The refractive index n , which depends on the wavelength λ , defines how much the light beam is bent (or refracted) upon entering or leaving a material, and the higher it is, the greater the extent to which the light is deflected. For an accurate description of the wavelength dependence of the refractive index, the Sellmeier equation can be used, and is given as:

$$n^2(\lambda) - 1 = \frac{k_1\lambda^2}{\lambda^2 - L_1} + \frac{k_2\lambda^2}{\lambda^2 - L_2} + \frac{k_3\lambda^2}{\lambda^2 - L_3}, \quad (6.2)$$

where $k_1, k_2, k_3, L_1, L_2,$ and L_3 are a set of coefficients assigned to a material through which n can be computed at any λ . For F2 these are: $k_1 = 1.345, k_2 = 2.091 \times 10^{-1}, k_3 = 9.374 \times 10^{-1}, L_1 = 9.977 \times 10^{-3} \mu\text{m}^2, L_2 = 4.705 \times 10^{-2} \mu\text{m}^2,$ and $L_3 = 1.119 \times 10^2 \mu\text{m}^2$.

Using Eq. (6.2), I show the index of refraction as a function of wavelength in Fig. 48. Presented in this figure are the plots for the F2 and N-SF11, which was also considered for my analysis. The Sellmeier equation is only accurate within the wavelength range specified by λ_{\min} and λ_{\max} . $\lambda_{\min} = 0.32 \mu\text{m}$ & $\lambda_{\max} = 2.5 \mu\text{m}$ for F2, and the N-SF11 prism has $\lambda_{\min} = 0.37 \mu\text{m}$ & $\lambda_{\max} = 2.5 \mu\text{m}$. From Fig. 48 we see that both prisms show an almost constant refractive index in the spectral range of interest ($1.2 - 1.8 \mu\text{m}$), with $n = 1.616$ (F2) and $n = 1.778$ (N-SF11) at the prisms design wavelength of $0.633 \mu\text{m}$. Indeed, the N-SF11, which is also a flint glass, exhibits a higher refractive index than the F2 prism. However, the F2 offers a superior chemical resistance and a slightly higher transmission (see Fig. 49).

Another important property of flint glass is that it has a low Abbe number. The Abbe number V_d , after the eponym who co-owned the optics manufacturer

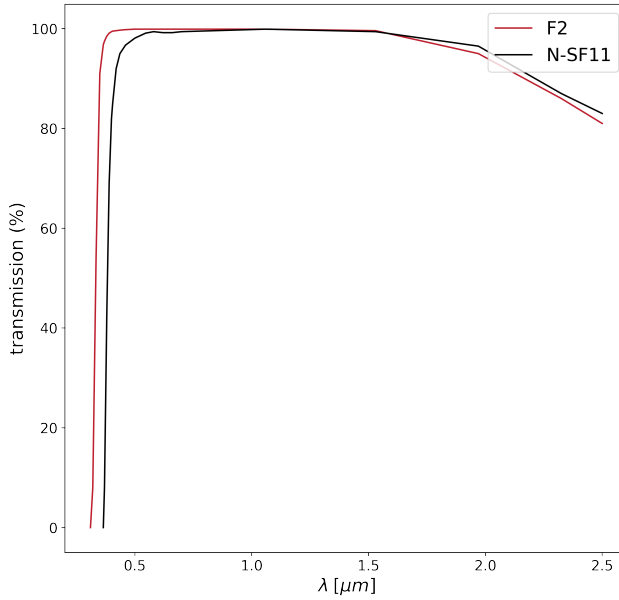


Figure 49: Transmission as a function of wavelength for the F2 and N-SF11 prisms. The transmission data, which is for a 10 mm thick sample for both prisms, was acquired from <http://thorlabs.com/>.

Carl Zeiss, is a measure of the material's dispersion (change of refractive index versus wavelength) and is given as:

$$V_d = \frac{n_d - 1}{n_F - n_C}, \quad (6.3)$$

where n_d , n_F and n_C are the refractive indices of the material at the wavelengths of the Fraunhofer's d, F and C spectral lines (helium d-line (587.6 nm), hydrogen F-line (486.1 nm), and the hydrogen C-line (656.3 nm), respectively). A low V_d indicates high dispersion, and for F2 $V_d = 36.37$ while the N-SF11 prism has $V_d = 25.76$. Low dispersion materials typically have $V_d > 55$.

In the 1.2 – 1.8 μm spectral range, we can compute an approximate average value of the dispersion $\delta n / \delta \lambda$ for both prisms as:

$$\frac{\delta n}{\delta \lambda} = \frac{n_{\max} - n_{\min}}{\lambda_{\max} - \lambda_{\min}}. \quad (6.4)$$

which gives $\delta n / \delta \lambda = -0.01303$ (F2) and $\delta n / \delta \lambda = -0.01896$ (N-SF11).

The performance of a spectrograph is characterised by its resolving power R (i.e., the ability of the prism to separate two closely spaced wavelengths):

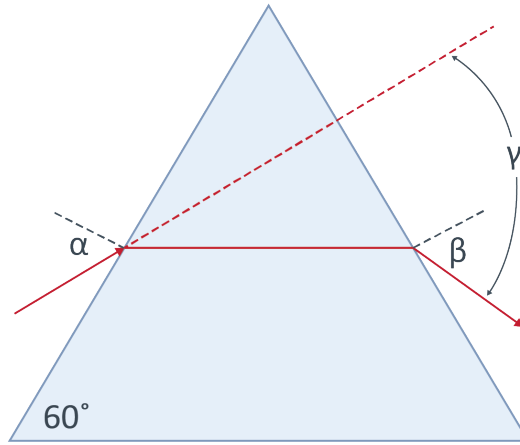


Figure 50: Angle of minimum deviation through an equilateral dispersive prism. The angle of minimum deviation γ occurs when the refracted light ray in the prism is parallel to its base (as shown above), and therefore, the angle of incidence and angle of emergence equal each other ($\alpha = \beta$). By applying Snell's Law, an equation of the relationship between the index of refraction (for $n < 2$) and γ can be derived. It is given by Eq. (6.7).

$$R = b \left(\frac{\delta n}{\delta \lambda} \right), \tag{6.5}$$

where b is the base length of the prism. During my analysis, the largest available prism sizes were 50-mm (F2) and 40-mm (N-SF11) from Thorlabs. Plugging these values into Eq. (6.5) produces $R = 651.33$ (F2) and $R = 758.55$ (N-SF11). Spectral resolution, usually designated by $\Delta\lambda$, is closely related to the resolving power of a spectrograph, and is given as:

$$\Delta\lambda = \frac{\lambda}{R}. \tag{6.6}$$

At $1.55 \mu\text{m}$, the minimum resolvable wavelength difference is $0.0024 \mu\text{m}$ and $0.002 \mu\text{m}$ for F2 and N-SF11, respectively.

Equilateral dispersive prisms create less stray light than diffraction gratings, thereby eliminating unwanted higher-order diffraction phenomena normally associated with gratings. They are typically used at the angle of minimum deviation γ , which occurs when the refracted light ray in the prism is parallel to its base (see Fig. 50), and therefore, the angle of incidence and angle of emergence equal each other ($\alpha = \beta$). By applying Snell's Law, one can derive an equation of the relationship between the index of refraction (for $n < 2$) and γ :

$$n = \frac{\sin\left(\frac{\gamma+60^\circ}{2}\right)}{\sin 30^\circ}. \quad (6.7)$$

Solving for γ at the prisms design wavelength in Eq. (6.7) yields 47.9° and 65.6° for F2 and N-SF11, respectively. Maximum transmission can be achieved by adjusting a prism to the position of minimum deviation.

A focusing lens (2-inch near-infrared achromatic doublet) directs the dispersed light from the prism through the cold pupil ($x = 9.5$ -mm diameter) of a detector located at a focal length L_F . This length includes the flange focal distance d , which is shown in Fig. 47 for the C-RED One. The camera is kept at a constant readout of 2 kHz. According to the Nyquist–Shannon theorem, the sampling frequency should be greater than twice the highest frequency contained in the signal. In the context of a spectrograph, this means that there must be at least two pixels per spectral resolution element, otherwise it is the size of the pixels that will define the resolution. For this 320×256 pixel detector, the pixel pitch (i.e., the distance from one pixel to the next) is $24\mu\text{m}$, with $\Delta\lambda$ occupying a minimum of $48\mu\text{m}$.

In addition to the spectral resolution, which sets the size of the smallest spectral features that can be studied in the spectrum, the linear spread (or dispersion) is another important property of a spectrograph. Linear dispersion sets the wavelength range of the spectrum and is given by the following expression shown in Bass et al. (1995) as:

$$\frac{\delta x}{\delta\lambda} = L_F \cdot \frac{\delta\gamma}{\delta\lambda}, \quad (6.8)$$

where $\delta\gamma/\delta\lambda$ is the angular dispersion that is defined as:

$$\frac{\delta\gamma}{\delta\lambda} = \frac{b}{w} \frac{\delta n}{\delta\lambda}. \quad (6.9)$$

Because of the different indices of refraction for the different wavelengths, γ varies with λ . Therefore, to predict the spectrograph's wavelength range, we can compute $\delta x/\delta\lambda$ from a particular wavelength (i.e., $1.55\mu\text{m}$) and translate this to a range along the length ($256 \text{ pixels} = 6.144\text{-mm}$) of the detector. A useful way to do this is by using a spot diagram, which I show in Sec. 3.2.

3.2 Spot diagrams

After determining the various optical elements and the parameters describing their relationships, we can evaluate the performance of the spectrograph with

the aid of spot diagrams. These plots show where light rays from a point source such as a single-mode fibre will occur on a detector. The spectrum produced by an input fibre is depicted with spots that have an irradiance profile of an ideal Gaussian distribution (see Fig. 51). Using Python modelling and the parameters defined in Sec. 3.1, I constructed a spot diagram (see Fig. 52) for an F2 prism with a pair of 2-inch achromatic doublets of focal lengths $L_C = 77\text{-mm}$ & $L_F = 400\text{-mm}$. Here, I show seven spectra (commensurate with the number of input fibres on the V-groove array) that are arranged vertically on the y-axis with an x-axis spacing $x: x = (p_s/p_p)M$, where p_s is the pitch spacing ($127\mu\text{m}$), p_p is the pixel pitch ($24\mu\text{m}$), and the magnification $M = L_F/L_C$. We can see from Fig. 52 that the width ($320\text{ pixels} = 7.68\text{-mm}$) of the detector easily accommodates the seven input fibres, and that the magnification provides a small spot size with a diameter $d: d = (MFD/p_p)M$, where $MFD = 10.4\mu\text{m}$. The red horizontal dashed lines mark the spots located at a wavelength of $1.6\mu\text{m}$, which is the starting point of the spot diagram construction. I selected the location of this wavelength on the detector array so as to maximise the distribution of the spectra in the $1.2 - 1.8\mu\text{m}$ spectral range of interest. Successive spots are arranged according to a separation $s: s = (y \cdot \frac{\Delta x}{\Delta \lambda}) / p_p$, where y is a wavelength separation, which was set at $0.02\mu\text{m}$.

Figure 53 shows a spot diagram constructed for the N-SF11 prism with the same achromatic doublets. Although this prism provides a higher resolving power, we see that the wavelength range is reduced. Whereas the F2 provides a spectral range of $1.28 - 1.8\mu\text{m}$, the N-SF11 offers a range of $1.32 - 1.76\mu\text{m}$. Indeed, one can attribute this advantage to the longer base length of the F2 prism. However, the sizes I adopt—for the respective prisms—were the largest available from Thorlabs during the design process. My analysis also considered a pair of 1-inch achromatic doublets of focal lengths $L_C = 45\text{-mm}$ & $L_F = 250\text{-mm}$ (see Fig. 54 & Fig. 55). Here, the spectral range was $1.28 - 1.78\mu\text{m}$ and $1.34 - 1.76\mu\text{m}$ for F2 and N-SF11, respectively.

3.3 Integration and wavelength calibration

Due to the limited kernel test bench area on which the various optical elements could be deployed, modelling their assembly was a relevant process in determining if the solutions obtained from the spot diagrams were practically feasible. Figure 56a shows a CAD modelling of the spectrograph in Autodesk Inventor. The approach of this assembly is the following: (1) a translation stage, which is mounted on a large right angle bracket, allows for the vertical alignment of the fibre array holder where light from separate SMF-28e optical fibres is directed towards a (2) collimating lens (2-inch near-infrared achromatic doublet,

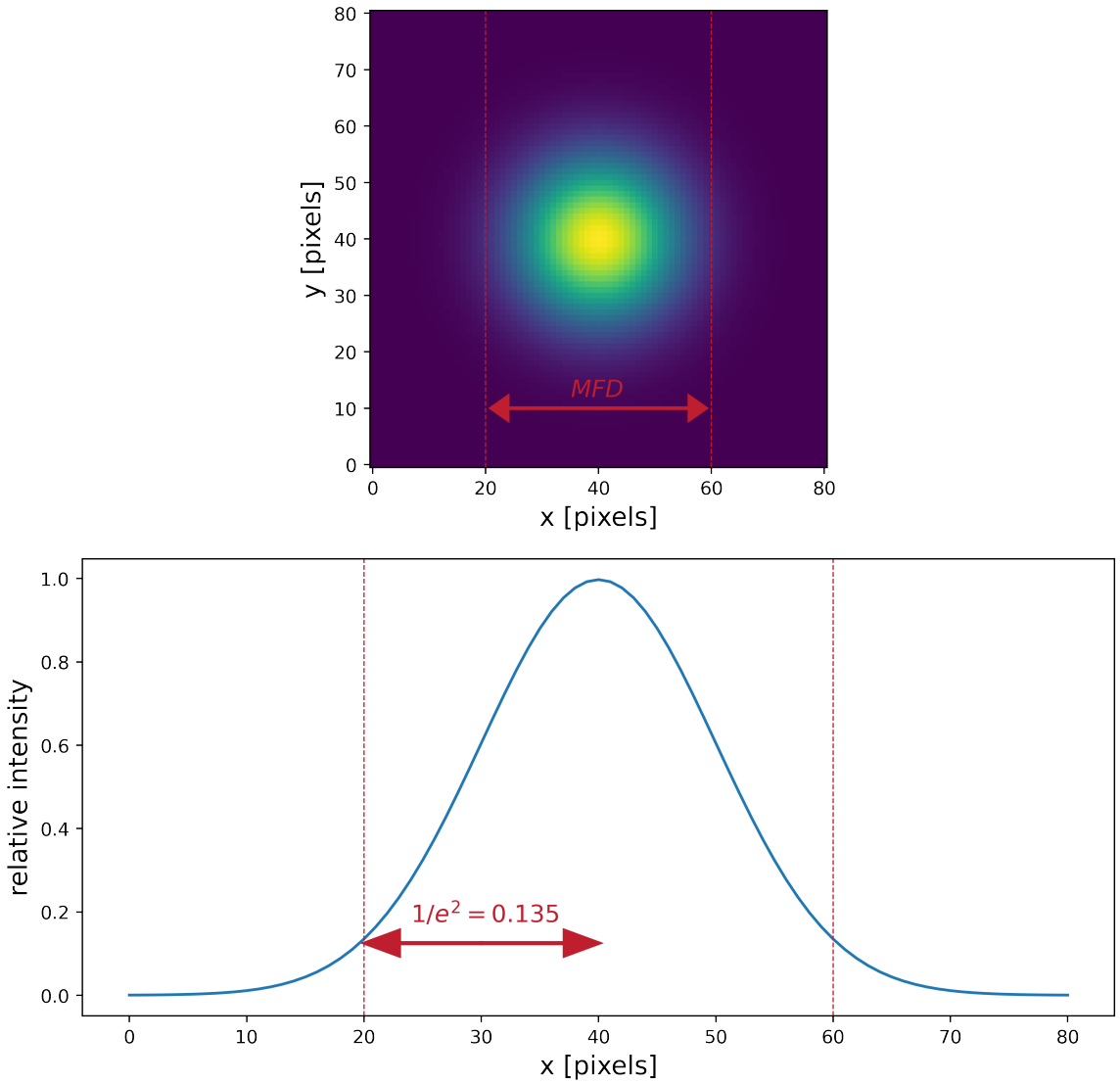


Figure 51: Spot with an irradiance profile that follows an ideal Gaussian distribution. **Top panel:** The mode field diameter (MFD) is a measure of the spot size or beam width of light propagating in a single-mode fibre. It is a function of source wavelength, fibre core radius, and fibre refractive index. Even with the narrowest of MFD, the spots on the spot diagram have an irreducible width due to the diffraction limit, which is imposed by the optics. **Bottom panel:** The waist of a Gaussian beam is defined as the location where the irradiance is reduced to $1/e^2$ (13.5%) of its maximum value.

F2, 2" lens ($F_C = 75\text{-mm}$ & $F_F = 400\text{-mm}$)

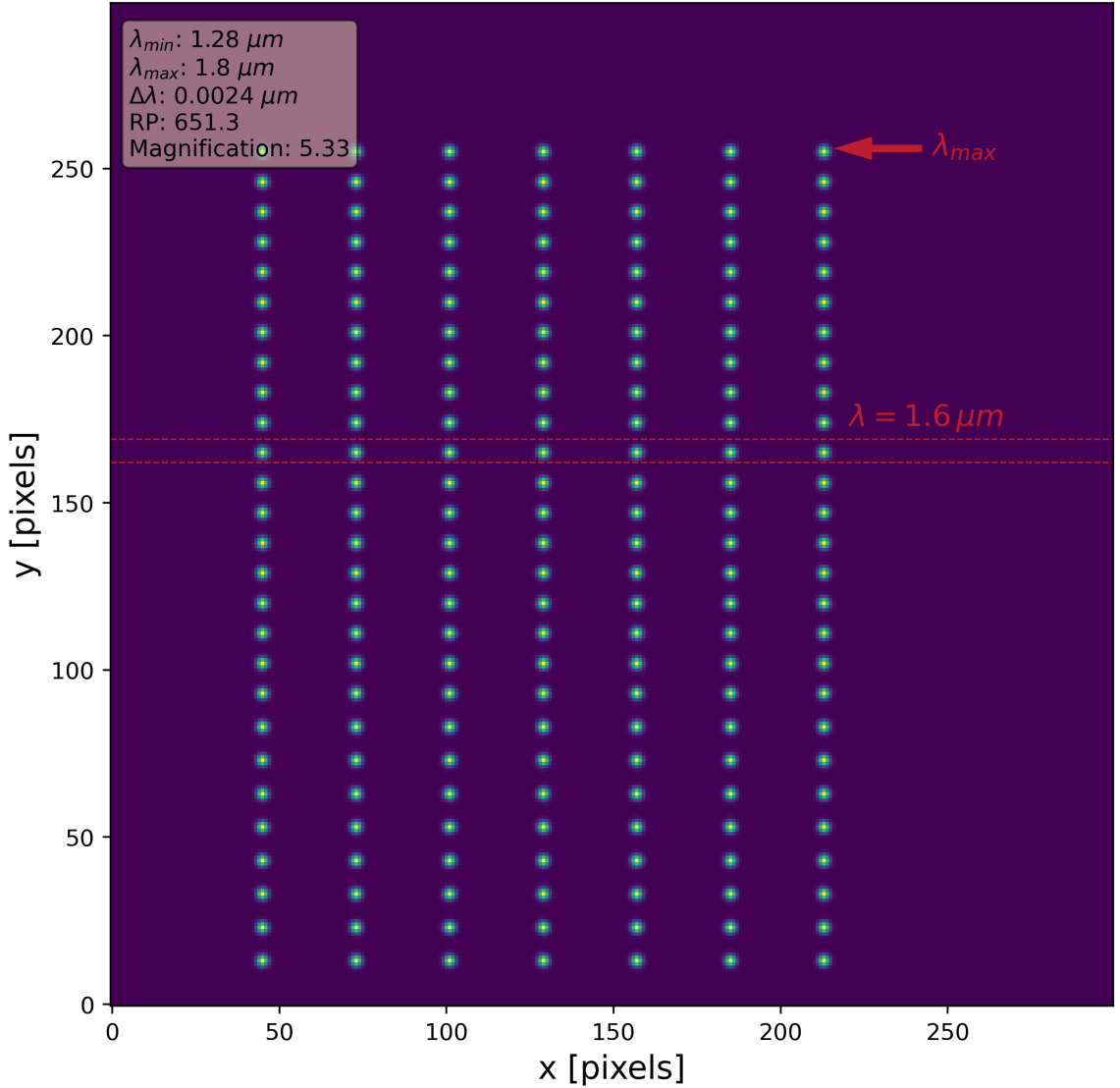


Figure 52: Spot diagram constructed for an F2 prism with a pair of 2-inch achromatic doublets of focal lengths $L_C = 75\text{-mm}$ & $L_F = 400\text{-mm}$. Spot diagrams are plots that show where light rays from a point source such as a single-mode fibre will occur on a detector. The spectrum produced by an input fibre is depicted with spots that have an irradiance profile of an ideal Gaussian distribution (see Fig. 51). Here, I show seven spectra (commensurate with the number of input fibres on the V-groove array) that are arranged vertically on the y-axis with an x-axis spacing that is proportional to the pitch spacing of the V-groove array. The red horizontal dashed lines mark the spots located at a wavelength of $1.6\ \mu\text{m}$, which is the starting point of the spot diagram construction. Successive spots are arranged according to a separation proportional to the linear dispersion. The parameters shown inset are the minimum λ_{\min} and maximum λ_{\max} wavelengths of the spectra, the spectral resolution $\Delta\lambda$, the resolving power RP , and the magnification.

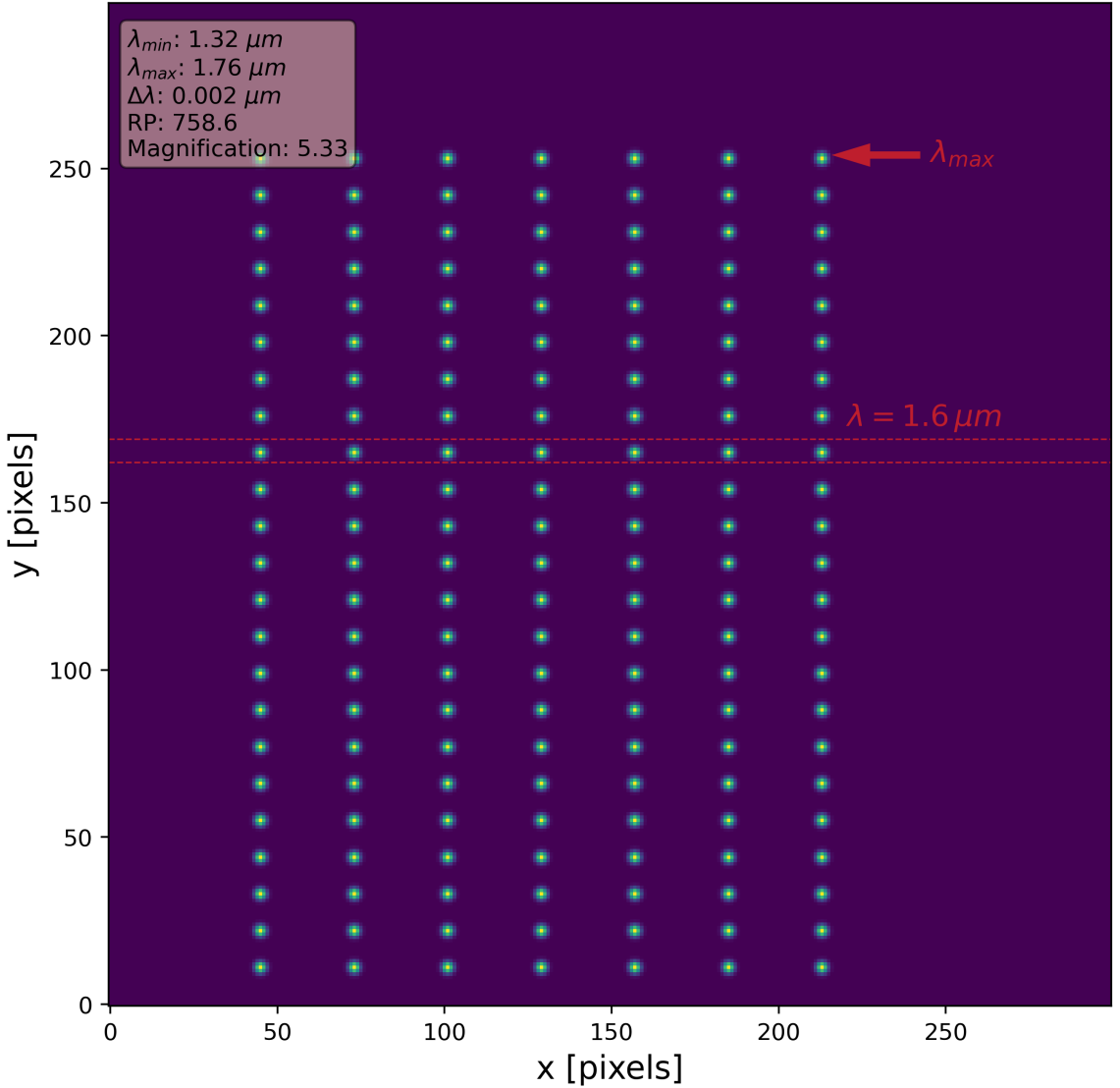
N-SF11, 2" lens ($F_C = 75\text{-mm}$ & $F_F = 400\text{-mm}$)

Figure 53: Spot diagram constructed for an N-SF11 prism with a pair of 2-inch achromatic doublets of focal lengths $L_C = 75\text{-mm}$ & $L_F = 400\text{-mm}$. Spot diagrams are plots that show where light rays from a point source such as a single-mode fibre will occur on a detector. The spectrum produced by an input fibre is depicted with spots that have an irradiance profile of an ideal Gaussian distribution (see Fig. 51). Here, I show seven spectra (commensurate with the number of input fibres on the V-groove array) that are arranged vertically on the y-axis with an x-axis spacing that is proportional to the pitch spacing of the V-groove array. The red horizontal dashed lines mark the spots located at a wavelength of $1.6 \mu\text{m}$, which is the starting point of the spot diagram construction. Successive spots are arranged according to a separation proportional to the linear dispersion. The parameters shown inset are the minimum λ_{min} and maximum λ_{max} wavelengths of the spectra, the spectral resolution $\Delta\lambda$, the resolving power RP , and the magnification.

F2, 1" lens ($F_C = 45\text{-mm}$ & $F_F = 250\text{-mm}$)

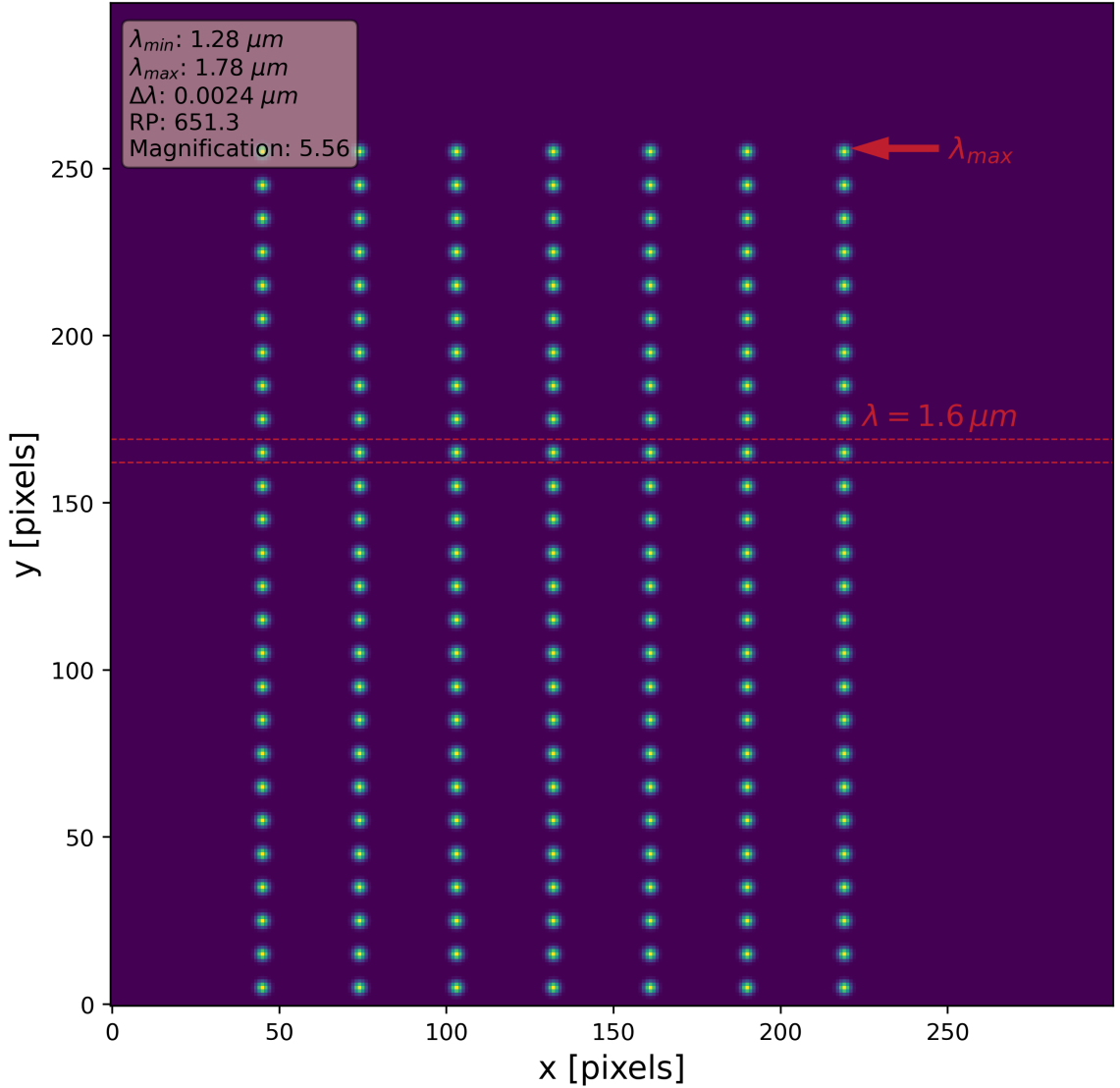


Figure 54: Spot diagram constructed for an F2 prism with a pair of 1-inch achromatic doublets of focal lengths $L_C = 45\text{-mm}$ & $L_F = 250\text{-mm}$. Spot diagrams are plots that show where light rays from a point source such as a single-mode fibre will occur on a detector. The spectrum produced by an input fibre is depicted with spots that have an irradiance profile of an ideal Gaussian distribution (see Fig. 51). Here, I show seven spectra (commensurate with the number of input fibres on the V-groove array) that are arranged vertically on the y-axis with an x-axis spacing that is proportional to the pitch spacing of the V-groove array. The red horizontal dashed lines mark the spots located at a wavelength of $1.6\ \mu\text{m}$, which is the starting point of the spot diagram construction. Successive spots are arranged according to a separation proportional to the linear dispersion. The parameters shown inset are the minimum λ_{\min} and maximum λ_{\max} wavelengths of the spectra, the spectral resolution $\Delta\lambda$, the resolving power RP , and the magnification.

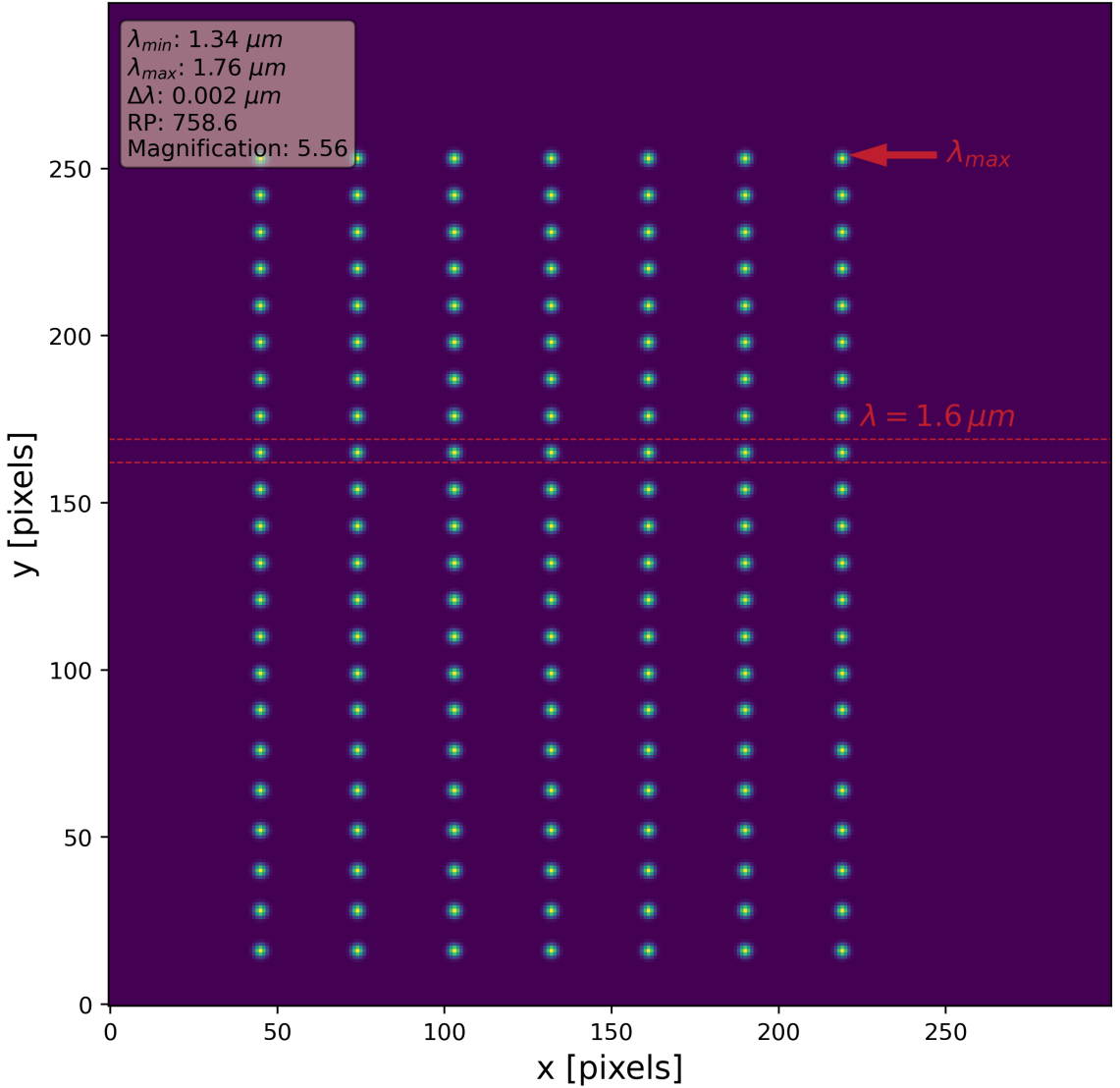
N-SF11, 1" lens ($F_C = 45\text{-mm}$ & $F_F = 250\text{-mm}$)

Figure 55: Spot diagram constructed for an N-SF11 prism with a pair of 1-inch achromatic doublets of focal lengths $L_C = 45\text{-mm}$ & $L_F = 250\text{-mm}$. Spot diagrams are plots that show where light rays from a point source such as a single-mode fibre will occur on a detector. The spectrum produced by an input fibre is depicted with spots that have an irradiance profile of an ideal Gaussian distribution (see Fig. 51). Here, I show seven spectra (commensurate with the number of input fibres on the V-groove array) that are arranged vertically on the y-axis with an x-axis spacing that is proportional to the pitch spacing of the V-groove array. The red horizontal dashed lines mark the spots located at a wavelength of $1.6 \mu\text{m}$, which is the starting point of the spot diagram construction. Successive spots are arranged according to a separation proportional to the linear dispersion. The parameters shown inset are the minimum λ_{min} and maximum λ_{max} wavelengths of the spectra, the spectral resolution $\Delta\lambda$, the resolving power RP , and the magnification.

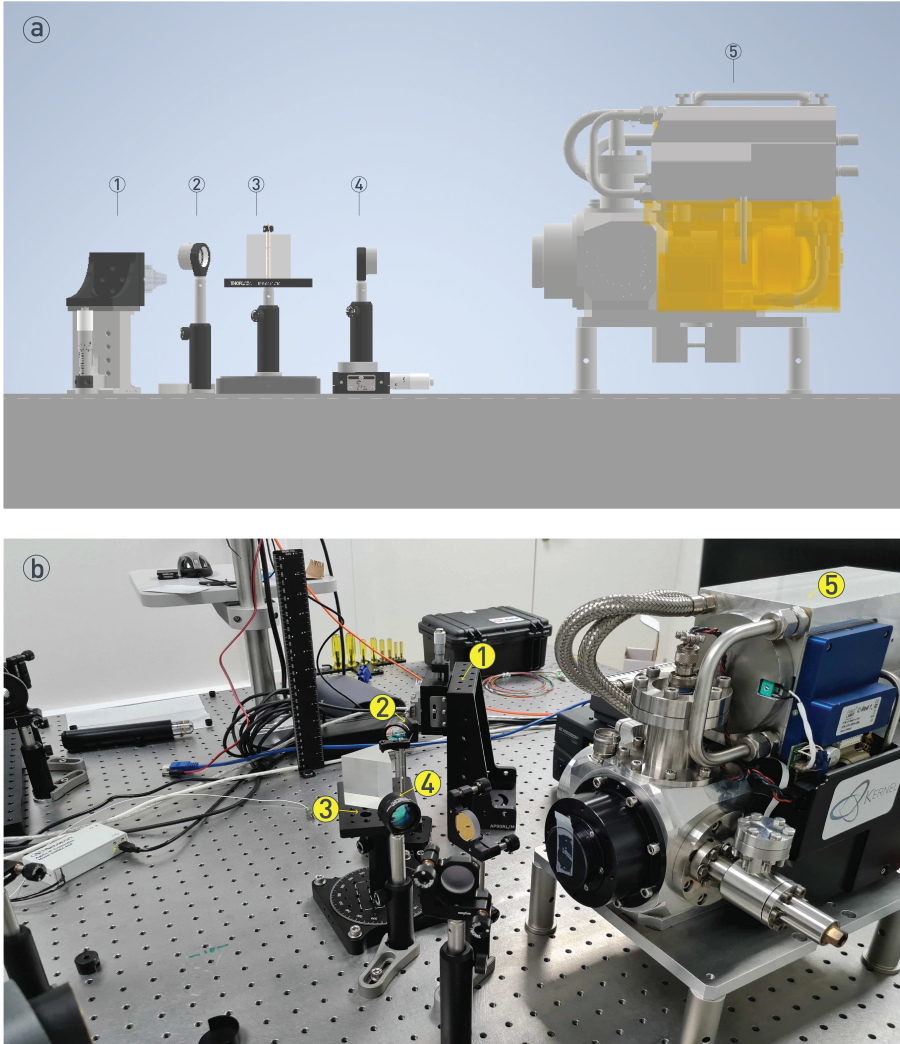


Figure 56: a) CAD modelling of the spectrograph in Autodesk Inventor. b) Spectrograph integrated on the kernel test bench shown in Fig. 43. The assembly of the spectrograph is the following: (1) a translation stage, which is mounted on a large right angle bracket, allows for the vertical alignment of the fibre array holder where light from separate SMF-28e optical fibres is directed towards a (2) collimating lens (2-inch near-infrared achromatic doublet, $L_C = 75\text{-mm}$). The collimated beam then travels through to an (3) F2 equilateral dispersive prism that sits on top of a manual rotation stage. This stage ensures that the light beams are incident with the prism such that the angle of minimum deviation can be achieved. (4) A focusing lens (2-inch near-infrared achromatic doublet, $L_F = 400\text{-mm}$) directs the dispersed light from the prism via a beam steering mirror onto the (5) detector (C-RED One Camera).

$L_C = 75\text{-mm}$). The collimated beam then travels through to an (3) F2 equilateral dispersive prism that sits on top of a manual rotation stage. This stage ensures that the light beams are incident with the prism such that the angle of minimum deviation can be achieved. (4) A focusing lens (2-inch near-infrared achromatic doublet, $L_F = 400\text{-mm}$) directs the dispersed light from the prism via a beam steering mirror onto the (5) detector (C-RED One Camera).

Upon establishing that the design did meet the spatial constraints, I purchased the equipment from Thorlabs and integrated the spectrograph on the kernel test bench as shown in Fig. 56b. The alignment of the various optical elements was quite straightforward, especially after the spots (obtained by referencing the $1.55\ \mu\text{m}$ bandpass filter in the upstream filter wheel) or the spectra from the different inputs were acquired on the detector that one can monitor for fine-tuning. As our setup allowed for optical fibre interchange, the chip outputs can be sampled in all seven spectrograph inputs as presented in Fig. 57. Indeed, one can detect a left to right slope in the alignment of these inputs, which was due to the fibres not being properly glued to the V-groove array. However, this did not affect the maximum achievable wavelength range for the five right-most inputs.

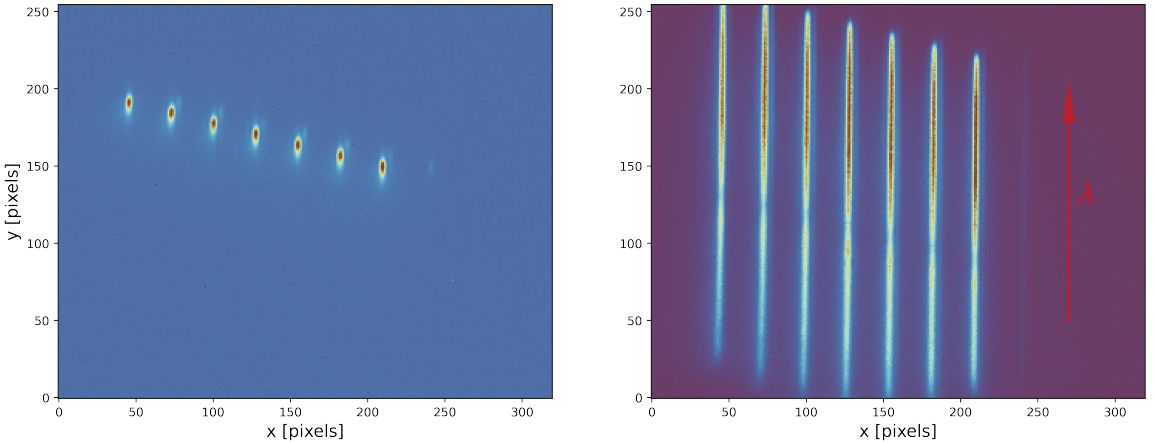


Figure 57: $1.55\ \mu\text{m}$ spots (*Left*) and broadband spectra (*Right*) of seven spectrograph inputs on a 320×256 pixel array. The spots were obtained by referencing a bandpass filter with a central wavelength of $1.55\ \mu\text{m}$ and a full width half maximum (FWHM) bandwidth of $12\ \text{nm}$ in the upstream filter wheel.

Considering that the angle of minimum deviation corresponds with the maximum transmission, one can locate it by adjusting the rotation stage whilst monitoring the spectra on the detector. When increasing or decreasing the angle of incidence, I observed that the spectra would move up or down with a corresponding fluctuation in intensity. A point is reached where the movement of the

spectra comes to a stop and the motion is reversed. This is the angle of minimum deviation.

Although I was able to obtain good quality spectra, I observed a "ghost" image on the detector for each of the spectrograph inputs, which could be due to reflection in the optical path. In Fig. 58, we can observe a secondary peak (on the right of the primary peak) for the respective input fibres. While the ghost of a preceding input (i.e., fibre 6) will not affect the flux count of the ensuing input (i.e., fibre 7), it is still necessary to eliminate any sources of background noise. This was done by shifting the spectrograph inputs as far as possible to the right of the detector (see Fig. 58), which removes the ghost of the right-most fibre.

The spectrograph is wavelength calibrated by referencing the various filters in the upstream filter wheel. Figure 59 shows the 1.55 μm spot and broadband spectrum of input fibre 7, which has been plotted along the y-axis (or wavelength axis) in the top panel of Fig. 60. The peak we see in the broadband spectrum (i.e., SuperK) at $y = 12$ is the pump wavelength of the supercontinuum source ($\lambda \sim 1.064\mu\text{m}$). Since 1.55 μm is located at $y = 186$, this gives a linear dispersion of ~ 2.8 nm/pix. By determining the linear dispersion, one can convert the pixels on the detector to a wavelength as shown in the bottom panel of Fig. 60. Further adjustments in the alignment led to a linear dispersion of 2.38 nm/pix, which was reported by Cvetojevic et al. (2022) during the experimental validation of a three-input/three-output kernel-nuller.

6 kernel-nulling for the direct detection of exoplanets

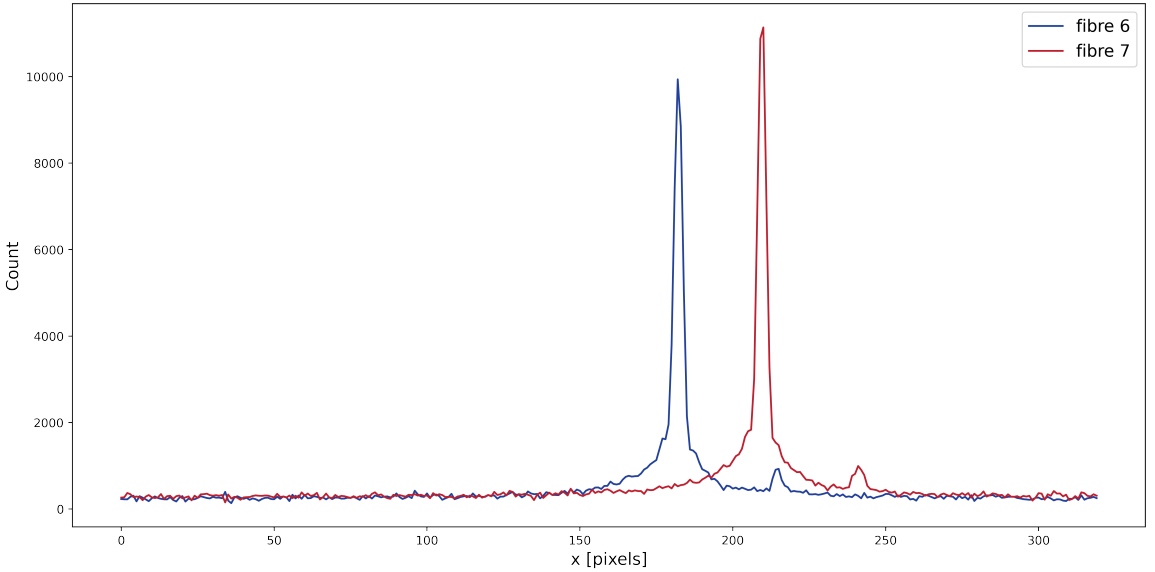


Figure 58: Flux count as a function of pixel position for input fibre 6 & 7 on the spectrograph V-groove array. Data recorded on a 320×256 pixel fast readout C-RED One camera.

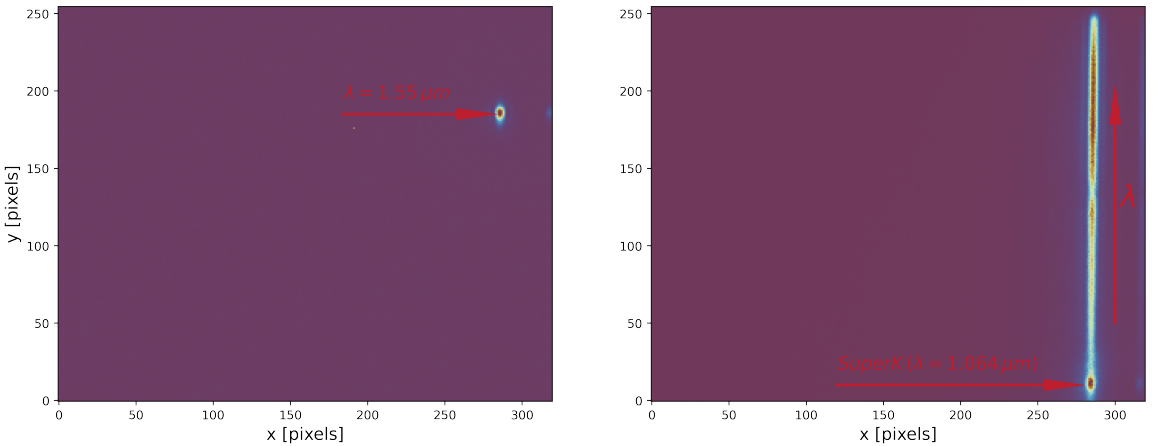


Figure 59: $1.55 \mu\text{m}$ spot (*Left*) and broadband spectrum (*Right*) of input fibre 7 on the V-groove array. Data recorded on a 320×256 pixel fast readout C-RED One camera. The spot is obtained by referencing a bandpass filter with a central wavelength of $1.55 \mu\text{m}$ and a full width half maximum (FWHM) bandwidth of 12 nm in the upstream filter wheel. Note the pump wavelength of the supercontinuum source at the bottom of the spectrum.

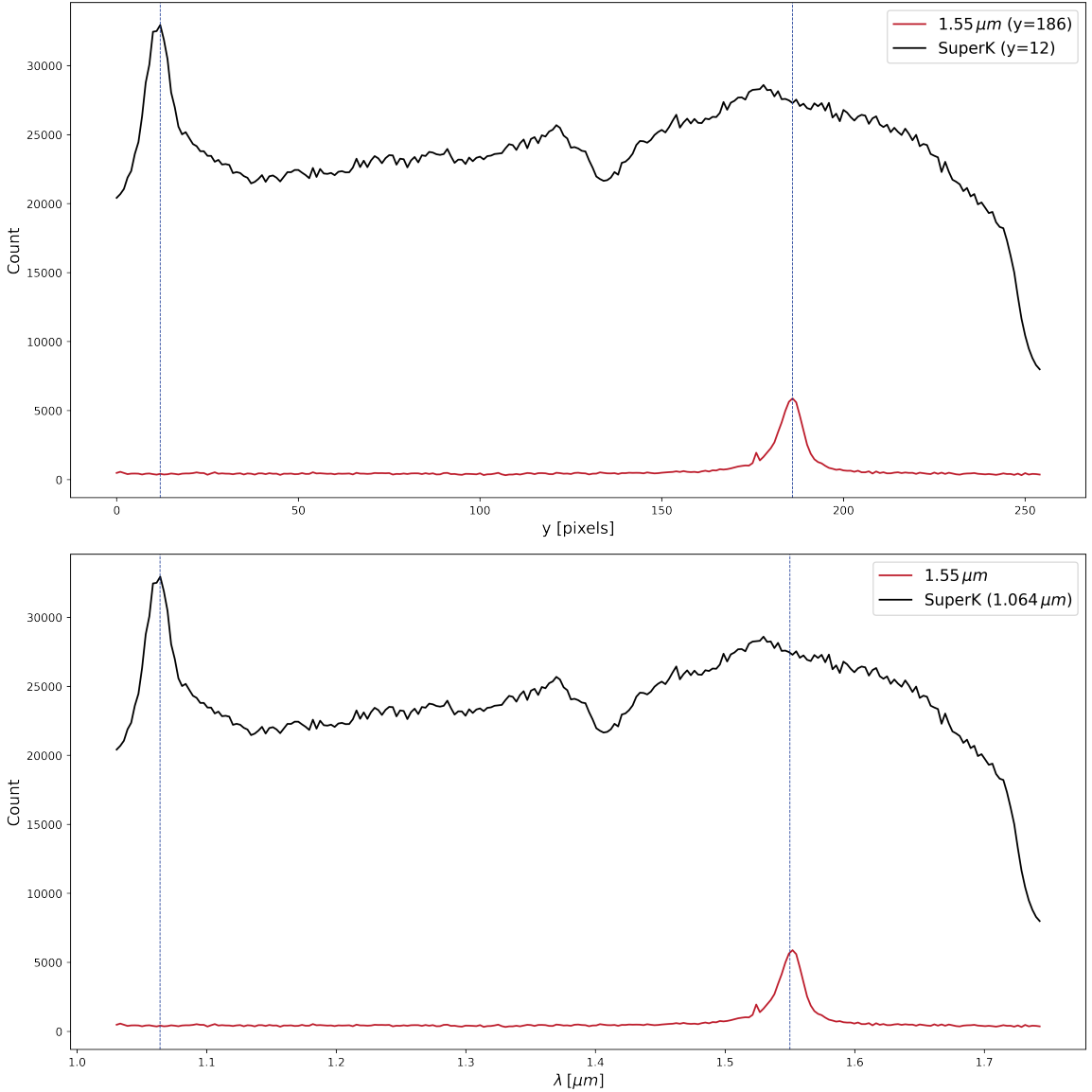


Figure 60: *Top*: Flux count as a function of pixel position for input fibre 7 on the spectrograph V-groove array. The blue vertical dashed lines mark $y = 12$ (Super K pump wavelength) and $y = 186$ ($1.55 \mu\text{m}$ bandpass filter). *Bottom*: Flux count as a function of wavelength for input fibre 7 on the spectrograph V-groove array. The blue vertical dashed lines mark $\lambda = 1.064 \mu\text{m}$ (Super K pump wavelength) and $\lambda = 1.55 \mu\text{m}$ (bandpass filter). Data recorded on a 320×256 pixel fast readout C-RED One camera.

4 Summary

The kernel test bench that is located at the Lagrange Laboratory in Nice has been designed for the spectral characterisation of the kernel-nuller photonic chip presented in Chapter 5. Broadband light from a supercontinuum source is injected into the bench, where a Boston Micromachines Hex-507 deformable mirror enables fast and accurate wavefront control. The precise and stable alignment of the photonic chip is facilitated by a pair of high-precision Nanomax 6-axis flexure stages and a 3-axis precision translation stage. The outputs of the device are coupled into individual SMF-28e optical fibres and redirected to a spectrograph. For each output, the dispersed light is binned into seventeen equally spaced spectral channels spanning the $1.2 - 1.75\mu\text{m}$ band-pass on a 320×256 pixel fast readout C-RED One camera. The 4-pixel spectral binning corresponds to a resolution of 9.5 nm.

Wavelength calibration of the spectrograph with the C-RED One camera was based on exploiting the relationship between wavelength and pixel position across the detector – using wavelength reference standards such as a bandpass filter and the supercontinuum source, which have well defined peak wavelengths (at $1.55\mu\text{m}$ and $1.064\mu\text{m}$, respectively).

Chapter 7

Spectral characterisation of a 4x4 kernel-nuller

Although we can image a planet by nulling at a single wavelength, we are also interested in obtaining its spectral information. Therefore, it is obvious that direct exoplanet detection should be performed over a broad wavelength band, which has the additional benefit of reducing the integration time needed to detect a planet.

Considering that our nuller (an MMI coupler) relies on the interference of modes and interactions between self-images, its response will depend on the accuracy of the amplitudes and phases of the input beams within the device (the complex terms of the nuller response matrix introduced in Chapter 2). In practice, imbalance in the beam splitting ratio, which is the fraction of the flux that makes it from a single input to the outputs, and errors in the phases of the self-images are both present. The sensitivity of the response to these effects will guide the operational steps needed to optimise the device with acceptable performance levels for deep broadband nulling.

The 4-input/4-output MMI (described in Chapter 5) I was tasked to characterise is optimised for a specific wavelength ($1.55 \mu\text{m}$). In order to use such a device for astrophysical applications, we need to study its behaviour over a broad wavelength band, which is why I designed the spectrograph presented in Chapter 6. In this chapter, I investigate the spectral behaviour of the device in the $1.4 - 1.6 \mu\text{m}$ range by measuring the beam splitting ratios and phases of the input electric field that are used to determine the experimental nulling matrix. The initial results of this work were published in the proceedings of the 2022 SPIE Montréal conference and are presented in Sect. 1. Section 2 builds up from this with the aim of providing a more detailed analysis.

1 SPIE publication

PROCEEDINGS OF SPIE

[SPIDigitalLibrary.org/conference-proceedings-of-spie](https://spiedigitallibrary.org/conference-proceedings-of-spie)

Four-input photonic kernel-nulling for the VLTI

Peter Marley Chingaïpe, Frantz Martinache, Nick Cvetojevic

Peter Marley Chingaïpe, Frantz Martinache, Nick Cvetojevic, "Four-input photonic kernel-nulling for the VLTI," Proc. SPIE 12183, Optical and Infrared Interferometry and Imaging VIII, 1218319 (26 August 2022); doi: 10.1117/12.2630050

SPIE.

Event: SPIE Astronomical Telescopes + Instrumentation, 2022, Montréal, Québec, Canada

4-input photonic kernel-nulling for the VLTI

Peter Marley Chingaipe^a, Frantz Martinache^a, and Nick Cvetojevic^a

^aLaboratoire Lagrange, Université Côte d'Azur, Observatoire de la Côte d'Azur, CNRS, Parc Valrose, Bât. H. Fizeau, 06108 Nice, France

ABSTRACT

Kernel-nulling is a beam combination architecture for a nulling interferometer optimized for high-contrast companion detection at high angular resolutions. This novel approach is able to suppress the photon noise from stellar light by coherent destructive interference, similar to a classical nuller, and in addition produces a pair of raw nulled outputs that possess the same response to instrumental/environmental perturbations while still producing distinct response to off-axis light. The difference between a pair of raw outputs will result in a kernel-null observable which is robust to piston induced phase error terms to second order, removing the dominant source of noise in classical nulling. We present initial laboratory characterization results of a four-input kernel-nuller photonic device at near-infrared wavelengths. The necessary routing, beam splitting, and recombination is performed within a planar silicon nitride (SiN) photonic chip fabricated using photo-lithography. The four input beams are recombined to create one bright output and three nulled outputs. The linear combination of a pair of these nulled outputs creates one kernel-null. This device is designed to explore the possible circuitry for the VIKiNG visitor instrument being commissioned for the VLTI. We also present simulation results of how kernel-nulling can be used at the VLTI for the astrophysical detection of high-contrast companions.

Keywords: instrumentation, optical interferometry, photonics

1. INTRODUCTION

Of the 5,000+ exoplanets detected thus far, indirect detection methods such as transit and radial velocity have provided the largest number, but these are mainly sensitive to planet's at small separations from their host star. On the other hand, direct imaging has had a lower yield due to the difficulty in suppressing the residual starlight at the planet's location in order to achieve the contrast ratio needed to distinguish the planetary light from the star's. The conventional approach to addressing this challenge has been the use of a single aperture coronagraph with wavefront correction via extreme adaptive optics. Such systems are limited to observing beyond an inner working (IWA) of a few λ/D . Nulling interferometry with two or more apertures can bridge the gap between these detection techniques as it has no fixed IWA, though planet flux transmission does decrease for star/planet separations below the diffraction limit. A key requirement for a nuller is therefore the stable destructive interference of the on-axis starlight which is optically redirected towards a bright output, while the off-axis planetary light interferes constructively and diverts through to the nulled outputs. Although modern adaptive optics does provide a stable wavefront to allow for this interference, residual instrumental or atmospheric perturbations can lead to stellar flux leakage in the nulled outputs. A novel beam combination architecture that produces observable quantities robust to these perturbations is kernel-nulling.¹ In this paper we present the first laboratory characterization results of a four-input photonic kernel-nuller.

The use of photonic chips facilitates the realization of an advanced nulling architecture such as the kernel-nuller due to their robustness and indifference to environmental changes. These chips guide, shape, and manipulate the light coming from multiple apertures and are already in use with the Guided-Light Interferometric Nulling Technology (GLINT)^{2,3} at the Subaru Telescope. When compared to their bulk optic counterparts, photonic chips are alignment-free and lightweight thus making them easier to handle, package, and control. This is particularly attractive when considering future space astronomical instruments.

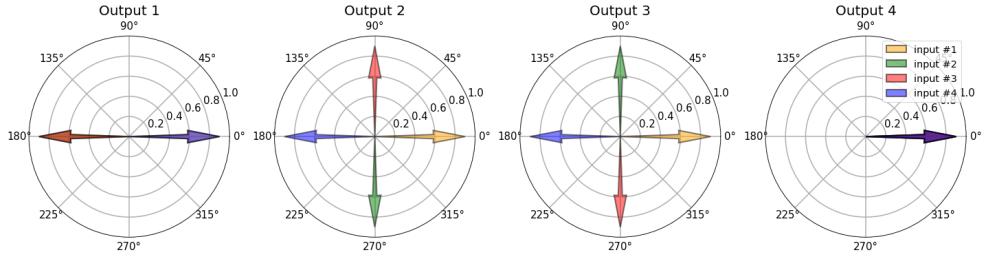


Figure 1. Theoretical complex matrix plot of the four nulled outputs of the 4x4 MMI. Input 1 is the phase reference so that the phases of the different electric fields sampled by the other inputs are measured relative to this reference. Nulled output 1 is a classical Bracewell null with two positive (zero phase shift) and two negative (π phase shifted) arrows. This output does not allow for the formation of a kernel. However, nulled outputs 2 & 3 are mirror images (conjugate pair) of each other and whose linear combination forms a kernel-null. Output 4 is set as the bright output, with all inputs combined constructively.

2. KERNEL-NULLER PHOTONIC CHIP

2.1 The response of a kernel-nuller

Kernel-nulling has been proposed in order to improve the robustness against various instrumental perturbations that can degrade the nulling performance. Any imperfection in phase will produce a spurious flux that leaks through to the nulled outputs and contaminates the transmitted off-axis flux. The multiple beam-combiner architecture of the kernel-nuller produces nulled outputs which combine to deliver observable quantities known as kernel-nulls. Similar to closure phase,⁴ kernel-nulls are independent of instrument-specific phase error induced by the atmosphere or optics to second order. To experimentally validate this concept, a prototype photonic kernel-nulling chip in the near infrared (NIR) is currently being characterized at Observatoire de la Côte d'Azur.

Kernel-nullers can be constructed from an arbitrary number of apertures⁵ and recently a 3-input version was experimentally demonstrated in Ref. 6. Here, we take a look at a four-input kernel-nuller which produces one bright output and three nulled outputs. The coherent interferometric beam combinations performed by this nuller are described by a nuller response matrix:

$$\mathbf{M} = \frac{1}{2} \times \begin{bmatrix} 1 & -1 & -1 & 1 \\ e^{\frac{3\pi j}{4}} & e^{-\frac{3\pi j}{4}} & e^{\frac{\pi j}{4}} & e^{-\frac{\pi j}{4}} \\ e^{-\frac{\pi j}{4}} & e^{-\frac{3\pi j}{4}} & e^{\frac{\pi j}{4}} & e^{\frac{3\pi j}{4}} \\ 1 & 1 & 1 & 1 \end{bmatrix} \quad (1)$$

The rows of \mathbf{M} represent the outputs and the columns represent the inputs. The first row forms a classical Bracewell null⁷ with two inputs combined constructively (zero phase shift) and two inputs combined destructively (π phase shifted). Row 2 & 3 form nulls that are complex conjugates of each other and whose linear combination will produce one kernel-null. Row 4 is the bright output, with all inputs combined constructively. An apt way to visually depict \mathbf{M} is with a complex matrix plot (CMP)⁵ as shown in Fig. 1. The amplitude and phase of the input electric fields are represented by the length and the pointing angle of the arrows respectively. Any of the four outputs (or rows of \mathbf{M}) can be set as the bright output and here we observe output 4 as the bright output. Indeed, output 2 & 3 are shown to be a pair and for this design a kernel-null is simply the difference in intensities of these two outputs. The intensity response of the k nulled outputs is given by:

$$\mathbf{I}_k = \left| \sum_{n=1}^n \mathbf{M}_{k,n} \cdot e^{(-2\pi i/\lambda) \cdot (x_n \alpha + y_n \delta)} \right|^2 \quad (2)$$

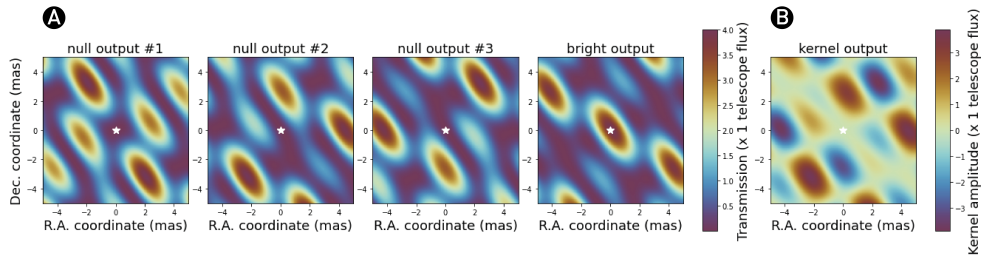


Figure 2. Nuller output transmission maps (a) of a kernel-nuller at the focus of the four VLTI UTs, observing a ± 5 mas field of view for a pointing exactly at zenith. The figure shows the maps of the four nuller outputs and we see that the nulled output maps differ from one another and this diversity in the output response provides a constraint on the properties of a potential companion in the vicinity of a much brighter star. A white star in each map marks the location of the central star where the transmission for all nulled channels, by design, is equal to zero. About the centre of the field, null output map 2 & 3 are asymmetrical. For transmission maps, this asymmetry is a desirable trait as it allows for the elimination of centro-symmetric astrophysical features that would otherwise hide a planetary companion. Null output map 1 is derived from a classical Bracewell null and here we observe a symmetry about the origin. All four maps share the same color scale where the transmission is expressed in units of the planet flux. The kernel output map (b) is simply the difference between null output map 2 & 3. A difference of output values means that unlike raw photometric-like outputs, kernel outputs can take negative values. This is shown on the color scale on the right of the map where the transmission is expressed in units of kernel amplitude.

where $\mathbf{M}_{k,n}$ is the nuller response matrix which will act on the input electric fields with wavelength λ collected by n telescopes; (x_n, y_n) are the coordinates of the telescopes; and (α, δ) are the right ascension and declination offset of an off-axis source. A kernel-null is therefore:

$$\kappa = \mathbf{I}_2 - \mathbf{I}_3 \quad (3)$$

The most direct way to interpret the effect of a nuller recombining more than two telescopes is to compute transmission maps which describe the response of the different outputs to the presence of a test point source over the field of view of the interferometer. These transmission maps predict what fraction of the total flux of an off-axis source will find its way through to the nulled outputs. We will refer to the two-dimensional response of the nuller outputs at time t :

$$\tau(\alpha, \delta, t) = |\mathbf{M} \cdot \mathbf{U}(\alpha, \delta, t)|^2 \quad (4)$$

as nuller output transmission maps. Here, \mathbf{U} is a vector of complex amplitudes at the aperture entrance:

$$\mathbf{U}(\alpha, \delta) \propto e^{(-2\pi i/\lambda) \cdot (x\alpha + y\delta)} \quad (5)$$

One example of such maps is represented in Fig. 2(a) for the kernel-nuller architecture described by \mathbf{M} and computed for the four UTs of the VLTI in the H-band ($\lambda = 1.55 \mu m$) for a hypothetical scenario of a pointing exactly at zenith. Each map features bumps and gaps at distinct locations which are imposed both by the arrangement of the telescopes on the ground and by \mathbf{M} . The transmission maps for outputs 2 & 3 also confirm that these outputs work in a pair. Therefore, the difference between these two consecutive raw outputs will result in the kernel output map shown in Fig. 2(b).

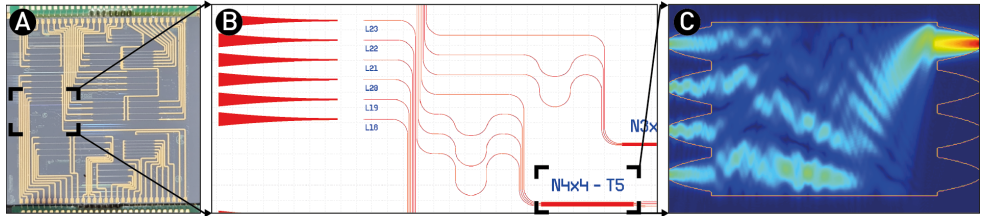


Figure 3. The kernel nuller photonic chip fabricated using photo-lithography in silicon nitride (a) which contains 12 independent kernel-nulling architectures that include 3 and 4 input MMIs and measures 16×16 mm in size. The electrodes shown in yellow enable active on-chip phase control which is not covered in this work. The 4×4 MMI (b) which has been characterized in this work produces the phase offsets at the input waveguides and the coherent interferometric beam combinations required by M. A beam propagation model (c) shows how the multiple inputs interfere inside the MMI cavity producing one bright output and three nulled outputs.

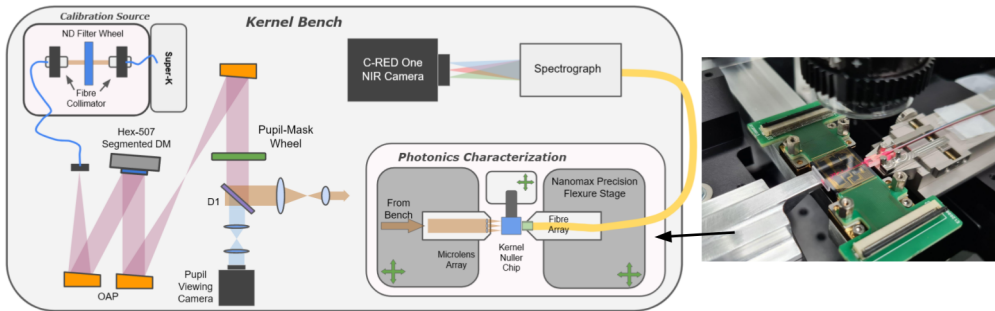


Figure 4. Schematic of the kernel test bench at Observatoire de la Côte d'Azur used to characterize the photonic chip (shown in right picture).

2.2 The photonic chip

The kernel-nulling photonic chip shown in Fig. 3(a) was fabricated using a silicon nitride (SiN) platform and has a design central wavelength of $1.55 \mu\text{m}$. The incident mode of standard SMF-28e optical fiber cables are efficiently converted to the single-mode waveguide core size of $\sim 1 \mu\text{m}$ at each input and output by waveguide tapers written on-chip. The high mode confinement of this SiN platform enables a more complex waveguide routing with low loss and a denser packing of the multi-mode interference (MMI) couplers that implement the input phase offsets and beam combinations required by M. Thus this 16×16 mm chip contains 12 independent kernel-nulling architectures that include 3 and 4 input MMIs.

MMI's are photonic devices that excite multiple modes in a wide waveguide segment which is referred to as the MMI cavity (see Fig. 3(c)). Light injected into the MMI cavity undergoes constructive and destructive interference such that the light periodically forms localised points of intensity that can then be segregated into multiple output waveguides. The 4×4 MMI shown in Fig. 3(c) has light launched into the four input waveguides and will redirect the light of an on-axis source to a bright output and split evenly the light of an off-axis source in each of the nulled outputs with minimal loss. The theory of light propagation in an MMI is described further in Ref. 8.

3. CHARACTERIZATION OF A PHOTONIC KERNEL-NULLER

3.1 The kernel test bench

The 4-input kernel-nuller was characterized on a similar experimental bench setup to that used for the 3-input kernel-nuller⁶ and for convenience is briefly set out here. Broadband light ($0.4\ \mu\text{m}$ - $2.2\ \mu\text{m}$) from a supercontinuum source is injected into the bench by a photonic crystal fibre (PCF) which is single-mode over a broad wavelength range with a constant mode-field diameter. The light beam then goes through a computer controlled filter wheel which houses several neutral density (ND) and wavelength filters. The total flux output from the supercontinuum can be too high for the detector used and so we modify the intensity of the beam by applying the ND filter with the appropriate optical density. The re-injection of the beam into the PCF prevents the downstream transmission of any wavefront aberrations induced by the ND filter as these are spatially filtered out. The beam is then reflected onto a deformable mirror (DM) by an off-axis parabolic mirror (OAP). The DM (Boston Micromachines Hex-507) divides the beam into 169 hexagonal segments, each of which has individual tip-tilt ($\pm 3\ \text{mrad}$) and piston ($\pm 2\ \mu\text{m}$) control with a modulation speed of $>25\ \text{kHz}$. Tip-tilt control is used to maximise the injection of the light into the chip input waveguides and piston control for the wavefront modulation between them. Following the DM, the beam is reflected via a set of OAPs onto a mask wheel which hosts numerous masks including a brass laser-cut mask consisting of four $620\ \mu\text{m}$ sized holes. This mask which forms the primary pupil for the setup blocks all but four active DM segments thus preventing unwanted light from entering the photonic chip and propagating through to the outputs. Stepper actuators are used to align these holes with the active DM segments and this is monitored in real-time with the pupil viewing camera at visible wavelengths. Immediately following the mask is a dichroic beam-splitter which reflects the visible light ($< 1\ \mu\text{m}$) and transmits the NIR ($> 1\ \mu\text{m}$). In the reflected beam path, a set of achromatic doublet lenses demagnify and re-image the pupil on the the pupil viewing camera. In the transmitted beam path, the pupil from the bench is re-imaged onto a microlens array (MLA) via a pair of NIR achromatic doublet lenses, which reduce the mask-hole size from $620\ \mu\text{m}$ to $\sim 124\ \mu\text{m}$. The MLA is aligned so that each of the four mask-holes overlap a single MLA lenslet of diameter $127\ \mu\text{m}$. The MLA forms four focal spots at the chip's input, and the chip is translated so that the light is injected into the corresponding chip input waveguides. The light propagates through the chip towards the output waveguides where a fiber array is aligned, coupling the light into individual fibers to be redirected to the spectrograph. A pair of high-precision Nanomax 6-axis flexure stages are used to align the MLA and the output fiber array to the photonic chip, which itself is on a 3-axis precision translation stage.

The light from the four separate output fibers are injected into the spectrograph from a fiber array holder attached to a single-axis translation stage. The translation stage which is mounted on a large right angle bracket allows for the vertical alignment of the light beams being fed into a 2 inch collimating lens (achromatic doublet). The fibre ends are firmly fixed at distance approximately equal to the focal length of $75\ \text{mm}$. The collimated beams then travel through to an F2 equilateral dispersive prism that sits on top of a manual rotation stage. This stage ensures that the light beams are incident with the prism such that the angle of minimum deviation can be achieved. The dispersed light from the prism is focused onto the detector (C-RED One Camera) by a second achromatic doublet lens ($F = 400\ \text{mm}$) via a beam steering mirror. The spectra are measured across a spectral range of $\lambda = 1.20 - 1.75\ \mu\text{m}$, a resolution of $\Delta\lambda = 5.2\ \text{nm}$ and a linear dispersion of $2.38\ \text{nm/pix}$. The detector records the flux count (summed over a 4 pixel bin width) at each measurement frame which is then converted to a normalized count by dividing by the total summed flux of all four outputs

3.2 How to measure the complex nulling matrix

To experimentally measure the complex nulling matrix M_E of the 4×4 MMI, we acquired two types of data sets for seventeen channels spanning from 1.4 to $1.6\ \mu\text{m}$. First are incoherent scans where light is injected into only one nuller input at a time and the DM segment for the active input is then pistoned over a $\pm 2000\ \text{nm}$ range. Next are pairwise coherent scans where each pair of nuller inputs defines a "baseline". The six baselines in turn are activated by switching on the relevant pair with one of the input's used as a reference and the corresponding input pistoned over a $\pm 2000\ \text{nm}$ range.

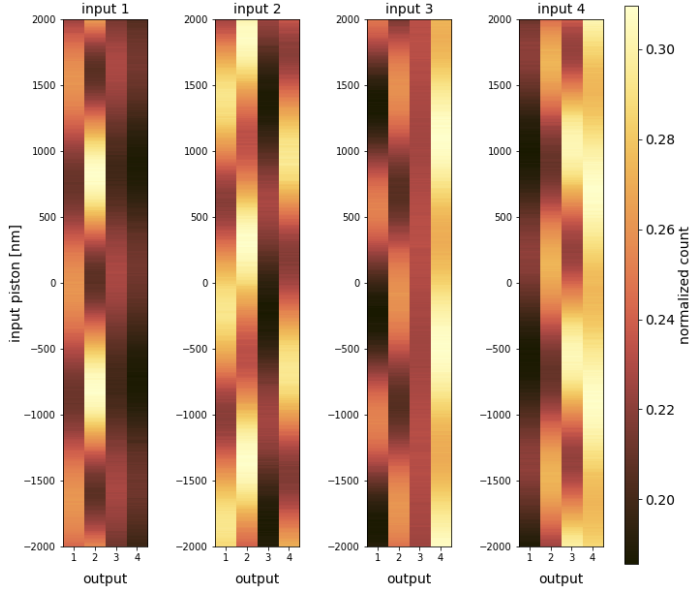


Figure 5. Incoherent phase scans at 1550 nm which show the variation in intensity for the four outputs of the chip as the phase is pistoned on input 1, 2, 3 & 4 respectively over a ± 2000 nm range.

The incoherent scans are used to measure the amplitude terms $a_{k,n}$ of \mathbf{M}_E at each wavelength and are computed as follows: for each pistoned input n , the intensity recorded by the detector at output k is $\mathbf{I}_{k,n}$ so that $a_{k,n} = \sqrt{\mathbf{I}_{k,n}}$. Fig. 5 shows the variation in intensity for the four outputs of the chip as the phase is pistoned on a single input waveguide. In the figure, four cases are shown where only one nuller input is active at a time. We observe an uneven splitting ratio between the four outputs and this can be attributed to fabrication imperfections in the chip and coupling losses at the MMI interface.

The pairwise coherent scans are used to measure the phase relationship $\phi_{k,n}$ between a pair of inputs. The phase angle for each pair is found through a non-linear least squares fit of the corresponding fringes (see Fig. 7). The phase angles between all four inputs are extracted from baselines 1-2($\phi_{k,2}$), 1-3($\phi_{k,3}$) & 1-4($\phi_{k,4}$). The other input combinations (2-3, 2-4, & 3-4) are linear combinations of the ones already measured and provide no additional information, but can be used to confirm the phase measurements from the primary baselines. Input 1 is used as a reference and left untouched and the corresponding input is pistoned. The measured phase offsets are combined in an array:

$$\phi_{k,n} = \begin{bmatrix} 0 & \dots & 0 \\ \phi_{1,2} - \phi_{k,2} & \dots & \phi_{k,2} - \phi_{k,2} \\ \vdots & & \vdots \\ \phi_{1,n} - \phi_{k,n} & \dots & \phi_{k,n} - \phi_{k,n} \end{bmatrix} \quad (6)$$

with the rows representing the inputs and the columns representing the outputs. Output 4 is the bright output and all input phases are combined constructively at this output. Therefore, we subtract the input phases from output 4 from the respective input phases at the other outputs. This array now represents $\phi_{k,n}$ and is applied for the various spectral channels to construct the CMP shown in Fig. 8. We observe from this plot that the 4x4

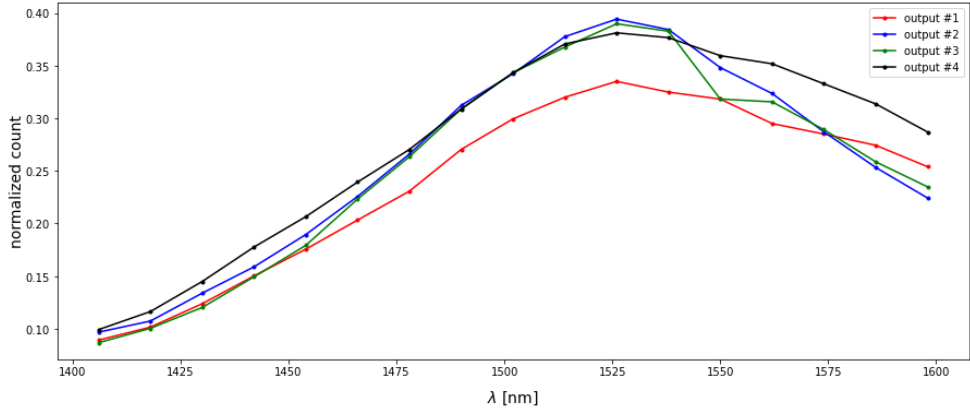


Figure 6. Flux count in output 1, 2, 3 & 4 as a function of wavelength. For all outputs the maximum flux is obtained at 1526 nm.

MMI performs best around the design central wavelength of 1550 nm, with performance degrading at higher and lower wavelengths.

The real and imaginary part of the complex amplitudes at each input/output are written as $a_{k,n} \cos \phi_{k,n} + a_{k,n} \sin \phi_{k,n}j$, so that the experimental complex nulling matrix is then equal to:

$$\mathbf{M}_E = \begin{bmatrix} a_{1,1} \cos \phi_{1,1} + a_{1,1} \sin \phi_{1,1}j & \cdots & a_{1,n} \cos \phi_{1,n} + a_{1,n} \sin \phi_{1,n}j \\ \vdots & & \vdots \\ a_{k,1} \cos \phi_{k,1} + a_{k,1} \sin \phi_{k,1}j & \cdots & a_{k,n} \cos \phi_{k,n} + a_{k,n} \sin \phi_{k,n}j \end{bmatrix} \quad (7)$$

\mathbf{M}_E completely characterizes the instrumental behaviour which will include the physical differences in optical path through the MMI for the 4 inputs. This could either be internal (manufacturing imperfections in the waveguides) or external (bulk optics prior to injecting into the chip). As the response of the nuller is sensitive to these optical path variations we can therefore calibrate them out of the final measurements. A separate \mathbf{M}_E was computed for each of the 17 spectral channels and the nuller response matrix at 1550 nm was found to closely match the theoretical \mathbf{M} .

4. KERNEL-NULLING

The primary aim of this work is to experimentally confirm the self-calibration properties of the kernel-nuller architecture with the 4x4 MMI. To demonstrate this, we use the same test bench setup as described in Sec. 3. Before any new measurements are taken, the photonic chip is re-aligned to mitigate any drift caused by the laboratory air conditioning. We also perform an injection optimization routine to find the optimal coupling location of the four MMI inputs. Misalignment of the photonic chip as well as read out noise from the detector are common contributing factors to flux leakage in the nulled outputs. To estimate the effect of the detector noise, the nulled outputs are recorded over 5,000 frames with no input light. The mean and standard deviations of the distributions for outputs 1 - 3 are: $\mu_{RN1} = -1.04 \times 10^{-4}$, $\sigma_{RN1} = 6.87 \times 10^{-4}$; $\mu_{RN2} = -1.11 \times 10^{-4}$, $\sigma_{RN2} = 6.93 \times 10^{-4}$; $\mu_{RN3} = -1.44 \times 10^{-4}$, $\sigma_{RN3} = 6.89 \times 10^{-4}$.

Optical path differences (OPDs) between the inputs may also lead to flux leakage in the nulled outputs and a reduction in intensity at the designated bright output. We can compensate for these OPDs by finding the piston

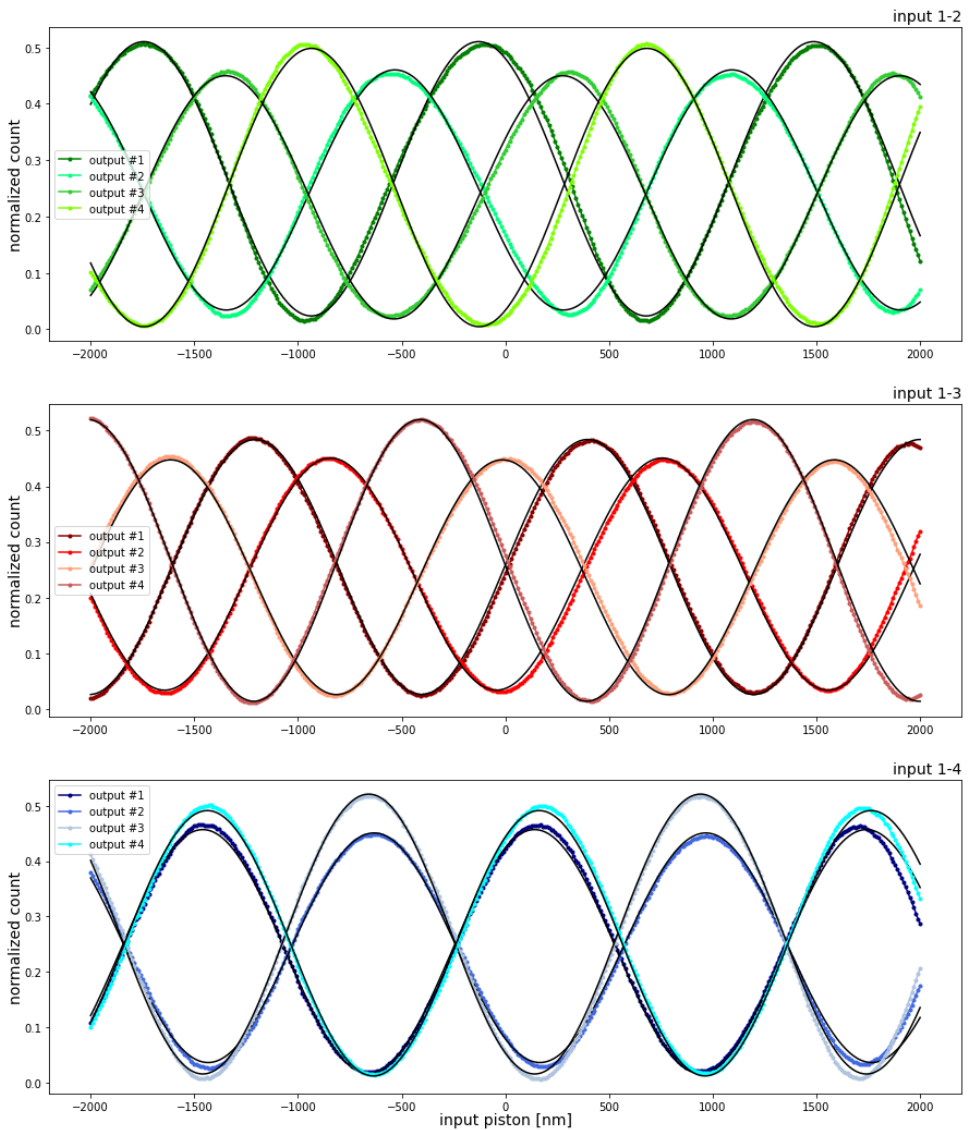


Figure 7. Pairwise coherent scans at 1550 nm for inputs 1-2 (a), 1-3 (b) & 1-4 (c). The pairwise coherent scans are used to measure the phase relationship $\phi_{k,n}$ between a pair of inputs. The phase angle for each pair is found through a least squares fit of the corresponding fringes. The colored curves in each plot are the data and the black curve is the fitted model.

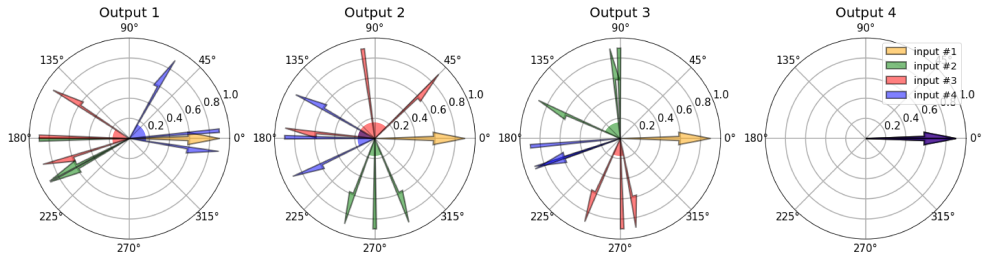


Figure 8. Experimental broadband complex matrix plot of the four nuller outputs of the 4x4 MMI. Input 1 is the phase reference so that the phases of the different electric fields sampled by the other inputs are measured relative to this reference. For input 2, 3 & 4, the solid line depicts the phase at 1550 nm which is the design central wavelength of the MMI. For each of these inputs, the left and right half arrows represent the phase at 1406 nm & 1598 nm respectively. Output 4 is set as the bright output, with all inputs combined constructively.

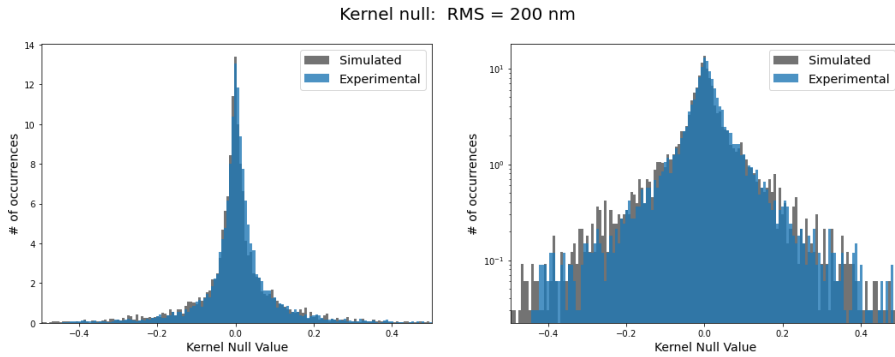


Figure 9. Statistical distribution of the measured kernel-null.

values to apply on the active DM segments that will bring the device as close as possible to a zero OPD state. This state which we'll refer to as the set point ensures that nulled outputs 1 - 3 are at their deepest nulls and bright output 4 has the maximum flux. To determine the set point, broadband light is injected into the chip and we simultaneously piston input 2, 3 & 4 over a range of ± 1000 nm in steps of 20 nm. Typically, input 1 is used as a reference and left untouched. At each step the flux on all four outputs at the 1550 nm spectral channel is recorded and this results in a multidimensional array for each output. The measured flux array for the three nulled outputs are merged to find the piston values of the active DM segments (inputs 2, 3 & 4) which produce the deepest combined null. These initial set point values also correspond to the maximum intensity recorded at the bright output. A higher resolution scan (range = ± 100 nm, step = 5 nm) is initiated from the initial set point values to better constrain the final set point. With every re-alignment of the chip, the set point changes, therefore it is pertinent to perform this function prior to every experimental cycle.

With the 4x4 MMI now brought to its set point, the nulled outputs are recorded over 5,000 frames with broadband light. The mean of these distributions are used to estimate the raw instrumental null values. For outputs 1 - 3 the null values and associated standard deviations are: $n_1 = 1.01 \times 10^{-2}$, $\sigma_{n1} = 6.70 \times 10^{-4}$, $n_2 = 1.10 \times 10^{-2}$, $\sigma_{n2} = 9.56 \times 10^{-4}$, $n_3 = 1.20 \times 10^{-2}$, $\sigma_{n3} = 8.00 \times 10^{-4}$. We then use the DM to apply 200 nm RMS residual piston excursions drawn from a normal distribution to inputs 2, 3 & 4. The flux is recorded on all four outputs for a series of 5,000 frames. At each measurement frame the intensity recorded by the detector at output k is I_k . Using Eq. 3 we can then compute our kernel and plot its distribution as shown in Fig. 9. In this

figure we also show the kernel-null distribution resulting from a Monte Carlo (MC) simulation of the 4x4 MMI experiencing the same phase perturbations. The MC model uses \mathbf{M}_E determined in Sec. 3 and here we see that this matches well with our actual experimental results. Because kernels can take negative values we observe a symmetrical distribution that is non-Gaussian about the median ($\kappa = 3.6 \times 10^{-3}$).

5. CONCLUSIONS

Kernel-nulling interferometry is a promising method to directly image high contrast exoplanets. The high angular resolving power provided by the four VLTI UTs can aid this endeavour. While the traditional approach is to use bulk-optics based interferometers, here we present a photonic approach where all the necessary routing, beam splitting, and recombination is performed within a planar silicon nitride (SiN) photonic chip via multi-mode interference (MMI) couplers. In this work, we have validated the kernel-nuller concept by experimentally creating a self-calibrating kernel-null and shown its behaviour under 200 nm RMS wavefront error. We characterized a 4x4 MMI and in this process demonstrated a method of determining the nuller response matrix. We have also presented transmission maps which show how a kernel-nuller can be used at the VLTI for the astrophysical detection of high-contrast companions. Having experimentally validated the 4x4 MMI, we can proceed to the more advanced 4x6 kernel-nulling architecture which also includes active on-chip phase control.

ACKNOWLEDGMENTS

The authors acknowledge the funding from the European Research Council (ERC) under the European Union's Horizon 2020 research and innovation program (grant agreement CoG - 683029).

REFERENCES

- [1] Martinache, F. and Ireland, M. J., "Kernel-nulling for a robust direct interferometric detection of extrasolar planets," **619**, A87 (Nov. 2018).
- [2] Norris, B. R. M., Cvetojevic, N., Lagadec, T., Jovanovic, N., Gross, S., Arriola, A., Gretzinger, T., Martinod, M.-A., Guyon, O., Lozi, J., Withford, M. J., Lawrence, J. S., and Tuthill, P., "First on-sky demonstration of an integrated-photonic nulling interferometer: the GLINT instrument," **491**, 4180–4193 (Jan. 2020).
- [3] Martinod, M.-A., Norris, B., Tuthill, P., Lagadec, T., Jovanovic, N., Cvetojevic, N., Gross, S., Arriola, A., Gretzinger, T., Withford, M. J., Guyon, O., Lozi, J., Vievard, S., Deo, V., Lawrence, J. S., and Leon-Saval, S., "Scalable photonic-based nulling interferometry with the dispersed multi-baseline GLINT instrument," *Nature Communications* **12**, 2465 (Jan. 2021).
- [4] Jennison, R. C., "A phase sensitive interferometer technique for the measurement of the Fourier transforms of spatial brightness distributions of small angular extent," **118**, 276 (Jan. 1958).
- [5] Laugier, R., Cvetojevic, N., and Martinache, F., "Kernel nullers for an arbitrary number of apertures," **642**, A202 (Oct. 2020).
- [6] Cvetojevic, N., Martinache, F., Chingaipe, P., Laugier, R., Lawniczuk, K., Broeke, R. G., Ligi, R., N'Diaye, M., and Mary, D., "3-beam self-calibrated Kernel nulling photonic interferometer," *arXiv e-prints*, arXiv:2206.04977 (June 2022).
- [7] Bracewell, R. N. and MacPhie, R. H., "Searching for nonsolar planets," **38**, 136–147 (Apr. 1979).
- [8] Soldano, L. B. and Pennings, E. C. M., "Optical multi-mode interference devices based on self-imaging: principles and applications," *Journal of Lightwave Technology* **13**, 615–627 (Apr. 1995).

2 Characterisation results continued

I begin this section by reviewing the properties of the simplified four-input nuller that produces four outputs, two of which can be combined in post-processing to form a kernel-null. This nuller is manufactured out of a silicon nitride (Si_3N_4) MMI, whose initial characterisation was presented in [Chingaipé et al. \(2022\)](#). Here, I further investigate the impact of the phase set-point (see Chapter 6) on the beam splitting ratios and phase deviations, initially focusing on the action of the device at $1.55 \mu\text{m}$. This leads to a derivation of the experimental response matrix \mathbf{M}^E , which is analogous to the visibility-to-pixel matrix (V2PM; [Tatulli et al. 2007](#)) in ABCD combiners. As \mathbf{M}^E completely characterises the instrumental behaviour, one can exploit it to perform Monte Carlo simulations of the nuller experiencing phase perturbations. I compare the results of these simulations under 200 nm RMS residual piston with the actual experimental data. To conclude this section, I present the spectral behaviour of the 4×4 MMI.

2.1 Nuller response matrix

Our nuller is an interferometric recombiner acting on four electric fields \mathbf{U} that, for astrophysical applications, would be collected by separate telescopes or sampled parts of a single aperture to be eventually coupled into the MMI access waveguides. The application of phase shifts on the different input electric fields, their splitting and linear combination can conveniently be represented by a single, complex, so-called nuller response matrix, noted \mathbf{M} . A detector located downstream of the nuller simultaneously records the intensity \mathbf{I} of the resulting outputs, that are computed as: $\mathbf{I} = \|\mathbf{M} \cdot \mathbf{U}\|^2$. The nuller that was specified is described by the following 4×4 complex matrix:

$$\mathbf{M} = \frac{1}{2} \times \begin{bmatrix} 1 & -1 & -1 & 1 \\ 1 & e^{\frac{3\pi j}{2}} & e^{\frac{\pi j}{2}} & -1 \\ 1 & e^{\frac{\pi j}{2}} & e^{\frac{3\pi j}{2}} & -1 \\ 1 & 1 & 1 & 1 \end{bmatrix}. \quad (7.1)$$

Fig. 61 provides a visual representation of the desired reorganisation of the input electric fields (represented by coloured arrows) in the complex plane that is summarised by this matrix. Since one can only record the intensity (absolute square), the setup is insensitive to any global phase shift applied to an output (or row of \mathbf{M}), which would correspond to an overall rotation of the arrows in a

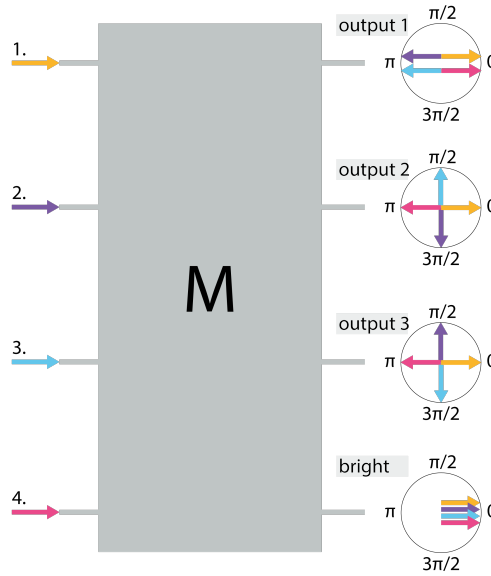


Figure 61: Schematic representation of an ideal four-input kernel-nuller beam combiner that is described by the complex matrix M and produces four nuller outputs. Distinct arrangements of the input electric field are combined to obtain the respective outputs, depicted here by complex matrix plots (Laugier et al. 2020). The input phase is represented by a colored arrow whose length encodes the amplitude. At each output, the resulting electric field is the sum of all arrows. In outputs 1-3, the on-axis light is nulled when the electric fields sum up to zero. For instance, output 1 has two arrows with a zero phase shift and two of equal amplitude with a π phase shift, adding together to form a classical Bracewell null. From these plots we can also see that outputs 2 & 3 are mirror images of each other, an attribute that allows them to form a kernel-null. The arrows sum up constructively to produce a bright output (where most of the on-axis light is directed).

complex matrix plot (visible in the right hand side of Fig. 61). Only relative phase offsets introduced by the device between the inputs matter, and our convention will be to take input 1 as the phase reference, explaining why the first column of M only contains 1, or equivalently, why all yellow arrows in Fig. 61 remain aligned with the real axis of the complex plane.

Output one of the device is a “conventional” null, where an equal fraction of input 2 and 3 are π phase-shifted so as to destructively interfere with the same fraction of input 1 and 4. The following two outputs both result in nulls (with the sum of the four arrows leading back to zero), though they differ in the applied input phase shifts that are multiples of $\pi/2$. These outputs, which are analogous to the double Bracewell (Angel & Woolf 1997, Lay 2004) observables, are mirror images (or complex conjugates) of each other, an attribute that allows them to form a kernel-null (see Laugier et al. 2020). Output four (bright output) is an in-

phase constructive recombination of the inputs. For this 4-input kernel-nuller, M represents a realisable yet lossless, and therefore idealised implementation.

2.2 Characterisation of a 4x4 MMI

I will now describe an experimental method to determine the beam splitting ratios and phase deviations of a non-ideal 4×4 MMI, and show how these values are used to reconstruct the experimental response matrix M^E at the design central wavelength of $1.55 \mu\text{m}$. Besides the characterisation of the device, I also demonstrate its self-calibration properties.

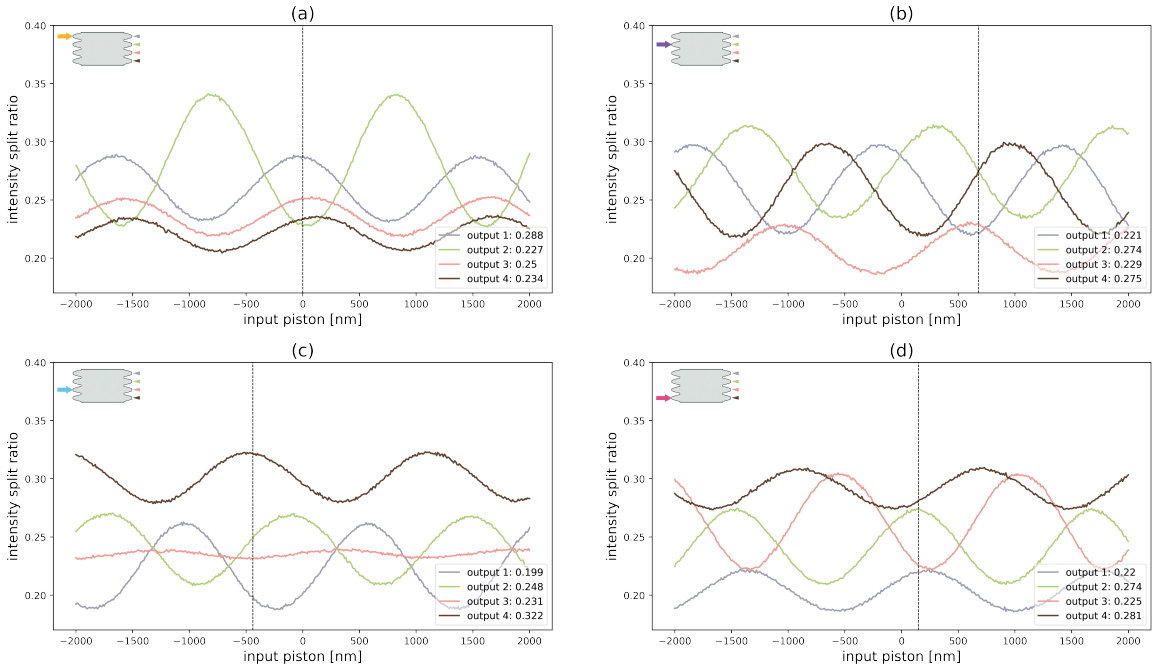


Figure 62: Variation of the beam splitting ratio at the outputs of the 4×4 MMI over a ± 2000 nm OPD modulation. Broadband light ($0.4 \mu\text{m} - 2.2 \mu\text{m}$) from a supercontinuum source is injected into a single input n and a mechanical stroke of ± 1000 nm is applied on the DM segment of the active input in increments of 5 nm. At each output k , the intensity $I_{k,n}$ is measured at the $1.55 \mu\text{m}$ spectral channel and the splitting ratio $a_{k,n}$ is computed with Eq. 7.2. The variation in splitting shown here is when (a) input one is pistoned (which measures $a_{k,1}$), (b) input two is pistoned ($a_{k,2}$), (c) input three is pistoned $a_{k,3}$ and (d) input four is pistoned ($a_{k,4}$). The active MMI input is depicted by a colored arrow and is shown inset in each figure. Black vertical dashed lines in the plots mark the phase set-point {input one: 0 nm, input two: +680 nm, input three: -440 nm, input four: +150 nm} and the legend shows the splitting at these OPD offsets for each output.

2.2.1 Beam splitting ratios

Fabrication defects introduce small variations in the dimensional parameters of an MMI coupler that result in imperfect splitting ratios. The idealised device (see Eq. 7.1) features a single common 0.5 factor, which is equivalent to a 0.25 intensity split ratio. Measuring the device's actual splitting ratios is done by injecting light into each MMI input n in turn. A mechanical stroke of ± 1000 nm (which translates into a ± 2000 nm OPD modulation) is applied on the DM segment of the active input in increments of 5 nm, and at each output k the intensity $I_{k,n}$ is measured. The splitting ratio $a_{k,n}$ is computed as:

$$a_{k,n} = \frac{I_{k,n}}{\sum_k I_{k,n}}. \quad (7.2)$$

Figure 62 shows that the splitting is a function of OPD, and we can observe that $a_{3,3}$ ($\pm 1\%$) fluctuates the least and $a_{2,1}$ ($\pm 14\%$) has the largest variation. Therefore, rather than taking the average for each output, I use the values at the phase set-point (marked by the black vertical dashed lines in each of the four plots) as the splitting ratios at the design central wavelength (see insets of Fig. 62), which range from 0.199 to 0.322, with a standard deviation of 0.04 and an average of 0.25.

2.2.2 Phase deviations

The response of an MMI coupler is also dependent on the relative phase between the different inputs and therefore of the propagating modes, which are affected by variations in the effective refractive index. To measure the relative phase $\phi_{k,n}$ applied by the device to the different input electric fields, I resort to study the evolution of the output intensities when simultaneously injecting light into pairs of inputs. With input 1 used as a phase reference, we are left with three degrees of freedom, and capture the behaviour of the device when injecting light into inputs 1-2 (which measures $\phi_{k,2}$), then inputs 1-3 ($\phi_{k,3}$) and finally inputs 1-4 ($\phi_{k,4}$). Using the upstream DM, I apply a ± 1000 nm mechanical stroke in increments of 5 nm (on input n , where $n = 2, 3, 4$) and record the intensity modulation of all outputs for the primary input pairs. The result of this exploration is represented in Fig. 63 where the black vertical dashed lines mark the OPD offset values that bring the device as close as possible to a zero OPD state. Even though the phase set-point does not perfectly match the minimum flux for all nulled outputs, this is still remarkable for a non-trivial 4×4 MMI.

7 kernel-nulling for the direct detection of exoplanets

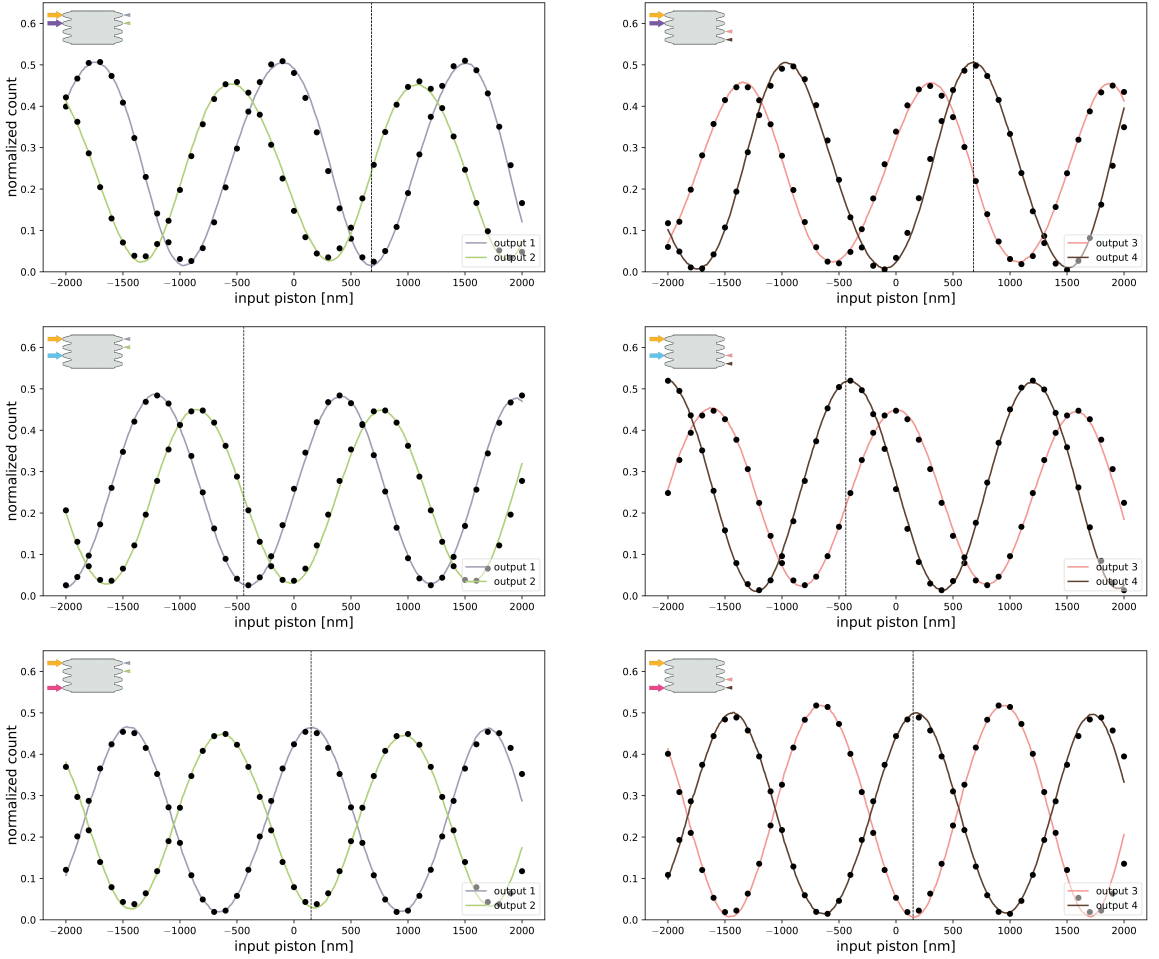


Figure 63: Intensity modulations at the outputs of the 4×4 MMI over a ± 2000 nm OPD modulation. The plots of the outputs are split in two on each row so as to make the intensity modulations, which are used to deduce the relative phase between the input fields, easier to interpret. To experimentally determine the relative phase, broadband light ($0.4 \mu\text{m} - 2.2 \mu\text{m}$) from a supercontinuum source is injected into pairs (1-2, 1-3 & 1-4) of input waveguides. Input one is set as the phase reference and a DM mechanical stroke of ± 1000 nm is applied on input n (where $n = 2, 3, 4$) in increments of 5 nm. At each output k , the intensity modulations are recorded (at the $1.55 \mu\text{m}$ spectral channel for this example), and whose phase $\alpha_{k,n}$ is retrieved by performing a non-linear least squares fit with the Python *curve_fit* routine from the *SCIPY* package. Coloured curves represent the data and the black dots depict the fitted model. The relative phase $\phi_{k,n}$ is computed with Eq. 7.3, and in the **Top Row**: $\phi_{k,2}$ is measured when input two is pistoned; **Middle Row**: $\phi_{k,3}$ when input three is pistoned; **Bottom Row**: $\phi_{k,4}$ when input four is pistoned. Black vertical dashed lines in the plots mark the phase set-point {input one: 0 nm, input two: +680 nm, input three: -440 nm, input four: +150 nm}. The active MMI inputs are depicted by coloured arrows and is shown inset in each figure.

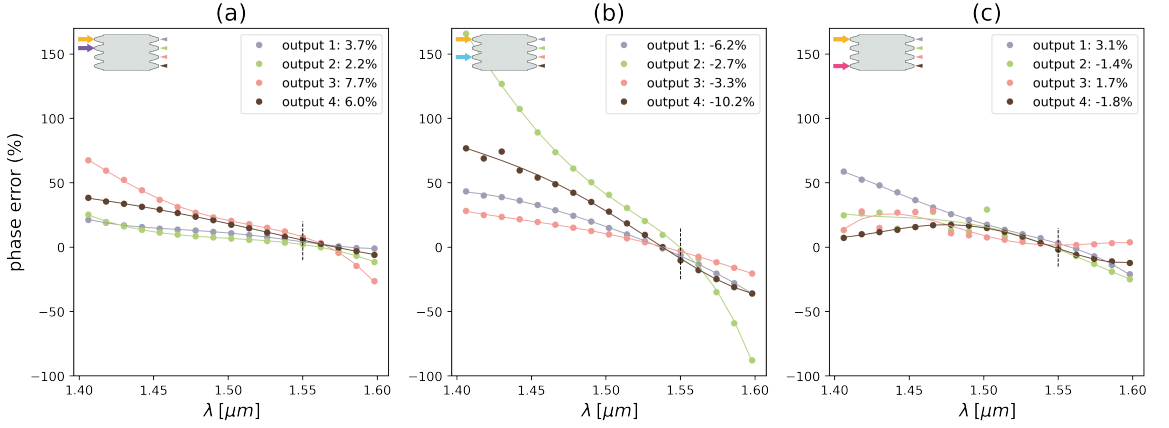


Figure 64: Variation of the relative phase error at the outputs of the 4×4 MMI for seventeen equally spaced spectral channels in the 1.4 - 1.6 μm range. The phase error, which has been computed at the phase set-point (see Eq. 7.3), is the deviation of the relative phase $\phi_{k,n}$ from the theoretical values specified in \mathbf{M} , and is shown for (a) $\phi_{k,2}$ (input two is pistoned), (b) $\phi_{k,3}$ (input three is pistoned), (c) $\phi_{k,4}$ (input four is pistoned). Black vertical dashed lines in the plots mark the design central wavelength of 1.55 μm and the legend shows the phase error at this wavelength for each output. Coloured dots depict the data and the curves represent the fitting of a fourth-order polynomial. The active MMI inputs are depicted by coloured arrows and is shown inset in each figure.

Considering that OPD offsets are applied in order to reproduce the specified design of the device, I take into account the accumulated input phase: $\varphi_n = 2\pi\rho_n/\lambda$, where ρ_n is the OPD offset at input n and λ is the wavelength of observation. Thus, $\phi_{k,n}$ is computed as:

$$\phi_{k,n} = \alpha_{k,n} + \varphi_n, \quad (7.3)$$

where $\alpha_{k,n}$ is the phase retrieved through a non-linear least squares fit (marked by black dots in Fig. 63) of the recorded intensity modulation at output k . In the top row of Fig. 63, $\phi_{1,2}$ is expected to be in phase opposition, $\phi_{2,2}$ & $\phi_{3,2}$ in quadrature, and $\phi_{4,2}$ in phase. Similar observations can also be made for the subsequent plots. Figure 64 represents the evolution of the phase error across the entire spectral band-pass of 1.4 - 1.6 μm . I measured phase errors at the design central wavelength (see inset of Fig. 64) ranging from -10.2% to 7.7%, with an average of -0.1%, which is remarkable for a non-trivial four-input/four-output device.

2.2.3 Experimental response matrix

The experimental response matrix of the device features 16 distinct complex coefficients $\mathbf{M}_{k,n}^E$ that can be split into an amplitude ($\sqrt{a_{k,n}}$) and a phase ($\phi_{k,n}$) term such that:

$$\mathbf{M}^E = \begin{bmatrix} \sqrt{a_{1,1}} & \sqrt{a_{1,2}}e^{j\phi_{1,2}} & \sqrt{a_{1,3}}e^{j\phi_{1,3}} & \sqrt{a_{1,4}}e^{j\phi_{1,4}} \\ \sqrt{a_{2,1}} & \sqrt{a_{2,2}}e^{j\phi_{2,2}} & \sqrt{a_{2,3}}e^{j\phi_{2,3}} & \sqrt{a_{2,4}}e^{j\phi_{2,4}} \\ \sqrt{a_{3,1}} & \sqrt{a_{3,2}}e^{j\phi_{3,2}} & \sqrt{a_{3,3}}e^{j\phi_{3,3}} & \sqrt{a_{3,4}}e^{j\phi_{3,4}} \\ \sqrt{a_{4,1}} & \sqrt{a_{4,2}}e^{j\phi_{4,2}} & \sqrt{a_{4,3}}e^{j\phi_{4,3}} & \sqrt{a_{4,4}}e^{j\phi_{4,4}} \end{bmatrix}. \quad (7.4)$$

With the beam splitting ratios and the relative phases I have experimentally determined in Sec. 2.2.1 and Sec. 2.2.2 respectively, I computed the response matrix at the design central wavelength as:

$$\mathbf{M}^{1.55\mu\text{m}} = \begin{bmatrix} 0.54 & -0.47 - 0.05j & -0.49 + 0.1j & 0.48 + 0.03j \\ 0.47 & 0.05 - 0.52j & 0.02 + 0.48j & -0.52 + 0.02j \\ 0.45 & -0.06 + 0.49j & -0.07 - 0.47j & -0.57 - 0.03j \\ 0.47 & 0.52 + 0.05j & 0.47 - 0.08j & 0.53 - 0.02j \end{bmatrix}, \quad (7.5)$$

In section 2.2.4, I demonstrate the self-calibration properties of the device, and compare the actual experimental results to Monte Carlo simulations performed with this matrix that completely characterises the instrumental behaviour.

2.2.4 Demonstration of self-calibration

With the device brought to its set-point (see Chapter 6), light is injected into the four MMI inputs and the intensity of the outputs is recorded over 5,000 frames. For each nuller output k , a detector records for an integration time t , the null-depth $N_k(t)$ as:

$$N_k(t) = \frac{I_k(t) - I_{k,d}(t)}{I_4(t) - I_{4,d}(t)}, \quad (7.6)$$

where $I_{k,d}(t)$ is the detector noise that is recorded over 5,000 frames with no input light, $I_4(t)$ is the intensity of the bright output, and $I_{4,d}(t)$ is the readout noise registered in this output. In the Top Panel of Fig. 65 I present the null-depth distribution of the nulled outputs and subsequent kernel-null distribution that is given as: $\kappa(t) = N_2(t) - N_3(t)$. Laugier et al. (2020) shows that the linear combination of

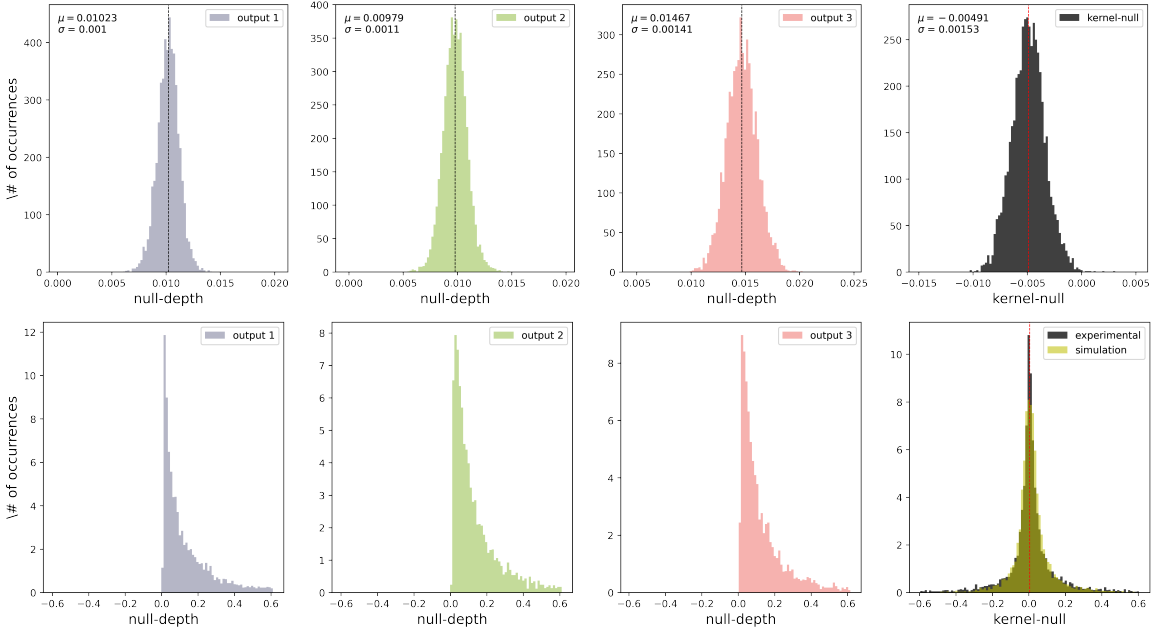


Figure 65: Statistical distribution of the experimentally measured instrumental null-depth at the nulled outputs of the 4×4 MMI and the subsequent kernel-null distribution at $1.55 \mu\text{m}$. **Top Panel:** Shows the measured distributions at the phase set-point {input one: 0 nm, input two: +680 nm, input three: -440 nm, input four: +150 nm}, which is used as a zero-point for all null-depth measurements. For each output k , the median μ (shown inset in each figure) of the distributions is used to estimate the instrumental null N_k values and is shown by the black vertical dashed line. μ is marked by the red vertical dashed line for the kernel-null distribution, which is given as $\kappa = N_2 - N_3$. The associated standard deviation σ of the respective distributions is also shown inset in each figure. **Bottom Panel:** Shows the measured distributions with 200 nm RMS. The distributions in the nulled outputs become skewed and would rely on NSC to retrieve the astrophysical null-depth. By comparison, the self-calibrating properties of the kernel-null are apparent as the distribution is symmetric with relatively straightforward statistics. The Monte Carlo simulations of $M^{1.55\mu\text{m}}$ under 200 nm RMS show a close fit with the experimental result.

a conjugate pair of nulled outputs produces a kernel-null that is robust to phase perturbations. In the absence of residual piston errors, one can simply estimate the instrumental null and the kernel-null values by computing the median μ of the respective distributions, marked by the vertical dashed lines. The 0.488×10^{-2} imbalance between the kernel forming outputs (i.e., N_2 & N_3) can be attributed to unavoidable optical losses through the device and a misalignment between the chip output waveguide/fibre array interface in the experimental setup. We can also observe that despite dark subtraction, the position of the distributions are shifted, while the standard deviation σ remains stable.

In reality, a nuller will not reside at the set-point due to phase errors induced by the atmosphere or optics. For VLTI/GRAVITY, [Lacour et al. \(2019\)](#) reports fringe tracker residuals of ~ 200 nm on the UTs and ~ 100 nm for the ATs. To demonstrate the benefit of the kernel-nuller architecture, I apply phase perturbations on the active DM segments and measure the null-depth at the outputs. The Bottom Panel of Fig. 65 shows the null-depth distributions recorded (over 5,000 frames) from the nulled outputs when the input beams experience OPD fluctuations drawn from a Gaussian distribution with a 200 nm standard deviation. We can see that the null-depth distributions are asymmetric, trailing off more sharply on one side than the other. On-sky observations with PFN and GLINT exhibit such skewed distributions that rely on the NSC procedure I described in Chapter 2 to deduce the astrophysical null-depth. By comparison, the self-calibrating properties of the kernel-null are apparent as the distribution is symmetric with relatively straightforward statistics which allow for a direct interpretation. It is this reality that motivated the kernel-nuller architecture, designed so that at any instant, simultaneously recorded values for the nulled outputs can be combined to form kernel-nulls, disentangling genuine astrophysical signals from seeing induced light leakage. The Monte Carlo simulations of $M^{1.55\mu\text{m}}$ under 200 nm RMS show a close fit with the experimental result.

2.3 Spectral behaviour of a 4x4 MMI

According to the self-imaging effect, every wavelength that enters the MMI cavity produces a direct or mirrored image of itself periodically. A full description of this self-imaging can be explored using guided-mode propagation analysis, proposed by [Ulrich \(1975\)](#) for the formulation of periodic imaging. This method decomposes an input field into all guided mode fields and propagates each of these modes independently. For each wavelength, the output field at any propagation length along the multimode cavity can be determined by recombining the guided modes to that length. Typically, the coupling length L_c between the first

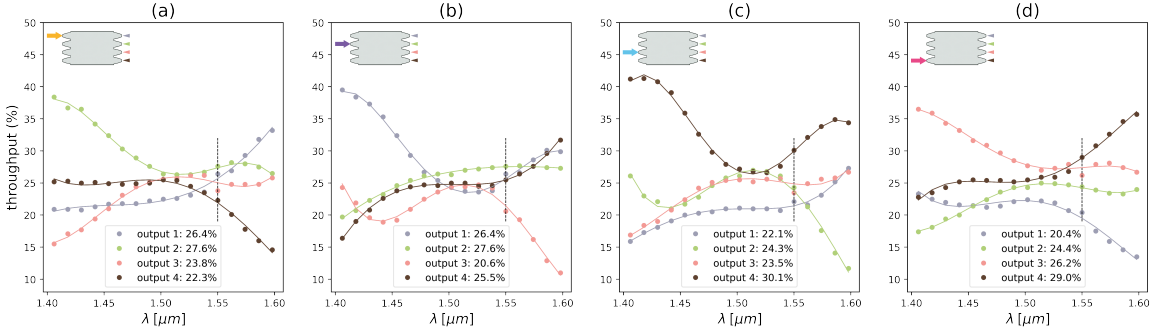


Figure 66: Variation of the splitting ratios at the outputs of the 4×4 MMI for seventeen equally spaced spectral channels in the 1.4 - 1.6 μm range. The idealised device (see Eq. 7.1) features a single common 0.5 factor, which is equivalent to a 0.25 intensity split ratio. To experimentally determine the splitting ratios, broadband light (0.4 μm - 2.2 μm) from a supercontinuum source is injected into a single input n and the DM segment for the active input is pistoned with a step size of 5 nm over a ± 1000 nm range. At each output k , the intensity $I_{k,n}$ is measured and the splitting ratio $a_{k,n}$ is computed with Eq. 7.2 when (a) input one is pistoned (which measures $a_{k,1}$), (b) input two is pistoned ($a_{k,2}$), (c) input three is pistoned $a_{k,3}$ and (d) input four is pistoned ($a_{k,4}$). Black vertical dashed lines in the plots mark the design central wavelength of 1.55 μm and the legend shows the splitting ratios at this wavelength. Coloured dots depict the data and the curves represent the fitting of a fourth-order polynomial. The active MMI input is depicted by a coloured arrow and is shown inset in each figure.

two lowest-order modes, which require the longest propagation length in order to couple, is used as a characteristic dimension:

$$L_c = \frac{4nW^2}{3\lambda}, \quad (7.7)$$

where n is the effective refractive index and W is the effective width of the 4×4 MMI Si_3N_4 cavity at a wavelength λ . Since $L_c \propto 1/\lambda$, and in our design L_c is optimised for 1.55 μm , presumably the device properties will deteriorate at other wavelengths.

2.3.1 Chromatic amplitude and phase

Fig. 66 presents the beam splitting ratios (computed with Eq. 7.2) for each input into four outputs over the 1.4 - 1.6 μm range, where the splitting varies from -88 - 165%, with the least ideal occurring at the edges and the most favourable at 1.502 μm {input one: $\mu = 25.0$ & $\sigma = 1.48$, input two: $\mu = 25.0$ & $\sigma = 0.8$, input three: $\mu = 24.975$ & $\sigma = 2.32$, input four: $\mu = 24.975$ & $\sigma = 1.92$ }. The splitting is on average $\sim 25\%$ and only varies from 20 - 30% in the 1.478 - 1.55 μm range, just as it is at the design central wavelength (see inset of Fig. 66).

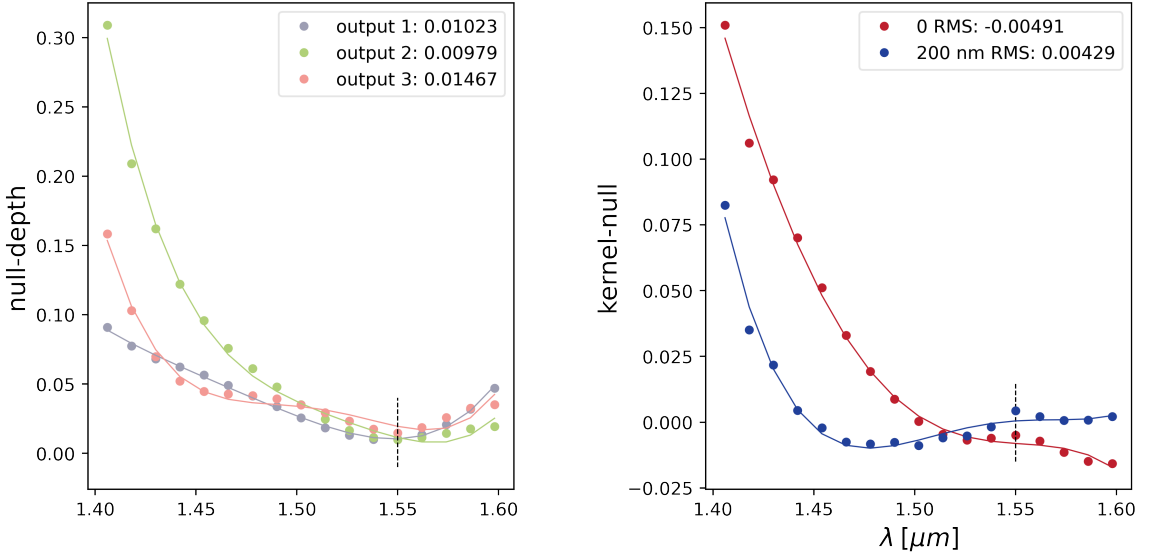


Figure 67: Variation of the experimentally measured instrumental null-depth and the subsequent kernel-null for seventeen equally spaced spectral channels in the 1.4 - 1.6 μm range. **Left Panel:** Shows the instrumental null for the nulled outputs at the phase set-point {input one: 0 nm, input two: +680 nm, input three: -440 nm, input four: +150 nm} of the 4 \times 4 MMI, which is used as a zero-point for all null-depth measurements. Coloured dots depict the data and the curves represent the fitting of a fourth-order polynomial. Black vertical dashed lines in the plot mark the design central wavelength of 1.55 μm and the legend shows the instrumental null at this wavelength for each output. **Right Panel:** Shows the kernel-null at the set-point and in the presence of 200 nm RMS residual piston. Coloured dots depict the data and the curves represent the fitting of a fourth-order polynomial. Black vertical dashed lines in the plot mark the design central wavelength of 1.55 μm and the legend shows the kernel-null at this wavelength.

By measuring the wavelength dependence of the phase error in the nulled outputs (see Fig. 64), I find that it varies from 0 - 80.5% over the 1.4 - 1.6 μm range, with a minimum average of $\sim 1.97\%$ at 1.514 μm and a maximum of $\sim 22.09\%$ at 1.406 μm . In the 1.478 - 1.55 μm range, the average phase error is $\sim 2.59\%$, with $\phi_{2,4}$ at 1.502 μm being an outlier in this approximation. This anomaly can be attributed to differential transmission caused by a drift in the alignment of the optics that comes from the laboratory air change cycle. An ISO-7 clean-room, in which the kernel test bench is installed, typically maintains 60-150 air changes per hour with a ceiling coverage of 15-25%. As such drifts would dominate our uncertainties, the characterisation measurements presented in section 2.2.1 and 2.2.2 are repeated 5 times.

Self-imaging depends on the interference of the different modes, and for it to occur (as shown in Fig. 37c), the amplitudes and phases of the guided modes must

fulfill the specific relations defined by \mathbf{M} . An MMI should provide the possibility to exploit a planet's photon flux if \mathbf{M} is achieved simultaneously for all wavelengths in a wide spectral band. The null-depth, which represents the contrast improvement between a star and a planet, can be used to determine how well \mathbf{M} is maintained across an operational bandwidth. Fig. 67 shows the null-depth of the nulled outputs and subsequent kernel-null that has been measured at the set-point of the 4×4 MMI and in the presence of 200 nm RMS residual piston. In the 1.478 - 1.55 μm range, the average null-depth for output 1 is 0.02176 (with a standard deviation $\sigma = 0.011$), 0.02955 ($\sigma = 0.018$) for output 2 and 0.02869 ($\sigma = 0.010$) for output 3. Meanwhile, the average kernel-null at the set-point is -0.00491 ($\sigma = 0.0015$) and 0.00429 ($\sigma = 0.4454$) under 200 nm RMS, though the salient point here is that there is a significant increase in the kernel-null uncertainty at the respective wavelengths with an increase in the piston error (as shown inset in the right Top & Bottom panel of Fig. 65). Indeed, the minimum null-depth for outputs 2 & 3, which combine to form a kernel-null, is found at 1.55 μm . However, as shown in Chapter 6, the null-depth measurements are optimised for this wavelength with the injection optimisation and set-point routines we perform.

With the complex matrix plots shown in Fig. 68 we can observe that $\mathbf{M}^{1.55\mu\text{m}}$ (Third row) closely matches the theoretical complex matrix \mathbf{M} (First row). The arrows are more or less equal in amplitude, and for the nulled outputs the opposite phases are almost identical. The design is of course to have perfect destructive interference in these outputs, however, phase and amplitude mismatch will affect the optical redirection of on-axis light toward the bright output, which can lead to some amount of light leakage, and therefore a finite extinction.

7 kernel-nulling for the direct detection of exoplanets

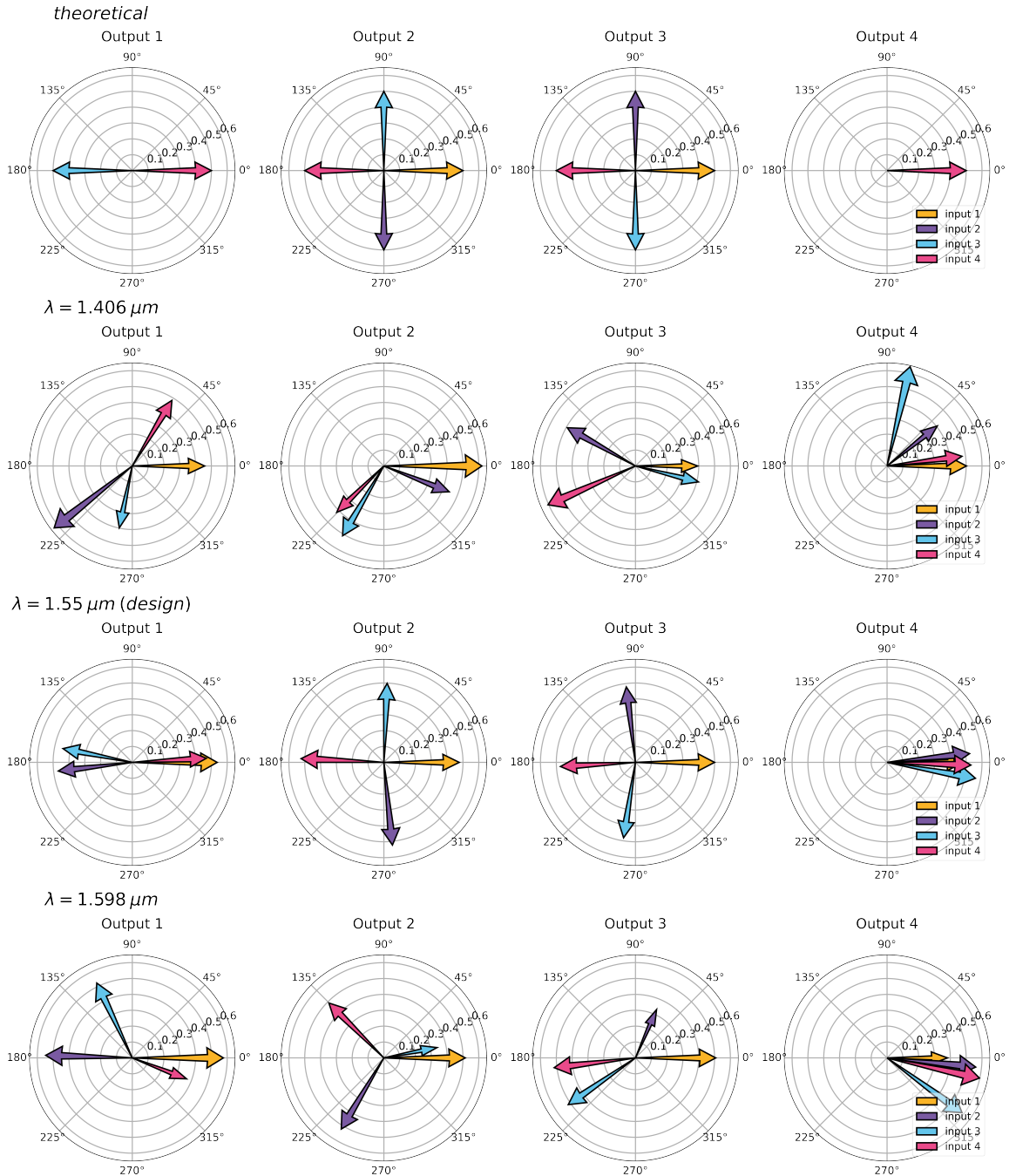


Figure 68: Complex matrix plots describing the theoretical \mathbf{M} and experimental nulling matrix \mathbf{M}_E that completely characterises the instrumental behaviour. The *First Row*: represents the theoretical complex matrix \mathbf{M} (Eq. 7.1); *Second Row*: \mathbf{M}_E at $1.406 \mu\text{m}$; *Third Row*: \mathbf{M}_E at the design central wavelength of $1.55 \mu\text{m}$; *Fourth Row*: \mathbf{M}_E at $1.598 \mu\text{m}$.

3 Summary

Kernel-nulling interferometry is a promising method to directly image high-contrast exoplanets in a region of the parameter space that has so far only been covered by indirect detection methods. The high angular resolving power provided by the VLTI can aid this endeavour. While the traditional approach is to use bulk-optics based interferometers, here I've presented a photonic approach where all the necessary routing, beam splitting, and recombination is performed within a planar silicon nitride (Si_3N_4) photonic chip via multi-mode interference (MMI) couplers. In this chapter, I have performed the spectral characterisation of a 4×4 MMI and described a method of determining the experimental nulling matrix which can be used to calibrate the device. I also validated the kernel-nuller concept by experimentally creating a self-calibrating kernel-null and demonstrated its behaviour under 200 nm RMS wavefront error.

Although this first prototype of the kernel nuller photonic chip was not fully optimised for broad-band use, the experimental nulling matrix derived at the design central wavelength does not deviate too much from the ideal scenario. I observed that the splitting ratios were affected by the value of the input electric phase. In the 1.478 - 1.55 μm range, where the average phase error is $\sim 2.59\%$, the splitting ratio varies from 20 - 30%. Even though this study is not finalised, the insights gained from these experiments will inform the design of the next generation of devices, whose behaviour can be achromatised. Besides, the overall response can be further improved by the active monitoring of the flux injected into the chip and bonding of the output fibres.

The scope of this experimental work was limited to demonstrating the non-ideal nature of a nuller, but is necessary in laying the foundations for future work that aims to mitigate the effects of amplitude and phase perturbations. This can include the use of kernel-nulling with data processing techniques such as NSC or deep neural networks (see [Norris et al. 2022](#)).

Chapter 8

Conclusions

15 years ago, a team of French astronomers yielded one of the most iconic images in astrophysics: a super-Jupiter orbiting β Pictoris. However, an image of a terrestrial planet in a terrestrial orbit remains an elusive goal that could be achieved with nulling interferometry as it can provide high-contrast observations at angles significantly smaller than those currently attainable. Such a nuller will require more than two sub-apertures, which not only enable a greater suppression of the on-axis source but also the implementation of nulling architectures that provide self-calibrating interferometric observables.

In this work, I have presented one such scheme —called kernel-nulling— that leads to a wider family of self-calibrating solutions that are applicable for ground or space-based interferometry. By taking into account baseline projection effects induced by Earth rotation, I was able to show the astrophysical potential of a four-input/seven-output kernel-nuller as the prime high-contrast imaging mode of the VLTI. With continued upgrades of the VLTI infrastructure, which will reduce fringe tracking residuals, this combiner should detect young giant exoplanets at separations <10 AU, where radial velocity and transit methods are more sensitive. A detailed analysis of the systematic errors introduced by the non-ideal nature of a nuller was beyond the scope of this work. This is required in order to draw more definitive conclusions as to the sensitivity limits of our approach.

Almost all of the directly imaged planets known thus far are young, self-luminous gas giants discovered from ‘blind’ surveys where targets are selected based on age and distance from Earth. For increased efficiency, an interferometric survey should focus on objects that are already suspected of harbouring one or more low-mass companions. With the aid of the unprecedented accuracy of Gaia astrometric measurements and its sensitivity to substellar companions, new techniques such as the proper motion anomaly can be applied. In this work, I show how I use this technique to identify 38 targets for a kernel-nuller observing program at the VLTI. A complete analysis of the targets identified would also need to take into account other indicators of binarity such as the renormalised unit

weight error and determine whether or not the potential giant planetary mass companions identified are gravitationally bound to their host star.

NOTT will be the first nulling interferometer at the VLTI, which will employ a double Bracewell architecture. In this work, we have seen that kernel-nulling solutions can be found with a reduced number of outputs that nevertheless result in the formation of at least one self-calibrating observable. A simplified four-input/four-output kernel-nuller is an obvious candidate as a first demonstrator of on-sky kernel-nulling. Besides, this combiner offers more nulled outputs than a double Bracewell, which could give it a higher scientific yield.

A simplified four-input kernel-nuller can be manufactured out a single multi-mode interference coupler. In this work, I have presented the spectral characterisation of this device. This prototype was not fully optimised for broadband use, and the self-calibration was found to degrade as the wavelength deviates from the design central wavelength of $1.55 \mu\text{m}$. A 4×4 MMI can be implemented with 2×2 MMIs that are also integrated on the kernel-nuller photonic chip. These MMIs that could exhibit less chromatic dispersion are yet to be tested, and their spectral behaviour should be determined. Indeed, the silicon nitride (Si_3N_4) platform cannot be implemented for the mid-infrared but allows for the low-cost prototyping of such devices. The NOTT beam combiner will be fabricated from a chalcogenide glass that offers a wider transparency, and MMIs fabricated from this substrate have been found to offer a reasonable achromatic response over a $\sim 300 \text{ nm}$ bandwidth.

High-contrast imaging demands precise photometric balancing at the outputs of the device in order to produce high-order nulls. The imperfect splitting I measured could perhaps be also due to inaccuracies in the coupling that stem from misalignment between the chip output waveguides and fibre array. In an improved implementation of the device, the fibre array would be bonded to the chip, though this is not the case with our current experimental setup. Besides, the setup does not allow us to quantify injection efficiency, therefore it is not possible to measure radiation losses that occur not only in the arrangement of the optical elements but also in the MMI cavity. Gauging the input intensity enables the estimation of insertion loss, which is the intensity ratio of an output over the input, consequently providing beam splitting ratios with higher accuracy. Beyond this, future iterations of photonic kernel-nullers should include photometric taps that independently measure the photometric fluctuations of the inputs.

Space is indeed the place for nulling because ground-based interferometry is limited by atmospheric turbulence and thermal emission that degrades the achievable contrast far from fundamental limits. Besides, it also offers the best

possible means of imaging an Earth analogue. Current active endeavours in space-based nulling such as LIFE have studied various kernel-nulling architectures, and a five-input/five-output solution has been found to provide a higher scientific yield than the double Bracewell/X-array employed for the ESA/Darwin and NASA/TPF-I space missions. However, the transmission maps—and subsequent kernel output maps—exhibit a five-fold symmetry around the central null for these apertures that would be arranged in a pentagonal array. By changing the geometry of the array to an ellipse, the central symmetry is broken for the respective maps. Indeed, an elliptical array could lead to an easier distinction between the signals emitted by planets, but this necessitates a comprehensive image reconstruction analysis with multiple companions in the field of view.

Appendix A:

Kernel-nulling at CHARA

The high-contrast imaging properties of a nulling instrument, most notably the general shape of the on-sky transmission map, will depend on the exact location and size of the sub-apertures of the interferometer feeding light to the re-combiner. Indeed, the largest operational optical interferometer is the Centre for High Angular Resolution Astronomy (CHARA) Array, located on Mount Wilson, California. This facility consists of six 1-m telescopes in a Y-shaped configuration – providing baselines ranging from 34 to 331-m. To illustrate the astrophysical information gathered by a kernel-nuller at the focus of the CHARA Array, we can compute the transmission maps and their subsequent kernel output maps.

[Laugier et al. \(2020\)](#) described a 6x21 kernel-nuller whose response matrix is given as:

$$\mathbf{M}_{6 \times 21} = \frac{1}{\sqrt{6}} \frac{1}{\sqrt{4}} \times \begin{bmatrix} 2 & 2 & 2 & 2 & 2 & 2 \\ 1 & e^{\frac{5\pi j}{3}} & e^{\frac{4\pi j}{3}} & -1 & e^{\frac{\pi j}{3}} & e^{\frac{2\pi j}{3}} \\ 1 & e^{\frac{\pi j}{3}} & e^{\frac{2\pi j}{3}} & -1 & e^{\frac{5\pi j}{3}} & e^{\frac{4\pi j}{3}} \\ 1 & -1 & e^{\frac{\pi j}{3}} & e^{\frac{2\pi j}{3}} & e^{\frac{5\pi j}{3}} & e^{\frac{4\pi j}{3}} \\ 1 & -1 & e^{\frac{5\pi j}{3}} & e^{\frac{4\pi j}{3}} & e^{\frac{\pi j}{3}} & e^{\frac{2\pi j}{3}} \\ 1 & e^{\frac{4\pi j}{3}} & e^{\frac{5\pi j}{3}} & e^{\frac{2\pi j}{3}} & e^{\frac{\pi j}{3}} & -1 \\ 1 & e^{\frac{2\pi j}{3}} & e^{\frac{\pi j}{3}} & e^{\frac{4\pi j}{3}} & e^{\frac{5\pi j}{3}} & -1 \\ 1 & -1 & e^{\frac{2\pi j}{3}} & e^{\frac{5\pi j}{3}} & e^{\frac{4\pi j}{3}} & e^{\frac{\pi j}{3}} \\ 1 & -1 & e^{\frac{4\pi j}{3}} & e^{\frac{\pi j}{3}} & e^{\frac{2\pi j}{3}} & e^{\frac{5\pi j}{3}} \\ 1 & e^{\frac{4\pi j}{3}} & e^{\frac{2\pi j}{3}} & e^{\frac{\pi j}{3}} & e^{\frac{5\pi j}{3}} & -1 \\ 1 & e^{\frac{2\pi j}{3}} & e^{\frac{4\pi j}{3}} & e^{\frac{5\pi j}{3}} & e^{\frac{\pi j}{3}} & -1 \\ 1 & e^{\frac{\pi j}{3}} & e^{\frac{2\pi j}{3}} & e^{\frac{4\pi j}{3}} & -1 & e^{\frac{5\pi j}{3}} \\ 1 & e^{\frac{5\pi j}{3}} & e^{\frac{4\pi j}{3}} & e^{\frac{2\pi j}{3}} & e^{\frac{\pi j}{3}} & -1 \\ 1 & e^{\frac{4\pi j}{3}} & e^{\frac{\pi j}{3}} & -1 & e^{\frac{2\pi j}{3}} & e^{\frac{5\pi j}{3}} \\ 1 & e^{\frac{2\pi j}{3}} & e^{\frac{5\pi j}{3}} & -1 & e^{\frac{4\pi j}{3}} & e^{\frac{\pi j}{3}} \\ 1 & e^{\frac{2\pi j}{3}} & e^{\frac{5\pi j}{3}} & e^{\frac{\pi j}{3}} & -1 & e^{\frac{4\pi j}{3}} \\ 1 & e^{\frac{4\pi j}{3}} & e^{\frac{\pi j}{3}} & e^{\frac{5\pi j}{3}} & -1 & e^{\frac{2\pi j}{3}} \\ 1 & e^{\frac{5\pi j}{3}} & -1 & e^{\frac{\pi j}{3}} & e^{\frac{4\pi j}{3}} & e^{\frac{2\pi j}{3}} \\ 1 & e^{\frac{\pi j}{3}} & -1 & e^{\frac{5\pi j}{3}} & e^{\frac{2\pi j}{3}} & e^{\frac{4\pi j}{3}} \\ 1 & e^{\frac{5\pi j}{3}} & -1 & e^{\frac{4\pi j}{3}} & e^{\frac{2\pi j}{3}} & e^{\frac{\pi j}{3}} \\ 1 & e^{\frac{\pi j}{3}} & -1 & e^{\frac{2\pi j}{3}} & e^{\frac{4\pi j}{3}} & e^{\frac{5\pi j}{3}} \end{bmatrix}. \quad (\text{A.1})$$

However, in Chapter 3 I showed that a simplified kernel-nulling architecture can maximise the throughput with a minimum number of outputs and only requires a single stage. A 6×6 kernel-nuller (computed via Eq. (3.21)) is summarised by this matrix:

$$\mathbf{M}_{6 \times 6} = \frac{1}{\sqrt{6}} \times \begin{bmatrix} 1 & 1 & 1 & 1 & 1 & 1 \\ 1 & e^{\frac{\pi j}{3}} & e^{\frac{2\pi j}{3}} & -1 & e^{\frac{-2\pi j}{3}} & e^{\frac{-\pi j}{3}} \\ 1 & e^{\frac{2\pi j}{3}} & e^{\frac{-2\pi j}{3}} & 1 & e^{\frac{2\pi j}{3}} & e^{\frac{-2\pi j}{3}} \\ 1 & -1 & 1 & -1 & 1 & -1 \\ 1 & e^{\frac{-2\pi j}{3}} & e^{\frac{2\pi j}{3}} & 1 & e^{\frac{-2\pi j}{3}} & e^{\frac{2\pi j}{3}} \\ 1 & e^{\frac{-\pi j}{3}} & e^{\frac{-2\pi j}{3}} & -1 & e^{\frac{2\pi j}{3}} & e^{\frac{\pi j}{3}} \end{bmatrix}. \quad (\text{A.2})$$

Figure 69 shows a graphical representation of the six-input combiner.

Utilising the methodology of the transmission maps in Chingaipe et al. (2023), Fig. 70 - Fig. 73 show such maps for a 6×6 kernel-nuller deployed on the six 1-m telescopes of the CHARA array.

Chingaipe et al. (2023) described a kernel-nuller discovery observing program for the direct imaging of exoplanets at the VLTI by exploiting the synergy between astrometry and direct imaging. I use the same methodology to identify 30 targets (see Table 1) for an observation program at CHARA. Figure 74 shows how the 30 identified companion candidates are distributed in an angular separation–contrast plot.

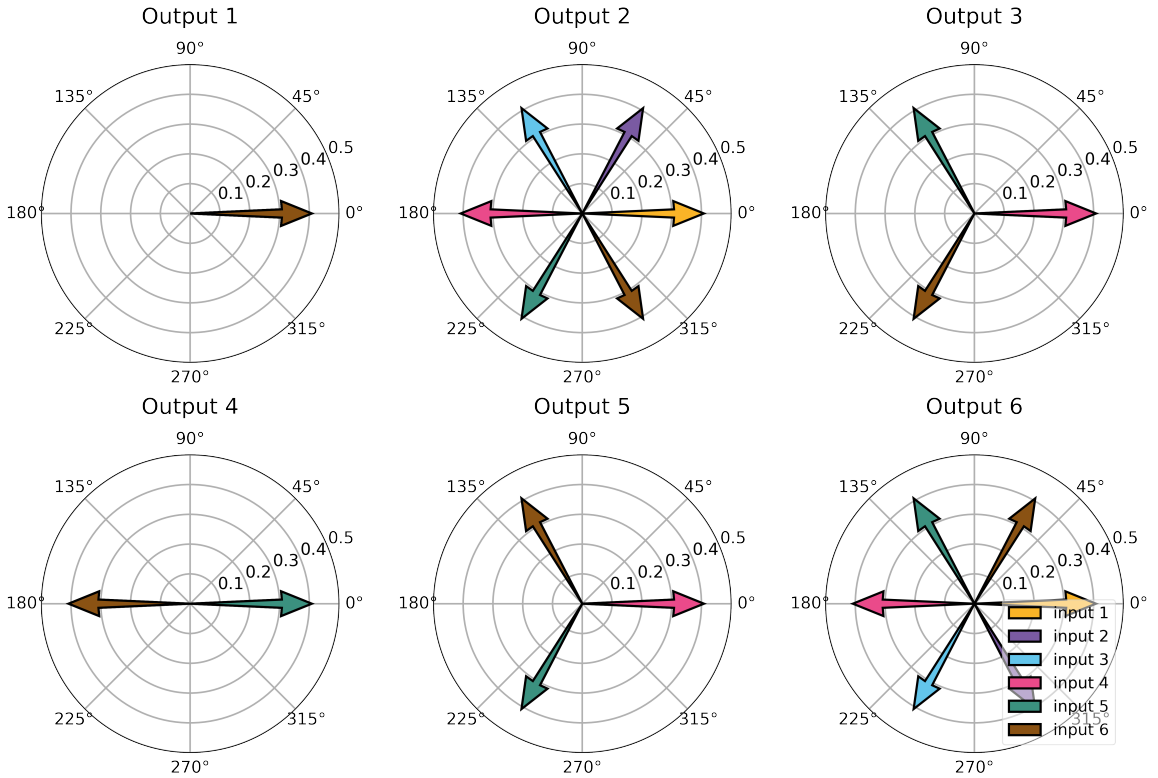


Figure 69: Complex matrix plots describing the theoretical $M_{6 \times 6}$ of a six-input/six-output (6×6) kernel-nuller. The phase of each input is represented by a colored arrow whose length encodes the amplitude. Since one can only record the intensity (absolute square), the nuller is insensitive to any global phase shift applied to an output (or row of $M_{5 \times 5}$), which would correspond to an overall rotation of the arrows in a complex matrix plot. Only relative phase offsets introduced by the device between the inputs matter, and our convention is to take input 1 as the phase reference, explaining why the first column of $M_{6 \times 6}$ only contains 1, or equivalently, why all yellow arrows remain aligned with the real axis of the complex plane. At each output, the resulting electric field is the sum of all arrows. Output 1 (bright outputs) is an in-phase constructive recombination of the inputs. Outputs 2, 3, 4, 5 & 6 all result in nulls (with the sum of the six arrows leading back to zero), though they differ in the applied input phase shifts that are multiples of $\pi/3$.

A kernel-nulling for the direct detection of exoplanets

Table 1: 30 identified targets for the kernel-nuller discovery observing program, derived from the proper motion anomaly (PMa, [Kervella et al. 2022](#)) catalogue of Hipparcos and Gaia EDR3 astrometry. The table includes the stellar R & K magnitudes, spectral type, parallax (ϖ), $\Delta v_{T,G3}$ is the norm of the tangential PMA vector converted to linear velocity using the Gaia EDR3 parallax, m_* the mass of the primary star, R_* the stellar radius and m_p is the mass of a companion assuming a 5 AU orbit. The angular separation estimate is given by the ratio between the semi-major axis (assumed to be 5 AU) and the distance to the system. The estimated contrast c of the companion is given as $\log(c)$. The full names of the young stellar associations listed are AB Doradus (ABDMG), Argus (ARG, [Zuckerman 2019](#)), β Pictoris (β PMG), Carina (CAR), Carina-Near (CARN), Lower Centaurus Crux (LCC), Octans (OCT), Tucana-Horologium Association (THA) and Upper Centaurus Lupus (UCL). The ages of the young associations are from [Gagné et al. \(2018\)](#).

| HIP | R (mag) | K (mag) | SpT | ϖ (mas) | $\Delta v_{T,G3}$ (m/s) | m_* (M_\odot) | R_* (R_\odot) | m_p (M_{Jup}) | Sep. (mas) | $\log(c)$ | Assoc. | Age (Myr) |
|--------|------------|------------|-------|-------------------|----------------------------|------------------------|------------------------|------------------------|---------------|-----------|--------|--------------|
| 17962 | — | 7.25 | K2V | 21.05 | 44.60 | 0.9 | 0.88 | 4.4 | 105.24 | -6.83 | HYA | 750 |
| 20890 | — | 6.91 | G5V | 20.84 | 46.83 | 1.0 | 0.95 | 5.06 | 104.22 | -7.02 | HYA | 750 |
| 13027 | — | 5.52 | G1V | 30.22 | 116.86 | 0.94 | 1.29 | 11.97 | 151.12 | -6.39 | ABDMG | 149 |
| 21637 | — | 6.16 | F5V | 23.07 | 35.89 | 1.16 | 1.14 | 4.13 | 115.35 | -7.63 | HYA | 750 |
| 20722 | — | 6.50 | G5V | 22.56 | 38.03 | 1.08 | 1.03 | 4.25 | 112.80 | -6.24 | ARG | 40 |
| 47110 | — | 6.51 | G5V | 25.87 | 23.53 | 0.98 | 0.92 | 2.5 | 129.35 | -6.08 | BPMG | 24 |
| 51955 | — | 6.76 | G0V | 17.46 | 36.79 | 1.16 | 1.14 | 4.24 | 87.28 | -6.96 | ABDMG | 149 |
| 77152 | — | 6.61 | G0V | 20.52 | 76.23 | 1.08 | 1.06 | 8.53 | 102.61 | -5.91 | ARG | 40 |
| 83546 | — | 7.12 | G0V | 16.11 | 56.06 | 1.1 | 1.07 | 6.32 | 80.56 | -6.13 | ARG | 40 |
| 60832 | — | 6.49 | G8V | 22.12 | 95.45 | 1.08 | 1.05 | 10.68 | 110.61 | -6.33 | CARN | 200 |
| 64532 | — | 5.33 | G1V | 39.77 | 39.78 | 1.08 | 0.99 | 4.45 | 198.85 | -6.87 | UMA | 414 |
| 103232 | — | 6.06 | G0V | 15.84 | 93.76 | 1.06 | 1.98 | 10.4 | 79.18 | -5.77 | CARN | 200 |
| 113052 | — | 6.70 | K0V | 14.08 | 96.67 | 0.92 | 1.68 | 9.72 | 70.4 | -5.99 | ARG | 40 |
| 114385 | — | 5.67 | G1V | 33.02 | 40.48 | 1.08 | 1.02 | 4.53 | 165.1 | -5.99 | BPMG | 24 |
| 114379 | — | 5.66 | K2V | 32.88 | 112.33 | 0.9 | 1.18 | 11.08 | 164.41 | -7.32 | ARG | 40 |
| 95319 | — | 4.49 | K0V | 64.1 | 75.86 | 0.98 | 0.97 | 8.06 | 320.48 | -5.49 | ARG | 40 |
| 88617 | — | 6.78 | K0V | 26.26 | 85.38 | 0.9 | 0.87 | 8.42 | 131.3 | -6.14 | CARN | 200 |
| 89005 | — | 6.33 | K2V | 31.81 | 28.74 | 0.87 | 0.9 | 2.73 | 159.05 | -5.83 | CARN | 200 |
| 6653 | — | 5.77 | G3V | 25.15 | 91.93 | 1.16 | 1.31 | 10.59 | 125.77 | -4.89 | BPMG | 24 |
| 544 | — | 4.31 | K0V | 72.68 | 10.05 | 0.98 | 0.91 | 1.07 | 363.39 | -6.87 | BPMG | 24 |
| 20673 | — | 5.73 | K1V | 24.63 | 48.20 | 1.1 | 1.38 | 5.43 | 123.16 | -6.59 | ARG | 40 |
| 53174 | — | 8.15 | K3V | 15.63 | 95.67 | 0.85 | 0.77 | 8.87 | 78.14 | -5.72 | CARN | 200 |
| 55638 | — | 6.96 | K0V | 22.5 | 34.74 | 0.98 | 0.88 | 3.69 | 112.49 | -6.38 | ABDMG | 149 |
| 60206 | — | 7.65 | F8V | 11.89 | 98.46 | 1.16 | 1.12 | 11.34 | 59.47 | -6.90 | CBER | 562 |
| 97030 | — | 6.42 | G3V | 23.97 | 48.54 | 1.08 | 0.99 | 5.43 | 119.85 | -6.52 | ABDMG | 149 |
| 17338 | — | 7.2 | G8V | 17.60 | 50.75 | 1.0 | 1.03 | 5.48 | 87.98 | -6.00 | OCT | 35 |
| 50032 | — | 7.06 | K2V | 24.35 | 27.26 | 0.9 | 0.8 | 2.69 | 121.76 | -5.49 | UCL | 16 |
| 47681 | — | 6.83 | G5V | 22.20 | 24.59 | 1.0 | 0.9 | 2.65 | 111.01 | -6.21 | ARG | 40 |
| 98839 | — | 6.63 | G1V | 21.14 | 43.76 | 1.08 | 1.03 | 4.89 | 105.70 | -5.95 | BPMG | 24 |
| 104687 | — | 6.25 | G2/3V | 21.55 | 75.41 | 0.94 | 1.29 | 7.72 | 107.74 | -6.33 | ARG | 40 |

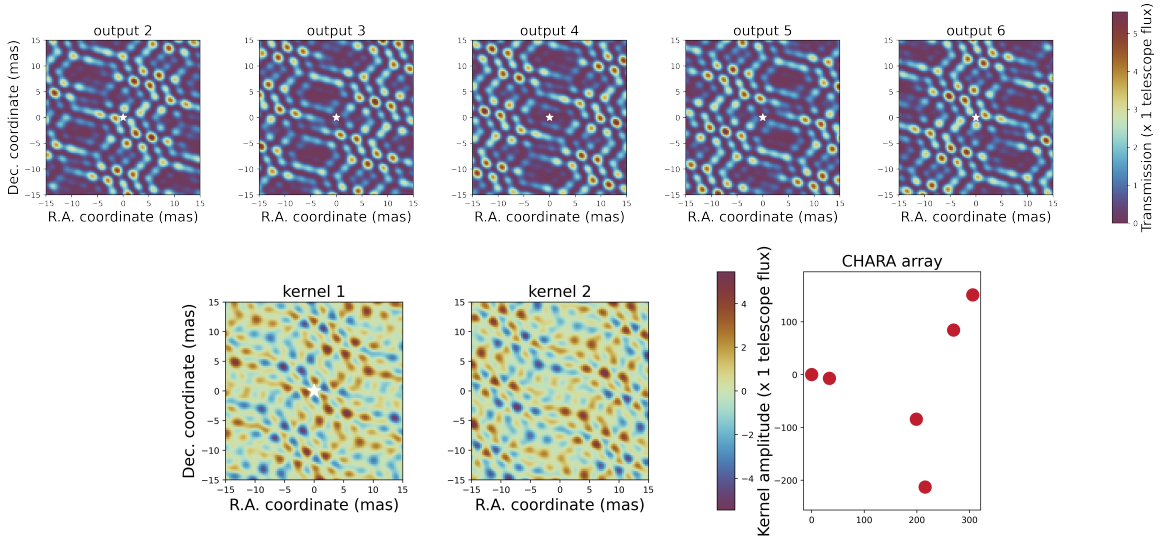


Figure 70: **Top panel:** Nuller output transmission maps of a kernel-nuller at the focus of the six CHARA array telescopes, observing a ± 15 mas FOV. The figure shows the maps of the five nuller outputs for a pointing exactly at zenith. We see that these maps differ from one another and this diversity in the output response provides a constraint on the properties of a potential companion in the vicinity of a much brighter star. A white star in each map marks the location of the central star where the transmission for all channels is equal to zero, by design. About the centre of the field, the maps are asymmetric. For transmission maps, this asymmetry is a desirable trait as it allows for the elimination of centro-symmetric astrophysical features that would otherwise hide a planetary companion. All five maps share the same color scale where the transmission is expressed in units of the planet flux. **Bottom panel:** Kernel output maps of the 5×5 kernel-nuller. A kernel output is simply the difference between the two nuller outputs for which the same pairs of inputs are nulled with each other (output 2–6, 3–5). Taking the difference of output values means that unlike raw photometric-like outputs, kernel outputs can take negative values. This is shown on the color scale on the right of the map where the transmission is expressed in units of kernel amplitude.

A kernel-nulling for the direct detection of exoplanets

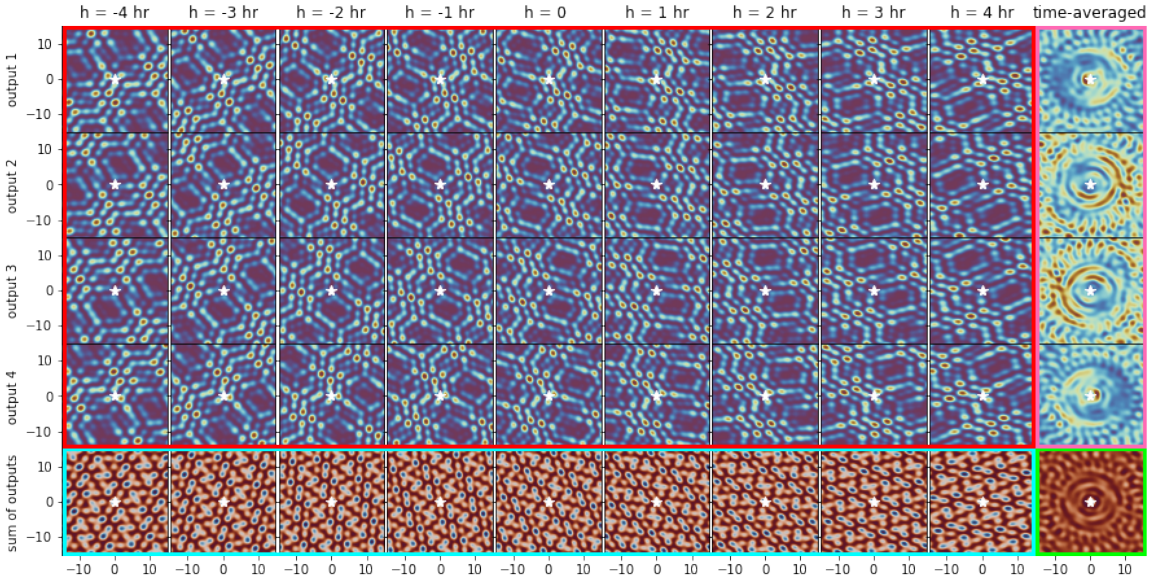


Figure 71: Evolution of the nuller output transmission maps of a kernel-nuller at the focus of the six CHARA array telescopes, observing a ± 15 mas FOV. The figure shows four blocks of maps altogether, which provide insights into the behaviour of the nulled outputs. The first block (red contour, top left) of 36 maps shows how the transmission maps of the six nuller outputs evolve over a ± 4 hour observing period centred on the target transit time ($h = 0$). These maps all share the same colour scale as Fig. 70. We can see the transmission patterns gradually rotating in a clockwise direction with time, scanning the FOV to intercept the light of any off-axis feature of the astrophysical scene. A white star in each plot marks the location of the central star where the transmission for all channels is equal to zero, by design. The second block (pink contour, rightmost column) of four maps shows the time-average of each nuller output transmission map, using the same colour scales and conventions. Looking at these, we can visually confirm that the outputs do indeed work in pairs characterised by asymmetric responses. The third block (blue contour, bottom row) of nine maps shows how at any instant, the sum of all output maps is spatially distributed. Summing the outputs shows that the overall instantaneous sensitivity of the nuller is much more uniform over the FOV, even if it nevertheless systematically features off-axis replicas of the on-axis null, which are referred to as transmission holes. The fourth block (green contour, single bottom right map) shows the time-averaged global throughput, which reveals that with a sufficiently wide observing window, the FOV is uniformly covered, and the nuller will be able to capture the light of a companion regardless of where it may reside.

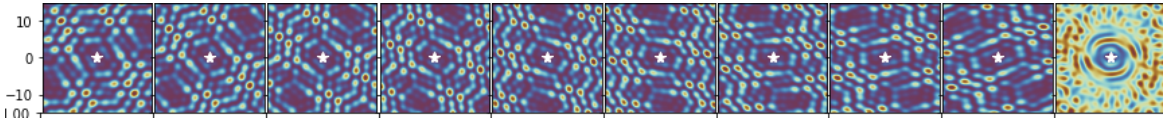


Figure 72: Evolution of the bracewell output transmission maps of a kernel-nuller at the focus of the six CHARA array telescopes, observing the ± 15 mas FOV surrounding the target HIP 107773.

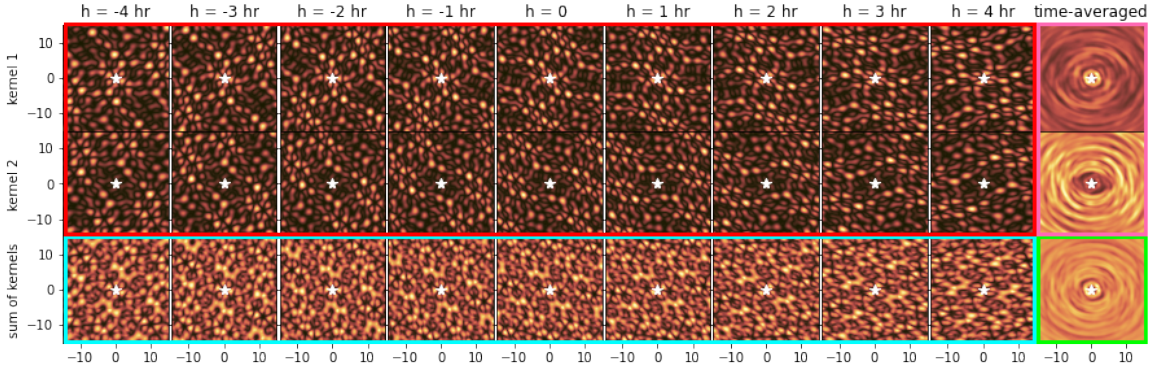


Figure 73: Evolution of the kernel magnitude maps of a kernel-nuller at the focus of the six CHARA array telescopes, observing a ± 15 mas FOV. The figure shows four blocks of maps altogether, which provide insights into the behaviour of the kernel outputs. The first block (red contour, top left) of 18 maps shows how the magnitude maps of the two kernel-nuller outputs evolve over a ± 4 hour observing period centred on the target transit time ($h = 0$). We can see the transmission patterns gradually rotating in a clockwise direction with time, scanning the FOV to intercept the light of any off-axis feature of the astrophysical scene. A white star in each plot marks the location of the central star where the transmission for all channels is equal to zero, by design. The second block (pink contour, rightmost column) of two maps shows the time-average of each kernel output magnitude map. The third block (blue contour, bottom row) of nine maps shows how at any instant, the sum of all kernel magnitude maps is spatially distributed. Summing the kernel outputs shows that the overall instantaneous sensitivity of the nuller is much more uniform over the FOV, even if it nevertheless systematically features off-axis replicas of the on-axis null, which are referred to as transmission holes. The fourth block (green contour, single bottom-right map) shows the time-averaged global throughput, which reveals that with a sufficiently wide observing window, the FOV is uniformly covered, and the nuller will be able to capture the light of a companion regardless of where it may reside.

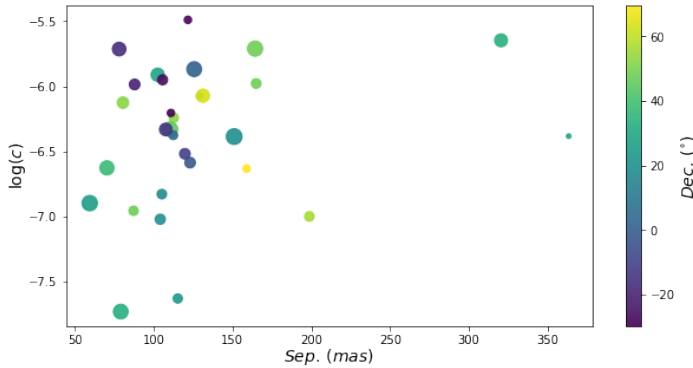


Figure 74: Identified companion candidates to the targets identified for a kernel-nuller discovery observing program at CHARA. These 30 targets are derived from the proper motion anomaly (PMA) catalogue (Kervella et al. 2022) of Hipparcos and Gaia EDR3 astrometry. The companion contrast c is presented as a function of the angular separation which is given by the ratio between the semi-major axis (assumed to be 5 AU) and the distance to the system. The color of the markers indicates the declination angle of the target system and the size depicts the mass of the companion (M_{Jup}).

References

- Absil, O., D. Defrère, V. Coudé du Foresto, E. Di Folco, A. Mérand, J. -C. Augereau, S. Ertel, C. Hanot, P. Kervella, B. Mollier, N. Scott, X. Che, J. D. Monnier, N. Thureau, P. G. Tuthill, T. A. ten Brummelaar, H. A. McAlister, J. Sturmann, L. Sturmann & N. Turner. 2013. A near-infrared interferometric survey of debris-disc stars. III. First statistics based on 42 stars observed with CHARA/FLUOR. 555, A104. A104. DOI: [10.1051/0004-6361/201321673](https://doi.org/10.1051/0004-6361/201321673).
- Absil, O., R. den Hartog, P. Gondoin, P. Fabry, R. Wilhelm, P. Gitton & F. Puech. 2006. Performance study of ground-based infrared Bracewell interferometers. Application to the detection of exozodiacal dust disks with GENIE. 448(2). 787–800. DOI: [10.1051/0004-6361:20053516](https://doi.org/10.1051/0004-6361:20053516).
- Absil, O., R. den Hartog, P. Gondoin, P. Fabry, R. Wilhelm, P. Gitton & F. Puech. 2011. *Performance study of ground-based infrared Bracewell interferometers . Application to the detection of exozodiacal dust disks with GENIE*. Astronomy & Astrophysics, Volume 527, id.C4, 1 pp. DOI: [10.1051/0004-6361/20053516e](https://doi.org/10.1051/0004-6361/20053516e).
- Absil, O., E. di Folco, A. Mérand, J. -C. Augereau, V. Coudé du Foresto, J. P. Aufdenberg, P. Kervella, S. T. Ridgway, D. H. Berger, T. A. ten Brummelaar, J. Sturmann, L. Sturmann, N. H. Turner & H. A. McAlister. 2006. Circumstellar material in the <ASTROBJ>Vega</ASTROBJ> inner system revealed by CHARA/FLUOR. 452(1). 237–244. DOI: [10.1051/0004-6361:20054522](https://doi.org/10.1051/0004-6361:20054522).
- Alfano, R. R. & S. L. Shapiro. 1970a. Emission in the Region 4000 to 7000 Å Via Four-Photon Coupling in Glass. 24(11). 584–587. DOI: [10.1103/PhysRevLett.24.584](https://doi.org/10.1103/PhysRevLett.24.584).
- Alfano, R. R. & S. L. Shapiro. 1970b. Observation of Self-Phase Modulation and Small-Scale Filaments in Crystals and Glasses. 24(11). 592–594. DOI: [10.1103/PhysRevLett.24.592](https://doi.org/10.1103/PhysRevLett.24.592).
- Angel, J. R. P., M. T. Adams, T. A. Boroson & R. L. Moore. 1977. A very large optical telescope array linked with fused silica fibers. 218. 776–782. DOI: [10.1086/155734](https://doi.org/10.1086/155734).
- Angel, J. R. P., A. Y. S. Cheng & N. J. Woolf. 1986. A space telescope for infrared spectroscopy of Earth-like planets. 322(6077). 341–343. DOI: [10.1038/322341a0](https://doi.org/10.1038/322341a0).
- Angel, J. R. P. & N. J. Woolf. 1997. An Imaging Nulling Interferometer to Study Extrasolar Planets. 475(1). 373–379. DOI: [10.1086/303529](https://doi.org/10.1086/303529).
- Angel, Roger. 1990. Use of 16m Telescope to Detect Earthlike Planets. In Pierre-Yves Bely, Christopher J. Burrows & Garth D. Illingworth (eds.), *The next generation space telescope*, 81.

- Anglada-Escudé, Guillem, Pedro J. Amado, John Barnes, Zaira M. Berdiñas, R. Paul Butler, Gavin A. L. Coleman, Ignacio de La Cueva, Stefan Dreizler, Michael Endl, Benjamin Giesers, Sandra V. Jeffers, James S. Jenkins, Hugh R. A. Jones, Marcin Kiraga, Martin Kürster, María J. López-González, Christopher J. Marvin, Nicolás Morales, Julien Morin, Richard P. Nelson, José L. Ortiz, Aviv Ofir, Sijme-Jan Paardekooper, Ansgar Reiners, Eloy Rodríguez, Cristina Rodríguez-López, Luis F. Sarmiento, John P. Strachan, Yiannis Tsapras, Mikko Tuomi & Mathias Zechmeister. 2016. A terrestrial planet candidate in a temperate orbit around Proxima Centauri. 536(7617). 437–440. DOI: [10.1038/nature19106](https://doi.org/10.1038/nature19106).
- Babcock, H. W. 1953. The Possibility of Compensating Astronomical Seeing. 65(386). 229. DOI: [10.1086/126606](https://doi.org/10.1086/126606).
- Bacon, R., Y. Copin, G. Monnet, Bryan W. Miller, J. R. Allington-Smith, M. Bureau, C. M. Carollo, Roger L. Davies, Eric Emsellem, Harald Kuntschner, Reynier F. Peletier, E. K. Verolme & P. Tim de Zeeuw. 2001. The SAURON project - I. The panoramic integral-field spectrograph. 326(1). 23–35. DOI: [10.1046/j.1365-8711.2001.04612.x](https://doi.org/10.1046/j.1365-8711.2001.04612.x).
- Baron, F., J. D. Monnier, L. L. Kiss, H. R. Neilson, M. Zhao, M. Anderson, A. Aarnio, E. Pedretti, N. Thureau, T. A. ten Brummelaar, S. T. Ridgway, H. A. McAlister, J. Sturmann, L. Sturmann & N. Turner. 2014. CHARA/MIRC Observations of Two M Supergiants in Perseus OB1: Temperature, Bayesian Modeling, and Compressed Sensing Imaging. 785(1), 46. DOI: [10.1088/0004-637X/785/1/46](https://doi.org/10.1088/0004-637X/785/1/46).
- Baron, Fabien, John D. Monnier & Brian Kloppenborg. 2010. A novel image reconstruction software for optical/infrared interferometry. In William C. Danchi, Françoise Delplancke & Jayadev K. Rajagopal (eds.), *Optical and infrared interferometry ii*, vol. 7734 (Society of Photo-Optical Instrumentation Engineers (SPIE) Conference Series), 77342I. DOI: [10.1117/12.857364](https://doi.org/10.1117/12.857364).
- Bass, Michael, Eric W. Van Stryland, David R. Williams & Williams L. Wolfe. 1995. *Handbook of Optics Volume II Devices, Measurements, and Properties 2nd edition*.
- Baudoz, Pierre, Raphael Galicher, Fabien Patru, Olivier Dupuis & Simone Thijs. 2018. Status and performance of the THD2 bench in multi-deformable mirror configuration. *arXiv e-prints*, arXiv:1801.06600. arXiv:1801.06600. DOI: [10.48550/arXiv.1801.06600](https://doi.org/10.48550/arXiv.1801.06600).
- Beichman, C. A., N. J. Woolf & C. A. Lindensmith. 1999. *The Terrestrial Planet Finder (TPF) : a NASA Origins Program to search for habitable planets*.
- Bell, Cameron P. M., Eric E. Mamajek & Tim Naylor. 2015. A self-consistent, absolute isochronal age scale for young moving groups in the solar neighbourhood. 454(1). 593–614. DOI: [10.1093/mnras/stv1981](https://doi.org/10.1093/mnras/stv1981).

- Benech, Pierre. 1997. Review on integrated optics technology. In Pierre Kern & Fabien Malbet (eds.), *Integrated optics for astronomical interferometry*, 115.
- Benisty, M., J. -P. Berger, L. Jocou, P. Labeye, F. Malbet, K. Perraut & P. Kern. 2009. An integrated optics beam combiner for the second generation VLTI instruments. 498(2). 601–613. DOI: [10.1051/0004-6361/200811083](https://doi.org/10.1051/0004-6361/200811083).
- Berger, J. P., P. Haguenaer, P. Kern, K. Perraut, F. Malbet, I. Schanen, M. Severi, R. Millan-Gabet & W. Traub. 2001. Integrated optics for astronomical interferometry. IV. First measurements of stars. 376. L31–L34. DOI: [10.1051/0004-6361:20011035](https://doi.org/10.1051/0004-6361:20011035).
- Berger, J. P., K. Rousselet-Perraut, P. Kern, F. Malbet, I. Schanen-Duport, F. Reynaud, P. Haguenaer & P. Benech. 1999. Integrated optics for astronomical interferometry. II. First laboratory white-light interferograms. 139. 173–177. DOI: [10.1051/aas:1999504](https://doi.org/10.1051/aas:1999504).
- Berger, Jean-Philippe, Pierre Haguenaer, Pierre Y. Kern, Karine Rousselet-Perraut, Fabien Malbet, Stephane Gluck, Laure Lagny, Isabelle Schanen-Duport, Emmanuel Laurent, Alain Delboulbe, Eric Tatulli, Wesley A. Traub, Nathaniel Carleton, Rafael Millan-Gabet, John D. Monnier, Ettore Pedretti & Sam Ragland. 2003. An integrated-optics 3-way beam combiner for IOTA. In Wesley A. Traub (ed.), *Interferometry for optical astronomy ii*, vol. 4838 (Society of Photo-Optical Instrumentation Engineers (SPIE) Conference Series), 1099–1106. DOI: [10.1117/12.457983](https://doi.org/10.1117/12.457983).
- Besse, Pierre A., Maurus Bachmann, Hans Melchior, Lucas B. Soldano & Meint K. Smit. 1994. Optical bandwidth and fabrication tolerances of multimode interference couplers. *Journal of Lightwave Technology* 12(6). 1004–1009. DOI: [10.1109/50.296191](https://doi.org/10.1109/50.296191).
- Beuzit, J. -L. et al. 2019. SPHERE: the exoplanet imager for the Very Large Telescope. 631, A155. A155. DOI: [10.1051/0004-6361/201935251](https://doi.org/10.1051/0004-6361/201935251).
- Birks, T. A., J. C. Knight & P. St. J. Russell. 1997. Endlessly single-mode photonic crystal fiber. *Optics Letters* 22(13). 961–963. DOI: [10.1364/OL.22.000961](https://doi.org/10.1364/OL.22.000961).
- Bland-Hawthorn, Joss, Jon Lawrence, Gordon Robertson, Sam Campbell, Ben Pope, Chris Betters, Sergio Leon-Saval, Tim Birks, Roger Haynes, Nick Cvetojevic & Nem Jovanovic. 2010. PIMMS: photonic integrated multimode microspectrograph. In Ian S. McLean, Suzanne K. Ramsay & Hideki Takami (eds.), *Ground-based and airborne instrumentation for astronomy iii*, vol. 7735 (Society of Photo-Optical Instrumentation Engineers (SPIE) Conference Series), 77350N. DOI: [10.1117/12.856347](https://doi.org/10.1117/12.856347).
- Borucki, William J., David Koch, Gibor Basri, Natalie Batalha, Timothy Brown, Douglas Caldwell, John Caldwell, Jørgen Christensen-Dalsgaard, William D. Cochran, Edna DeVore, Edward W. Dunham, Andrea K. Dupree, Thomas

- N. Gautier, John C. Geary, Ronald Gilliland, Alan Gould, Steve B. Howell, Jon M. Jenkins, Yoji Kondo, David W. Latham, Geoffrey W. Marcy, Søren Meibom, Hans Kjeldsen, Jack J. Lissauer, David G. Monet, David Morrison, Dimitar Sasselov, Jill Tarter, Alan Boss, Don Brownlee, Toby Owen, Derek Buzasi, David Charbonneau, Laurance Doyle, Jonathan Fortney, Eric B. Ford, Matthew J. Holman, Sara Seager, Jason H. Steffen, William F. Welsh, Jason Rowe, Howard Anderson, Lars Buchhave, David Ciardi, Lucianne Walkowicz, William Sherry, Elliott Horch, Howard Isaacson, Mark E. Everett, Debra Fischer, Guillermo Torres, John Asher Johnson, Michael Endl, Phillip MacQueen, Stephen T. Bryson, Jessie Dotson, Michael Haas, Jeffrey Kolodziejczak, Jeffrey Van Cleve, Hema Chandrasekaran, Joseph D. Twicken, Elisa V. Quintana, Bruce D. Clarke, Christopher Allen, Jie Li, Haley Wu, Peter Tenenbaum, Ekaterina Verner, Frederick Bruhweiler, Jason Barnes & Andrej Prsa. 2010. Kepler Planet-Detection Mission: Introduction and First Results. *Science* 327(5968). 977. DOI: [10.1126/science.1185402](https://doi.org/10.1126/science.1185402).
- Boss, A. P. 1997. Giant planet formation by gravitational instability. *Science* 276. 1836–1839. DOI: [10.1126/science.276.5320.1836](https://doi.org/10.1126/science.276.5320.1836).
- Bracewell, R. N. 1978. Detecting nonsolar planets by spinning infrared interferometer. 274(5673). 780–781. DOI: [10.1038/274780a0](https://doi.org/10.1038/274780a0).
- Bracewell, R. N. & R. H. MacPhie. 1979. Searching for nonsolar planets. 38(1). 136–147. DOI: [10.1016/0019-1035\(79\)90093-9](https://doi.org/10.1016/0019-1035(79)90093-9).
- Carleton, Nathaniel P., Wesley A. Traub, Marc G. Lacasse, Peter Nisenson, Michael R. Pearlman, Robert D. Reasenberg, Xinqi Xu, Charles M. Coldwell, Alexander Panasyuk, James A. Benson, Costas Papaliolios, Read Predmore, F. P. Schloerb, H. M. Dyck & David M. Gibson. 1994. Current status of the IOTA interferometer. In James B. Breckinridge (ed.), *Amplitude and intensity spatial interferometry ii*, vol. 2200 (Society of Photo-Optical Instrumentation Engineers (SPIE) Conference Series), 152–165. DOI: [10.1117/12.177236](https://doi.org/10.1117/12.177236).
- Charbonneau, David, Timothy M. Brown, David W. Latham & Michel Mayor. 2000. Detection of Planetary Transits Across a Sun-like Star. 529(1). L45–L48. DOI: [10.1086/312457](https://doi.org/10.1086/312457).
- Chauvin, G., A. -M. Lagrange, C. Dumas, B. Zuckerman, D. Mouillet, I. Song, J. -L. Beuzit & P. Lowrance. 2004. A giant planet candidate near a young brown dwarf. Direct VLT/NACO observations using IR wavefront sensing. 425. L29–L32. DOI: [10.1051/0004-6361:20040005610.48550/arXiv.astro-ph/0409323](https://doi.org/10.1051/0004-6361:20040005610.48550/arXiv.astro-ph/0409323).
- Chauvin, G. et al. 2017. Discovery of a warm, dusty giant planet around HIP 65426. 605, L9. L9. DOI: [10.1051/0004-6361/201731152](https://doi.org/10.1051/0004-6361/201731152).

- Chazelas, Bruno, Frank Brachet, Pascal Bordé, Bertrand Mennesson, Marc Olivier, Olivier Absil, Alain Labèque, Claude Valette & Alain Léger. 2006. Instrumental stability requirements for exoplanet detection with a nulling interferometer: variability noise as a central issue. 45(5). 984–992. DOI: [10.1364/AO.45.000984](https://doi.org/10.1364/AO.45.000984).
- Chingaipe, Peter Marley, Frantz Martinache & Nick Cvetojevic. 2022. Four-input photonic kernel-nulling for the VLTI. In Antoine Mérand, Stephanie Sallum & Joel Sanchez-Bermudez (eds.), *Optical and infrared interferometry and imaging viii*, vol. 12183 (Society of Photo-Optical Instrumentation Engineers (SPIE) Conference Series), 1218319. DOI: [10.1117/12.2630050](https://doi.org/10.1117/12.2630050).
- Chingaipe, Peter Marley, Frantz Martinache, Nick Cvetojevic, Roxanne Ligi, David Mary, Mamadou N'Diaye, Denis Defrère & Michael J. Ireland. 2023. High-contrast detection of exoplanets with a kernel-nuller at the VLTI. 676, A43. A43. DOI: [10.1051/0004-6361/202346118](https://doi.org/10.1051/0004-6361/202346118).
- Cockell, C. S., A. Léger, M. Fridlund, T. M. Herbst, L. Kaltenegger, O. Absil, C. Beichman, W. Benz, M. Blanc, A. Brack, A. Chelli, L. Colangeli, H. Cottin, V. Coudé du Foresto, W. C. Danchi, D. Defrère, J. -W. den Herder, C. Eiroa, J. Greaves, T. Henning, K. J. Johnston, H. Jones, L. Labadie, H. Lammer, R. Launhardt, P. Lawson, O. P. Lay, J. -M. LeDuigou, R. Liseau, F. Malbet, S. R. Martin, D. Mawet, D. Mourard, C. Moutou, L. M. Mugnier, M. Ollivier, F. Paresce, A. Quirrenbach, Y. D. Rabbia, J. A. Raven, H. J. A. Rottgering, D. Rouan, N. C. Santos, F. Selsis, E. Serabyn, H. Shibai, M. Tamura, E. Thiébaud, F. Westall & G. J. White. 2009. Darwin-A Mission to Detect and Search for Life on Extrasolar Planets. *Astrobiology* 9(1). 1–22. DOI: [10.1089/ast.2007.0227](https://doi.org/10.1089/ast.2007.0227).
- Colavita, M. M. 1999. Fringe Visibility Estimators for the Palomar Testbed Interferometer. 111(755). 111–117. DOI: [10.1086/316302](https://doi.org/10.1086/316302).
- Colavita, M. M., E. Serabyn, R. Millan-Gabet, C. D. Koresko, R. L. Akeson, A. J. Booth, B. P. Mennesson, S. D. Ragland, E. C. Appleby, B. C. Berkey, A. Cooper, S. L. Crawford, M. J. Creech-Eakman, W. Dahl, C. Felizardo, J. I. Garcia-Gathright, J. T. Gathright, J. S. Herstein, E. E. Hovland, M. A. Hrynevych, E. R. Ligon, D. W. Medeiros, J. D. Moore, D. Morrison, C. G. Paine, D. L. Palmer, T. Panteleeva, B. Smith, M. R. Swain, R. F. Smythe, K. R. Summers, K. Tsubota, C. Tyau, G. Vasisht, E. Wetherell, P. L. Wizinowich & J. M. Woillez. 2009. Keck Interferometer Nuller Data Reduction and On-Sky Performance. 121(884). 1120. DOI: [10.1086/606063](https://doi.org/10.1086/606063).
- Colavita, M. M., P. L. Wizinowich, R. L. Akeson, S. Ragland, J. M. Woillez, R. Millan-Gabet, E. Serabyn, M. Abajian, D. S. Acton, E. Appleby, J. W. Beletic, C. A. Beichman, J. Bell, B. C. Berkey, J. Berlin, A. F. Boden, A. J. Booth, R. Boutell, F. H. Chaffee, D. Chan, J. Chin, J. Chock, R. Cohen, A. Cooper, S. L.

- Crawford, M. J. Creech-Eakman, W. Dahl, G. Eychaner, J. L. Fanson, C. Felizardo, J. I. Garcia-Gathright, J. T. Gathright, G. Hardy, H. Henderson, J. S. Herstein, M. Hess, E. E. Hovland, M. A. Hrynevych, E. Johansson, R. L. Johnson, J. Kelley, R. Kendrick, C. D. Koresko, P. Kurpis, D. Le Mignant, H. A. Lewis, E. R. Ligon, W. Lupton, D. McBride, D. W. Medeiros, B. P. Mennesson, J. D. Moore, D. Morrison, C. Nance, C. Neyman, A. Niessner, C. G. Paine, D. L. Palmer, T. Panteleeva, M. Papin, B. Parvin, L. Reder, A. Rudeen, T. Saloga, A. Sargent, M. Shao, B. Smith, R. F. Smythe, P. Stomski, K. R. Summers, M. R. Swain, P. Swanson, R. Thompson, K. Tsubota, A. Tumminello, C. Tyau, G. T. van Belle, G. Vasisht, J. Vause, F. Vescelus, J. Walker, J. K. Wallace, U. Wehmeier & E. Wetherell. 2013. The Keck Interferometer. 125(932). 1226. DOI: [10.1086/673475](https://doi.org/10.1086/673475).
- Corwin, K. L., N. R. Newbury, J. M. Dudley, S. Coen, S. A. Diddams, B. R. Washburn, K. Weber & R. S. Windeler. 2003. Fundamental amplitude noise limitations to supercontinuum spectra generated in a microstructured fiber. *Applied Physics B: Lasers and Optics* 77(2-3). 269–277. DOI: [10.1007/s00340-003-1175-x](https://doi.org/10.1007/s00340-003-1175-x).
- Coudé du Foresto, V., G. Perrin & M. Boccas. 1995. Minimization of fiber dispersion effects in double Fourier stellar interferometers. 293. 278–286.
- Coudé du Foresto, V., S. Ridgway & J. -M. Mariotti. 1997. Deriving object visibilities from interferograms obtained with a fiber stellar interferometer. 121. 379–392. DOI: [10.1051/aas:1997290](https://doi.org/10.1051/aas:1997290).
- Coudé du Foresto, V. & S. T. Ridgway. 1992. Fluor - a Stellar Interferometer Using Single-Mode Fibers. In *European southern observatory conference and workshop proceedings*, vol. 39 (European Southern Observatory Conference and Workshop Proceedings), 731.
- Coudé du Foresto, Vincent, Guy Perrin, Jean-Marie Mariotti, Marc Lacasse & Wes Traub. 1997. The FLUOR/IOTA fiber stellar interferometer. In Pierre Kern & Fabien Malbet (eds.), *Integrated optics for astronomical interferometry*, 115.
- Cvetojevic, Nick, Frantz Martinache, Peter Chingaïpe, Romain Laugier, Katarzyna Ławniczuk, Ronald G. Broeke, Roxanne Ligi, Mamadou N'Diaye & David Mary. 2022. 3-beam self-calibrated Kernel nulling photonic interferometer. *arXiv e-prints*, arXiv:2206.04977. arXiv:2206.04977. DOI: [10.48550/arXiv.2206.04977](https://doi.org/10.48550/arXiv.2206.04977).
- Cvetojevic, Nick, Frantz Martinache, Michael J. Ireland, Roxanne Ligi, Mamadou N'Diaye, Peter Chingaïpe & David Mary. 2023. Experimental validation of the Heimdallr higher-order fringe-tracker for long-baseline interferometry. , *in prep*.
- Defrère, D., P. M. Hinz, A. J. Skemer, G. M. Kennedy, V. P. Bailey, W. F. Hoffmann, B. Mennesson, R. Millan-Gabet, W. C. Danchi, O. Absil, P. Arbo, C. Beichman, G. Brusa, G. Bryden, E. C. Downey, O. Durney, S. Esposito, A. Gaspar, P. Grenz,

- C. Haniff, J. M. Hill, J. Lebreton, J. M. Leisenring, J. R. Males, L. Marion, T. J. McMahon, M. Montoya, K. M. Morzinski, E. Pinna, A. Puglisi, G. Rieke, A. Roberge, E. Serabyn, R. Sosa, K. Stapelfeldt, K. Su, V. Vaitheeswaran, A. Vaz, A. J. Weinberger & M. C. Wyatt. 2015. First-light LBT Nulling Interferometric Observations: Warm Exozodiacal Dust Resolved within a Few AU of η Crv. 799(1), 42. 42. DOI: [10.1088/0004-637X/799/1/42](https://doi.org/10.1088/0004-637X/799/1/42).
- Dudley, John M. & Stephane Coen. 2002. Coherence properties of supercontinuum spectra generated in photonic crystal and tapered optical fibers. *Optics Letters* 27(13). 1180–1182. DOI: [10.1364/OL.27.001180](https://doi.org/10.1364/OL.27.001180).
- Eisenhauer, Frank, Roberto Abuter, Klaus Bickert, Fabio Biancat-Marchet, Henri Bonnet, Joar Brynnel, Ralf D. Conzelmann, Bernard Delabre, Robert Donaldson, Jacopo Farinato, Enrico Fedrigo, Reinhard Genzel, Norbert N. Hubin, Christof Iserlohe, Markus E. Kasper, Markus Kissler-Patig, Guy J. Monnet, Claudia Roehrle, Juergen Schreiber, Stefan Stroebele, Matthias Tecza, Niranjana A. Thatte & Harald Weisz. 2003. SINFONI - Integral field spectroscopy at 50 milli-arcsecond resolution with the ESO VLT. In Masanori Iye & Alan F. M. Moorwood (eds.), *Instrument design and performance for optical/infrared ground-based telescopes*, vol. 4841 (Society of Photo-Optical Instrumentation Engineers (SPIE) Conference Series), 1548–1561. DOI: [10.1117/12.459468](https://doi.org/10.1117/12.459468).
- Errmann, Ronny, Stefano Minardi, Lucas Labadie, Balaji Muthusubramanian, Felix Dreisow, Stefan Nolte & Thomas Pertsch. 2015. Interferometric nulling of four channels with integrated optics. 54(24). 7449. DOI: [10.1364/AO.54.007449](https://doi.org/10.1364/AO.54.007449).
- Ertel, S., O. Absil, D. Defrère, J. -B. Le Bouquin, J. -C. Augereau, L. Marion, N. Blind, A. Bonsor, G. Bryden, J. Lebreton & J. Milli. 2014. A near-infrared interferometric survey of debris-disk stars. IV. An unbiased sample of 92 southern stars observed in H band with VLT/PIONIER. 570, A128. A128. DOI: [10.1051/0004-6361/201424438](https://doi.org/10.1051/0004-6361/201424438).
- Ertel, S., D. Defrère, O. Absil, J. -B. Le Bouquin, J. -C. Augereau, J. -P. Berger, N. Blind, A. Bonsor, A. -M. Lagrange, J. Lebreton, L. Marion, J. Milli & J. Olofsson. 2016. A near-infrared interferometric survey of debris-disc stars. V. PIONIER search for variability. 595, A44. A44. DOI: [10.1051/0004-6361/201527721](https://doi.org/10.1051/0004-6361/201527721).
- Ertel, S., D. Defrère, P. Hinz, B. Mennesson, G. M. Kennedy, W. C. Danchi, C. Gelino, J. M. Hill, W. F. Hoffmann, J. Mazoyer, G. Rieke, A. Shannon, K. Stapelfeldt, E. Spalding, J. M. Stone, A. Vaz, A. J. Weinberger, P. Willems, O. Absil, P. Arbo, V. P. Bailey, C. Beichman, G. Bryden, E. C. Downey, O. Durney, S. Esposito, A. Gaspar, P. Grenz, C. A. Haniff, J. M. Leisenring, L. Marion, T. J. McMahon, R. Millan-Gabet, M. Montoya, K. M. Morzinski, S. Perera, E. Pinna, J. -U. Pott, J. Power, A. Puglisi, A. Roberge, E. Serabyn, A. J. Skemer, K. Y. L. Su, V. Vaitheeswaran & M. C. Wyatt. 2020. The HOSTS Survey for Exozodiacal

- Dust: Observational Results from the Complete Survey. 159(4), 177. 177. DOI: [10.3847/1538-3881/ab7817](https://doi.org/10.3847/1538-3881/ab7817).
- Fischer, Debra A., Geoffrey W. Marcy, R. Paul Butler, Steven S. Vogt, Greg Laughlin, Gregory W. Henry, David Abouav, Kathryn M. G. Peek, Jason T. Wright, John A. Johnson, Chris McCarthy & Howard Isaacson. 2008. Five Planets Orbiting 55 Cancri. 675(1). 790–801. DOI: [10.1086/525512](https://doi.org/10.1086/525512).
- Fried, D. L. 1966. Optical Resolution Through a Randomly Inhomogeneous Medium for Very Long and Very Short Exposures. *Journal of the Optical Society of America (1917-1983)* 56(10). 1372.
- Froehly, C. 1981. Coherence and interferometry through optical fibers. In *Scientific importance of high angular resolution at infrared and optical wavelengths*, 285–293.
- Gagné, Jonathan, Eric E. Mamajek, Lison Malo, Adric Riedel, David Rodriguez, David Lafrenière, Jacqueline K. Faherty, Olivier Roy-Loubier, Laurent Pueyo, Annie C. Robin & René Doyon. 2018. BANYAN. XI. The BANYAN Σ Multivariate Bayesian Algorithm to Identify Members of Young Associations with 150 pc. 856(1), 23. 23. DOI: [10.3847/1538-4357/aae09](https://doi.org/10.3847/1538-4357/aae09).
- Galicher, R., E. Huby, P. Baudoz & O. Dupuis. 2020. A family of phase masks for broadband coronagraphy example of the wrapped vortex phase mask theory and laboratory demonstration. 635, A11. A11. DOI: [10.1051/0004-6361/201936971](https://doi.org/10.1051/0004-6361/201936971).
- Gautier, III, Thomas N., David Charbonneau, Jason F. Rowe, Geoffrey W. Marcy, Howard Isaacson, Guillermo Torres, Francois Fressin, Leslie A. Rogers, Jean-Michel Désert, Lars A. Buchhave, David W. Latham, Samuel N. Quinn, David R. Ciardi, Daniel C. Fabrycky, Eric B. Ford, Ronald L. Gilliland, Lucianne M. Walkowicz, Stephen T. Bryson, William D. Cochran, Michael Endl, Debra A. Fischer, Steve B. Howell, Elliott P. Horch, Thomas Barclay, Natalie Batalha, William J. Borucki, Jessie L. Christiansen, John C. Geary, Christopher E. Henze, Matthew J. Holman, Khadeejah Ibrahim, Jon M. Jenkins, Karen Kinemuchi, David G. Koch, Jack J. Lissauer, Dwight T. Sanderfer, Dimitar D. Sasselov, Sara Seager, Kathryn Silverio, Jeffrey C. Smith, Martin Still, Martin C. Stumpe, Peter Tenenbaum & Jeffrey Van Cleve. 2012. Kepler-20: A Sun-like Star with Three Sub-Neptune Exoplanets and Two Earth-size Candidates. 749(1), 15. 15. DOI: [10.1088/0004-637X/749/1/15](https://doi.org/10.1088/0004-637X/749/1/15).
- Genzel, Reinhard, Frank Eisenhauer & Stefan Gillessen. 2010. The Galactic Center massive black hole and nuclear star cluster. *Reviews of Modern Physics* 82(4). 3121–3195. DOI: [10.1103/RevModPhys.82.3121](https://doi.org/10.1103/RevModPhys.82.3121).

- Gillon, Michaël, Amaury H. M. J. Triaud, Brice-Olivier Demory, Emmanuël Jehin, Eric Agol, Katherine M. Deck, Susan M. Lederer, Julien de Wit, Artem Burdanov, James G. Ingalls, Emeline Bolmont, Jeremy Leconte, Sean N. Raymond, Franck Selsis, Martin Turbet, Khalid Barkaoui, Adam Burgasser, Matthew R. Burleigh, Sean J. Carey, Aleksander Chaushev, Chris M. Copperwheat, Laetitia Delrez, Catarina S. Fernandes, Daniel L. Holdsworth, Enrico J. Kotze, Valérie Van Grootel, Yaseen Almleaky, Zouhair Benkhaldoun, Pierre Magain & Didier Queloz. 2017. Seven temperate terrestrial planets around the nearby ultracool dwarf star TRAPPIST-1. 542(7642). 456–460. DOI: [10.1038/nature21360](https://doi.org/10.1038/nature21360).
- GRAVITY Collaboration, R. Abuter, A. Amorim, N. Anugu, M. Bauböck, M. Benisty, J. P. Berger, N. Blind, H. Bonnet, W. Brandner, A. Buron, C. Collin, F. Chapron, Y. Clénet, V. Coudé Du Foresto, P. T. de Zeeuw, C. Deen, F. Delplancke-Ströbele, R. Dembet, J. Dexter, G. Duvert, A. Eckart, F. Eisenhauer, G. Finger, N. M. Förster Schreiber, P. Fédou, P. Garcia, R. Garcia Lopez, F. Gao, E. Gendron, R. Genzel, S. Gillessen, P. Gordo, M. Habibi, X. Haubois, M. Haug, F. Haußmann, Th. Henning, S. Hippler, M. Horrobin, Z. Hubert, N. Hubin, A. Jimenez Rosales, L. Jochum, K. Jocu, A. Kaufer, S. Kellner, S. Kendrew, P. Kervella, Y. Kok, M. Kulas, S. Lacour, V. Lapeyrère, B. Lazareff, J. -B. Le Bouquin, P. Léna, M. Lippa, R. Lenzen, A. Mérand, E. Müller, U. Neumann, T. Ott, L. Palanca, T. Paumard, L. Pasquini, K. Perraut, G. Perrin, O. Pfuhl, P. M. Plewa, S. Rabien, A. Ramírez, J. Ramos, C. Rau, G. Rodríguez-Coira, R. -R. Rohloff, G. Rousset, J. Sanchez-Bermudez, S. Scheithauer, M. Schöller, N. Schuler, J. Spyromilio, O. Straub, C. Straubmeier, E. Sturm, L. J. Tacconi, K. R. W. Tristram, F. Vincent, S. von Fellenberg, I. Wank, I. Waisberg, F. Widmann, E. Wieprecht, M. Wiest, E. Wozzorek, J. Woillez, S. Yazici, D. Ziegler & G. Zins. 2018. Detection of the gravitational redshift in the orbit of the star S2 near the Galactic centre massive black hole. 615, L15. L15. DOI: [10.1051/0004-6361/201833718](https://doi.org/10.1051/0004-6361/201833718).
- GRAVITY Collaboration, S. Lacour, M. Nowak, J. Wang, O. Pfuhl, F. Eisenhauer, R. Abuter, A. Amorim, N. Anugu, M. Benisty, J. P. Berger, H. Beust, N. Blind, M. Bonnefoy, H. Bonnet, P. Bourget, W. Brandner, A. Buron, C. Collin, B. Charney, F. Chapron, Y. Clénet, V. Coudé Du Foresto, P. T. de Zeeuw, C. Deen, R. Dembet, J. Dexter, G. Duvert, A. Eckart, N. M. Förster Schreiber, P. Fédou, P. Garcia, R. Garcia Lopez, F. Gao, E. Gendron, R. Genzel, S. Gillessen, P. Gordo, A. Greenbaum, M. Habibi, X. Haubois, F. Haußmann, Th. Henning, S. Hippler, M. Horrobin, Z. Hubert, A. Jimenez Rosales, L. Jocu, S. Kendrew, P. Kervella, J. Kolb, A. -M. Lagrange, V. Lapeyrère, J. -B. Le Bouquin, P. Léna, M. Lippa, R. Lenzen, A. -L. Maire, P. Mollière, T. Ott, T. Paumard, K. Perraut, G. Perrin, L. Pueyo, S. Rabien, A. Ramírez, C. Rau, G. Rodríguez-Coira, G. Rousset, J.

- Sanchez-Bermudez, S. Scheithauer, N. Schuhler, O. Straub, C. Straubmeier, E. Sturm, L. J. Tacconi, F. Vincent, E. F. van Dishoeck, S. von Fellenberg, I. Wank, I. Waisberg, F. Widmann, E. Wieprecht, M. Wiest, E. Wiezorrek, J. Woillez, S. Yazici, D. Ziegler & G. Zins. 2019. First direct detection of an exoplanet by optical interferometry. Astrometry and K-band spectroscopy of HR 8799 e. 623, L11. L11. DOI: [10.1051/0004-6361/201935253](https://doi.org/10.1051/0004-6361/201935253).
- Guyon, Olivier. 2004. Imaging Faint Sources within a Speckle Halo with Synchronous Interferometric Speckle Subtraction. 615(1). 562–572. DOI: [10.1086/423980](https://doi.org/10.1086/423980).
- Guyon, Olivier, Bertrand Mennesson, Eugene Serabyn & Stefan Martin. 2013. Optimal Beam Combiner Design for Nulling Interferometers. 125(930). 951. DOI: [10.1086/671816](https://doi.org/10.1086/671816).
- Guyon, Olivier, Claude Roddier, J. Elon Graves, François Roddier, Salvador Cuevas, Carlos Espejo, Salustio Gonzalez, Andrea Martinez, Gianfranco Bisiacchi & Valeri Vuntsemeri. 1999. The Nulling Stellar Coronagraph: Laboratory Tests and Performance Evaluation. 111(764). 1321–1330. DOI: [10.1086/316445](https://doi.org/10.1086/316445).
- Haguenauer, Pierre, Jean-Philippe Berger, Karine Rousselet-Perraut, Pierre Kern, Fabien Malbet, Isabelle Schanen-Duport & Pierre Benech. 2000. Integrated Optics for Astronomical Interferometry. III. Optical Validation of a Planar Optics Two-Telescope Beam Combiner. 39(13). 2130–2139. DOI: [10.1364/AO.39.002130](https://doi.org/10.1364/AO.39.002130).
- Hanot, C., B. Mennesson, S. Martin, K. Liewer, F. Loya, D. Mawet, P. Riaud, O. Absil & E. Serabyn. 2011. Improving Interferometric Null Depth Measurements using Statistical Distributions: Theory and First Results with the Palomar Fiber Nuller. 729(2), 110. 110. DOI: [10.1088/0004-637X/729/2/110](https://doi.org/10.1088/0004-637X/729/2/110).
- Hansen, Jonah T., Michael J. Ireland & LIFE Collaboration. 2022. Large Interferometer For Exoplanets (LIFE). IV. Ideal kernel-nulling array architectures for a space-based mid-infrared nulling interferometer. 664, A52. A52. DOI: [10.1051/0004-6361/202243107](https://doi.org/10.1051/0004-6361/202243107).
- Hartmann, J. 1900a. Remarks on the Construction and Adjustment of Spectrographs. I. 11. 400. DOI: [10.1086/140709](https://doi.org/10.1086/140709).
- Hartmann, J. 1900b. Remarks on the Construction and Adjustment of Spectrographs. II. 12. 30. DOI: [10.1086/140723](https://doi.org/10.1086/140723).
- Hawley, Suzanne L. & Bjorn R. Pettersen. 1991. The Great Flare of 1985 April 12 on AD Leonis. 378. 725. DOI: [10.1086/170474](https://doi.org/10.1086/170474).
- Herbig, George H. 1960. The Spectra of Be- and Ae-Type Stars Associated with Nebulosity. 4. 337. DOI: [10.1086/190050](https://doi.org/10.1086/190050).
- Hill, J. M., J. R. P. Angel, J. S. Scott, D. Lindley & P. Hintzen. 1980. Multiple object spectroscopy: the medusa spectrograph. 242. L69–L72. DOI: [10.1086/183405](https://doi.org/10.1086/183405).

- Hinz, Philip M., J. Roger P. Angel, William F. Hoffmann, Donald W. McCarthy, Patrick C. McGuire, Matt Cheselka, Joseph L. Hora & Neville J. Woolf. 1998. Imaging circumstellar environments with a nulling interferometer. 395(6699). 251–253. DOI: [10.1038/26172](https://doi.org/10.1038/26172).
- Hinz, Philip M., James Roger P. Angel, Neville J. Woolf, William F. Hoffmann & Donald W. McCarthy. 2000. BLINC: a testbed for nulling interferometry in the thermal infrared. In Pierre Léna & Andreas Quirrenbach (eds.), *Interferometry in optical astronomy*, vol. 4006 (Society of Photo-Optical Instrumentation Engineers (SPIE) Conference Series), 349–353. DOI: [10.1117/12.390225](https://doi.org/10.1117/12.390225).
- Hubbard, E. N., J. R. P. Angel & M. S. Gresham. 1979. Operation of a long fused silica fiber as a link between telescope and spectrograph. 229. 1074–1078. DOI: [10.1086/157041](https://doi.org/10.1086/157041).
- Ireland, M. 2020. Kernel nulling: fundamental limitations and technological pathways from ground and space. In *Advances in optical astronomical instrumentation 2019*, vol. 11203 (Society of Photo-Optical Instrumentation Engineers (SPIE) Conference Series), 112030U. DOI: [10.1117/12.2540970](https://doi.org/10.1117/12.2540970).
- Ireland, Michael J., Denis Defrère, Frantz Martinache, John D. Monnier, Barnaby Norris, Peter Tuthill & Julien Woillez. 2018. Image-plane fringe tracker for adaptive-optics assisted long baseline interferometry. In Michelle J. Creech-Eakman, Peter G. Tuthill & Antoine Mérand (eds.), *Optical and infrared interferometry and imaging vi*, vol. 10701 (Society of Photo-Optical Instrumentation Engineers (SPIE) Conference Series), 1070111. DOI: [10.1117/12.2314393](https://doi.org/10.1117/12.2314393).
- Ireland, Michael J., John D. Monnier & Nathalie Thureau. 2006. Monte-Carlo imaging for optical interferometry. In John D. Monnier, Markus Schöller & William C. Danchi (eds.), *Society of photo-optical instrumentation engineers (spie) conference series*, vol. 6268 (Society of Photo-Optical Instrumentation Engineers (SPIE) Conference Series), 62681T. DOI: [10.1117/12.670940](https://doi.org/10.1117/12.670940).
- Iserlohe, Christof, Matthias Tecza, Frank Eisenhauer, Reinhard Genzel, Niranjan A. Thatte, Roberto Abuter, Matthew J. Horrobin, Alexander Schegerer, Jürgen Schreiber & Henri Bonnet. 2004. On-sky performance of SPIFFI: the integral field spectrometer for SINFONI at the VLT. In Alan F. M. Moorwood & Masanori Iye (eds.), *Ground-based instrumentation for astronomy*, vol. 5492 (Society of Photo-Optical Instrumentation Engineers (SPIE) Conference Series), 1123–1134. DOI: [10.1117/12.552197](https://doi.org/10.1117/12.552197).
- IYE, Masanori. 2021. Subaru Telescope —History, active/adaptive optics, instruments, and scientific achievements—. *Proceedings of the Japan Academy, Series B* 97(7). 337–370. DOI: [10.2183/pjab.97.019](https://doi.org/10.2183/pjab.97.019).

- Jennison, R. C. 1958. A phase sensitive interferometer technique for the measurement of the Fourier transforms of spatial brightness distributions of small angular extent. 118. 276. DOI: [10.1093/mnras/118.3.276](https://doi.org/10.1093/mnras/118.3.276).
- Jovanovic, N., F. Martinache, O. Guyon, C. Clergeon, G. Singh, T. Kudo, V. Garrel, K. Newman, D. Doughty, J. Lozi, J. Males, Y. Minowa, Y. Hayano, N. Takato, J. Morino, J. Kuhn, E. Serabyn, B. Norris, P. Tuthill, G. Schworer, P. Stewart, L. Close, E. Huby, G. Perrin, S. Lacour, L. Gauchet, S. Vievard, N. Murakami, F. Oshiyama, N. Baba, T. Matsuo, J. Nishikawa, M. Tamura, O. Lai, F. Marchis, G. Duchene, T. Kotani & J. Woillez. 2015. The Subaru Coronagraphic Extreme Adaptive Optics System: Enabling High-Contrast Imaging on Solar-System Scales. 127(955). 890. DOI: [10.1086/682989](https://doi.org/10.1086/682989).
- Jovanovic, N., P. G. Tuthill, B. Norris, S. Gross, P. Stewart, N. Charles, S. Lacour, M. Ams, J. S. Lawrence, A. Lehmann, C. Niel, J. G. Robertson, G. D. Marshall, M. Ireland, A. Fuerbach & M. J. Withford. 2012. Starlight demonstration of the Dragonfly instrument: an integrated photonic pupil-remapping interferometer for high-contrast imaging. 427(1). 806–815. DOI: [10.1111/j.1365-2966.2012.21997.x](https://doi.org/10.1111/j.1365-2966.2012.21997.x).
- Jovanovic, Nemanja, Pradip Gatkin, Boqiang Shen, Maodong Gao, Nick Cvetojevic, Katarzyna Ławniczuk, Ronald Broeke, Charles Beichman, Stephanie Leifer, Jeffery Jewell, Gautam Vasisht & Dimitri Mawet. 2022. Flattening laser frequency comb spectra with a high dynamic range, broadband spectral shaper on-a-chip. *Optics Express* 30(20). 36745. DOI: [10.1364/OE.470143](https://doi.org/10.1364/OE.470143).
- Joy, Alfred H. 1945. T Tauri Variable Stars. 102. 168. DOI: [10.1086/144749](https://doi.org/10.1086/144749).
- Karlsson, Anders L., Oswald Wallner, Josep M. Perdigues Armengol & Olivier Absil. 2004. Three telescope nuller based on multibeam injection into single-mode waveguide. In Wesley A. Traub (ed.), *New frontiers in stellar interferometry*, vol. 5491 (Society of Photo-Optical Instrumentation Engineers (SPIE) Conference Series), 831. DOI: [10.1117/12.550307](https://doi.org/10.1117/12.550307).
- Kasting, James F., Daniel P. Whitmire & Ray T. Reynolds. 1993. Habitable Zones around Main Sequence Stars. 101(1). 108–128. DOI: [10.1006/icar.1993.1010](https://doi.org/10.1006/icar.1993.1010).
- Kenchington Goldsmith, Harry-Dean, Nick Cvetojevic, Michael Ireland & Stephen Madden. 2017. Fabrication tolerant chalcogenide mid-infrared multi-mode interference coupler design with applications for Bracewell nulling interferometry. *Optics Express* 25(4). 3038. DOI: [10.1364/OE.25.003038](https://doi.org/10.1364/OE.25.003038).
- Kenchington Goldsmith, Harry-Dean, Michael Ireland, Pan Ma, Nick Cvetojevic & Stephen Madden. 2017. Improving the extinction bandwidth of MMI chalcogenide photonic chip based MIR nulling interferometers. *Optics Express* 25(14). 16813. DOI: [10.1364/OE.25.016813](https://doi.org/10.1364/OE.25.016813).

- Kenyon, Scott J. & Lee Hartmann. 1995. Pre-Main-Sequence Evolution in the Taurus-Auriga Molecular Cloud. 101. 117. DOI: [10.1086/192235](https://doi.org/10.1086/192235).
- Keppler, M. et al. 2018. Discovery of a planetary-mass companion within the gap of the transition disk around PDS 70. 617, A44. A44. DOI: [10.1051/0004-6361/201832957](https://doi.org/10.1051/0004-6361/201832957).
- Kern, Pierre, Fabien Malbet, Isabelle Schanen-Duport & Pierre Benech. 1997. Integrated optics single-mode interferometric beam combiner for near infrared astronomy. In Pierre Kern & Fabien Malbet (eds.), *Integrated optics for astronomical interferometry*, 115.
- Kervella, Pierre, Frédéric Arenou & Frédéric Thévenin. 2022. Stellar and substellar companions from Gaia EDR3. Proper-motion anomaly and resolved common proper-motion pairs. 657, A7. A7. DOI: [10.1051/0004-6361/202142146](https://doi.org/10.1051/0004-6361/202142146).
- Kuhn, J. R., D. Potter & B. Parise. 2001. Imaging Polarimetric Observations of a New Circumstellar Disk System. 553(2). L189–L191. DOI: [10.1086/320686](https://doi.org/10.1086/320686).
- Kühn, J., B. Mennesson, K. Liewer, S. Martin, F. Loya, R. Millan-gabet & E. Serabyn. 2015. Exploring Intermediate (5–40 au) Scales around AB Aurigae with the Palomar Fiber Nuller. 800(1), 55. 55. DOI: [10.1088/0004-637X/800/1/55](https://doi.org/10.1088/0004-637X/800/1/55).
- Labeyrie, A. 1970. Attainment of Diffraction Limited Resolution in Large Telescopes by Fourier Analysing Speckle Patterns in Star Images. 6. 85.
- Labeyrie, A. 1975. Interference fringes obtained on Vega with two optical telescopes. 196. L71–L75. DOI: [10.1086/181747](https://doi.org/10.1086/181747).
- Lacour, S., R. Dembet, R. Abuter, P. Fédou, G. Perrin, É. Choquet, O. Pfuhl, F. Eisenhauer, J. Woillez, F. Cassaing, E. Wieprecht, T. Ott, E. Wiezorrek, K. R. W. Tristram, B. Wolff, A. Ramírez, X. Haubois, K. Perraut, C. Straubmeier, W. Brandner & A. Amorim. 2019. The GRAVITY fringe tracker. 624, A99. A99. DOI: [10.1051/0004-6361/201834981](https://doi.org/10.1051/0004-6361/201834981).
- Lacour, S., P. Tuthill, J. D. Monnier, T. Kotani, L. Gauchet & P. Labeye. 2014. A new interferometer architecture combining nulling with phase closure measurements. 439(4). 4018–4029. DOI: [10.1093/mnras/stu258](https://doi.org/10.1093/mnras/stu258).
- Lafrenière, David, Christian Marois, René Doyon, Daniel Nadeau & Étienne Artigau. 2007. A New Algorithm for Point-Spread Function Subtraction in High-Contrast Imaging: A Demonstration with Angular Differential Imaging. 660(1). 770–780. DOI: [10.1086/513180](https://doi.org/10.1086/513180).
- Lagadec, Tiphaine, Barnaby Norris, Simon Gross, Alexander Arriola, Thomas Gretzinger, Nick Cvetojevic, Jon Lawrence, Michael Withford & Peter Tuthill. 2018. GLINT South: a photonic nulling interferometer pathfinder at the Anglo-Australian Telescope for high contrast imaging of substellar companions. In Michelle J. Creech-Eakman, Peter G. Tuthill & Antoine Mérand (eds.), *Optical and infrared interferometry and imaging vi*, vol. 10701 (Society of Photo-

- Optical Instrumentation Engineers (SPIE) Conference Series), 107010V. DOI: [10.1117/12.2313171](https://doi.org/10.1117/12.2313171).
- Lane, Benjamin F., Matthew W. Muterspaugh & Michael Shao. 2006. Calibrating an Interferometric Null. 648(2). 1276–1284. DOI: [10.1086/506020](https://doi.org/10.1086/506020).
- Laugier, Romain, Nick Cvetojevic & Frantz Martinache. 2020. Kernel nullers for an arbitrary number of apertures. 642, A202. A202. DOI: [10.1051/0004-6361/202038866](https://doi.org/10.1051/0004-6361/202038866).
- Laugier, Romain, Denis Defrère, Julien Woillez, Benjamin Courtney-Barrer, Felix A. Dannert, Alexis Matter, Colin Dandumont, Simon Gross, Olivier Absil, Azzurra Bigioli, Germain Garreau, Lucas Labadie, Jérôme Loicq, Marc-Antoine Martinod, Alexandra Mazzoli, Gert Raskin & Ahmed Sanny. 2023. Asgard/NOTT: L-band nulling interferometry at the VLTI. I. Simulating the expected high-contrast performance. 671, A110. A110. DOI: [10.1051/0004-6361/202244351](https://doi.org/10.1051/0004-6361/202244351).
- Lay, Oliver, Muthu Jeganathan & Robert Peters. 2003. Adaptive nulling: a new tool for interferometric exo-planet detection. In Malcolm Fridlund, Thomas Henning & Huguette Lacoste (eds.), *Earths: darwin/tpf and the search for extra-solar terrestrial planets*, vol. 539 (ESA Special Publication), 503–506.
- Lay, Oliver P. 2004. Systematic Errors in Nulling Interferometers. 43(33). 6100–6123. DOI: [10.1364/AO.43.006100](https://doi.org/10.1364/AO.43.006100).
- Lay, Oliver P. 2006. Removing instability noise in nulling interferometers. In John D. Monnier, Markus Schöller & William C. Danchi (eds.), *Society of photo-optical instrumentation engineers (spie) conference series*, vol. 6268 (Society of Photo-Optical Instrumentation Engineers (SPIE) Conference Series), 62681A. DOI: [10.1117/12.670603](https://doi.org/10.1117/12.670603).
- Lay, Oliver P. & Serge Dubovitsky. 2004. Nulling interferometers: the importance of systematic errors and the X-array configuration. In Wesley A. Traub (ed.), *New frontiers in stellar interferometry*, vol. 5491 (Society of Photo-Optical Instrumentation Engineers (SPIE) Conference Series), 874. DOI: [10.1117/12.552109](https://doi.org/10.1117/12.552109).
- Le Bouquin, J. -B., J. -P. Berger, B. Lazareff, G. Zins, P. Haguenaer, L. Jocou, P. Kern, R. Millan-Gabet, W. Traub, O. Absil, J. -C. Augereau, M. Benisty, N. Blind, X. Bonfils, P. Bourget, A. Delboulbe, P. Feautrier, M. Germain, P. Gitton, D. Gillier, M. Kiekebusch, J. Kluska, J. Knudstrup, P. Labeye, J. -L. Lizon, J. -L. Monin, Y. Magnard, F. Malbet, D. Maurel, F. Ménard, M. Micallef, L. Michaud, G. Montagnier, S. Morel, T. Moulin, K. Perraut, D. Popovic, P. Rabou, S. Rochat, C. Rojas, F. Rousel, A. Roux, E. Stadler, S. Stefl, E. Tatulli & N. Ventura. 2011. PIONIER: a 4-telescope visitor instrument at VLTI. 535, A67. A67. DOI: [10.1051/0004-6361/201117586](https://doi.org/10.1051/0004-6361/201117586).

- Léger, A., J. M. Mariotti, B. Mennesson, M. Ollivier, J. L. Puget, D. Rouan & J. Schneider. 1996. Could We Search for Primitive Life on Extrasolar Planets in the Near Future? *123*(2). 249–255. DOI: [10.1006/icar.1996.0155](https://doi.org/10.1006/icar.1996.0155).
- Leon-Saval, S. G., T. A. Birks, J. Bland-Hawthorn & M. Englund. 2005. Multimode fiber devices with single-mode performance. *Optics Letters* 30(19). 2545–2547. DOI: [10.1364/OL.30.002545](https://doi.org/10.1364/OL.30.002545).
- Lopez, B. et al. 2022. MATISSE, the VLTI mid-infrared imaging spectro-interferometer. 659, A192. A192. DOI: [10.1051/0004-6361/202141785](https://doi.org/10.1051/0004-6361/202141785).
- Lyot, Bernard. 1939. The study of the solar corona and prominences without eclipses (George Darwin Lecture, 1939). 99. 580. DOI: [10.1093/mnras/99.8.580](https://doi.org/10.1093/mnras/99.8.580).
- Macintosh, B., J. R. Graham, T. Barman, R. J. De Rosa, Q. Konopacky, M. S. Marley, C. Marois, E. L. Nielsen, L. Pueyo, A. Rajan, J. Rameau, D. Saumon, J. J. Wang, J. Patience, M. Ammons, P. Arriaga, E. Artigau, S. Beckwith, J. Brewster, S. Bruzzone, J. Bulger, B. Burningham, A. S. Burrows, C. Chen, E. Chiang, J. K. Chilcote, R. I. Dawson, R. Dong, R. Doyon, Z. H. Draper, G. Duchêne, T. M. Esposito, D. Fabrycky, M. P. Fitzgerald, K. B. Follette, J. J. Fortney, B. Gerard, S. Goodsell, A. Z. Greenbaum, P. Hibon, S. Hinkley, T. H. Cotten, L. -W. Hung, P. Ingraham, M. Johnson-Groh, P. Kalas, D. Lafreniere, J. E. Larkin, J. Lee, M. Line, D. Long, J. Maire, F. Marchis, B. C. Matthews, C. E. Max, S. Metchev, M. A. Millar-Blanchaer, T. Mittal, C. V. Morley, K. M. Morzinski, R. Murray-Clay, R. Oppenheimer, D. W. Palmer, R. Patel, M. D. Perrin, L. A. Poyneer, R. R. Rafikov, F. T. Rantakyro, E. L. Rice, P. Rojo, A. R. Rudy, J. -B. Ruffio, M. T. Ruiz, N. Sadakuni, L. Saddlemyer, M. Salama, D. Savransky, A. C. Schneider, A. Sivaramakrishnan, I. Song, R. Soummer, S. Thomas, G. Vasisht, J. K. Wallace, K. Ward-Duong, S. J. Wiktorowicz, S. G. Wolff & B. Zuckerman. 2015. Discovery and spectroscopy of the young jovian planet 51 Eri b with the Gemini Planet Imager. *Science* 350(6256). 64–67. DOI: [10.1126/science.aac5891](https://doi.org/10.1126/science.aac5891).
- Macintosh, Bruce, James R. Graham, Patrick Ingraham, Quinn Konopacky, Christian Marois, Marshall Perrin, Lisa Poyneer, Brian Bauman, Travis Barman, Adam S. Burrows, Andrew Cardwell, Jeffrey Chilcote, Robert J. De Rosa, Daren Dillon, Rene Doyon, Jennifer Dunn, Darren Erikson, Michael P. Fitzgerald, Donald Gavel, Stephen Goodsell, Markus Hartung, Pascale Hibon, Paul Kalas, James Larkin, Jerome Maire, Franck Marchis, Mark S. Marley, James McBride, Max Millar-Blanchaer, Katie Morzinski, Andrew Norton, B. R. Oppenheimer, David Palmer, Jennifer Patience, Laurent Pueyo, Fredrik Rantakyro, Naru Sadakuni, Leslie Saddlemyer, Dmitry Savransky, Andrew Serio, Remi Soummer, Anand Sivaramakrishnan, Inseok Song, Sandrine Thomas, J. Kent Wallace, Sloane Wiktorowicz & Schuyler Wolff. 2014. First light of the Gemini

- Planet Imager. *Proceedings of the National Academy of Science* 111(35). 12661–12666. DOI: [10.1073/pnas.1304215111](https://doi.org/10.1073/pnas.1304215111).
- Marois, Christian, David Lafrenière, René Doyon, Bruce Macintosh & Daniel Nadeau. 2006. Angular Differential Imaging: A Powerful High-Contrast Imaging Technique. 641(1). 556–564. DOI: [10.1086/500401](https://doi.org/10.1086/500401).
- Martinache, Frantz. 2010. Kernel Phase in Fizeau Interferometry. 724(1). 464–469. DOI: [10.1088/0004-637X/724/1/464](https://doi.org/10.1088/0004-637X/724/1/464).
- Martinache, Frantz & Michael J. Ireland. 2018. Kernel-nulling for a robust direct interferometric detection of extrasolar planets. 619, A87. A87. DOI: [10.1051/0004-6361/201832847](https://doi.org/10.1051/0004-6361/201832847).
- Martinod, Marc-Antoine, Barnaby Norris, Peter Tuthill, Tiphaine Lagadec, Nemanja Jovanovic, Nick Cvetojevic, Simon Gross, Alexander Arriola, Thomas Gretzinger, Michael J. Withford, Olivier Guyon, Julien Lozi, Sébastien Vievard, Vincent Deo, Jon S. Lawrence & Sergio Leon-Saval. 2021. Scalable photonic-based nulling interferometry with the dispersed multi-baseline GLINT instrument. *Nature Communications* 12, 2465. 2465. DOI: [10.1038/s41467-021-22769-x](https://doi.org/10.1038/s41467-021-22769-x).
- Mawet, D., P. Riaud, O. Absil & J. Surdej. 2005. Annular Groove Phase Mask Coronagraph. 633(2). 1191–1200. DOI: [10.1086/462409](https://doi.org/10.1086/462409).
- Mayor, Michel & Didier Queloz. 1995. A Jupiter-mass companion to a solar-type star. 378(6555). 355–359. DOI: [10.1038/378355a0](https://doi.org/10.1038/378355a0).
- Mennesson, B., P. Haguenaer, E. Serabyn & K. Liewer. 2006. Deep broad-band infrared nulling using a single-mode fiber beam combiner and baseline rotation. In John D. Monnier, Markus Schöller & William C. Danchi (eds.), *Society of photo-optical instrumentation engineers (spie) conference series*, vol. 6268 (Society of Photo-Optical Instrumentation Engineers (SPIE) Conference Series), 626830. DOI: [10.1117/12.672157](https://doi.org/10.1117/12.672157).
- Mennesson, B., E. Serabyn, C. Hanot, S. R. Martin, K. Liewer & D. Mawet. 2011. New Constraints on Companions and Dust within a Few AU of Vega. 736(1), 14. 14. DOI: [10.1088/0004-637X/736/1/14](https://doi.org/10.1088/0004-637X/736/1/14).
- Mennesson, Bertrand, Alain Léger & Marc Ollivier. 2005. Direct detection and characterization of extrasolar planets: The Mariotti space interferometer. 178(2). 570–588. DOI: [10.1016/j.icarus.2005.05.012](https://doi.org/10.1016/j.icarus.2005.05.012).
- Mennesson, Bertrand & Jean Marie Mariotti. 1997. Array Configurations for a Space Infrared Nulling Interferometer Dedicated to the Search for Earthlike Extrasolar Planets. 128(1). 202–212. DOI: [10.1006/icar.1997.5731](https://doi.org/10.1006/icar.1997.5731).
- Meshkat, T., V. Bailey, J. Rameau, M. Bonnefoy, A. Boccaletti, E. E. Mamajek, M. Kenworthy, G. Chauvin, A. -M. Lagrange, K. Y. L. Su & T. Currie. 2013. Further

- Evidence of the Planetary Nature of HD 95086 b from Gemini/NICI H-band Data. 775(2), L40. L40. DOI: [10.1088/2041-8205/775/2/L40](https://doi.org/10.1088/2041-8205/775/2/L40).
- Michelson, A. A. 1920. On the Application of Interference Methods to Astronomical Measurements. 51. 257. DOI: [10.1086/142550](https://doi.org/10.1086/142550).
- Michelson, A. A. & F. G. Pease. 1921. Measurement of the Diameter of α Orionis with the Interferometer. 53. 249–259. DOI: [10.1086/142603](https://doi.org/10.1086/142603).
- Miller, Stewart E. 1969. Integrated optics: an introduction. *The Bell System Technical Journal* 48(7). 2059–2069. DOI: [10.1002/j.1538-7305.1969.tb01165.x](https://doi.org/10.1002/j.1538-7305.1969.tb01165.x).
- Monnier, John D., Jean-Philippe Berger, Rafael Millan-Gabet & Theo A. ten Brummelaar. 2004. The Michigan Infrared Combiner (MIRC): IR imaging with the CHARA Array. In Wesley A. Traub (ed.), *New frontiers in stellar interferometry*, vol. 5491 (Society of Photo-Optical Instrumentation Engineers (SPIE) Conference Series), 1370. DOI: [10.1117/12.550804](https://doi.org/10.1117/12.550804).
- Mottier, Patrick. 1997. Integrated optics and micro-optics at LETI. In Pierre Kern & Fabien Malbet (eds.), *Integrated optics for astronomical interferometry*, 115.
- Murphy, Simon J., Warrick A. Lawson & Michael S. Bessell. 2013. Re-examining the membership and origin of the ϵ Cha association. 435(2). 1325–1349. DOI: [10.1093/mnras/stt1375](https://doi.org/10.1093/mnras/stt1375).
- N'Diaye, M., K. Dohlen, T. Fusco & B. Paul. 2013. Calibration of quasi-static aberrations in exoplanet direct-imaging instruments with a Zernike phase-mask sensor. 555, A94. A94. DOI: [10.1051/0004-6361/201219797](https://doi.org/10.1051/0004-6361/201219797).
- Nikolov, N., D. K. Sing, J. J. Fortney, J. M. Goyal, B. Drummond, T. M. Evans, N. P. Gibson, E. J. W. De Mooij, Z. Rustamkulov, H. R. Wakeford, B. Smalley, A. J. Burgasser, C. Hellier, Ch. Helling, N. J. Mayne, N. Madhusudhan, T. Kataria, J. Baines, A. L. Carter, G. E. Ballester, J. K. Barstow, J. McCleery & J. J. Spake. 2018. An absolute sodium abundance for a cloud-free ‘hot Saturn’ exoplanet. 557(7706). 526–529. DOI: [10.1038/s41586-018-0101-7](https://doi.org/10.1038/s41586-018-0101-7).
- Norris, Barnaby R. M., Nick Cvetojevic, Tiphaine Lagadec, Nemanja Jovanovic, Simon Gross, Alexander Arriola, Thomas Gretzinger, Marc-Antoine Martinod, Olivier Guyon, Julien Lozi, Michael J. Withford, Jon S. Lawrence & Peter Tuthill. 2020. First on-sky demonstration of an integrated-photonics nulling interferometer: the GLINT instrument. 491(3). 4180–4193. DOI: [10.1093/mnras/stz3277](https://doi.org/10.1093/mnras/stz3277).
- Norris, Barnaby R. M., Marc-Antoine Martinod, Peter Tuthill, Simon Gross, Nick Cvetojevic, Nemanja Jovanovic, Tiphaine Lagadec, Teresa Klinner-teo, Olivier Guyon, Julien Lozi, Vincent Deo, Sébastien Vievard, Alex Arriola, Thomas Gretzinger, Jon S. Lawrence & Michael J. Withford. 2022. Optimal self-calibration and fringe tracking in photonic nulling interferometers using machine learning. In Antoine Mérand, Stephanie Sallum & Joel Sanchez-

- Bermudez (eds.), *Optical and infrared interferometry and imaging viii*, vol. 12183 (Society of Photo-Optical Instrumentation Engineers (SPIE) Conference Series), 121831J. DOI: [10.1117/12.2629873](https://doi.org/10.1117/12.2629873).
- Ohnaka, K., G. Weigelt & K. -H. Hofmann. 2017. Vigorous atmospheric motion in the red supergiant star Antares. 548(7667). 310–312. DOI: [10.1038/nature23445](https://doi.org/10.1038/nature23445).
- Pannetier, Cyril, Philippe Bério, Denis Mourard, Sylvain Rousseau, Fatmé Alouche, Julien Dejonghe, Christophe Bailet, Daniel Lecron, Frédéric Cassaing, Jean-Baptiste Le Bouquin, Karine Perraut, John Monnier, Narsireddy Anugu & Theo ten Brummelaar. 2022. SPICA-FT: the new fringe tracker of the CHARA array. In Antoine Mérand, Stephanie Sallum & Joel Sanchez-Bermudez (eds.), *Optical and infrared interferometry and imaging viii*, vol. 12183 (Society of Photo-Optical Instrumentation Engineers (SPIE) Conference Series), 1218309. DOI: [10.1117/12.2628897](https://doi.org/10.1117/12.2628897).
- Pecaut, Mark J. & Eric E. Mamajek. 2016. The star formation history and accretion-disc fraction among the K-type members of the Scorpius-Centaurus OB association. 461(1). 794–815. DOI: [10.1093/mnras/stw1300](https://doi.org/10.1093/mnras/stw1300).
- Pennings, E. C. M., R. van Roijen, M. J. N. van Stralen, P. J. de Waard, R. G. M. P. Koumans & B. H. Verbeek. 1994. Reflection properties of multimode interference devices. *IEEE Photonics Technology Letters* 6(6). 715–718. DOI: [10.1109/68.300172](https://doi.org/10.1109/68.300172).
- Penny, Matthew T., B. Scott Gaudi, Eamonn Kerins, Nicholas J. Rattenbury, Shude Mao, Annie C. Robin & Sebastiano Calchi Novati. 2019. Predictions of the WFIRST Microlensing Survey. I. Bound Planet Detection Rates. 241(1), 3. 3. DOI: [10.3847/1538-4365/aafb69](https://doi.org/10.3847/1538-4365/aafb69).
- Perraut, K., L. Jocou, J. P. Berger, A. Chabli, V. Cardin, G. Chamot-Maitral, A. Delboulbé, F. Eisenhauer, Y. Gámbérini, S. Gillessen, S. Guieu, J. Guerrero, M. Haug, F. Hausmann, F. Joulain, P. Kervella, P. Labeye, S. Lacour, C. Lanthermann, V. Lapras, J. B. Le Bouquin, M. Lippa, Y. Magnard, T. Moulin, P. Noël, A. Nolot, F. Patru, G. Perrin, O. Pfuhl, S. Pocas, S. Poulain, C. Scibetta, E. Stadler, R. Templier, N. Ventura, C. Vizios, A. Amorim, W. Brandner & C. Straubmeier. 2018. Single-mode waveguides for GRAVITY. I. The cryogenic 4-telescope integrated optics beam combiner. 614, A70. A70. DOI: [10.1051/0004-6361/201732544](https://doi.org/10.1051/0004-6361/201732544).
- Peters, Robert D., Oliver P. Lay & Peter R. Lawson. 2010. Mid-Infrared Adaptive Nulling for the Detection of Earthlike Exoplanets. 122(887). 85. DOI: [10.1086/649850](https://doi.org/10.1086/649850).
- Petrov, R. G., F. Malbet, G. Weigelt, P. Antonelli, U. Beckmann, Y. Bresson, A. Chelli, M. Dugué, G. Duvert, S. Gennari, L. Glück, P. Kern, S. Lagarde, E. Le Coarer, F. Lisi, F. Millour, K. Perraut, P. Puget, F. Rantakyro, S. Robbe-Dubois,

- A. Roussel, P. Salinari, E. Tatulli, G. Zins, M. Accardo, B. Acke, K. Agabi, E. Altariba, B. Arezki, E. Aristidi, C. Baffa, J. Behrend, T. Blöcker, S. Bonhomme, S. Busoni, F. Cassaing, J. -M. Clause, J. Colin, C. Connot, A. Delboulbé, A. Domiciano de Souza, T. Driebe, P. Feautrier, D. Ferruzzi, T. Forveille, E. Fos-
sat, R. Foy, D. Fraix-Burnet, A. Gallardo, E. Giani, C. Gil, A. Glentzlin, M. Hei-
den, M. Heininger, O. Hernandez Utrera, K. -H. Hofmann, D. Kamm, M. Kieke-
busch, S. Kraus, D. Le Contel, J. -M. Le Contel, T. Lesourd, B. Lopez, M. Lopez,
Y. Magnard, A. Marconi, G. Mars, G. Martinot-Lagarde, P. Mathias, P. Mège,
J. -L. Monin, D. Mouillet, D. Mourard, E. Nussbaum, K. Ohnaka, J. Pacheco,
C. Perrier, Y. Rabbia, S. Rebattu, F. Reynaud, A. Richichi, A. Robini, M. Sac-
chettini, D. Schertl, M. Schöller, W. Solscheid, A. Spang, P. Stee, P. Stefanini,
M. Tallon, I. Tallon-Bosc, D. Tasso, L. Testi, F. Vakili, O. von der Lüche, J. -C.
Valtier, M. Vannier & N. Ventura. 2007. AMBER, the near-infrared spectro-
interferometric three-telescope VLT instrument. 464(1). 1–12. DOI: [10.1051/
0004-6361:20066496](https://doi.org/10.1051/0004-6361:20066496).
- Pollack, James B., Olenka Hubickyj, Peter Bodenheimer, Jack J. Lissauer, Morris
Podolak & Yuval Greenzweig. 1996. Formation of the Giant Planets by Concur-
rent Accretion of Solids and Gas. 124(1). 62–85. DOI: [10.1006/icar.1996.0190](https://doi.org/10.1006/icar.1996.0190).
- Quanz, S. P., M. Ottiger, E. Fontanet, J. Kammerer, F. Menti, F. Dannert, A. Ghe-
orghe, O. Absil, V. S. Airapetian, E. Alei, R. Allart, D. Angerhausen, S. Blu-
menthal, L. A. Buchhave, J. Cabrera, Ó. Carrión-González, G. Chauvin, W. C.
Danchi, C. Dandumont, D. Defrére, C. Dorn, D. Ehrenreich, S. Ertel, M. Frid-
lund, A. García Muñoz, C. Gascón, J. H. Girard, A. Glauser, J. L. Grenfell, G.
Guidi, J. Hagelberg, R. Helled, M. J. Ireland, M. Janson, R. K. Kopparapu, J. Ko-
rth, T. Kozakis, S. Kraus, A. Léger, L. Leedjäv, T. Lichtenberg, J. Lillo-Box,
H. Linz, R. Liseau, J. Loicq, V. Mahendra, F. Malbet, J. Mathew, B. Mennes-
son, M. R. Meyer, L. Mishra, K. Molaverdikhani, L. Noack, A. V. Oza, E. Pallé,
H. Parviainen, A. Quirrenbach, H. Rauer, I. Ribas, M. Rice, A. Romagnolo, S.
Rugheimer, E. W. Schwieterman, E. Serabyn, S. Sharma, K. G. Stassun, J. Szulá-
gyi, H. S. Wang, F. Wunderlich, M. C. Wyatt & LIFE Collaboration. 2022. Large
Interferometer For Exoplanets (LIFE). I. Improved exoplanet detection yield es-
timates for a large mid-infrared space-interferometer mission. 664, A21. A21.
DOI: [10.1051/0004-6361/202140366](https://doi.org/10.1051/0004-6361/202140366).
- Racine, René, Gordon A. H. Walker, Daniel Nadeau, René Doyon & Christian
Marois. 1999. Speckle Noise and the Detection of Faint Companions. 111(759).
587–594. DOI: [10.1086/316367](https://doi.org/10.1086/316367).
- Ragazzoni, Roberto. 1996. Pupil plane wavefront sensing with an oscillat-
ing prism. *Journal of Modern Optics* 43(2). 289–293. DOI: [10 . 1080 /
09500349608232742](https://doi.org/10.1080/09500349608232742).

- Rameau, J., G. Chauvin, A. -M. Lagrange, A. Boccaletti, S. P. Quanz, M. Bonnefoy, J. H. Girard, P. Delorme, S. Desidera, H. Klahr, C. Mordasini, C. Dumas & M. Bonavita. 2013. Discovery of a Probable 4-5 Jupiter-mass Exoplanet to HD 95086 by Direct Imaging. *772(2)*, L15. DOI: [10.1088/2041-8205/772/2/L15](https://doi.org/10.1088/2041-8205/772/2/L15).
- Roddiier, F. & C. Roddiier. 1997. Stellar Coronagraph with Phase Mask. *109*. 815–820. DOI: [10.1086/133949](https://doi.org/10.1086/133949).
- Rouan, D., P. Riaud, A. Boccaletti, Y. Clénet & A. Labeyrie. 2000. The Four-Quadrant Phase-Mask Coronagraph. I. Principle. *112(777)*. 1479–1486. DOI: [10.1086/317707](https://doi.org/10.1086/317707).
- Rousselet-Perraut, K., E. Stadler, P. Feautrier, E. Le Coarer, P. Petmezakis, P. Haguenauer, P. Kern, F. Malbet, J. -P. Berger, I. Schanen-Duport, P. Benech & L. Delage. 1999. The Integrated Optics Near-infrared Interferometric Camera (IONIC). In Stephen Unwin & Robert Stachnik (eds.), *Working on the fringe: optical and ir interferometry from ground and space*, vol. 194 (Astronomical Society of the Pacific Conference Series), 344.
- Samra, Dominic, Christiane Helling, Katy Chubb, Michiel Min, Ludmila Carone & Aaron Schneider. 2022. Clouds form on the hot Saturn JWST ERO target WASP-96b. *arXiv e-prints*, arXiv:2211.00633. arXiv:2211.00633.
- Sanny, A., S. Gross, L. Labadie, D. Defrère, A. Bigioli, R. Laugier, C. Dandumont & M. Withford. 2022. Development of the four-telescope photonic nuller of Hi-5 for the characterization of exoplanets in the mid-IR. In Antoine Mérand, Stephanie Sallum & Joel Sanchez-Bermudez (eds.), *Optical and infrared interferometry and imaging viii*, vol. 12183 (Society of Photo-Optical Instrumentation Engineers (SPIE) Conference Series), 1218316. DOI: [10.1117/12.2628903](https://doi.org/10.1117/12.2628903).
- Schwartz, Noah, Edgard Renault, William Ceria, Martin Black, Kjetil Dohlen, Kacem El Hadi, Jean-François Sauvage, Lisa Bardou, Tim Morris, Benoit Neichel, Thierry Fusco, Fraser Clarke, David Melotte & Niranjana Thatte. 2022. HARMONI at ELT: adaptive optics calibration unit from design to prototyping. In Laura Schreiber, Dirk Schmidt & Elise Vernet (eds.), *Adaptive optics systems viii*, vol. 12185 (Society of Photo-Optical Instrumentation Engineers (SPIE) Conference Series), 121855E. DOI: [10.1117/12.2627247](https://doi.org/10.1117/12.2627247).
- Scott, N. J., R. Millan-Gabet, E. Lhomé, T. A. Ten Brummelaar, V. Coudé Du Foresto, J. Sturmann & L. Sturmann. 2013. Jouvence of Fluor: Upgrades of a Fiber Beam Combiner at the CHARA Array. *Journal of Astronomical Instrumentation* *2(2)*, 1340005. DOI: [10.1142/S2251171713400059](https://doi.org/10.1142/S2251171713400059).
- Serabyn, E., B. Mennesson, M. M. Colavita, C. Koresko & M. J. Kuchner. 2012. The Keck Interferometer Nuller. *748(1)*, 55. DOI: [10.1088/0004-637X/748/1/55](https://doi.org/10.1088/0004-637X/748/1/55).

- Serabyn, E., B. Mennesson, S. Martin, K. Liewer & J. Kühn. 2019. Nulling at short wavelengths: theoretical performance constraints and a demonstration of faint companion detection inside the diffraction limit with a rotating-baseline interferometer. 489(1). 1291–1303. DOI: [10.1093/mnras/stz2163](https://doi.org/10.1093/mnras/stz2163).
- Serabyn, E., B. Mennesson, S. Martin, K. Liewer, D. Mawet, C. Hanot, F. Loya, M. M. Colavita & Sam Ragland. 2010. The potential of rotating-baseline nulling interferometers operating within large single-telescope apertures. In William C. Danchi, Françoise Delplancke & Jayadev K. Rajagopal (eds.), *Optical and infrared interferometry ii*, vol. 7734 (Society of Photo-Optical Instrumentation Engineers (SPIE) Conference Series), 77341E. DOI: [10.1117/12.857753](https://doi.org/10.1117/12.857753).
- Serabyn, Eugene. 2000. Nulling interferometry: symmetry requirements and experimental results. In Pierre Léna & Andreas Quirrenbach (eds.), *Interferometry in optical astronomy*, vol. 4006 (Society of Photo-Optical Instrumentation Engineers (SPIE) Conference Series), 328–339. DOI: [10.1117/12.390223](https://doi.org/10.1117/12.390223).
- Shack, R. V., J. D. Rancourt & H. Morrow. 1971. Effects of dilution on a six-element synthetic aperture. 10(2). 257–259. DOI: [10.1364/AO.10.000257](https://doi.org/10.1364/AO.10.000257).
- Shao, M. & D. H. Staelin. 1980. First fringe measurements with a phase-tracking stellar interferometer. 19. 1519–1522. DOI: [10.1364/AO.19.001519](https://doi.org/10.1364/AO.19.001519).
- Silaj, J. & J. D. Landstreet. 2014. Accurate age determinations of several nearby open clusters containing magnetic Ap stars. 566, A132. A132. DOI: [10.1051/0004-6361/201321468](https://doi.org/10.1051/0004-6361/201321468).
- Soldano, Lucas B. & Erik C. M. Pennings. 1995. Optical multi-mode interference devices based on self-imaging: principles and applications. *Journal of Light-wave Technology* 13(4). 615–627. DOI: [10.1109/50.372474](https://doi.org/10.1109/50.372474).
- Tatulli, E., F. Millour, A. Chelli, G. Duvert, B. Acke, O. Hernandez Utrera, K. -H. Hofmann, S. Kraus, F. Malbet, P. Mège, R. G. Petrov, M. Vannier, G. Zins, P. Antonelli, U. Beckmann, Y. Bresson, M. Dugué, S. Gennari, L. Glück, P. Kern, S. Lagarde, E. Le Coarer, F. Lisi, K. Perraut, P. Puget, F. Rantakyro, S. Robbe-Dubois, A. Roussel, G. Weigelt, M. Accardo, K. Agabi, E. Altariba, B. Arezki, E. Aristidi, C. Baffa, J. Behrend, T. Blöcker, S. Bonhomme, S. Busoni, F. Cassaing, J. -M. Clause, J. Colin, C. Connot, A. Delboulbé, A. Domiciano de Souza, T. Driebe, P. Feautrier, D. Ferruzzi, T. Forveille, E. Fossat, R. Foy, D. Fraix-Burnet, A. Gallardo, E. Giani, C. Gil, A. Glentzlin, M. Heiden, M. Heininger, D. Kamm, M. Kiekebusch, D. Le Contel, J. -M. Le Contel, T. Lesourd, B. Lopez, M. Lopez, Y. Magnard, A. Marconi, G. Mars, G. Martinot-Lagarde, P. Mathias, J. -L. Monin, D. Mouillet, D. Mourard, E. Nussbaum, K. Ohnaka, J. Pacheco, C. Perrier, Y. Rabbia, S. Rebattu, F. Reynaud, A. Richichi, A. Robini, M. Sacchettini, D. Schertl, M. Schöller, W. Solscheid, A. Spang, P. Stee, P. Stefanini, M. Tallon, I. Tallon-Bosc, D. Tasso, L. Testi, F. Vakili, O. von der Lühe, J. -C. Valtier & N. Ventura.

2007. Interferometric data reduction with AMBER/VLTI. Principle, estimators, and illustration. 464(1). 29–42. DOI: [10.1051/0004-6361:20064799](https://doi.org/10.1051/0004-6361:20064799).
- Thatte, Niranjan, Mathias Tecza, Fraser Clarke, Roger L. Davies, Alban Remilieux, Roland Bacon, David Lunney, Santiago Arribas, Evencio Mediavilla, Fernando Gago, Naidu Bezawada, Pierre Ferruit, Ana Fragoso, David Freeman, Javier Fuentes, Thierry Fusco, Angus Gallie, Adolfo Garcia, Timothy Good-sall, Felix Gracia, Aurelien Jarno, Johan Kosmalski, James Lynn, Stuart McLay, David Montgomery, Arlette Pecontal, Hermine Schnetler, Harry Smith, Dario Sosa, Giuseppina Battaglia, Neil Bowles, Luis Colina, Eric Emsellem, Ana Garcia-Perez, Szymon Gladysz, Isobel Hook, Patrick Irwin, Matt Jarvis, Robert Kennicutt, Andrew Levan, Andy Longmore, John Magorrian, Mark McCaughrean, Livia Origlia, Rafael Rebolo, Dimitra Rigopoulou, Sean Ryan, Mark Swinbank, Nial Tanvir, Eline Tolstoy & Aprajita Verma. 2010. HARMONI: a single-field wide-band integral-field spectrograph for the European ELT. In Ian S. McLean, Suzanne K. Ramsay & Hideki Takami (eds.), *Ground-based and air-borne instrumentation for astronomy iii*, vol. 7735 (Society of Photo-Optical Instrumentation Engineers (SPIE) Conference Series), 77352I. DOI: [10.1117/12.857445](https://doi.org/10.1117/12.857445).
- Trauger, John T., Chris Burrows, Brian Gordon, Joseph J. Green, Andrew E. Lowman, Dwight Moody, Albert F. Niessner, Fang Shi & Daniel Wilson. 2004. Coronagraph contrast demonstrations with the high-contrast imaging testbed. In John C. Mather (ed.), *Optical, infrared, and millimeter space telescopes*, vol. 5487 (Society of Photo-Optical Instrumentation Engineers (SPIE) Conference Series), 1330–1336. DOI: [10.1117/12.552520](https://doi.org/10.1117/12.552520).
- Trauger, John T. & Wesley A. Traub. 2007. A laboratory demonstration of the capability to image an Earth-like extrasolar planet. 446(7137). 771–773. DOI: [10.1038/nature05729](https://doi.org/10.1038/nature05729).
- Ulrich, R. 1975. Light-propagation and imaging in planar optical waveguides. *Nouvelle Revue d'Optique* 6(5). 253–262. DOI: [10.1088/0335-7368/6/5/302](https://doi.org/10.1088/0335-7368/6/5/302).
- van Cittert, P. H. 1934. Die Wahrscheinliche Schwingungsverteilung in Einer von Einer Lichtquelle Direkt Oder Mittels Einer Linse Beleuchteten Ebene. *Physica* 1(1). 201–210. DOI: [10.1016/S0031-8914\(34\)90026-4](https://doi.org/10.1016/S0031-8914(34)90026-4).
- Velusamy, T. & C. A. Beichman. 2001. Nulling interferometry for extra-solar planet detection: sensitivity and image reconstruction. In UNKNOWN. DOI: [2014/16305](https://doi.org/10.1016/16305). <https://hdl.handle.net/2014/16305>.
- Wolszczan, A. & D. A. Frail. 1992. A planetary system around the millisecond pulsar PSR1257 + 12. 355(6356). 145–147. DOI: [10.1038/355145a0](https://doi.org/10.1038/355145a0).

- Woolf, N. J. & J. R. P. Angel. 1997. Planet Finder Options I: New Linear Nulling Array Configurations. In David Soderblom (ed.), *Planets beyond the solar system and the next generation of space missions*, vol. 119 (Astronomical Society of the Pacific Conference Series), 285.
- York, Donald G. et al. 2000. The Sloan Digital Sky Survey: Technical Summary. 120(3). 1579–1587. DOI: [10.1086/301513](https://doi.org/10.1086/301513).
- Zernike, F. 1934. Diffraction theory of the knife-edge test and its improved form, the phase-contrast method. 94. 377–384. DOI: [10.1093/mnras/94.5.377](https://doi.org/10.1093/mnras/94.5.377).
- Zernike, F. 1938. The concept of degree of coherence and its application to optical problems. *Physica* 5(8). 785–795. DOI: [10.1016/S0031-8914\(38\)80203-2](https://doi.org/10.1016/S0031-8914(38)80203-2).
- Zuckerman, B. 2019. The Nearby, Young, Argus Association: Membership, Age, and Dusty Debris Disks. 870(1), 27. 27. DOI: [10.3847/1538-4357/aace66](https://doi.org/10.3847/1538-4357/aace66).